Development of Processing Strategies for the Additive Layer Manufacture of Aerospace Components in Inconel 718

Robert James Deffley

The University Of Sheffield.

Thesis submitted for the degree of Doctor of Philosophy

Department of Materials Science and Engineering
The University of Sheffield

January 2012

Abstract

Additive Layer Manufacturing, ALM, of metal components has been steadily developed over the past decade. Further work is necessary to understand the metallurgical response of alloys to user defined processing parameters to establish the robustness of individual ALM systems and how the response affects microstructure and mechanical properties. This thesis addresses several areas to this end for the Nickel-Iron superalloy Inconel 718;

- Identification of key process variables for two types of commercially available additive systems (powder-bed EOS M270 and blown-powder Trumf DMD505).
- Development of a processing theme for Inconel 718 on the EOS M270 to build simple 3D shapes.
- The melting response to user defined variables.
- Analytical modelling of the melt pool geometry and the local solidification conditions (i.e. cooling rate, temperature gradient, and isotherm velocity).
- A microstructural investigation of the as-deposited grain structure
- Simple mechanical testing.

Statistical Design of Experiments (DOE) in the form of Central Composite Design (CCD) was used extensively to minimise experimental effort throughout the project.

For the investigation of the EOS M270, processing maps were produced to identify a processing window where fully-dense, pore-free parts were obtained with the key variables being beam velocity and offset distance between adjacent melted lines. This was necessary as Inconel 718 had no defined processing conditions at the time of the investigation.

Test samples were built and their microstructure investigated for a range of processing conditions. The grain structure of all samples was seen to consist of fine, dendritic, columnar grains orientated with a strong <001> fibre texture aligned perpendicular to the horizontal layers being melted.

The DMD505 investigation considered single track thin walls deposited over a range of laser powers and beam velocities. The grain structures obtained varied across the process window but did not fit into classical 'equiaxed' or 'columnar' morphologies. 'Mixed' microstructures consisting of long grains which are continuous across melted layer boundaries and short discontinuous grains were

observed at high laser powers and beam velocities. This corresponded to fluctuations in the top surface of the weld tracks. At lower powers, long continuous grains were observed along the total wall height. As velocity decreases there is a change to elongated grains which are contained within a single melted layer.

Melt pool geometry and solidification conditions were modelled using analytical heat transfer equations which showed good agreement (±10%) with experimental results for geometry and cooling rate for both processes. The shape of the melt pool is shown to influence heavily the resulting grain structure.

Other materials and processing issues in ALM are considered such as surface roughness and thermally induced stress. These are discussed in relation to material response to user defined processing parameters and a material's thermal and physical properties which are related by underlying heat transfer equations. Material selection charts are used to compare the properties of different engineering alloys which in turn can be used as a basis for parameter selection during processing.

Contents

List of figures

List of tables

Nomenclature

Symbol	**Definition**	*Units*
A	Surface area	m^2
b	Wall thickness	m
bcc	Body centred cubic	-
bct	Body centred tetragonal	-
c	Specific heat capacity	J/kgK
CCD	Central composite design	-
CET	Columnar to equiaxed transition	-
D	Thermal diffusivity	m^3/s
df_s/dt	Rate of formation of solid	$atoms/s$
DOE	Design of experiments	-
DS	Directional solidification	-
dT/dr	Temperature gradient	K/m
dT/dt	Cooling rate	K/s
e	Charge on electron, $1.6x10^{-19}$	C
E	Young's modulus	GPa
E_ρ	Specific energy or energy density (linear, surface, volume)	J/mm, J/mm^2, J/mm^3
fcc	Face centred cubic	-
FZ	Fusion zone	-
G	Temperature gradient	K/m
h	Plank's constant, $6.6x10^{-34}$	Js
H/LAGB	High/low angle grain boundary	-
hcp	Hexagonal close packed	-
k	Thermal conductivity	W/mK
$K_{0/1}$	Modified Bessel function of the second kind order 0/1	-
k_B	Boltzmann constant, $1.38x10^{-23}$	J/K
K_e	Thermal conductivity of electron	-
k_e	Effective partition coefficient	-
L_0	Constant = $\pi^2/3$	-
M	Mass of electron, $9.1x10^{-31}$	kg
MUD	Multiples of uniform distribution	-
OIM	Orientation imaging map	-
OS	Beam offset	m
P	Laser power	W
Q	Activation energy for self-diffusion	kJ/mol

Q	Heat flux	-
Q	Laser power	W
R	Beam radius	m
R	Distance from heat source	m
R_a	Surface roughness	m
RMS	Root mean square	-
SEM	Scanning electron microscopy	-
SS	Sum of square	-
SX	Single crystal	-
T	Temperature	$°C, K$
T_0	Substrate temperature	$°C, K$
TCP	Topologically close packed	-
TEM	Transmission electron microscopy	-
TEM	Transverse electromagnetic mode	-
TET	Turbine entry temperature	-
$T_{l/s}$	Liquidus/solidus temperature	$°C, K$
V	Accelerating voltage	kV, keV
V	Growth velocity	m/s
V	Poisons ratio	-
V	Volume	$m3$
v_b	beam velocity	m/s
V_{ios}	Isotherm velocity	m/s
α	Absorption coefficient	-
α	Fitting parameter	-
α	Semi-angle	°
α	Thermal diffusivity	
α_{CTE}	Coefficient of thermal expansion	K^{-1}
γ	Gamma matrix	-
γ'	Gamma-prime precipitate	-
γ''	Gamma-double-prime precipitate	-
Δh_f	Latent heat of fusion per unit volume	kJ/mol
$\eta\lambda$	Absorptivity	-
θ	Meltpool inclination angle	°
λ	Wavelength	m
$\lambda_{1,2}$	Primary/secondary dendrite arm spacing	m
$\rho(T)$	Electrical resistivity	Ωm
Σ	Thermal conductivity	W/mK

Acknowledgements

I would like to thank everyone who has made the completion of this thesis possible, there are far too many people to name individually but their work in whatever capacity is very much appreciated. Above all I would like to offer special thanks to the following people;

I thank my Supervisor Dr Iain Todd who I have had the pleasure of working with for many years now. Without his support, dedication and hard work I cannot begin to imagine where I would be today. His technical knowledge has been invaluable and his enthusiasm for his work a constant inspiration.

I would like to acknowledge the financial support of the EPSRC and TWI: The Welding Institute, who have funded this work. I also thank Dr Rob Scudamore and Dr Phil Carroll for their technical input, time and use of equipment at TWI South Yorkshire.

I acknowledge the work done by Martyn Jones (Masters Student, University of Sheffield) for work carried out on Inconel 625 in parallel to this project which has been used for comparison. I also acknowledge the work done by Dr Wufei Zhang (PDRA, the University of Sheffield), Dr Richard Moat (PDRA, the University of Manchester) and Professor Michael Preuss (the University of Manchester) for the residual stress work used to support some of the discussion in Chapter 6.

The Technical Staff in the Department of Engineering Materials have worked tirelessly to maintain equipment and provide training and assistance throughout my project and without their efforts we would all be lost.

I thank my colleagues at the University; Academic Staff and Students, and especially the numerous members of D1 for endless support and countless laughs on a daily basis. In particular I thank Dr Mike Blackmore and Dr Sinan Al-Bermani, without whom the work on ALM would have been lonely!

It goes without saying that I thank and I love my family for supporting me throughout. Mum, Dad, Lou and John, and Grandma Iris, your constant encouragement has seen me through all the tough times and I couldn't have done it without you.

My friends have been superb at providing the often-needed distractions; the fun times shared will never be forgotten. I especially thank the Lads; Ryan, Craig, Tom, Drew and Rich, and all of The Gig-goers.

Charlotte, I don't even know where to begin. You have been amazing. You have put up with me through the toughest part of all, and I would not have survived writing-up without you. Your patience has been that of a saint and all the messages I (still) keep finding bring a much needed smile to my face every day. I am sorry for how distracted I have been and am very much looking forward to all the adventures we are now free to have. Loves you x

1 Introduction

Additive Layer Manufacturing, ALM, of metal components has been developed from the Rapid Prototyping industry over the past decade and is becoming accepted as a manufacturing option for a wide range of products. The manufacture of tooling and moulds, for example, is common and increasing interest has come from the aerospace, biomedical and automotive industries as the benefits of ALM are hoped to be exploited. For this to happen there must be considerable research into microstructure and properties of engineering alloys from part production through to post-process treatments such as finishing procedures and heat treatments. This knowledge will facilitate the transition of ALM processes from an area such as prototyping were a components '*form*' is critical to one of structural component manufacturing where '*function*' is of highest importance.

The aim of the present work is to investigate the effect of key process variables of two ALM systems (the EOS M270 *Powder-bed* system at The University Of Sheffield and the Trumf DMD505 which as a *Blown-powder* technique at TWI: The Welding Institute, South Yorkshire) on the melting response and solidification microstructure of Nickel alloy Inconel 718. Processing maps are produced which enable the production of structurally sound (fully-dense) parts and which will show the effect of processing parameters on solidification conditions with the view to identifying parameters which can significantly alter the deposited grain structure.

Statistical Design of Experiments (DOE) is employed to minimise the experimental effort by reducing the number of tests to be carried out and to test the accuracy and significance of the relationships between processing parameters and the measured responses.

Chapter 4 begins with the development of a processing theme for Inconel 718 on the EOS M270 which, at present, does not exist by considering the effect of processing parameters on the size, shape and overlap of individual weld tracks. This is expanded on to build simple 3D structures and the effect of processing parameters on porosity, surface roughness and microstructure is investigated.

Chapter 5 of the thesis looks at the effect of processing parameters on the microstructure of laser deposited thin walls using the DMD 505, in both Chapters 4 and 5, modelling of the solidification conditions is carried out to explain the observed microstructures.

Chapter 6 introduces a discussion of the rationale for selecting processing parameters for new materials for ALM and other considerations which should be taken into account such as material properties and their implications on melting and processing.

2 Literature review

This chapter provides an introduction to laser processing of materials and a description of Additive Manufacturing (AM). The current focus of research into AM is discussed, in particular the processing of Nickel-based Superalloys and the relevance to the aerospace industry.

The underlying physical processes of solidification during laser melting are presented and current examples of heat transfer modelling are explored.

The use of statistically designed experiments for process control and optimisation is introduced through studies spanning a broad range of the manufacturing industry.

2.1 Superalloys

2.1.1 Superalloys for high temperature applications

'The Superalloys' are a class of high-temperature materials used in such applications as gas turbine engines because of their ability to maintain structural integrity at elevated temperatures and their ability to withstand harsh, corrosive environments. The main drive for their development came with the necessity to increase Turbine Entry Temperatures (TET) in jet engines as higher temperatures result in improved efficiency and hence better fuel economy along with an increase in power output as shown in Figure 2.1(a). (Donachie 2002, Reed 2006). This required the development of new alloys, processing methods and the introduction of cooled turbine blades and thermal barrier coatings as described graphically in Figure 2.1(b).

Three categories of superalloy exist; originally Iron-based superalloys were developed from advances in stainless steels, followed by high temperature Cobalt- and Nickel-based alloys. All three types have a face centred cubic (fcc) crystal structure, this is inherent in Ni-based alloys but is brought about by alloying additions in Fe-based and Co-based alloys which stabilise the high temperature fcc structures associated with Fe and Co. Superalloys do not undergo phase transformations with changing temperature and so any limits to their high temperature properties can be attributed to incipient melting of secondary phases and the dissolution of strengthening phases such as precipitates.

(a)

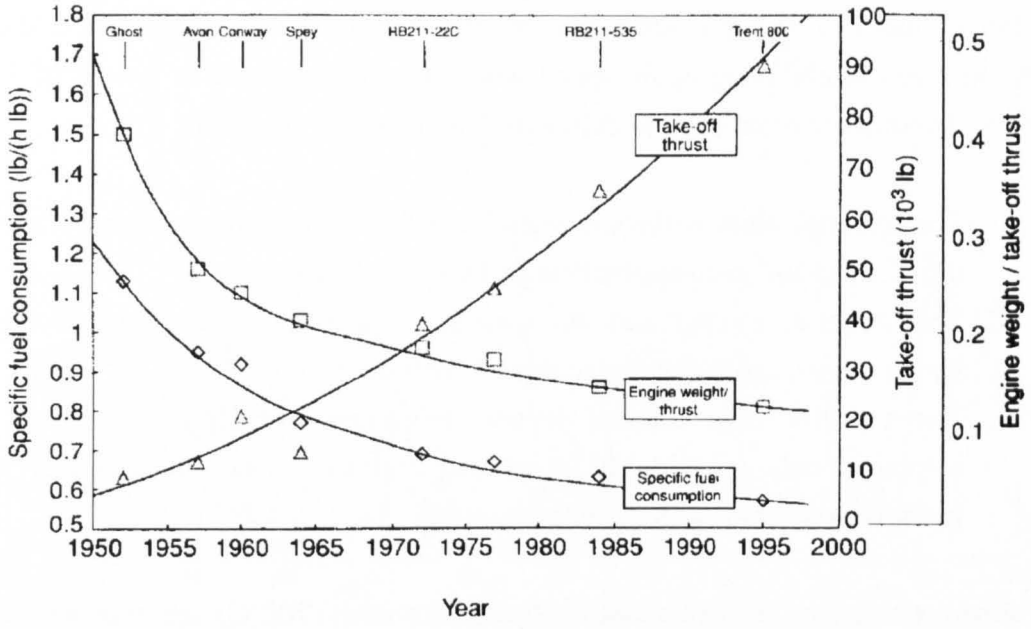

(b)

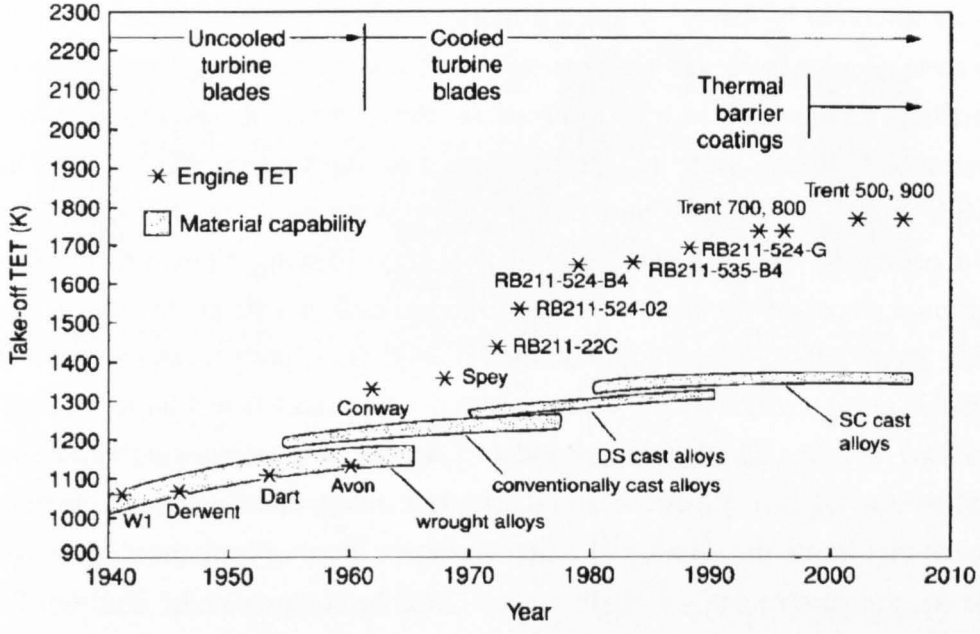

Figure 2.1 – (a) efficiency of aero-engines and (b) turbine entry temperature as a function of the year specific alloys were developed (from Reed 2006).

Superalloys are classed as 'high temperature materials' which means they have the ability to maintain their properties consistently with increasing temperature, they are used in many engineering applications where temperatures are in excess of 700°C. Three attributes are often used to define high temperature materials:

1. The material must withstand significant load at homologous temperatures of 0.6 ($0.6T_m$) and even approaching its melting temperature.
2. The material must resist mechanical degradation over time at elevated temperatures, i.e. thermally activated, inelastic creep.
3. The material must tolerate severe environments such as hot gases, high sulphur levels (i.e. highly corrosive) and the intake of seawater which promotes oxidation at high temperatures.

Where moderate temperatures (up to approximately 700°C) are experienced, Fe-Ni-based alloys are utilised because of their lower cost, when higher temperatures must be tolerated Ni-based alloys are more suitable. The preference of Nickel over other metals is due to its atomic/electronic structure; considering the transition metals, the melting temperature is a function of atomic number; there is a peak in melting temperature in the middle of each row of transition metal elements (Vanadium, Molybdenum and Tungsten) and an increase moving down the rows from the 3d to the 5d elements. This is shown in Figure 2.2(a). Moving from left to right in the transition metals on the periodic table also reveals a change in crystal structure, moving from left to right the structures change from body centred cubic (bcc) to hexagonal close packed (hcp) to face centred cubic (fcc) (see Figure 2.2(b)), this is due to the bonding characteristics induced by the increasing number of outer 'd' electrons. An fcc structure is desirable when a more ductile and tough material is required; this limits the number of suitable metals. Further limitation arises from cost as the fcc transition metals include the so-called 'precious metals' and the 'Platinum Group Metals', these are also undesirable in applications such as aerospace because of their high density as weight is a critical consideration.

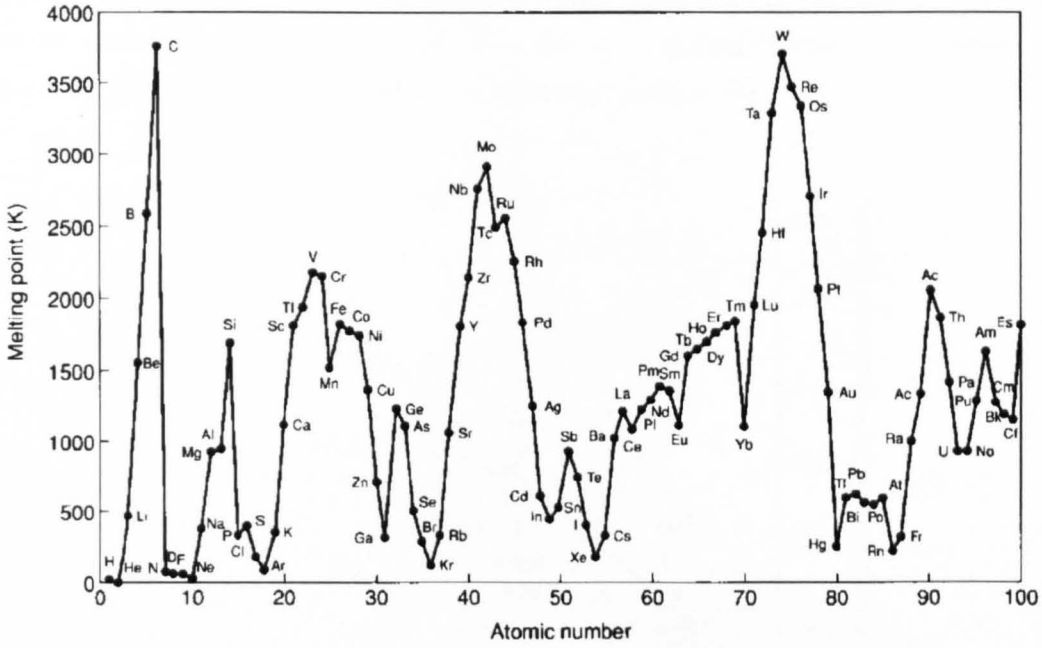

(a)

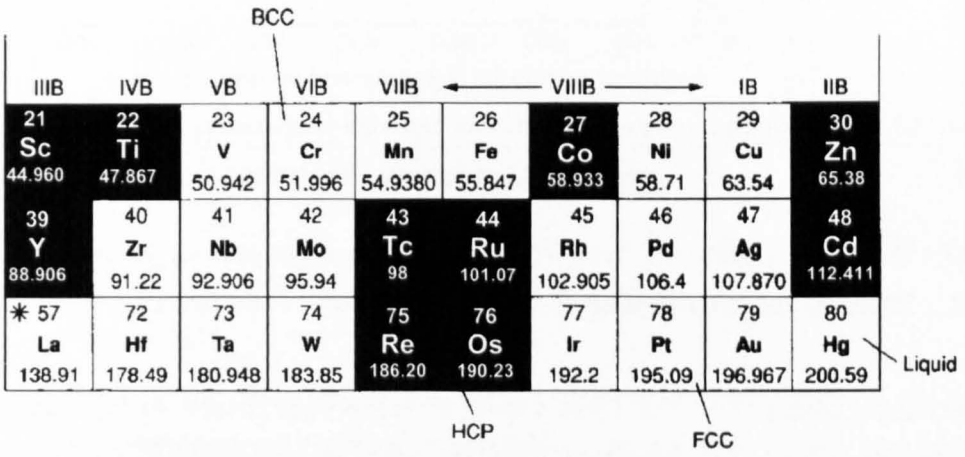

(b)

Figure 2.2 (a) Elements' melting temperature as a function of atomic number (b) section of the periodic table showing crystal structures of transition metals from bcc to hcp to fcc. (Reed 2006)

The fcc metals are also preferred due to their retention of mechanical properties at elevated temperatures. Two properties are important in this respect; the activation energy, Q, for self-diffusion and high temperature creep and the thermal diffusivity, D. For good high temperature properties, Q should be maximised and D minimised, which is the case for fcc over bcc and hcp metals, this can be seen in Figure 2.3.

Nickel fulfils these criteria by having an fcc crystal structure, which is a stable phase until its melting point. Phase transformations in other systems can result in contraction/expansion which can cause distortion and stress build up in components during service. The alternative crystal structures and materials to fcc Nickel are discounted for various reasons; for example hcp Cobalt has found use but is more expensive than nickel. Re and Ru are very expensive and so are used as alloying

additions in superalloys only. Os forms a poisonous oxide and Tc is radioactive. Bcc Cr suffers from lower ductility.

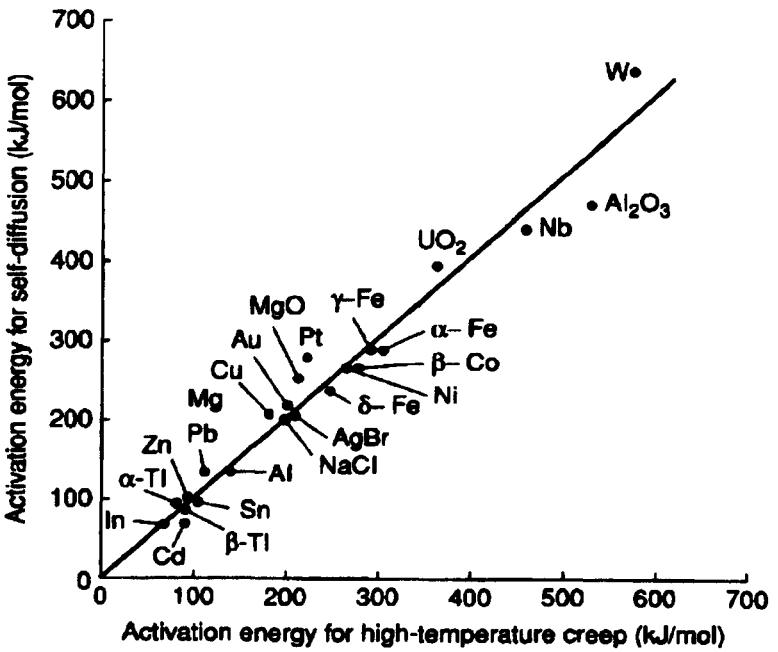

Figure 2.3 – Activation energies of self-diffusion and high temperature creep for different metals, phases and metal oxides. (Reed 2006)

2.1.2 Historical development of superalloys

Superalloys emerged in the 1940's with development driven by the need for high temperature alloys for aerospace. Data is often reported relative to turbine blade applications where high temperature creep properties are paramount and discussed as a function of alloy composition and processing route. Early Ni-based materials were produced by traditional ingot metallurgy; however these had limited creep strength compared to materials processed by powder metallurgy due to the high degree of segregation on freezing when solute concentrations are large (Williams 2003).

Figure 2.4 depicts the development of creep properties in superalloys. Early properties in wrought alloys were improved by alloy development until vacuum induction casting technology was introduced in the 1950's which further improved properties through better cleanliness. Improvements in casting processes followed to greatly improve creep life in turbine blade alloys until Directionally Solidified (DS) blades were developed to give a columnar grain structure thus removing transverse grain boundaries which limited creep tolerance. Later still, the development of Single Crystal (SX) blades meant that grain boundaries were absent and hence led to the removal of grain boundary strengthening elements Boron and Carbon. This in turn

resulted in improved heat treatments with reduced micro-segregation and eutectic formation during casting which result from the inclusion of Carbon and Boron, this removed the risk of incipient melting and improved fatigue life.

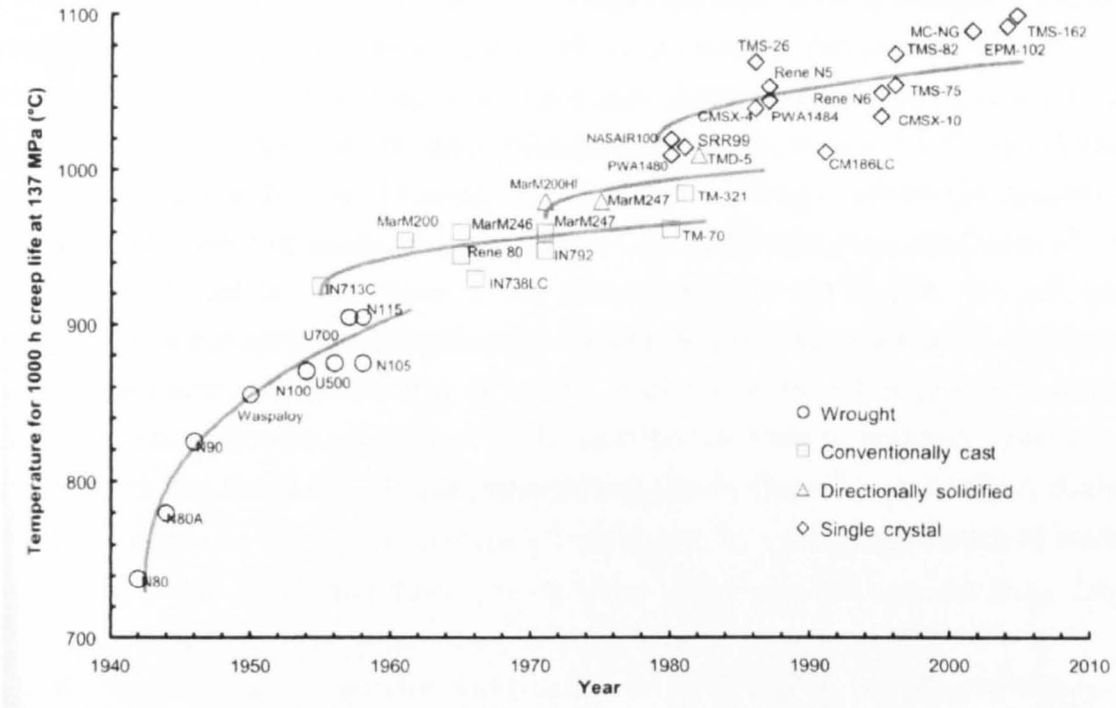

Figure 2.4 – Improvement in high temperature behaviour of superalloys since the 1940's to current alloys used in modern aero-engines (Reed 2006)

Since the 1980's, the first generation of SX alloys, improvements were made through better understanding physical mechanisms which affect high temperature behaviour. The first generation (G1) alloys contained appreciable amounts of Al, Ti and Ta which form γ' (Gamma-prime) precipitates $Ni_3(Al,Ti,Ta)$ in volume fractions as high as 75% which improves creep life.

The G2 alloys contained 3% Re which increased to 6% in the G3 alloys replacing W and Ta due to its increased potency to provide solid-solution strengthening. Modern alloys contain less Cr and more Al and Re as Cr is a γ (Gamma matrix) stabiliser; however Al forms Al_2O_3 instead of Cr_2O_3 which reduces the hot corrosion resistance. The Ti content was also reduced as it increases the oxidation rate which has a negative effect on the retention of thermal barrier coatings. The G4 alloys contain Ru in place of Re since Re promotes the formation of Topologically Closed Packed (TCP) phases which reduce rupture life.

In turbine disc applications the component is designed to resist general yielding and low-cycle fatigue cracking rather than high temperature creep and as such the emphasis of processing is on grain refinement and γ' precipitation.

2.1.3 Physical metallurgy of superalloys

Superalloys often contain more than ten alloying additions resulting in complex alloy systems. Their high-end applications in the aerospace industry mean that superalloys have been studied in great detail and much is known about their often complex metallurgy. There are some broad rules which apply to the roles of certain alloying additions; Superalloys typically contain Cr, Co, Al and Ti as well as small amounts of B, Zr and C. In some alloys Re, W, Ta and Hf (5d block transition metal elements) and Ru, Mo, Nb, Zr (4d block elements) and in alloys such as Inconel 718, Fe is present in significant amounts. The role of some alloying elements in a superalloy are outlined in Figure 2.5, for example Zr, B and C will, under appropriate processing conditions, partition to grain boundaries, Al, Ti and Nb are among several elements which partition to secondary phases (precipitates) and W, Mo and Re all favour the γ phase (the matrix).

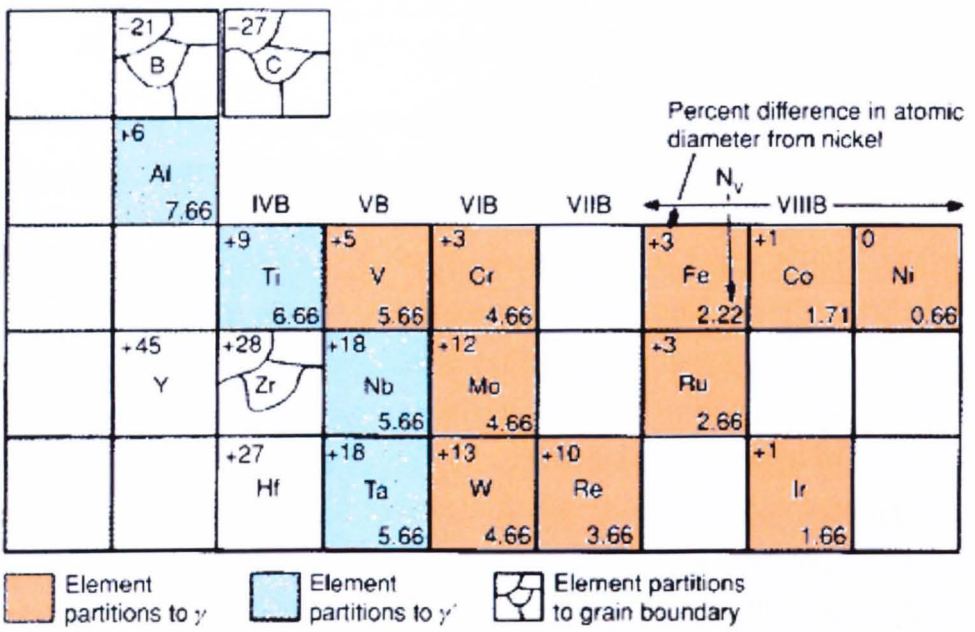

Figure 2.5 – Section of the periodic table of elements showing common metals used in superalloys and their partitioning characteristics. (Reed 2006)

Typical Superalloys are made up of an austenitic Ni matrix (γ) with the following additions:

1. Co, Fe, Cr, Re and W have similar atomic radii to Ni and partition to the γ phase and have stabilising effect.
2. Al, Ti, Nb, and Ta have larger atomic radii and so promote the formation of ordered second phases such as γ', Ni_3(Al, Ti, Ta) and γ", Ni_3Nb.
3. B, C and Zr have different atomic radii compared to Ni and segregate to the grain boundaries of the γ matrix
4. Cr, Mo, W, Nb, Ta and Ti also form carbides when present in the right concentrations and after appropriate processing.
5. Cr and Mo also form Borides
6. Co, Cr, Mo, Ru and Re provide solid solution strengthening of the matrix

The typical microstructure of Superalloys contains a combination of phases, including the following;

1. A continuous, solid solution, fcc matrix (γ).
2. A coherent, fcc, $L1_2$ precipitate (γ') which acts as a strengthening phase.
3. In Fe-Ni alloys, and those rich in Nb, a body-centred tetragonal (bct), $D0_{22}$ ordered precipitate is the strengthening phase (γ").
4. Grain boundary carbides and borides; at carbon levels of 0.2wt% MC-type carbides (M=Ti, Ta, Hf) are formed which can decompose in service to $M_{23}C_6$ and M_6C (M=Cr, Mo, W).
5. Topologically Closed Packed (TCP) phases such as μ (bct Ni_2Ta), σ (btc $CrMo_xNiCo_y$) and Laves phases (hcp Fe_2Ti,Mo Ni_2Nb and fcc Co_2Ta). These often form in the service-aged condition and are generally considered detrimental to mechanical properties, an alloy's composition is chosen to minimise the chance of forming these phases.

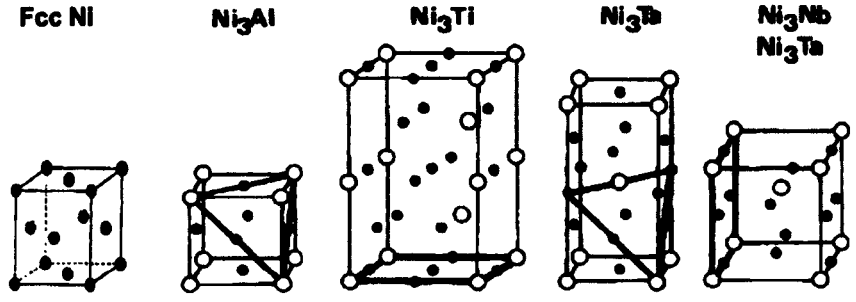

Figure 2.6 – Unit cells for various common phases in Superalloys (Durand-Charre 1997)

2.1.4 Fe-based/rich alloys

Fe is much cheaper than Ni and so is an attractive addition to Ni-based alloys in significant amounts. However the electronic structure of Fe has an increased propensity to form the embrittling TCP phases than Ni, this has the effect of reducing the amount of other alloying elements that can be tolerated. Replacing Ni with Fe also reduces the oxidation resistance. The electronic structure of Fe also means that Fe-rich alloys favour the formation of alternate secondary phases to the γ' strengthening phase, which if present at all is metastable. γ' provides the most efficient strengthening, other phases tend to form coarse platelets and long exposure at temperatures in excess of 650°C turns γ' into η which leads to a reduction in strength (Durand-Charre 1997).

Alternative practice is to add Nb which will form a stable orthorhombic δ (Ni_3Nb) which itself is not an effective strengthening phase, but at moderate temperatures (<650°C) a metastable, bct γ" phase. This phase is usually disc-shaped with dimensions of 10nm thickness and 50nm diameter. The high temperature properties of γ"-containing alloys arises due to the coherency strains (of several %) between the second phase and the matrix and the limited number of slip planes in the precipitate. The coherence strains also mean that the precipitation kinetics are sluggish.

The most common example of an Fe-Ni superalloy is the 718-type alloy which has γ" at levels of 11-20% giving it a higher yield strength than most γ' containing alloys. However at temperatures >650°C γ" transforms to δ, thus imposing a limit to operating temperature. Despite this limit Alloy 718, which has the trade name Inconel 718, is the most commonly used Superalloy in terms of tonnage.

The γ"-precipitate forms with specific orientation relationships as fine, coherent platelets in the matrix aligned along the <001> directions. Nucleation sites for the precipitation of γ" are provided by previously formed metastable γ' particles. Careful heat treatments are necessary to form the most effective strengthening phase which has an unusual morphology. It is necessary to initially form fine cubic γ' onto which the γ" nucleates before coating it on all six sides resulting in a stable phase with a slow coarsening rate. This is more effective as a strengthening phase than the fine platelets usually associated with γ".

2.2 Solidification processes

Solidification has been an important process for engineering materials, especially the production of metal components, and so has been subject to much research. Its importance arises since the shaping of metals is easier in the molten state since the shear stress approaches zero as the viscosity decreases, this is compared to the much higher flow stress of solid material which must be overcome in solid state forming such as forging.

Simply, solidification involves the removal of heat from a liquid, but the sophistication comes from the control of the extraction of energy and understanding the impact this has on the resulting microstructures and, in turn, the desired properties of a component. This is not only important in processes such as casting directly from the liquid but also solid state forming processes as the starting microstructure is often evident through subsequent stages (Tin 2005). Heat extraction requires the creation of a heat flux from the system which is achieved by applying a negative temperature gradient to induce cooling. The cooling rate, dT/dt, is a function of this heat flux (q) as well as the geometry (surface area to volume ratio, A/v) of the cooling liquid, the rate of formation of solid (df_s/dt), the specific heat (c), and the latent heat of fusion per unit volume (Δh_f). This is given by Equation 2.1 (Kurz 1992):

$$\frac{dT}{dt} = \dot{T} = -q\left(\frac{A}{vc}\right) + \frac{df_s}{dt}\left(\frac{\Delta h_f}{c}\right)$$

Equation 2.1

From Equation 2.1 it is shown that cooling occurs when the left-hand term is greater than the right-hand term, i.e. the rate of heat removal from the system is greater than the rate of heat generated in the system.

The heat flux is important in determining the grain structure of the solidified metal; columnar grains with a high aspect ratio are obtained in the presence of a heat-sink such as a mould wall. The columnar structure is achieved as grains grow parallel to heat flux in the opposite direction; the flux in this case is from the melt into the heat-sink. For equiaxed grains which are rounder with low aspect ratios, the melt must be supercooled and this acts as the heat sink around a nucleation site. The heat flux in this case is the same direction as growth i.e. into the melt. The local solidification conditions are important in solidification, particularly the scale of the resulting microstructure. The growth rate of the solid crystals, V, and the temperature gradient, G, are independent of each other and related to the cooling rate by Equation 2.2.

$$\dot{T} = \frac{dT}{dt} = \frac{dT}{dr} \cdot \frac{dr}{dt} = G \cdot V$$

Equation 2.2

2.2.1 Dendrites

The solidification microstructure of alloys is controlled by cooling conditions i.e. local solidification conditions (cooling rate, temperature gradient and crystal growth velocity) and by alloy composition. The resulting microstructures can be one of two basic types; dendritic (single phase) and eutectic (polyphase). The most relevant to this study is dendritic growth.

The solidification of metals and alloys can occur as a planar front or cells, however, when a stable front breaks down dendrites are formed (Kurz 1992). Cells and planar fronts grow anti-parallel to the heat flux in the system, whereas dendrites grow preferentially along specific crystallographic directions due to anisotropy in surface tension and attachment kinetics, for example, in cubic materials such as Ni-based superalloys, the preferred direction is along one of the six <001> directions. Figure 2.7 shows examples of columnar and equiaxed dendrites.

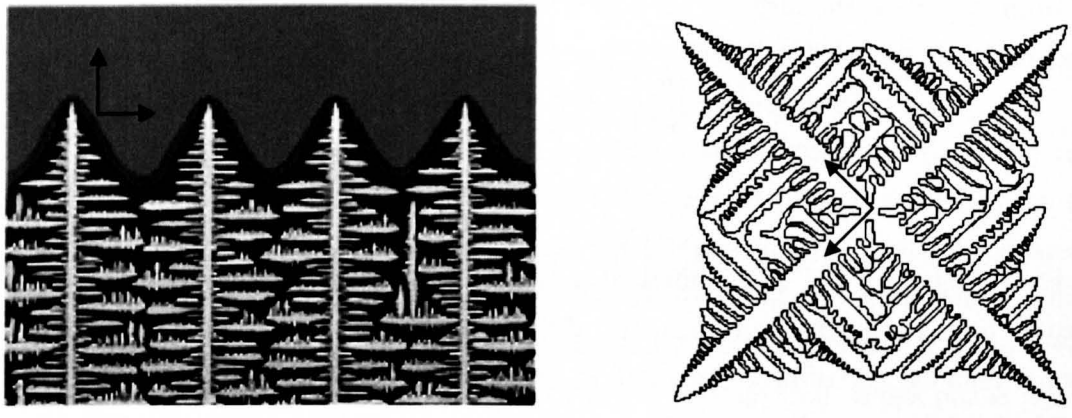

(a) **(b)**

Figure 2.7 (a) columnar and (b) equiaxed dendrites, arrows show the x-y <100> directions, the z axis is perpendicular to the page. After Wang et al. (Wang 2003). The four vertical trunks in (a) are primary dendrite arms and similarly in (b) the larger trunks forming an 'x'.

At low solidification velocities a planar solidification front is possible, i.e. a flat interface with uniform temperature (McLean 1983). As the solidification velocity increases the diffusion of solute atoms at the interface becomes localised, this causes a composition gradient ahead of the advancing front and leads to the temperature of the liquid in this region falling below the liquidus temperature. This means that the liquid

is constitutionally undercooled; in this region the planar front becomes unstable and perturbations develop and the advancing front becomes cellular, as V increases the cells become unstable and dendrites are formed. This is shown schematically in Figure 2.8;

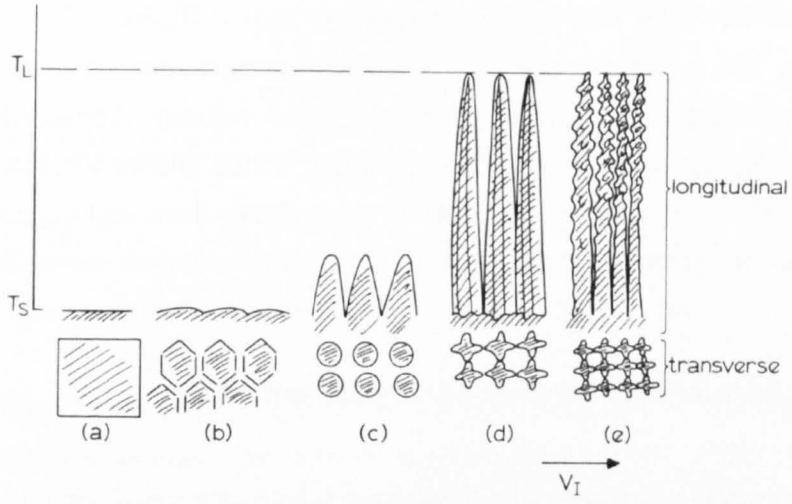

Figure 2.8 – Schematic illustration showing the change in growth morphology with increasing isotherm velocity (a) planar, (b) and (c) Cells, (d) and (e) dendrites. (McLean 1983)

Columnar dendrites are a result of *constrained* growth, as is the case in directional solidification where a heat sink is present, this means that the rate of advance of isotherms constrains the growing dendrites to grow at a specific velocity and forces them to adopt the corresponding tip undercooling. In directional growth, dendrites are typically arranged with primary trunks parallel to each other. The space between these is known as the Primary Dendrite Arm Spacing (λ_1) and is a function of the local solidification conditions. Grain boundaries are parallel to primary dendrites with low angle grain boundaries present at dendrite interfaces.

Initially, growth of a primary arm occurs followed by branching of secondary arms which are perpendicular along the other <001> directions and have a spacing λ_2 (Secondary Dendrite Arm Spacing). Ternary branching perpendicular to the secondary arms also occurs close to the solidification front, but these are mostly consumed during the growth/coarsening of secondary arms.

During directional solidification, isotherms move due to an imposed heat flux. Under these conditions, thin needle-like crystals are more likely to arise than a flat planar front as solute redistribution is more efficient, i.e. as solute is rejected from the solid there is a larger volume of liquid for it to diffuse into which leads to a smaller diffusion boundary layer compared to that of a planar interface.

During Directional Solidification of cubic metals such as Ni a <001> texture arises due to competitive growth (Reed 2006) as the <001> direction is the preferred

crystallographic growth direction for cubic crystals. Nuclei which form adjacent to a chill-block are randomly orientated, but following this, subsequent solidification is dominated by faster growing grains orientated so that the <001> direction is anti-parallel to the direction of heat transfer. After less than 1mm a strong <001> texture is established assuming that a strong temperature gradient is maintained. This occurs because dendrites grow at a rate controlled by solute diffusion. Since the solid phase grows from the liquid which has a different composition, the local dendrite-tip undercooling scales monotonically with the growth velocity. Any dendrites which are misaligned must grow at a greater undercooling which allows secondary and tertiary dendrites of perfectly aligned dendrites to grow faster than, and suppress the growth of primary arms that are misaligned.

2.2.2 Solidification during laser processing and welding

The melt pool geometry plays an important role in the development of micro- and macro-structures in welding and melting processes as this influences the direction of heat flux. Fluid flow in the pool affects weld penetration and also influences the solidification conditions; this in turn influences microstructures, segregation and porosity (David 1993). The microstructures produced by processes such as welding are complicated and difficult to interpret and have a profound effect on mechanical properties. Important parameters in the development of such microstructures are similar to casting; temperature gradient, G, growth velocity, V, degree of undercooling and alloy composition. G and V are vital in the control of grain morphology and scale of the microstructure. In the solidification region or fusion zone (FZ) the temperature gradient and growth velocity vary along the solidification front towards the rear of the pool (Liu 2004) and influences the grain morphology as depicted in Figure 2.9.

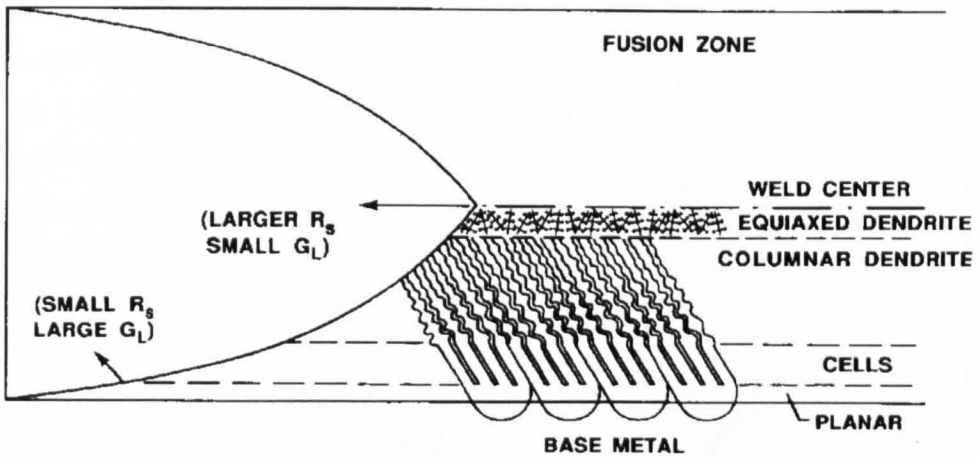

Figure 2.9 – Schematic diagram showing change in morphology along the fusion zone during welding-type processes (R_s=grain growth rate, G_L=thermal gradient in the liquid) (David 1993)

Microstructures are commonly interpreted by classic nucleation and growth theory. In welding-type solidification, the formation of the solid phase in the melt pool by homogeneous nucleation can be ignored as epitaxy dominates (Porter 1988). During autogenous welding (that is welding which does not use a filler material such as laser and electron beam welding) the special case of heterogeneous nucleation known as epitaxy occurs with virtually no barrier to nucleation, as shown in Figure 2.10. During epitaxial solidification, growth occurs by addition of atoms from the liquid to the adjacent solid. The ease at which epitaxy occurs (i.e. the kinetics of the growth process) is controlled by the solid/liquid interface structure on the atomic scale.

Additive manufacturing processes, like welding and cladding, experience directional solidification as the substrate acts as a heat-sink; this makes directional growth of the microstructure favourable and leads to columnar and even the possibility of single crystal deposits.

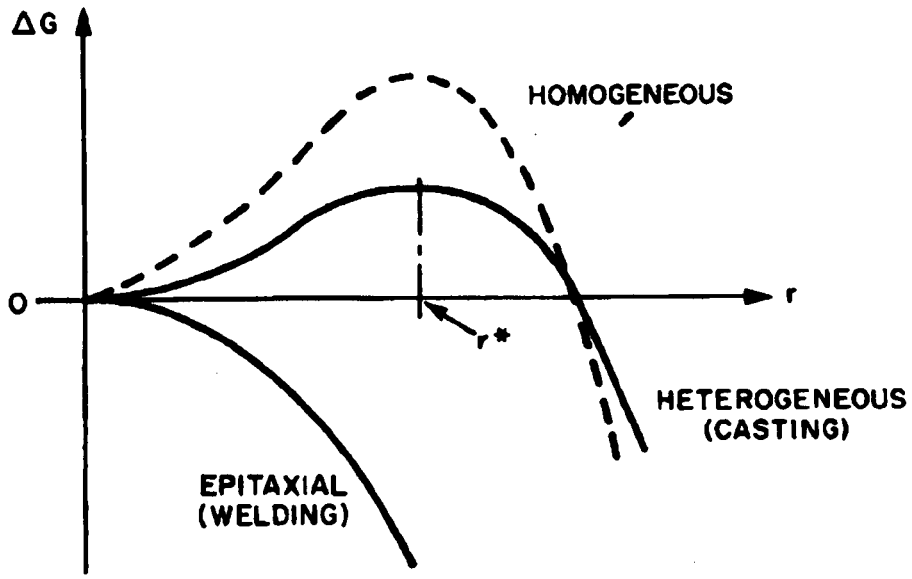

Figure 2.10 – Free energy of formation vs. particle radius for homogeneous, heterogeneous and epitaxial nucleation. (Davis 1993)

2.2.3 Columnar to equiaxed transition (CET)

Dendrites are said to grow in either a constrained or unconstrained manner. During constrained growth the rate of advance of the isotherms in the melt restrict the growth rate and forces undercooling at the tip of the growing dendrite i.e. growth is along the preferred <100> direction which is closest (but opposite) to the heat flux, this results in directional or columnar growth. In a columnar microstructure the grain boundaries are parallel to the primary dendrite arms and each dendrite forms a low angle boundary with its neighbour. Many trunks growing parallel to each other form one grain and each grain will be continuous across a solid.

During unconstrained growth it is possible for heat to flow from a crystal into the melt in all directions so the dendrite can grow freely, this results in an equiaxed microstructure made up of round, randomly orientated grains. This can be common in alloy solidification as solute atoms pile up ahead of the growing interface which causes a local change in concentration and hence local equilibrium solidus temperature. When the actual temperature of the melt (as controlled by heat extraction through the solid) is lower than the equilibrium liquidus temperature, constitutional undercooling occurs. In the undercooled region, nuclei form and grow radially along the six <001> directions until they meet a neighbouring grain resulting in a grain boundary, which form a continuous network throughout the solid. The transition from columnar to equiaxed morphology occurs when a melt loses its superheat and becomes undercooled (Kurz 1992). Again local solidification conditions G, V and

dT/dt (Equation 2.2) are important in determining the size and volume fraction of equiaxed grains.

In a similar way to the destabilisation of a planar front, the CET is influenced by the constitutionally undercooled zone ahead of the solidification front. During columnar growth the actual temperature is controlled by heat extraction through the solid, the change in composition due to solute pile up causes local change in equilibrium liquidus temperature which causes undercooling in a limited region, the size of this region increases with increasing isotherm velocity as shown in Figure 2.11. If nucleation undercooling is reached then equiaxed nuclei form in varying volume fractions depending on the amount of time available for growth and the local solidification conditions. These nuclei grow to form grains but will be incorporated in the columnar structure if their volume fraction is below a critical value, conversely if a critical value is exceeded the equiaxed grains will remain. Kurz et al (Kurz 2001) uses the following criteria; a fully columnar microstructure is retained when the volume fraction of equiaxed grains is less than 0.66% and a fully equiaxed structure when the volume fraction exceeds 49% (Figure 2.12).

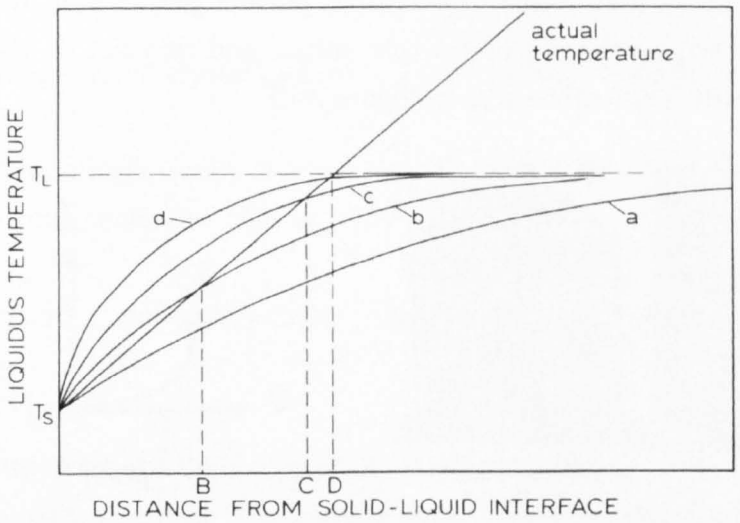

Figure 2.11 – Effect of increasing isotherm velocity (a to d) on the size of the undercooled region for a constant temperature gradient (McLean 1983)

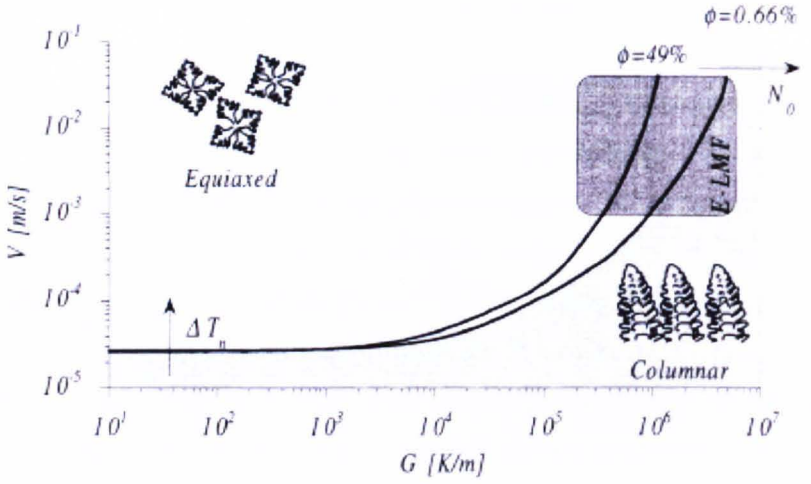

Figure 2.12 – Graph of G vs. V showing criterion for equiaxed and columnar morphology. Grey square shows processing window for E-LMF process. Φ is volume fraction of equiaxed grains (Kurz 2001)

The work by Kurz et al. (Kurz 2001) shows how an epitaxial, single crystal deposit of Ni alloy CMSX-4 contains equiaxed grains at the surface due to a decrease in G and increase in V; they also speculate that powder particles at the surface are not melted by subsequent passes of the heat source and may act as nucleation sites for equiaxed growth. This can be seen in Figure 2.13.

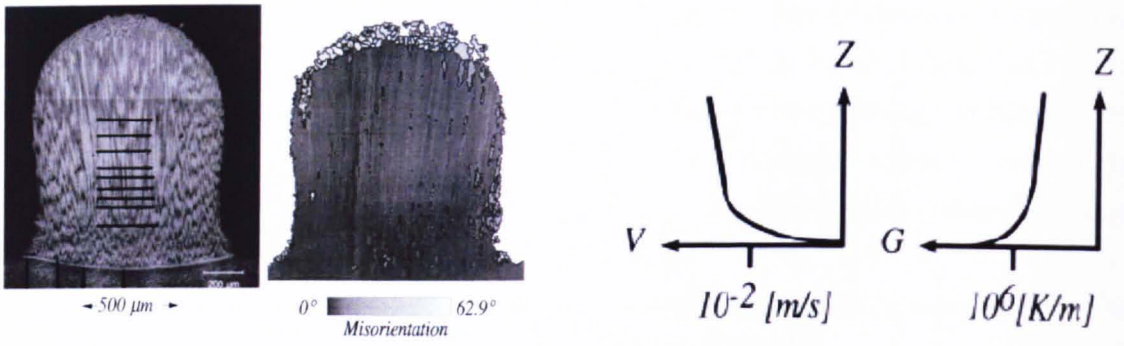

Figure 2.13 – Optical micrograph and electron backscatter diffraction image of a single-crystal wall-build cross-section. Graph of G and V at the solidification front (z axis represents depth of the meltpool) (Kurz 2001)

This area has been studied since the 1990's with the repair of single crystal turbine blades in mind. In this respect it is crucial to maintain epitaxy and avoid nucleation of new grains and a criterion for such was outlined by Kurz et al. (Kurz 2001) in terms of a processing map of temperature gradient vs. growth velocity for CMSX4 (Figure 2.12), this was also referred to by Pinkerton et al. (Pinkerton 2006) and applied to a study involving Waspaloy. This limit for maintaining columnar growth is given by

Equation 2.3 and Equation 2.4 where n=3.4 and $K=2.7x10^{24}$, conversely, to obtain a fully equiaxed grain structure $K=1.0x10^{22}$ with units $K^{3.4}/m^{4.4}s$.

$$\frac{G^n}{V} = a\left\{\sqrt[3]{\frac{-4\pi N_0}{3\ln[1-\Phi]}} \cdot \frac{1}{n+1}\right\}^n$$

Equation 2.3

$$\frac{G^n}{V} > K$$

Equation 2.4

n and K are specific to the alloy and process and as such are untested for ALM and Inconel 718 but as the study uses a laser melting process and a nickel based superalloy it is assumed to be a reasonable limit in the absence of specific data.

2.2.4 Rapid solidification

Rapid solidification or rapid crystal growth is brought about in two ways:

1) Bulk undercooling - slowly cooling the melt in the absence of efficient heterogeneous nucleation sites or rapid quenching.

2) Rapidly moving temperature fields – typical of surface treatments and welding processes.

Finer microstructures generally result from faster cooling rates and result in superior mechanical properties. Fast cooling rates are traditionally associated with regions close to the mould of castings, in thin sections of castings and at laser-remelted surfaces (Kurz 1992). In the more recent field of Rapid Solidification Rate (RSR) processing, specific processes are designed to achieve rapid cooling to exploit the associated fine microstructures, examples are atomised powders, splat quenching and melt spinning.

A study of the effect of cooling rate on the solidification of Inconel 718 was undertaken by Antonsson et al. (Antonsson 2005). They used three techniques, Differential Thermal Analysis, Mirror Furnace and Levitation Casting to test a range of cooling rates from 0.2K/s, 100K/s to 20000K/s respectively for the three processes. They report secondary dendrite arm spacings from 1μm to 4μm in the levitation

samples which correspond to cooling rates showing good agreement with measured values.

The solidification sequence for equilibrium cooling rates was determined to be;

$L \rightarrow TiN(s)$	$T>T_L$
$L \rightarrow \gamma$	$T\sim1340°C$
$L \rightarrow \gamma + NbC$	$1280°C\text{-}1265°C$
$L + NbC \rightarrow \gamma + Laves$	$T\sim1160°C$
$L \rightarrow \gamma + Laves$	$1160°C\text{-}1075°C$

The phases formed change as cooling rate increases as the formation of NbC and Laves is suppressed. This is attributed to changes in the segregation of niobium as the effective partition coefficient, k_e, increases as a result of solute trapping.

2.3 Laser processing of materials

2.3.1 Lasers in materials processing

Industrial lasers are flexible tools, which are used in the processing of a variety of materials including; metals and alloys, glasses and ceramics, polymers and composites. One reason for the wide application of lasers in industry is their flexibility and the number of different ways they are utilised. This may be for their thermal properties, as in cutting and welding, or their optical properties, as in measuring and light projection.

Within each area of application there is further range and flexibility, due to the ability to manipulate the laser device to vary its output. A laser device produces a beam of coherent, monochromatic light with low divergence and high brightness which can be accurately controlled. For example, in thermal applications, focussing the beam gives a small spot size, providing an intense energy source capable of penetrating most non-reflecting materials. Alternatively defocusing the beam gives a diffuse heating pattern that can be used for treating larger areas. Optical manipulation also means that the light can be directed to various positions and locations, adding to the flexibility of lasers in materials processing, this can be achieved by optical systems of reflectors and lenses and/or optical fibres.

It is important to identify the two key modes of operation for industrial lasers, these being; thermal and athermal. Processing based on thermal modes involves the heating of a material to heat-treat, melt or vaporise it (e.g. surface hardening, welding and cutting/drilling). Athermal modes involve the making or breaking of chemical

bonds and are induced by changes on the atomic scale (an example would be the curing of photo-sensitive polymers like in stereolithography) (Ion 2005).

2.3.2 Generating light

LASER is an acronym of Light Amplification by Stimulated Emission of Radiation. Electromagnetic radiation in the form of laser light (photons) is released due to electron transitions from excited energy levels to lower energy levels within the atoms, ions and molecules (collectively termed species) of a so-called 'active medium'. Species in their simplest form, isolated atoms, exist as discrete energy levels or states, the lowest, in terms of the associated energy, is known as the ground-state, and any higher energy level (of which there may be numerous) is termed 'excited'. In molecules, either in gases, liquids or solids, the energy levels differ due to the interactions between neighbouring atoms. The energy levels are modified, and in solids and liquids, they broaden or merge into almost continuous bands of closely spaced energy states.

When an active medium is under thermodynamic equilibrium, it has a normal distribution of energy (Maxwell-Boltzmann distribution) i.e. the species population of the lower states exceeds that of the higher, this means that there is no driving force for energy to be released from the system. Laser light production requires a population inversion, where more species exist in the higher energy state, thus providing a driving force. The inversion can be achieved by external excitation or 'pumping' by an external energy source, which can be done electrically, optically or chemically depending on the type of laser being used.

The energy level transitions responsible for the release of laser light can be 2, 3 or 4-level transitions. The simplest, 2-level, is the excitation of a species from the ground state to a higher one (the upper lasing level, ULL), followed by the release of the excess energy as light and the species returning to the ground state, this is shown in Figure 2.14 in the transitions 0→3→0. This is not useful in practical applications because as the radiation is emitted the number of excited species falls to that of the ground state, the population inversion is lost and the absorption of further excited species falls to zero. A more useful approach is 3 and 4-level transitions, where species are excited to an absorption level, which is higher in energy than the ULL. Rapid, non-radiative decay occurs to the ULL with little energy loss, followed by radiative decay to the lower laser level (LLL), which may be the ground state or a fourth level just above it (this time transitions 0→3→2→1→0 in Figure 2.14). This

process describes how photons of light are generated and is known as stimulated emission, however, this does not describe the full working of a laser device.

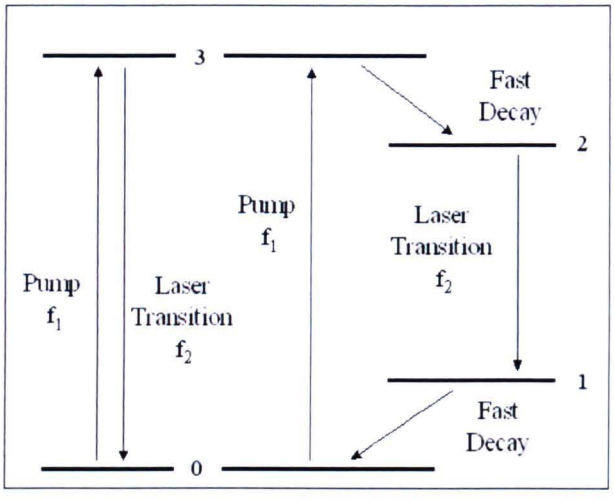

Figure 2.14 Two and four level energy transitions in an excited species (CVI Melles Groit 2006)

The key to how lasers work is 'light amplification'. This is achieved when stimulated emission is used to increase the number of photon oscillations in an 'optical cavity'. Within an optical cavity, photons collide with excited species causing them to release their energy prematurely as another photon of the same phase, frequency and polarisation. These secondary photons travel in the same direction and participate in further collisions and build up a steady stream whose density increases with each collision, Figure 2.15 shows a schematic of this action.

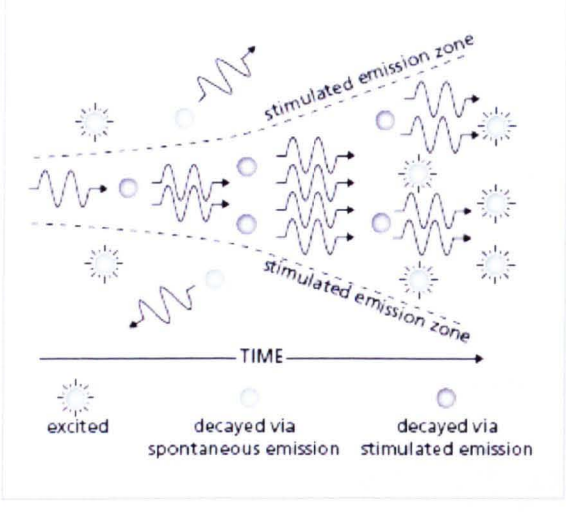

Figure 2.15 stimulated and spontaneous emission of an excited species by a photon within an optical cavity (CVI Melles Groit 2006)

2.3.3 Laser devices

There are four main components to a laser device;

- The *active medium*, which may be a solid, liquid or gas. This contains the species which are excited and emit photons where the light amplification occurs.
- A '*pumping source*'. A means of exciting the medium to maintain the population inversion. The most common method in industrial lasers is electrical pumping; using a RF, AC or DC current. Species in the active medium are excited by collisions with electrons.
- An *optical cavity* to give feedback. The cavity holds the active medium, which is contained by a mirror at each end. The photons are reflected back and forth through the active medium setting up a standing wave. This increases the probability of stimulated emission due to the increased residence time and the increasing number of photons. Feedback allows the standing wave to grow in coherency as out of phase photons are lost through destructive interference and non-parallel photons are absorbed at the cavity edge to give the characteristic low divergence of laser light.
- The *output coupler*. A way of releasing light from the standing wave in the optical cavity. This may be a partially transmitting window at one end of the cavity; this will allow some light to be released while some is reflected back, maintaining the standing wave of photons and allowing further amplification.

Losses of photons in the cavity may arise from a number of sources. Transmission through the output coupler is required for a useful device; non-useful sources include optical scattering and absorption by inhomogeneities in the active medium (i.e. non-laser energy level transition) and absorption by the mirrors. Therefore the materials used to make laser devices must be made to precise degrees of accuracy and purity.

2.3.4 Transverse electromagnetic mode (TEM)

The laser power and beam diameter are two important parameters in laser processing. The Transverse electromagnetic mode (TEM) is also important in describing the output beam characteristics and performance of industrial lasers. It describes the radial variation in beam intensity and it is a function of the optical cavity geometry and the alignment and spacing of the containing mirrors (Steen 1991).

TEM is denoted by two subscripts; p and l, (TEM_{pl}). p and l are the nodes along the radius and circumference of the beam intensity cross-section respectively. TEM_{00}

is common in laser processing. It is cylindrical and symmetrical, and has a Gaussian profile (Figure 2.16a). However, another mode described as 'top-hat' is also favoured for its more even radial intensity distribution, it is described as TEM_{00} + TEM_{01*} (Gaussian + normalised annular distribution, Figure 2.16c).

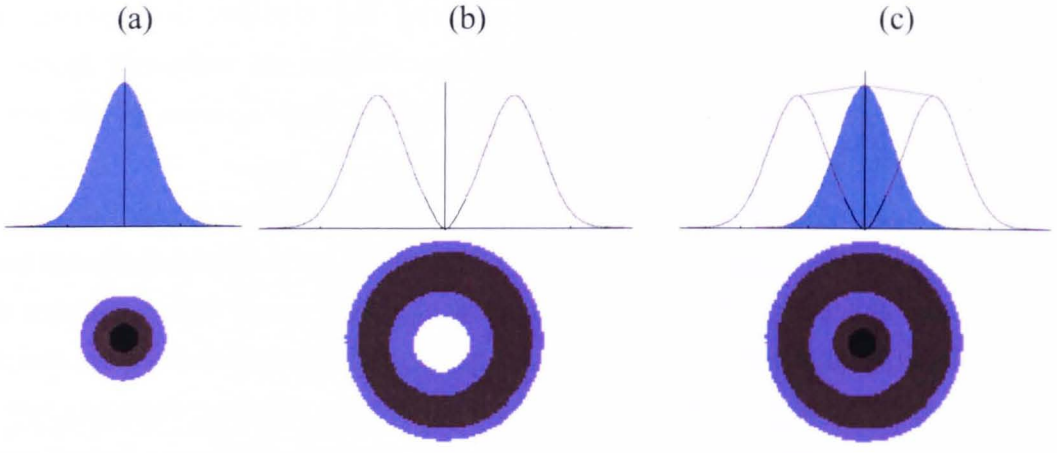

Figure 2.16 (a) Gaussian intensity profile (TEM_{00}), (b) normalised annular profile (TEM_{01*}), (c) top-hat profile (TEM_{00}+TEM_{01*})

2.3.5 Types of lasers used in materials processing

Lasers are generally classified by their active medium since it is the state of the medium that determines the principal characteristics of the beam produced. As mentioned in previous sections, the active medium can be a solid (insulators or semiconductors), liquid (organic dyes) or gas (atomic, molecular, ionic or excimers).

The range of properties provided by the different materials is shown in the Figure 2.17.

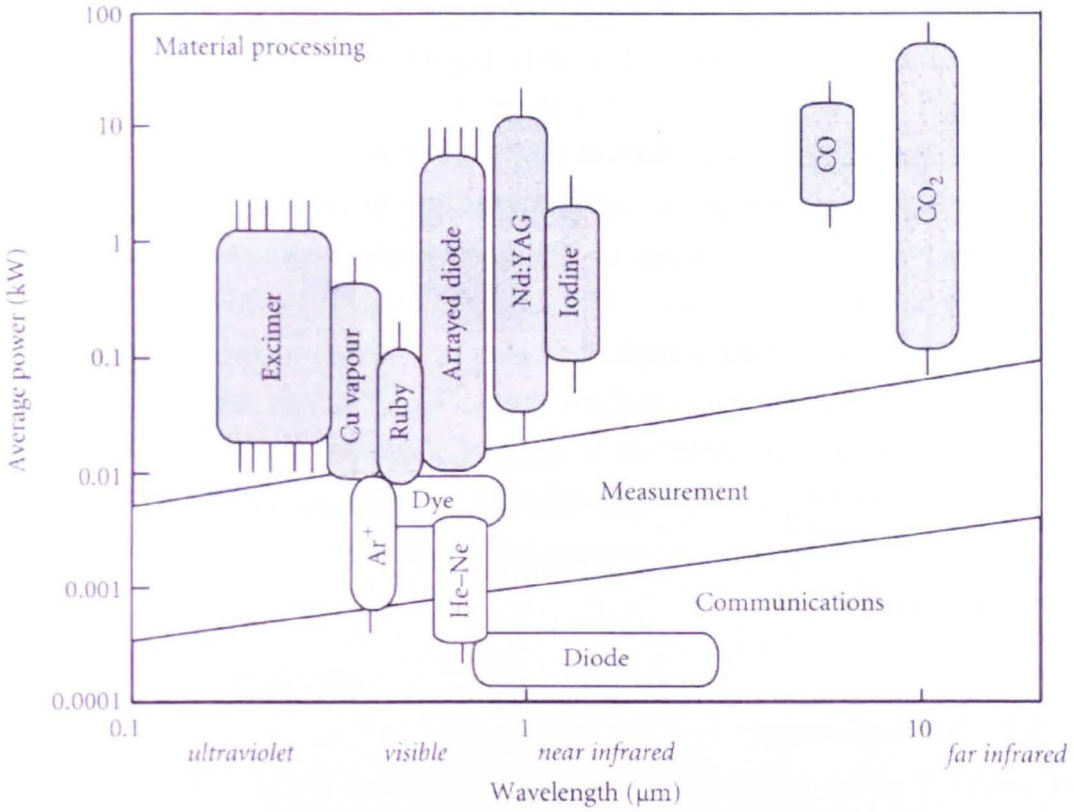

Figure 2.17 – Graph showing the range of powers and wavelengths achievable from different materials used as the active medium in laser devices. The background is divided into some applications for the different types of lasers (Ion 2005).

The two most common types of laser used in materials processing are carbon dioxide (CO_2) and Neodymium doped Yttrium Aluminium Garnet (Nd:YAG). These are discussed further in sections 2.3.6 and 2.3.7 along with Fibre lasers in 2.3.8 which are an increasingly used type of laser.

2.3.6 Carbon dioxide lasers

The optical cavity of CO_2 lasers contain 1-9% CO_2 (the active medium) as well as 60-85% Helium and 13-35% Nitrogen. The N_2 increases the efficiency of excitation by facilitating the absorption of energy from 'pumping' and then transferring it to the CO_2 molecules. The carbon dioxide can be directly excited by electrons during pumping but the molecules are excited to states other than the upper laser level, which reduces the efficiency of the process. Since N_2 is diatomic it has just one mode of vibration, which is easily induced by electrons, the vibrations are similar in energy to the ULL of CO_2 molecules and the lifetime of excited N_2 is high, hence the probability of energy transfer between the nitrogen and CO_2 is high (Steen 1991, Ion

2005). The Helium is used as a means to cool the system through collisions, which return excited CO_2 the ground state, rendering them available for further excitation to the ULL.

The light produced has a wavelength, λ, of 10.6μm, which lies in the far infrared region of the electromagnetic spectrum, and a power range of 0.1-100kW. The devices have efficiency between 15-20% and are cheaper and more easily maintained than other lasers.

A 2kW CO_2 can be focussed to about a 0.2mm diameter spot size, which correlates to a power density of 60kW/mm^2 compared to an electric arc whose power density is around 0.5kW/mm^2. This means that even modest power levels can yield high power densities, defocusing results in lower densities and a vast range of values are possible making laser processing highly flexible and a good heat source for industrial applications.

2.3.7 Nd:YAG lasers

A Nd:YAG laser is a solid state device made from a yttrium aluminium oxide crystal with a garnet like structure ($Y_3Al_5O_{12}$), which is doped with 1weight % neodymium ions (Nd^{3+}) which are similar in size to the yttrium and take their place in the lattice (Steen 1991, Ion 2005).

Light is generated through electron transitions between energy levels in the Nd^{3+} ions, the electrons being available from partially filled 4f sub-shells. Excitation (pumping) is achieved by optical means, i.e. a flash lamp, as the species absorb energy provided by visible or infra red light.

Nd:YAG lasers are expensive due to the difficulty of producing the $Y_3Al_5O_{12}$ crystals, which are cut from larger ones that take around 8 weeks to grow. Other drawbacks compared to CO_2 are the limited power output, lower efficiency and poorer beam quality; however, they do exhibit good absorptivity and surface coupling with metals and alloys compared to larger wavelengths. The wavelength of the light produced is 1.06μm (near infrared), which makes it possible to deliver a very small beam diameter and hence a high power density as well as being highly accurate for processing, all of this amounts to a large processing window.

2.3.8 Fibre Lasers

An increasingly common type of laser is the solid-state fibre laser; these types of laser use an optical fibre doped with Rare-earth elements as the active medium as well as a

way of delivering the beam to the work piece (Snitzer 1991). The fibre is doped with rare-earth elements such as Ytterbium, Erbium and Neodymium and work in a similar way to amplifiers in long distance signal transmission via optical cables. Fibre lasers have the flexibility of fibre delivery systems inherent in their design as well as a high power output thanks to the potentially long active regions (which can be kilometres long) and they have effective, efficient cooling because of the fibre's large surface area to volume ratio. The devices are relatively compact compared to gas and rod type lasers since the fibre can be coiled, they exhibit good reliability and operating lifetime and have excellent beam quality and efficiency. (Armitage 1991)

The highest powers come from Yb^{3+}-doper silica fibres which emit in the 1-1.1μm wavelength range which have very high powder conversion efficiency >80% (Jeong, 2004).

2.3.9 Lasers as a heat source

When electromagnetic (EM) radiation interacts with a surface, some radiation is reflected, some absorbed and some transmitted through the medium. It is the absorption of the energy which is important when using lasers as a heat source.

EM radiation exists as discrete 'packets' of light known as photons and can be represented as two perpendicular vector fields – electric and magnetic. When a photon passes over small electrically bound, charged particles the electric field causes the particle to vibrate, but not with enough energy to cause significant heating or melting. For this to cause significant heating, photon-electron interactions are required, and are known as the reverse Bremsstrahlung effect (this is the opposite of photon emission from electron transitions in excited species). As an electron vibrates it is restrained by the lattice phonons (the bonding energy within a medium), this results in the vibration being transmitted through the structure via normal diffusion processes. The vibrations are what are detected as heat and if the photons have sufficient energy and this energy is absorbed by the material the bonds in the lattice are stretched to the point where they lose their mechanical strength, when this occurs the material is said to have melted.

2.3.10 Absorptivity

Incident radiation on a surface is transmitted, absorbed and reflected by the medium it interacts with. At the wavelengths associated with lasers (~1μm for fibre lasers and ~10μm for CO_2) metals are typically opaque and so transmission is negligible. Instead

the energy is absorbed (causing the metal to be heated) and reflected. The surface roughness causes multi-direction reflections which can increase absorption by stimulation due to constructive interference from the sideways reflected radiation, when the surface roughness, R_a, is less than the wavelength then this effect is negligible and the surface is perceived as 'flat'.

Reflectivity is difficult to control during laser melting as the melting process itself causes variations in the surface. Reflectivity decreases (absorption increases) on heating due to an increase in phonon concentration indicated by the Bramson equation (Equation 2.5) (Bramson 1968, Zhao 1999) which is based on an expansion series and shows that as a materials electrical resistivity (ρ) increases so does the absorptivity (η) and that coupling between the beam and the surface improves with smaller wavelengths (λ) of light;

$$\eta_\lambda(T) = 0.365\sqrt{\frac{\rho(T)}{\lambda}} - 0.0667\left(\frac{\rho(T)}{\lambda}\right) + 0.006\sqrt{\left(\frac{\rho(T)}{\lambda}\right)^3}$$

Equation 2.5

This is true until heating is sufficient to vaporise the metal substrate and a plasma forms which interacts with the laser beam and shields the surface.

2.4 Additive Layer Manufacturing

This section provides an overview of Additive manufacturing, a brief description of the different processes available, some of the issues faced by the process, the state of the art and the on-going areas of research.

2.4.1 Additive layer manufacturing overview

Additive Layer Manufacturing (ALM) of metal parts is a powder metallurgy route, so-called to differentiate it from traditional manufacturing techniques, in particular machining, which would be described as 'subtractive' since material is removed from a larger billet or preform. Broadly speaking ALM involves the consolidation of a powder to form a 3-dimensional solid part; the method by which this is achieved varies according to the process.

The consolidation technique is typically a thermal process in which a heat source is used to sinter or melt the powder to create the required form directly. Alternatively a low melting point material can be used to bond powder particles together; the low melting point material is then removed to leave a porous metal part. Where a fully dense final part is desired, these processes require post-process consolidation such as hot isostatic pressing (HIP) or densification heat treatments, therefore it is desirable to select a process which produces a fully dense part in one step.

There are many variations on ALM processes but on the whole they can be split into two categories; layer-by-layer, where a part is built by successive layers being consolidated on top of each other, much like a wall or building would be built. This layer-by-layer approach is often referred to as '*powder-bed*' and involves a pre-placed, thin layer of powder which is selectively melted in areas corresponding to the cross-section of a part, this is followed by subsequent layers being melted in a similar fashion (O'Neill 1999, Murali 2003, Xie 2005). Alternatively, a '*freeform*' or '*blown-powder*' technique is where powder is delivered to the heat source where melting takes place leaving a deposition track as in cladding processes; these are more commonly used to repair or modify existing forms and don't necessarily need a flat layer to add material to (Kobryn 2000, Choi 2001, Liu 2006).

Whether powder-bed or blown-powder, there is variability from machine to machine in how the process operates; in a powder bed system there may be different ways to pre-place a layer of powder such as scrapers, rakes, rollers or hoppers, and in a blow-powder system the delivery of material can be from a single point, multiple points or coaxially from 360° (the feedstock in this case can also be in wire form as

opposed to powder) (Ul Haq Syed 2006, Nurminen 2006). Wire-fed systems have the advantages of a simpler delivery system and higher deposition rate compared to blown-powder systems (Choi 2001). In industrial processes where consolidation is achieved by thermal means a variety of heat sources such as various lasers, electron beams (Matz 2002) and welding torches (Baufeld 2009) can also be used, each having their own benefits and limitations. A list of the different names for the various processes is given in Table 2.1

Most ALM systems are fully automated processes; blown-powder systems often utilise CNC and robotics to accurately position the laser head and powder delivery nozzle whereas powder-bed systems often work directly from CAD models which are sliced into thin layers to define an area to be melted in each layer, the laser being moved by an arrangement of optics.

In this study the focus is placed on a powder-bed system (the EOS M270) and a blown-powder system (the Trumpf DMD505) the details of these individual processes are described in Chapter 4.

Table 2.1 list of different trade names for Additive Layer Manufacturing process.

Process name	Shorthand	Group/Company
Direct (laser) metal deposition	D(L)MD	(Mazumder 1999, Pinkerton 2004b, Pinkerton 2005a)
Selective Laser Sintering/Melting	SLS/M	(Maeda 2004)
Leaser engineered net shaping	LENS	Sandia Labs, Optimec (Bontha 2006)
Direct laser fabrication	DLF	(Peng 2005) (Wang 2006)
Epitaxial – laser melt forming	E-LMF	(Gaumann 1999a/b)
Shaped metal deposition	SMD	(Clark 2007)
Solid freeform fabrication	SFF	(Vasinonta 2001)
Laser metal deposition shaping	LMDS	(Zhang 2007)
Laser powder deposition	LPD	(Costa 2005)
Direct Metal Laser Sintering	DMLS	EOS GmbH (O'Neill 1999)
Electron Beam Melting	EBM	Arcam AB (Strondl 2007)
Shaped deposition manufacturing	SDM	(Nickel 2001)

A brief history of additive manufacturing was outlined by Hopkins et al. (Hopkins 2005) describing the progression from Stereolithography being developed in the mid-1980's through to some current areas of development:

- 1986 – Stereolithography (SL) patented
  - UV laser used to cure photosensitive polymers to build near-net-shaped components layer by layer.
- 1988 – SL becomes commercially available
  - Birth of Rapid Prototyping (RP).
- 1990's – RP established
  - Quick & accurate method to produce 3D prototypes
  - Direct from CAD solid models
  - Fast design validation possible with the ability to accommodate late design changes.
- Late 90's – RP expanded into direct fabrication of metal parts
  - Early success includes injection moulding tools from hardened tool steel, and non-structural part builds.
- Recently/future – Rapid Manufacture
  - Near-net-shape *component* fabrication
  - Functional, long-term, end-use products.

2.4.2 Benefits of ALM

ALM, in its many forms, developed from Rapid Prototyping of polymeric materials into a process for producing metal parts. Prototypes are often single-use and non-structural for which geometry is key and early work was focussed on control of shape and accuracy (Milewski 1999, Pinkerton 2005a, Peng 2005). By their nature, a prototype has small lot sizes or production runs as low as a single part making tooling, moulds and fixturing a large proportion of the total cost for traditional manufacturing processes; ALM does not require these and so, despite the often higher production costs of the process, a part can actually be produced relatively cheaply. For similar reasons, multiple prototypes can be produced incorporating different stages of the design phase and can accommodate late design changes right up to final part production.

The non-structural nature of prototypes also means that, especially for metals, there need be little consideration of microstructure, porosity and mechanical properties; more recent work is dedicated to understanding the development of microstructure in

ALM materials and the resulting mechanical properties. This is discussed in more detail in Sections 2.4.4 and 2.4.5.

ALM processes are usually expensive to operate due to high machine prices, high energy consumption, long operating times and often expensive raw materials (atomised metal powders), so components with high added value and small production runs are good candidates for the process. ALM has the ability to produce highly complex shapes and internal structures which are difficult or impossible to achieve by any other means. Cooling channels are an example of internal structures which can improve the performance of a part by improving heat transfer and ALM has been shown to be successful in injection moulding tools with conformal cooling which can follow the contours of the cavity rather than being limited to drilled holes which are necessarily straight (Simchi 2003, Coulon 2006), and fine net structures or controlled porosity can be used for weight reduction of parts or bone inter-growth in biomedical implants (Hollander 2006).

Processing materials such as titanium and nickel is attractive to the aerospace industry especially for use in gas turbine engines, since they are difficult to process conventionally. Hard materials or those which readily work-harden are costly to machine as tools are worn out quickly (Wang 2002, Maeda 2004) and alloys with long freezing ranges are difficult to cast due to hot tearing or solidification cracking. Some Nickel alloys are often subject to strain rate hardening and so require heavy duty lubricants in forming procedures, these lubricants can become entrapped in the surface and degrade properties (Milewski 1999). ALM does not require such precautions and the use of controlled atmospheres can control surface cleanliness.

Additive manufacturing only melts the material required to produce a part and any unmelted powder from the process can be reused after sieving. This leads to high material utilisation compared to subtractive processes such as machining which produces large amounts of waste material in the form of 'swarf' which is often difficult to recycle and is particularly undesirable for expensive materials.

Blown-powder and wire-fed ALM is also capable of producing functionally grade materials where the composition can be altered in specific regions by controlling the material being fed into the molten pool (Peyre 2006). One area where these have been studied is the transition from a Ti-6Al-4V material to a BurTi burn resistant material (e.g. Ti-25V-15Cr-2Al-0.2C) with the view to manufacture parts with localised regions of burn resistance (Wang 2006b).

2.4.3 Common areas of research

Blown-power and powder-bed ALM processes are often reported in the literature from different areas of research. These range from the process driven studies which consider the 'form' of a part (geometry, accuracy and porosity) of highest priority, to more functional, scientific studies focusing on microstructure and properties. The former is more commonly associated with powder-bed systems which were developed from Rapid Prototyping of polymers and adapted to produce tooling products where surface roughness and geometrical accuracy are critical (Simichi 2003). In contrast the blown-powder systems are a development of cladding and repair where common areas of research involve hard-facing alloys and single crystal technology in which microstructural control is most critical and the areas of interest are industries such as biomedical and aerospace. With this in mind there is no unifying way to group the research literature of ALM, this is made all the more difficult by the vast number of engineering alloys available, all of which could respond differently to processing. The high processing costs and limited availability of equipment has made computer simulation a large area of research into ALM processes, but this is mostly limited to blown-powder techniques.

In the following sections some of the most common areas of research are reviewed to put the current project into context.

2.4.4 Blown-powder

2.4.4.1 Control of deposits

There are many different operator defined processing parameters in ALM processes and these vary from machine to machine and need to be adjusted according to many different criteria, for example the alloys being melted will have different material properties such as thermal conductivity and absorptivity, the part being produced could be thin walled or thick sectioned which will affect the resolution required and the final use of the part may be intolerant to porosity or certain microstructural features.

An early attempt to show that laser additive processing using a blown powder system could be used to form a fully dense metal deposit was made by Milewski et al. (Milewski 1999). They showed that Computer Aided Design and Manufacturing (CAD/CAM) could be used to control and simulate a metal deposition process to fabricate a complex, near-net shaped component in Inconel 690. The process achieved dimensional accuracy to 0.1μm and fully dense parts after tool path modifications were made using the CAD/CAM software and tested with relative ease in a short turnaround time because of the high level of flexibility in the ALM process. Subsequent studies have looked to provide closer control over deposits by better understanding the effect of processing parameters on the deposition track geometry.

Peng et al. (Peng 2005) investigated the Direct Laser Fabrication of nickel alloy samples using a blown powder system and reported the effect of laser power, beam velocity, powder feed rate and deposition track overlap on individual track geometry and part integrity. They used an orthogonal array experiment to test power, velocity and feed rate at three levels, however, they report their findings as a function of 'Specific Energy' (power/(velocity x beam diameter) in J/m^2). This misses the point of an orthogonal array which makes it possible to look at the interactions of parameters. Specific energy is reported often on the literature (for example by Kobryn et al. (Kobryn 2000)) with regard to the heat input of a laser, the problem with this approach is that it does not account for the effect of different parameter combinations having the same value but notably different effects, this leads to a large degree of scatter in results. Peng et al. (Peng 2005) showed that the specific energy has a positive effect on track height and width as more material is melted but also that there is a large increase in the remelted depth relative to the track height above the surface as specific energy increases which implies that with increasing power or decreasing velocity there is a greater increase in penetration depth than track height for a given powder flow rate. They also showed that reducing specific energy below an optimum

range of 100-200Jmm^{-2} causes a concave top surface of the deposit and conversely above this range the top surface is convex, this is undesirable as the process stability is linked to a flat working surface. These observations do not however take into account the different powder feed rates used across the experiment.

Pinkerton et al. (Pinkerton 2006) showed that laser power has a more pronounced positive effect on mean layer width and powder flow rate has a larger positive effect on mean layer height after these two primary variables were investigated using a 2-factor, 2-level factorial experiment. They report that final wall height was accurate to within +/-1mm along the wall.

Work has been carried out by Zhang et al. (Zhang 2007) to establish how these control parameters affect the shape of the build; laser power, beam velocity, beam diameter, and powder feed rate were investigated to determine their effect on width and height of a simple line-build. The graphs in Figure 2.18 show that increasing power, beam diameter and powder feed rate gives higher, wider tracks, whereas, increasing beam velocity gives narrow tracks which are not as high. The results of this study, while providing good insight into the effects of various processing parameters, do not consider the interactions of the different parameters. This is a fundamental problem with a 'one parameter at a time' approach, another is the number of tests required to gather sufficient information, making the experimentation process very inefficient and costly.

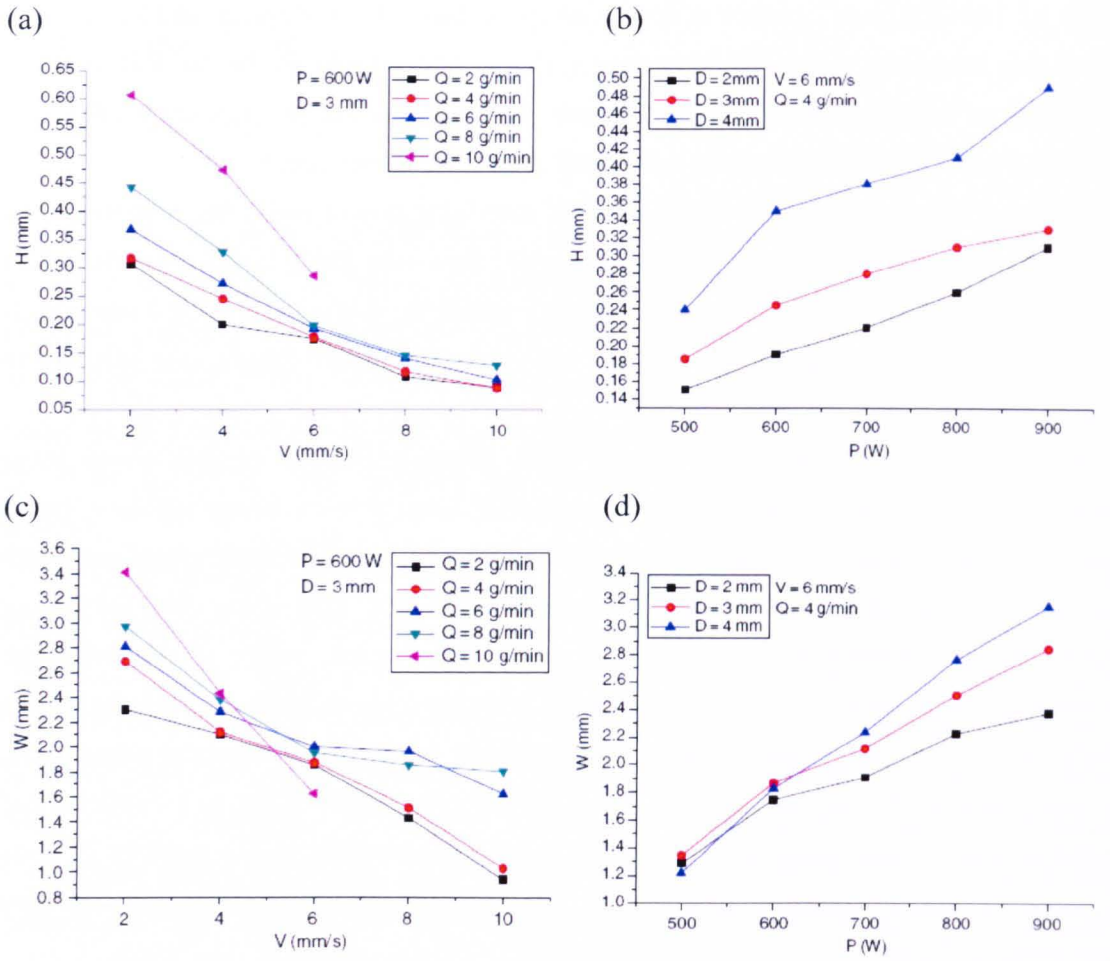

Figure 2.18 graphs showing the effect of beam velocity, V, laser power, P, beam diameter, D, and powder feed rate, Q, on deposition track height, (a) and (b), and width, (c) (d). (Zhang 2007)

2.4.4.2 Porosity

Porosity is a key defect associated with ALM due to the use of powder which is usually gas atomised and can have residual porosity and the potential to incorporate the carrier or shielding gas during processing. It is easily avoided through control of process variables but does represent limits in processing window where fully dense parts are necessary, there are however potential applications for porous materials such as in bearings where pores act as reservoirs for lubricating fluid or in biomedical applications where bone-integration with prosthetics can be utilised.

Kobryn et al. (Kobryn 2000) reported varying levels of porosity in laser deposited Ti-6Al-4V, two types of porosity were described; 'lack-of-fusion' porosity caused by incomplete melting of a layer or poor bonding to adjacent and underlying material, and gas porosity, which is caused by entrapped gas from the delivery system or raw materials. Lack-of-fusion pores are irregular shapes and often interconnected to form

long voids corresponding to inter-track regions whereas gas porosity is spherical and can occur in any area of the deposit. According to the investigation increasing power and velocity resulted in less porosity; this was rationalised since lack-of-fusion pores tend to form when insufficient energy is available to melt the required amount of material so higher powers are capable of melting more material and higher velocity means that less material is delivered to the melt pool in a given time hence there is less material to absorb the incident energy for the laser.

Wu et al. also reported that low laser powers result in increasing porosity (Wu 2004), examples of the two types of porosity is shown in Figure 2.19.

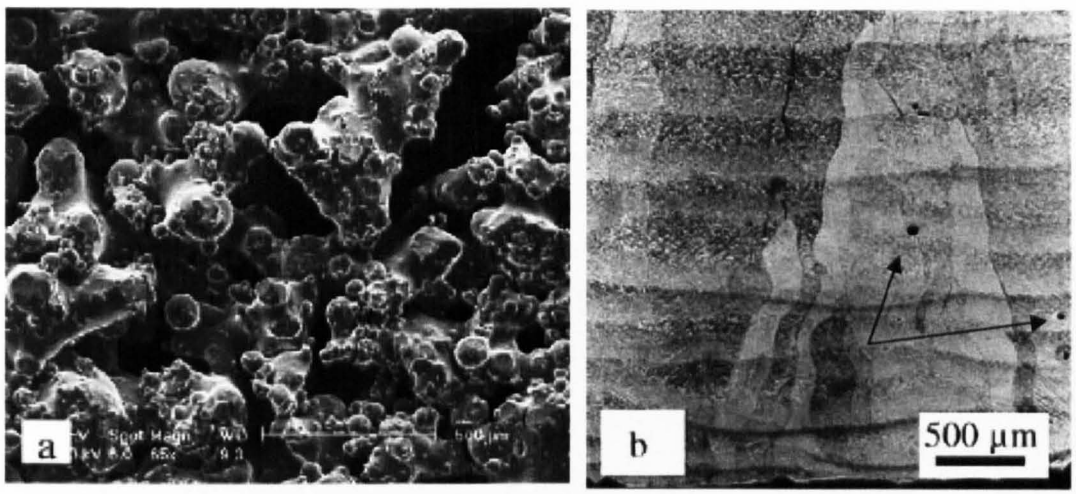

Figure 2.19 – Laser deposited Ti-6-4 after Wu et al. (Wu 2004b) (a) lack-of-fusion porosity (b) entrapped gas porosity indicated by arrow.

2.4.4.3 Microstructure and mechanical properties

The majority of work regarding the microstructure and mechanical properties of materials produced by ALM is focussed on Titanium and Nickel alloys which are important in aerospace and automotive components.

In the vast majority of cases columnar grain structures are reported (Kobryn 2000 & 2003, Wu 2004, Dinda 2006) and attributed to the strong temperature gradient and directional heat transfer imposed by the focussed heat source and the relatively large substrate which acts as a an efficient heat sink. Kobryn (Kobryn 2000) describes the prior-beta grain structure in Ti-6Al-4V as being similar to typical columnar grains parallel to the z-axis (vertical) with a region of low aspect-ratio grains close to the substrate where many grains nucleate before the fastest growing are selected and continue to grow. Within the large prior-beta grains, which are 94-165µm wide, the microstructure is made up of fine Widmanstätten grains of fine equiaxed alpha grains

which are a result of a solid state phase transformation at 980°C on cooling after solidification. The fine alpha laths indicate a high cooling rate after solidification. The width of the columnar grains was shown to decrease with increasing beam velocity due to the higher cooling rates imposed but the grain widths were relatively insensitive to laser power. An extension to this study was published by Kobryn and Semiatin (Kobryn 2003). This compared the previous work using a Nd:YAG laser to similar samples produced using a higher power CO_2 laser. The main difference between the two types of laser is wavelength of the laser (the relevance of this is discussed in Section 2.3.10) and the beam diameter; Nd:YAG 1mm, CO_2 13mm. The results showed that the columnar grains produces by the Nd:YAG laser were wavy as a result of the rastering of the laser whereas the CO_2 produced straight columnar grains, these are shown in Figure 2.20. The alpha particles in the Nd:YAG sample were finer than the CO_2 which also shows the presence of a layer of grain boundary alpha, this indicate a lower cooling rate after solidification for the CO_2 laser.

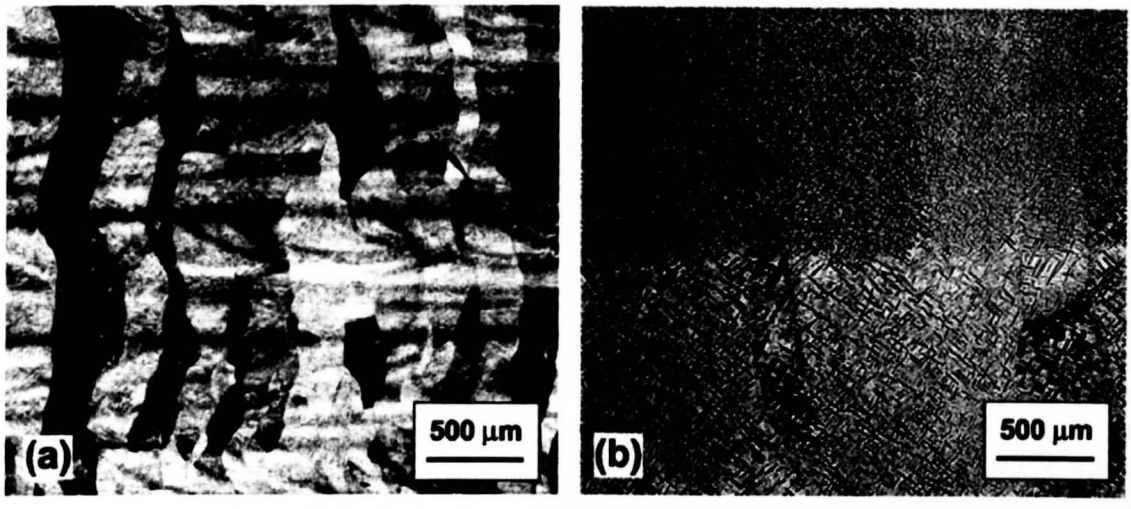

Figure 2.20 – Columnar grains of Ti-6-4 afrom Kobryn and Semiatin (Kobryn 2003) (a) Nd:YAG laser (b) CO_2 laser

The solidification conditions were extracted from Finite Element models and plotted on the solidification map shown in Figure 2.21 and the resulting microstructures agreed with those observed. The CO_2 samples are shown to have a lower temperature gradient which is consistent with the reduced cooling rate, however the effect of changing processing parameters and the variation in solidification conditions along the melt pool surface are not clearly indicated or rationalised.

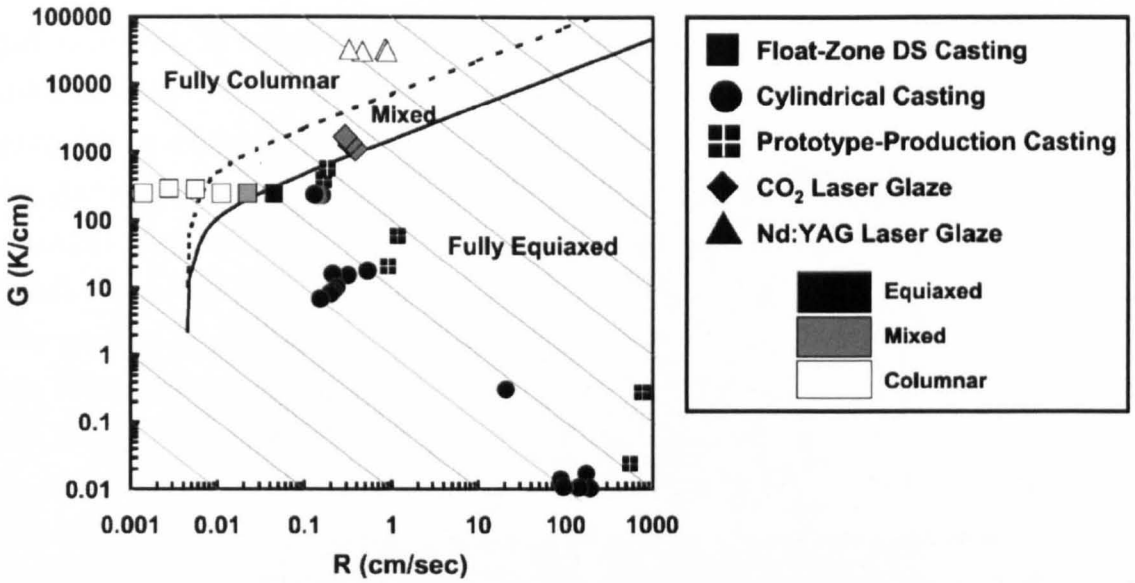

Figure 2.21 – The Ti–6Al–4V solidification map showing effect of temperature gradient (G) and growth velocity ® on microstructure for different processes, diagonal line show iso-cooling-rates which increase from bottom left to top right. (Kobryn 2003)

Wu et al. (Wu 2004b) described similar columnar grains in Ti-6Al-4V and showed that increasing the beam velocity reduces the width of the columnar grains. The alpha and beta laths of the transformed Widmanstätten were also shown to be coarser when heat accumulation occurs such as in the upper regions of thin wall deposits and the heat affected zone (HAZ) between layers in the lower region of a wall. Wu explains that the columnar structure is caused by the directional heat transfer imposed by the process and the re-melting of underlying material which acts as nucleation sites promoting grain growth by epitaxy, it is also speculated that equiaxed grains will only be achieved if additional nuclei are introduced into the molten pool. Wu also shows that 'large equiaxed grains' are present at the bottom of walls which are continuous across several layers but not the total wall height, but it is likely these are grains which were out-competed by faster growing neighbours.

Several Ni-based superalloys have also been investigated, for example; Inconel 718 (Blackwell 2005), Waspaloy (Pinkerton 2006) and Inconel 625 (Dinda 2009). Blackwell reports that the as-deposited microstructure for Inconel 718 is fine dendritic similar to that seen in cast parts where high cooling rates are experienced. The sample specimen produced was a rectangular deposit on a substrate from which tensile coupons were taken. The deposition was a side-by-side rastering with alternate layers being rotated 90°. He reports that a banding is observed in the grain structure (Figure 2.22) with one layer showing fine equiaxed grains and the next coarser columnar. This was said to be because of the difference in track lengths for deposited layers where the shorter tracks have less time to cool before the next pass of the laser, this results in lower cooling rates in this layer due to heat accumulation and therefore

larger grains. However, this may also be a result of the orientation of the grains and the perceived fine equiaxed grains are the cross-sections of elongated grains which are orientated perpendicular to the observed plane. Epitaxy was not evident in the grain structure which is contrary to much of the other related literature, the author argues that this is because Inconel 718 has a higher thermal conductivity than Titanium alloys (on which much of the other literature is based) and so will experience faster cooling rates. From Figure 2.21, though, it is not apparent that rapid cooling will necessarily result in equiaxed grains, rather the lack of epitaxy is a result of not remelting the underlying material. This is revealed by the tensile tests carried out which showed poor ductility and a hatch pattern on the fracture surface which included unmelted powder. The lack of bonding with underlying material means that rather than epitaxial growth of the previous grains, new grains are nucleated at the bottom of the track and grow towards the top surface.

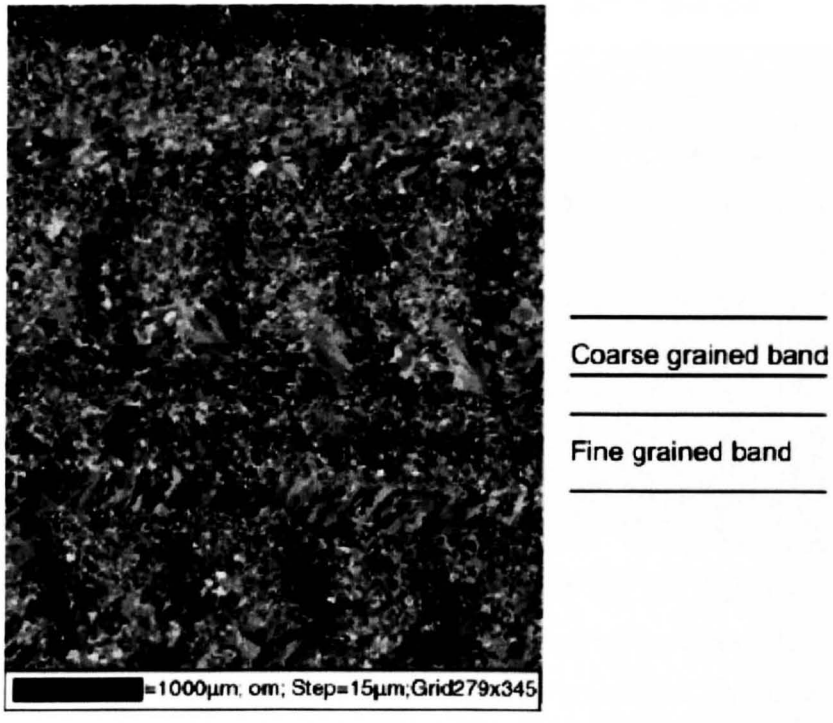

Figure 2.22 – Grain structure of Inconel 718 after Blackwell (Blackwell 2005)

Blackwell explains that the as-deposited microstructure was essentially in a solution-treated condition due to the high cooling rates which are sufficient to suppress aging. This means that the optimum mechanical properties will only be achieved after heat treatment; the reported mechanical properties show that strength in the as-deposited condition is lower and ductility higher than wrought values of Inconel 718, a direct age increased strength and reduced ductility (to above and below wrought) and solution treatment followed by aging increased strength further with no change in ductility. The reduced ductility is a result of the poor bonding between

layers so this was improved by a post process Hot Isostatic Press treatment which resulted in the deposited material having equivalent wrought properties.

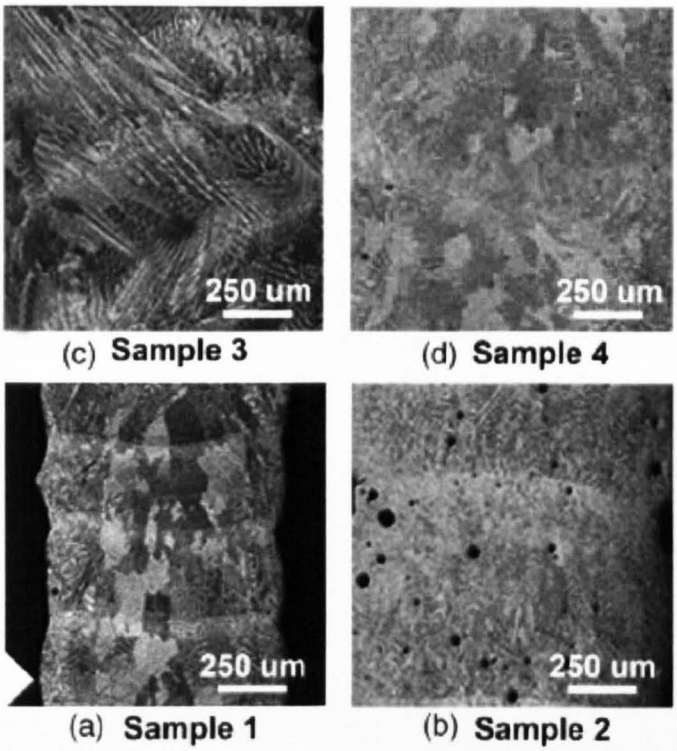

Figure 2.23 – Cross-sections of Waspaloy single track walls (Pinkerton 2006)

Pinkerton et al. investigated the effect of laser power and powder flow rate on the microstructure of Waspaloy. Cross-sections of the four deposits produced are shown in Figure 2.23 set out in the Factorial arrangement where power is on the vertical axis and powder flow on the horizontal. It is observed that low power and low powder flow result in thinner walls as previously discussed, Sample 2 was deposited at high powder flow and low power and shows both porosity and equiaxed grains, these occurrences may be related. The increased powder flow and reduced energy available to melt led to the inclusion of gas in the solidifying track, the instability of the solidification front in this case may disrupt epitaxial growth, however where fully dense deposits are necessary in structurally critical parts this would not be useful. Figure 2.24 shows Electron Backscatter Diffraction (EBSD) images to reveal the grain structure. This confirms the presents of epitaxy in the three fully dense samples and show the extent of the equiaxed grains, there is also a region of very fine grains at the layer interfaces which would suggest that the bonding between layers is poor and little or none of the underlying material is remelted to ensure a good metallurgical bond. The fine grains could be a result of nucleation of new grains at the bottom of the new deposition layer.

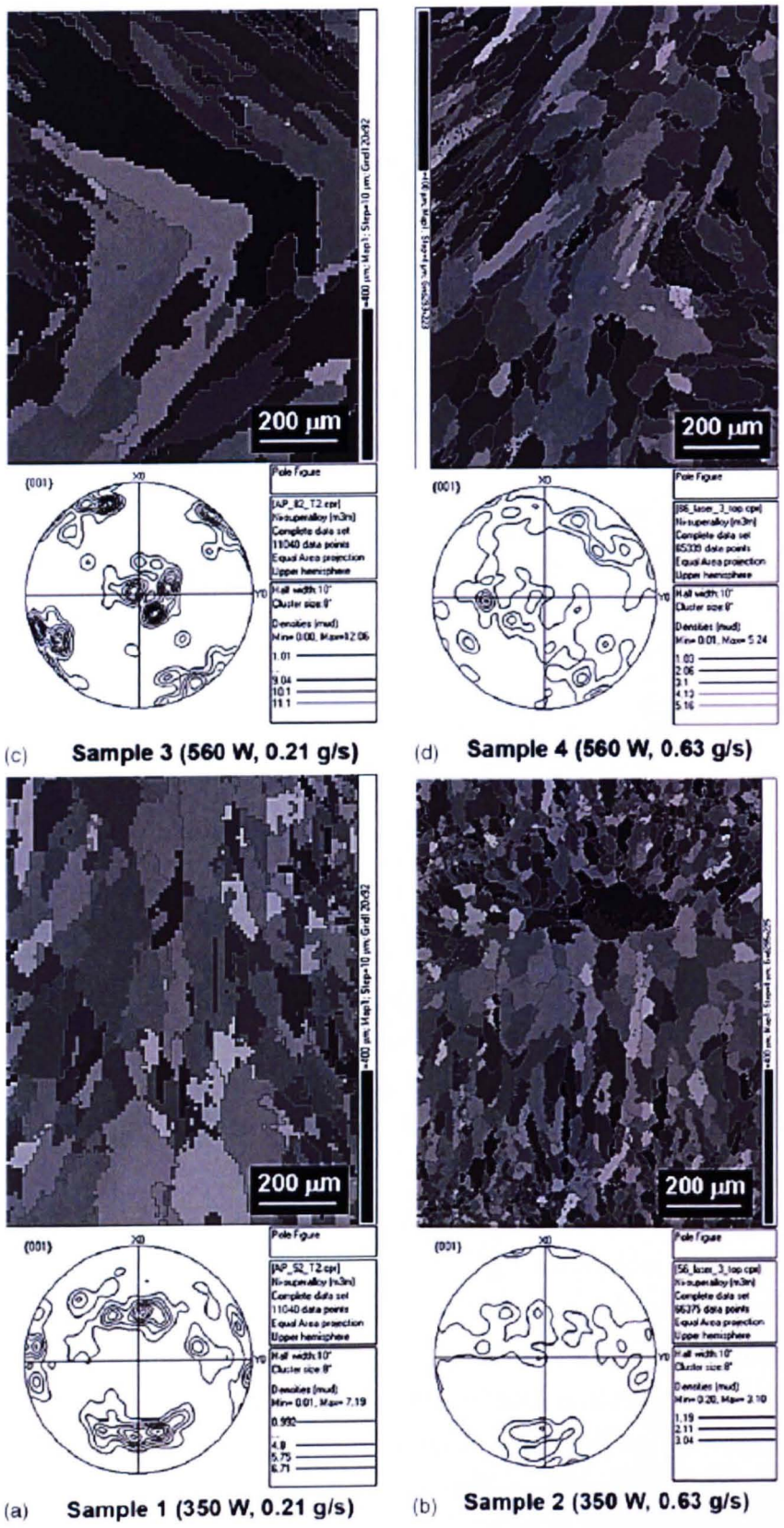

Figure 2.24 – EBSD of Waspaloy samples (Pinkerton 2006)

Figure 2.24 also gives an indication of the texture in the deposits, the weakest texture is observed in Sample 2 which reflects the randomly orientated equiaxed grains whereas the remaining deposits have stronger textures indicative of columnar

structures. The texture is stronger in high power low powder flow rates as more of the incident energy is available to melt the underlying material which means that epitaxy will dominate over nucleation.

Dinda et al. showed that similar behaviour is observed during laser deposition of Inconel 625, columnar dendrites grew along <001> directions closest to (but in the opposite direction) the direction of heat flow with epitaxial growth evident. The thickness of single track walls also increased with power, mass flow rate but increased with reducing beam velocity. They showed that high temperature heat treatment (>1000°C for 1hour) resulted in significant grain growth and with it a reduction in Vickers hardness. This is in keeping with the work carried out by Blackwell (Blackwell 2005) who showed that high temperature HIPping caused significant grain growth in Inconel 718.

In contrast to the literature where columnar grain morphology is reported to exist in laser deposited materials over a range of alloys and processing conditions, Wu et al. (Wu 2004a) report the presence of equiaxed grains in a burn resistant Ti alloy (BurTi, Ti-25V-15Cr-2Al-0.2C) processed by laser deposition as shown in Figure 2.25.

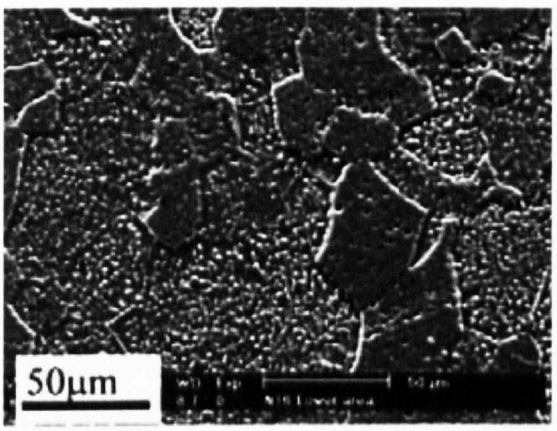

Figure 2.25 – Wu 2004 mat des 25 103-139, BurTi equiaxed grains

The equiaxed grains are beta phase and contain significant amounts of precipitate distributed uniformly within the grains and at grain boundaries; this is reported to be Ti_2C. Some increase in grain size with increasing laser power is observed and an increase in volume fraction of precipitate was also seen, this value was 16% which is 4 times higher than the expected equilibrium volume fraction. Increasing beam velocity was shown to produce elongated grains in some cases and result in finer precipitates.

Wang et al. (Wang 2006b) showed that equiaxed grains were also produced in a functionally graded material (FGM) of Ti-6Al-4V and BurTi. Increasing amounts of BurTi powder were fed into the melt pool as the height of a single track wall

increased; the starting composition was Ti-6Al-4V which was delivered by a wire feedstock. The initial layers of Ti-6Al-4V displayed the characteristic columnar grains but adding BurTi powder caused a change to equiaxed morphology, and grain refinement was seen with increasing amounts of BurTi. This is shown in Figure 2.26.

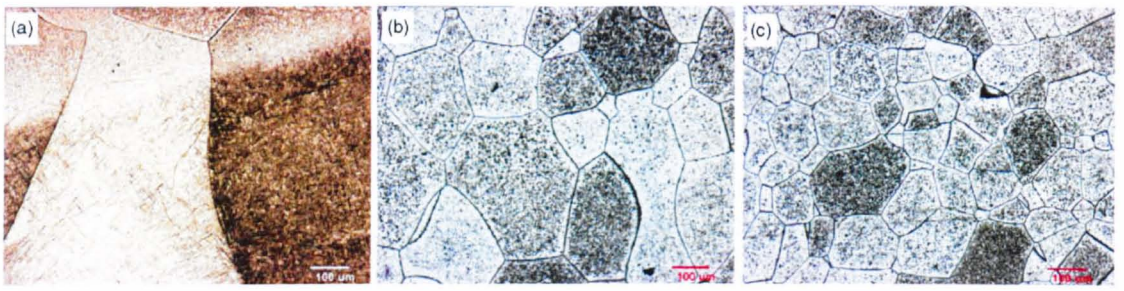

Figure 2.26 – (a-c) increasing BurTi content (Wang 2006)

An explanation offered by Wu in the two studies (Wu 2004a, Wu 2004b) is that the grain morphology is related to the intrinsic differences in solidification between the BurTi alloy and Ti-6Al-4V since the solidification conditions and external nuclei are similar during deposition of each alloy. This is explained using the binary phase diagrams for the primary constituents of the alloy; Ti-Al for Ti-6Al-4V and Ti-V for BurTi, these are shown in Figure 2.27. The slope and the freezing range for the Ti-Al system is large then that for the Ti-V, this means that a larger undercooling is required in Ti-Al to drive the growth of any nuclei formed in the first stage of solidification compared to the Ti-V where growth will occur at very small values of undercooling. The short amount of time available for the liquid to cool during laser processing means that epitaxial growth will dominate in the Ti-Al system.

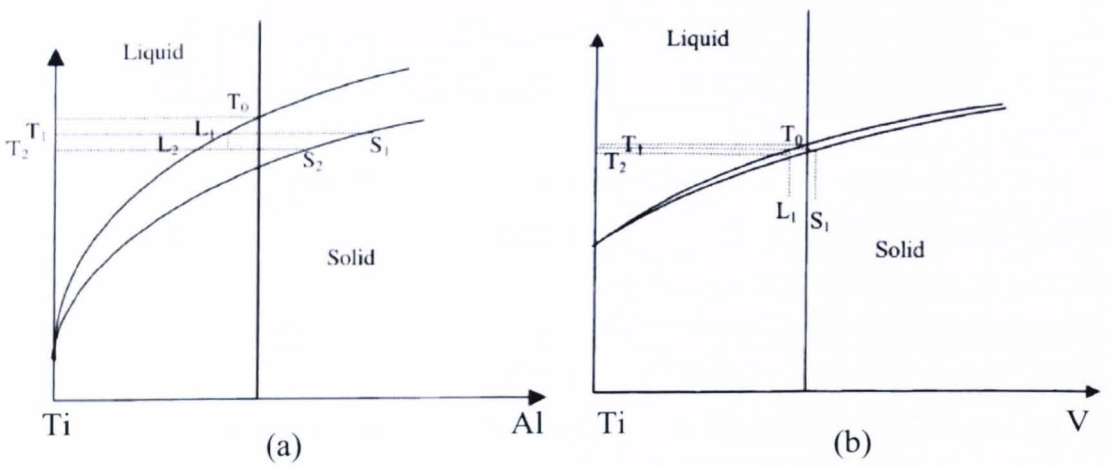

Figure 2.27 – Wu 2004a and Wu 2004b (a) Ti-6Al-4V (Ti-Al binary) (b) BurTi (Ti-V binary)

2.4.5 Powder-bed

Much of the literature relating to powder-bed systems is focused on optimising the laser parameters to produce parts which are fully dense with some studies considering the generation of thermal stresses during melting/solidification and the development of novel materials or powder blends being processed.

In many cases the process is referred to as Direct Metal Laser Sintering despite the absence of any significant levels of sintering of powders, more accurately the powder is melted and consolidated. The key difference being that a single melted track is often fully dense compared to a sintering process where the heat-affected powder would retain some of the porosity associated with the loose powder.

The source of porosity in laser melted ALM techniques is more likely related to the arrangement of the single tracks, what is referred to as a 'hatching technique' which describes the path of a laser used to melt a desired area. 316L stainless steel was processed by O'Neill et al. (O'Neill 1999) using a pulsed laser to build simple cubic samples. They investigated the effect of pulse frequency on density using a 300μm laser beam diameter on 40μm thick layers of powder, varying the processing parameters to melt a single layer successfully before melting subsequent layers to produce the 3-dimensional form. Their results showed that higher incident energy densities brought about by reducing beam diameter for example, increases porosity in the cubes. It was concluded that this was caused by excessive heating of the powder and underlying material being heated rapidly and vaporising causing an increase in gas pressure in the vicinity of the laser, the resulting shockwave and recoil physically displaced the powder layer resulting in incomplete tracks which are made worse in the following layers due to the increasing proportion of powder and gas in that layer.

Further work on 316L by Morgan et al. (Morgan 2002) showed that improved hatching can yield parts >99% dense, it was noted that in parts with <100% density the mechanical properties are determined and indeed limited by the level of porosity. Parameters such as laser power, beam velocity and diameter were optimised to give a coherent layer but when subsequent layers were melted the resulting parts were not necessarily pore free. Instead long diagonal pores were observed and were continuous across many layers; these were attributed to the rastering pattern of the hatching technique where pores occur in the inter-track region. When such a pattern is used the inter-track regions are aligned vertically in the following layers causing a local increase in the thickness of the powder layer. Expansion of the gas in these regions when heated by the laser can displace the loose powder and cause areas where no new material is added to the underlying part. This effect was overcome by an intermediate

powder layer being melted to fill in the gaps in the inter-track regions as well as a further melting stage to remelt the new layer to ensure all loose powder is bonded and improve the surface quality of the top layer. This, while successful in reducing porosity is a very time consuming and detrimental to process speed. The group also reported that rotating the hatching pattern 90° in alternate layers can improve part integrity by eliminating the interconnectivity of pores between layers (as shown in Figure 2.28).

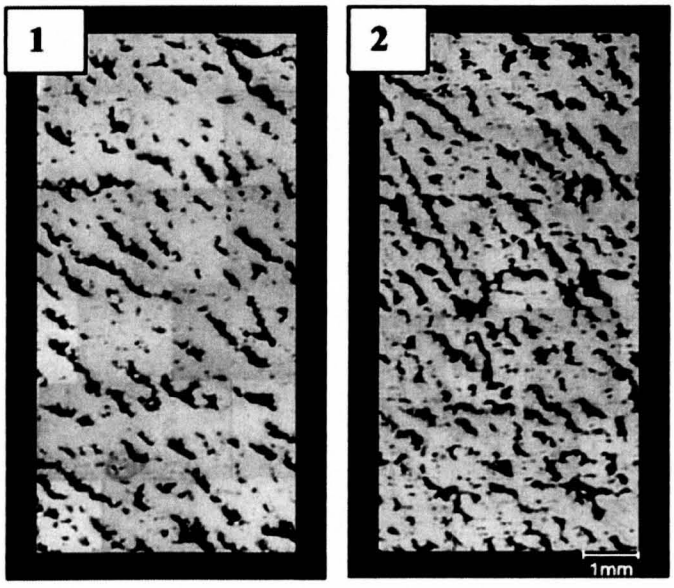

Figure 2.28 – Interconnected porosity in 316L samples made by selective laser melting (Morgan 2002)

Simich et al. and Morgan et al. (Simich 2003) investigated the effect of various processing parameters on part density for Fe and 316L powders respectively, for continuous wave lasers. Both report that for specific energy input the density of a part generally increases, this is shown in Figure 2.29. Specific energy was used by each author to combine multiple processing parameters but is defined differently by each; Equation 2.6 was used by Simich et al. (2003) and Equation 2.7 by Morgan (2003).

$$E_\rho = \left(\frac{P}{v_b \times OS \times layer \cdot thickness} \right)$$

Equation 2.6

$$E_\rho = \left(\frac{P}{\pi r^2} \right) \left(\frac{2r}{v_b} \right) \left(\frac{2r}{OS} \right)$$

Equation 2.7

Where E_p is specific energy input, P is laser power, v_b is beam velocity, OS is the offset of the beam between adjacent tracks and r is beam radius. In Equation 2.6 the expression is a measure of how the energy is distributed per unit volume of melted material and in Equation 2.7 the first term is an expression for the power density, the second term represents the exposure time for a given point and the third term the number of exposures a give point will receive, this reduces down to give an expression of the energy distribution over the exposed area. The problem with each of these is that there is no accounting for interactions between process variables, i.e. the same energy input can be achieved with different combinations of parameters but the resulting parts have different densities. This is evident in Figure 2.29 where a significant amount of scatter is observed, in some cases as much as 5% density and in the case of Morgan et al. (Morgan 2003) as much as 10% density.

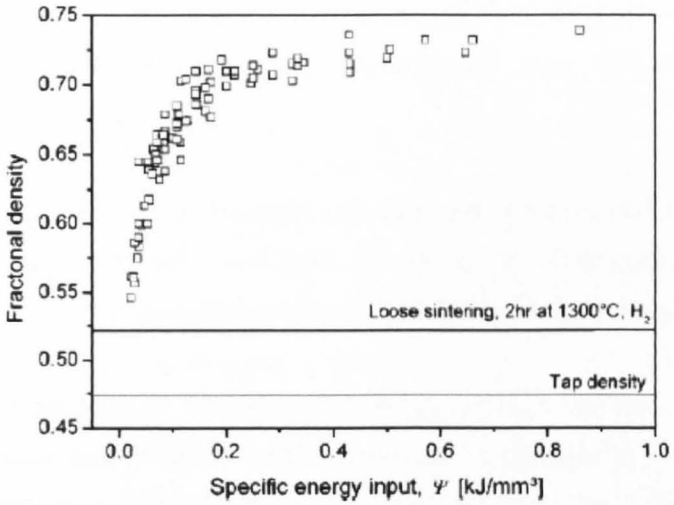

Figure 2.29 – Effect of specific energy input on part density (Simich 2003)

Xie et al. (Xie 2005) reported the density of simple shapes produced by ALM achieving values up to 84% for M2 and H13 tool steel by optimising the hatching technique by re-applying a layer of powder to the melted layer without changing the height of the build and melting this new powder in the gaps between tracks of the previous. This study uses thicker powder layers of 80-150μm and also reported that at a critical beam velocity the onset of 'balling' is observed where surface tension on the molten pool causes the track to break up into balls, the discontinuity in this case will also cause porosity in the final part. They suggest that when beam velocity is lower than this critical value balling is avoided and residual porosity is caused by poor hatching technique.

2.5 Heat transfer modelling

2.5.1 Introduction

Mathematical modelling is a tool used to aid the understanding and control of a process. Models can be 'Empirical', derived from experimental observations, or 'Physical', based on a physical understanding of the mechanisms taking place in a process (Steen 1991). These are often termed 'Black-box' and 'White-box' modelling respectively, with models incorporating both observational data and physical understanding being dubbed 'Grey-box' models.

With all modelling there are several targets;

- Gaining a semi-quantitative understanding of the mechanisms involved in a process for the purpose of Experimental Design and the display of results. Examples of this are dimensional analysis and order of magnitude calculations.

- Parametric understanding for process control i.e. relating the effect of processing parameters to a given response, for example in empirical modelling, statistical charts and analytical models.

- Developing a detailed understanding of a process to analyse precise process mechanisms for prediction of outcomes, process improvement and knowledge generation. These can be in the form of analytical and/or numerical models.

A number of analytical models exist which describe the thermal conditions and heat flow for a moving heat source. One example describes a 'quasi-stationary' system for heat flow in 1, 2 and 3 dimension (1D, 2D, 3D) for a moving point heat source traversing the edge of a plate. This initial work was carried out by Rosenthal (Rosenthal 1946).

Rosenthal integrated the point source solution over a given time, t, and moved it by letting $x=(x_0+v_bt)$ where x is the new position of the point source, x_0 is the starting point and v_b is the velocity of the moving point source. This resulted in the fundamental heat transfer equation for a moving heat source which was applied to welding, cladding, flame cutting and continuous casting. The solution was resolved into one-dimensional heat transfer which can be used to describe the melting of welding rods, the two-dimensional model used a linear heat source and is applied to deep penetration welding, welding of thin sheets, and flame cutting, and the three-

dimensional model which is used to describe laser surface treatments. It assumes a semi-infinite substrate and constant, temperature-independent thermal properties and neglects thermal loss through radiation and convection.

Expressions for temperature profile were derived from the differential equation for heat flow in the quasi-stationary state;

$$\frac{\partial^2 T}{\partial x^2}+\frac{\partial^2 T}{\partial y^2}+\frac{\partial^2 T}{\partial z^2}=\frac{1}{D}\frac{\partial T}{\partial t}$$

Equation 2.8

Where T is temperature, D is thermal diffusivity. Rosenthal (Rosenthal 1946) shows how Equation 2.8 equates to give 2D and 3D temperature profile expressions that are functions of the processing parameters v_b and Q (laser beam velocity and power respectively), the case for 2-dimentional heat flow is:

$$T=T_0+\frac{\alpha Q}{\pi k b}e^{\frac{-v_b x}{2D}}K_0\left(\frac{v_b r}{2D}\right)$$

Equation 2.9

Where α is the absorptivity of the target/substrate, b is wall/plate thickness, k is thermal conductivity, D is thermal diffusivity, T_0 is the far field temperature (or the substrate temperature), K_0 is the modified Bessel function of the second kind, order zero, and where $r^2=x^2+y^2$ *(2D) or* $r^2=x^2+y^2+z^2$ *(3D)* and x, y, z are spatial coordinates relative to the heat source.

This is obtained by considering the case where a linear heat source traverses the edge of a thin and narrow plate (b is plate thickness). No surface losses are assumed and the solid is assumed to be bound by planes corresponding to the free sides of the plate. This is achieved mathematically by the Method of Images which involves the use of fictitious heat sources at the free sides which are used in such a way that these bounding planes become planes of symmetry.

The case for 3-dimentional heat transfer is given in Equation 2.10;

$$T=T_0+\frac{\alpha Q}{2\pi k r}e^{\frac{-v_b(x+r)}{2D}}$$

Equation 2.10

In this case the bounding planes (no surface losses) are assumed to be the top and bottom surface of a thick plate which encounters a point heat source.

The 2D and 3D heat transfer models can be used to describe laser Additive Manufacturing techniques similar to those discussed in Section 2.4. Equation 2.9 is best suited for describing the temperature profile during laser deposition of thin walls where the wall thickness is similar to the beam diameter as it can be assumed that heat flow is 2D, i.e. through the solid and into the substrate, which acts as a heat sink. This approach was used in a number of studies in laser welding, surface hardening and Direct Metal Deposition (DMD) (e.g. Cline 1977, Dye 2001, Vasinonta 2001, and Bontha 2006a/b,).

Equation 2.10 can be used to describe deposition of bulk structures by DMD and melting of a thin powder layer on a thick substrate such as in the case in powder-bed additive manufacturing.

Cline and Anthony (Cline 1977) showed how to overcome the problem for the singularity associated with the point heat source used in the Rosenthal solution which leads to an infinite temperature directly beneath the heat source (i.e. when r=0). This was achieved by summing a series of heat sources to model a Gaussian power distribution rather than a single point. This was used to assess the validity of a model to describe the temperature fields of surface heating and surface melting and was shown to be accurate for 304-stainless steel at a variety of process speeds. The authors also note that the model is relevant to electron beam processes and that these can be more realistic because of the improved coupling between the heat source and the surface. However the use of the adapted model requires more complicated numerical calculations to solve the integral over the Gaussian power profile.

Nguyen et al. (Nguyen 1999) also used a modified heat source to improve accuracy near to this region. They used a 3D moving heat source with the form of semi- or double-ellipsoid to model GMA welds on HT-780 carbon steel and showed that good agreement was observed with thermocouple measurements but conceded that the transverse cross-section of the weld was not accurately modelled due to simplifying assumptions as convection in the pool causes a 'screw-head' shape rather than an ellipse.

A number of studies have used analytical heat transfer models based on the Rosenthal solution to investigate the effect of processing parameters on single and multi-layer cladding track geometry (Pinkerton 2004a, Liu 2007). Pinkerton et al. used the models for energy and mass balances to model the melt pool size of 316L stainless steel and H13 tool steel, the models showed that track heights and widths increase with laser power for a given powder delivery rate and track height increases with powder delivery rate. Liu et al. (Liu 2007) considered the effect of process variables on track thickness and powder melting efficiency. They report that absorptivity, laser power, beam velocity, substrate temperature and thermo-physical

properties are key in describing track thickness and are all considered in the Rosenthal model, however powder flow rate is not, this is said to reduce absorptivity at increasing levels because of reflections at the powder particles' surface and the shadowing effect which increase when more particles are delivered per unit time.

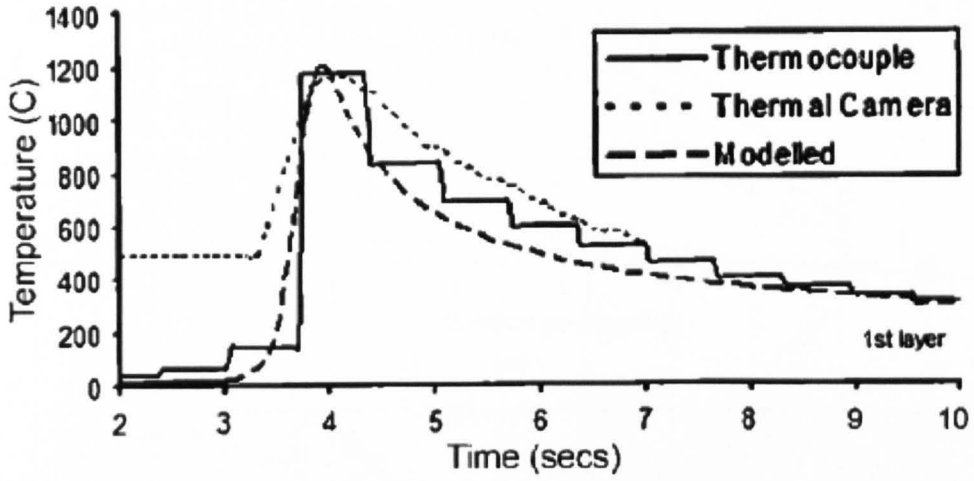

Figure 2.30 - Comparison on analytical model to pyrometer and thermocouple readings (Pinkerton 2006)

The Rosenthal 2-dimentional model was validated by Pinkerton et al. (Pinkerton 2006) for Waspaloy deposited by Laser DMD. Weld pools were monitored by pyrometers and underlying tracks were monitored using contact thermocouples and agreement was observed to be within 150°C as shown in Figure 2.30. Another analytical model and a numerical model developed for ANSYS was examined by Labudovic et al. (Labudovic 2003) and excellent agreement was observed for pool geometry between the models and experimental data for MONEL-400 alloy powder deposited on AISI 1006 steel plate, this is shown in Figure 2.31.

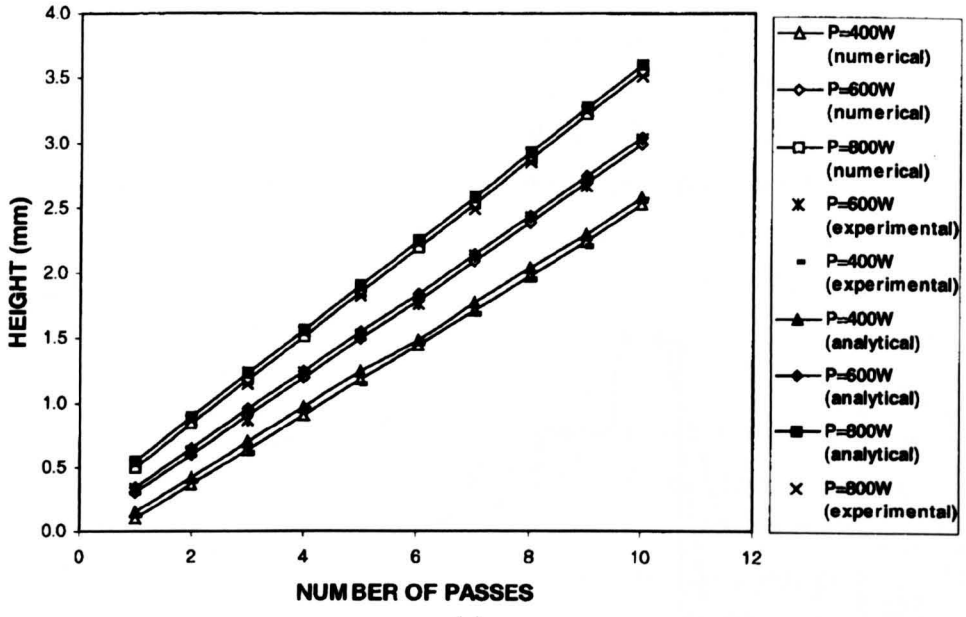

(a)

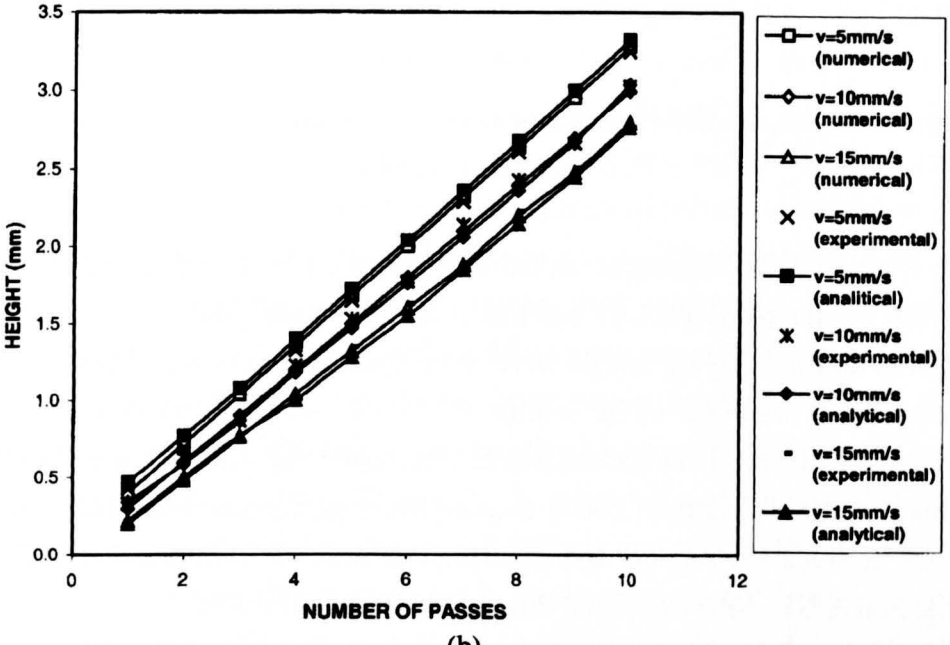

(b)

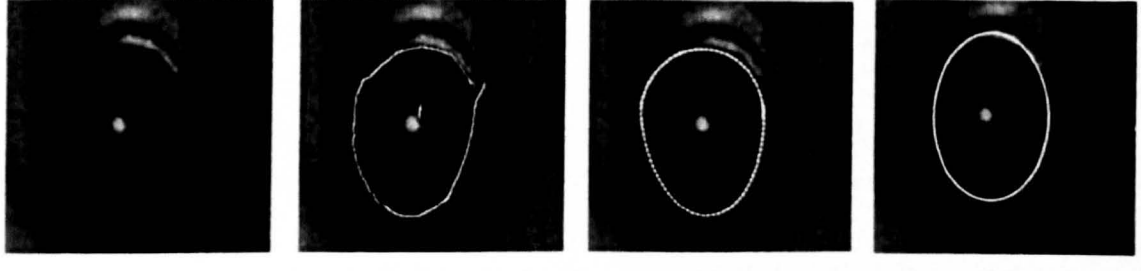

(c) (d) (e) (f)

Figure 2.31 – Effect of laser power and beam velocity on melt pool depths (a and b) established by experiment, analytical and numerical models. (c) imaging of top of weld pool and comparisons to edge detection software (d), numerical model (e) and analytical model (f), after Labudovic et al.

Vasinonta et al. (Vasinonta 2001) applied the 2-D Rosenthal model to Solid Freeform Fabrication (SFF) by converting the expression to dimensionless numbers to note the effect of changing processing parameters on pool length and wall height for any alloy of known thermo-physical properties. Process maps were produced (Figure 2.32) as a function of dimensionless wall height, melting temperature and meltpool length to show the interactions between laser power, beam velocity and material properties. The model was tested using experimental data for 304-stainless steel with good accuracy in particular at higher beam velocities.

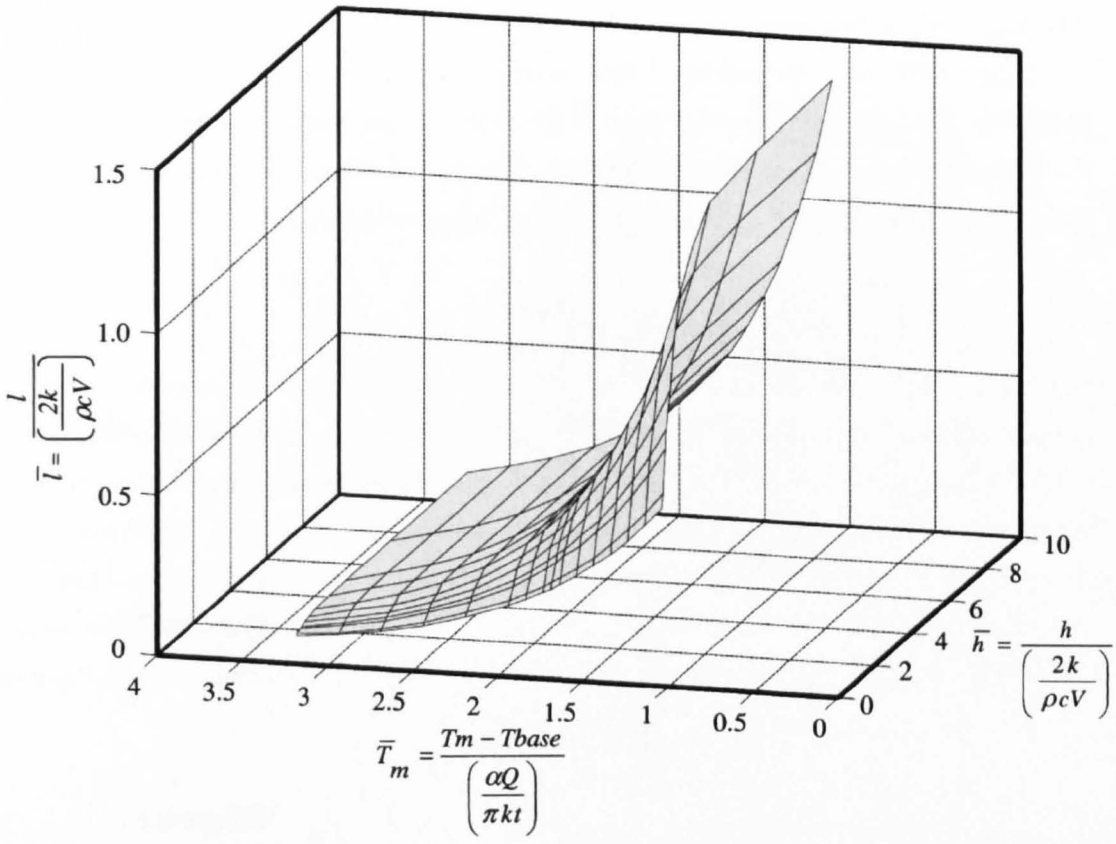

Figure 2.32 – Processing map produced by Vasinonta et al. showing interaction of processing variables and material properties on weld pool and wall geometry.

2.5.2 Solidification conditions

Predicting and controlling microstructure in laser deposited structures is the focus of the current study and requires knowledge of the thermal conditions during solidification, namely cooling rate and thermal gradient. Several investigations have been reported in the literature with a similar focus.

Bontha (Bontha 2006b) used the Rosenthal solution for 2-dimensional heat transfer and extended the work done by Vasinonta (Vasinonta 2001) to include cooling rates and temperature gradients. This was applied to the laser-engineered net shaping (LENS) process.

In the case of 2-dimensional heat transfer; by differentiating Equation 2.9 with respect to time and spatial co-ordinates gives an expression for cooling rate (Equation 2.11) and temperature gradient (Equation 2.12 to Equation 2.14) in 2-dimensions at a given point in the region affected by the moving heat source.

$$\frac{\partial T}{\partial t} = \left(\frac{\alpha Q v_b^2}{2\pi D k b}\right) e^{\frac{-v_b x}{2D}} \left(\frac{x}{r} \cdot K_1\left(\frac{v_b r}{2D}\right) + K_0\left(\frac{v_b r}{2D}\right)\right)$$

Equation 2.11

$$|\nabla T| = \left(\frac{\alpha Q v_b}{2\pi D k b}\right) \sqrt{G_x + G_z}$$

Equation 2.12

Where

$$G_x = -e^{\frac{-v_b r}{2D}} \left(\frac{x}{r} \cdot K_1\left(\frac{v_b r}{2D}\right) + K_0\left(\frac{v_b r}{2D}\right)\right)$$

Equation 2.13

$$G_z = -e^{\frac{-v_b r}{2D}} \left(\frac{z}{r} \cdot K_1\left(\frac{v_b r}{2D}\right)\right)$$

Equation 2.14

Where K_1 is the modified Bessel function of the second kind, order one and all other variables have been described previously.

Similarly Bontha (Bontha 2006a) developed expressions for cooling rate and temperature gradient in 3-dimensions by differentiation of Equation 2.10 to give Equation 2.15 to Equation 2.19.

$$\frac{\partial T}{\partial t} = \left(\frac{\alpha Q v_b^2}{4\pi D k r}\right) e^{\frac{-v_b(x+r)}{2D}} \left(1 + \frac{x}{r} + \frac{2xD}{v_b r^2}\right)$$

Equation 2.15

$$|\nabla T| = \left(\frac{\alpha Q v_b^2}{4\pi D^2 k}\right) \sqrt{G_x + G_y + G_z}$$

Equation 2.16

Where

$$G_x = -\frac{D}{v_b r} e^{\frac{-v_b(x+r)}{2D}} \left(1 + \frac{x}{r} + \frac{2Dx}{v_b r^2}\right)$$

Equation 2.17

$$G_y = -\frac{yD}{v_b r^2} e^{\frac{-v_b(x+r)}{2D}} \left(1 + \frac{2D}{v_b r}\right)$$

Equation 2.18

$$G_z = -\frac{zD}{v_b r^2} e^{\frac{-v_b(x+r)}{2D}} \left(1 + \frac{2D}{v_b r}\right)$$

Equation 2.19

Bontha (Bontha 2006a, Bontha 2006b) produced processing maps to show dimensionless cooling rate and temperature gradient as functions of laser processing parameters, materials properties and depth in the melt pool; these are shown in Figure 2.33. The results show that increasing power and decreasing velocity reduces the temperature gradient and cooling rate, and relative to depth in the pool temperature gradient decreases slightly towards the bottom and cooling rate tends towards zero where there is a transition from melting to solidification (heating to cooling).

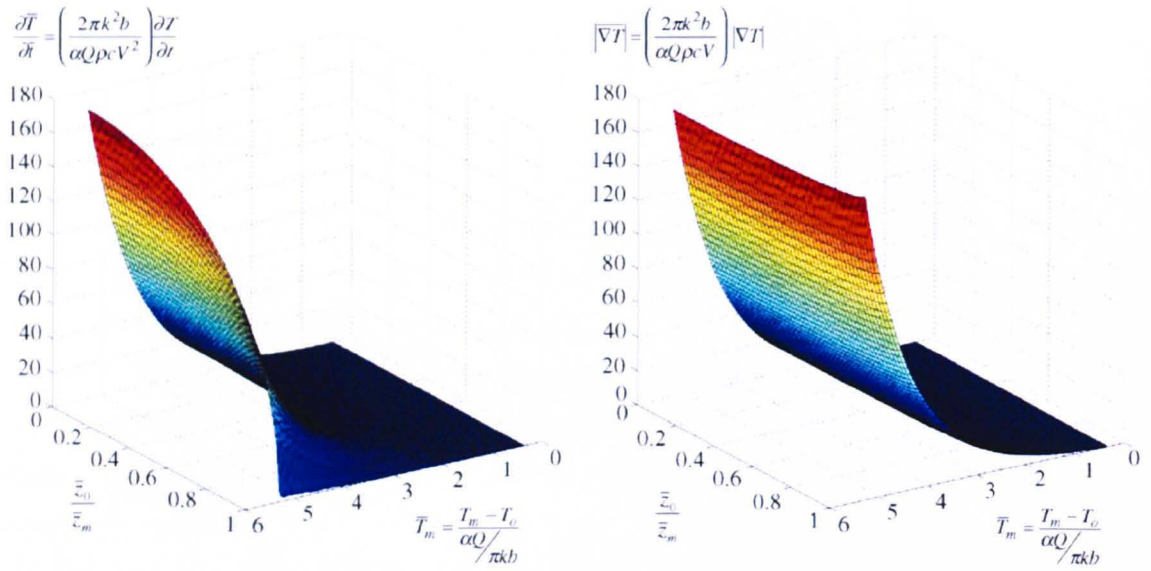

Figure 2.33 - Dimensionless cooling rate and temperature gradient process maps after Bontha 2006b

2.5.3 Effect of process parameters

The microstructure of metals and alloys is determined by the local solidification conditions and so understanding how these are affected by processing parameters is important. Gäumann (Gäumann 1999a) showed in the special case of a stationary point source on a large substrate (v=0 in Equation 2.10), simple differentiation can show a link between two processing parameters (laser power Q and substrate temperature T_0) and the temperature gradient in the system. Equation 2.20 shows this simplification;

$$T = T_0 + \frac{Q}{4\pi kr}$$

Equation 2.20

When v=0 the meltpool becomes circular with radius r_l, this can be calculated by rearranging Equation 2.20 and assuming T is equal to the liquidus temperature T_l to give;

$$r_l = \frac{Q}{4\pi k(T_l - T_0)}$$

Equation 2.21

Differentiating Equation 2.21 with respect to T gives an expression for reciprocal temperature gradient along the liquidus isotherm; hence the gradient, G, is defined by Equation 2.22.

$$G = \frac{dT}{dr} = \frac{-2\pi k(T_l - T_0)^2}{Q}$$

Equation 2.22

Equation 2.22 gives a simple expression which clearly links the temperature gradient to T_0 and Q. It is clear that increasing T_0 will reduce the gradient and, despite increasing the heat input, increasing the laser power will also reduce the gradient. The latter effect is more surprising, but, the physical result is an increase in meltpool size, hence flux through the solid/liquid interface decreases.

Steen (Steen 1991) discusses a similar simplified situation for the Rosenthal solution where the cooling rate at the surface of a weld pool along the centreline is considered. Equation 2.23 and Figure 2.34 shows that in this case the cooling rate increases proportional to the beam velocity and decreases with increasing laser power and substrate temperature.

$$\frac{dT}{dt} = -2\pi k\left(\frac{v_b}{Q}\right)(T - T_0)^2$$

Equation 2.23

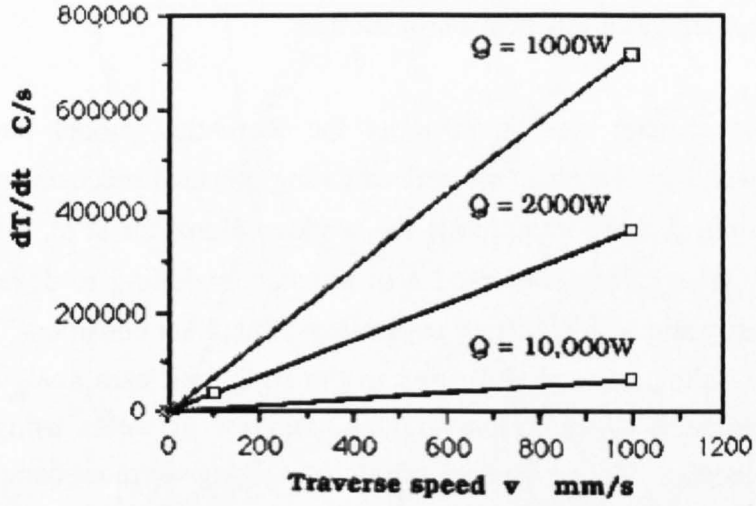

Figure 2.34 – Effect of processing parameters on cooling rate for a moving point heat source (Steen 1991).

2.5.4 Limitations of analytical solutions

The analytical solutions described in Section 2.1.2 are based on some simplifying assumptions which detract from their accuracy and relevance when applied to DMD. Rosenthal's original work (Rosenthal 1946) assumes constant physical properties i.e. that thermal conductivity and diffusivity are all independent of temperature; the effect of powder flow into the molten pool is neglected as are convective effects in the pool and latent heat of fusion. Another fundamental assumption is that 100% of the heat is transferred through the solid. Losses due to convection and radiation are also ignored.

The complexity of the ALM process i.e. the number of processing parameters, and the high operating costs make experimentation expensive and time consuming, therefore modelling can be a more cost effective method of analysis. The thermal history of a deposition is also complex; it may differ greatly from point to point within a final part, for example in regions where a laser changes direction there is an increase in heat build-up (Hoffmeister 1999) and in thin walled structures as distance from the substrate increases the heat-sink effect is diminished. As with any type of modelling or simulation, comparison to physical data is critical to validate any calculations, the amount of data available for ALM processes to do this is small due to its limited use, the number of materials and processing parameters which can be used and lasers have a highly localised nature, making direct observations difficult.

2.5.5 Development and application of models

Analytical heat transfer models such as the Rosenthal model have been used previously in welding as a basis for understanding physical mechanisms taking place during processing. A good example is the work of Hunziker et al. (Hunziker 2000) and Dye et al. (Dye 2001) who used heat transfer modelling to develop models to predict the quality and weldability of superalloys. Hunziker considers TIG welding of Inconel 718 to validate the models used in the study and uses analytical models to predict the formation of centreline grain boundaries in welds using a variety of powers and velocities. The advantages of this approach over more complex modelling such as Cellular Automata (CA) is the higher speed of processing allowing comparisons to be made much more rapidly. The work coupled the heat transfer model to the growth velocity/growth undercooling relationship of the dendrite tips during solidification, it is understood that increasing weld velocity increases the growth undercooling. The models allowed the production of a weldability map

showing a region were centreline grain boundaries are avoided along with the limits showing lack of penetration and excessive melting; this is reproduced in Figure 2.35.

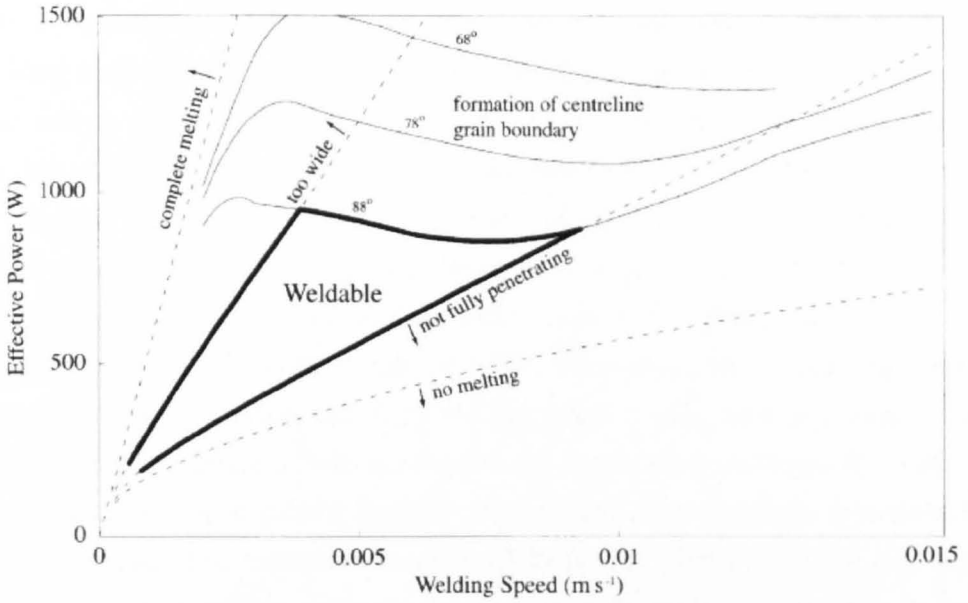

Figure 2.35 - Weldability map for TIG welding of Inconel 718 (Hunziker 2000).

This work was expanded on by Dye et al. (Dye 2001) to include models to predict the onset of carbide liquation in the heat affected zone (HAZ), solidification cracking and the formation of porosity to give a detailed weldability map (shown in Figure 2.36)

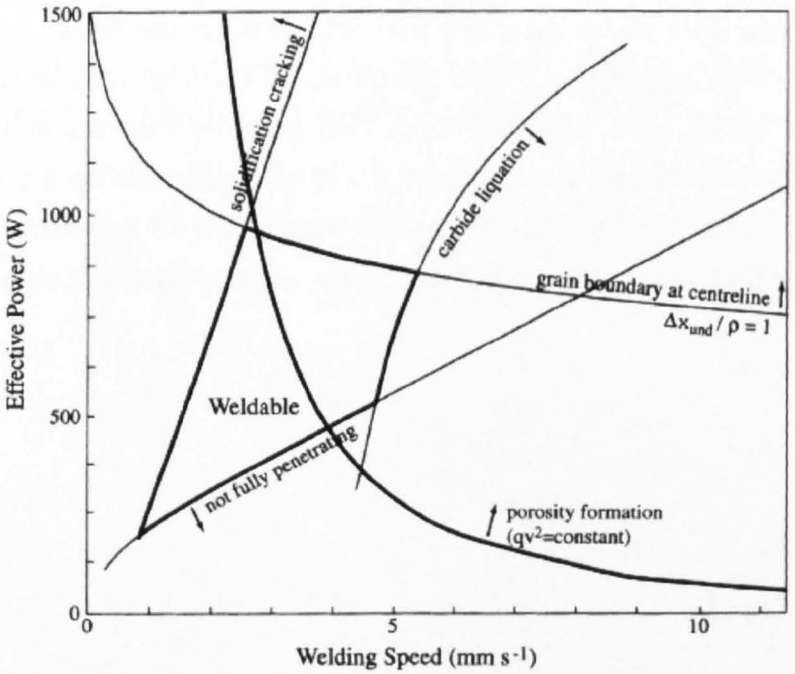

Figure 2.36 - Weldability map for TIG welding of Inconel 718 (Dye 2001).

Further attempts to couple heat transfer models with physical models have been attempted using numerical modelling or Finite Element (FE) models. Bontha (Bontha 2006b) used FE to take into account the temperature dependence of material properties on the solidification conditions through the depth of a molten pool (this is assumed constant in most analytical models). It was shown by the author that this causes a slight difference in the absolute values produced by a FE model and the Rosenthal solution but that they are in good agreement.

More complicated FE models were developed by Wang et al. (Wang 2007) and Costa et al. (Costa 2005). They used more sophisticated techniques to simulate the deposition process in blown-powder ALM by the creation or 'birthing' of elements beneath a transient heat source using SYSWELD and ABAQUS software packages respectively. Wang et al. considered the deposition of 410-stainless steel and Costa et al. 420-stainless steel but both coupled the thermal model to a phase transformation and hardness model to predict the final fractions of austenite and martensite phases to indicate the effect of various process variables on the resulting microstructure and properties. Both suggest that a thin wall built on a large substrate has a final microstructure consisting of a hard austenitic upper region and a softer lower region composed of tempered martensite. The Wang approach fails to take into account the effect of changing beam velocity on wall thickness which is kept constant for different processing conditions; however the model is successful in establishing a link between the beam velocity and the uniformity of the microstructure. At high processing speeds the amount of tempered martensite is reduced as more of the part is held at temperatures above the martensite start temperature before cooling to room temperature. This is in keeping with the results of Costa et al. who showed that the same result is achieved with conditions that promote heat accumulation such as shorter residence times between layers and a smaller substrate i.e. a poorer heat sink. The effect of residence time (Δt) is shown in Figure 2.37 for heat accumulation, phase fractions and hardness which represent the three coupled models (Costa 2005).

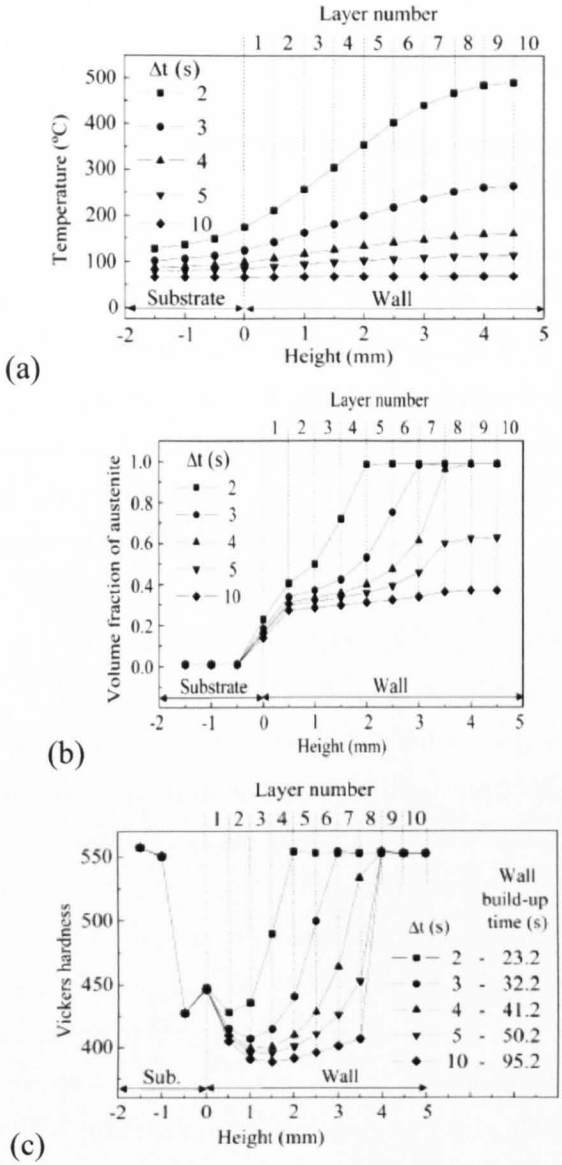

Figure 2.37. Temperature along the wall height centre line (a), volume fraction of austenite (b) and Vickers hardness (c) for different values of Δt (Costa 2005).

2.6 Design of experiments

2.6.1 The use of statistically designed experiments

Experimentation has many approaches, broadly speaking there two types; a study of fundamental relationships based on physical mechanisms or, alternatively, an empirical study to observe the direct effect of changing a process. The former uses physical quantities and theories as a basis to make predictions of outcomes and the effect of changes, the latter uses direct measurements of a response to changes made in a process without necessarily being concerned about the physical mechanisms causing the response. These two methods are often represented in practice (synonymously) with Academia, where the goal of research is to understand and generate knowledge, and Industry, where the emphasis is on process optimisation with a goal to maximise quality and production (Davis 1978).

An empirical study can often provide an understanding of how processing conditions effect an output but with little explanation as to the reasons the behind the response and a more fundamental, scientific study is often based on simplified ideas or assumptions and will represent an 'idealised' system. This is something to be mindful of when applying a scientific study to a real, 'industrial' situation as final adjustments will most likely be necessary to optimise a process. A more useful approach may be one which combines the two, where an empirical investigation is run in conjunction with an academic one to explain the responses observed. This will maximise the understanding of a process which in turn will aid in its development and optimisation.

Such an approach would be time consuming which is undesirable in an industrial environment, but a well-designed experiment will provide the required information with minimum experimental effort. Statistical Design of Experiments (DOE) is one way to achieve this.

DOE is a systematic approach to experimentation for solving engineering and scientific problems by changing one or more variables which can incorporate statistical design depending on the desired outcome. The underlying principals are to improved efficiency in data gathering and analysis over 'one variable at a time' methods by reducing the number of experiments required to generate sufficient data, hence reducing cost and time. The general procedure for DOE involves three steps; choice of an **appropriate design** to provide enough reliable information to be analysed, **regression analysis** to approximate or fit measured data to a mathematical model, and **diagnostics** of the model to test the validity (Montgomery 1997).

There are different types of outcome which can then be generated through this process;

- A **comparative** study seeks to determine whether changing a given input (in DOE this is called the 'factor' and will be referred to as such in the present work) will affect an output (or 'response') – this might be material from one supplier over another or the performance of a new material verses an existing one.

- A **characterisation** study has the aim of screening multiple factors to establish key processing parameters, how these alter a measurable response and which have a greater effect than others. This is crucial in developing an understanding of a process and may include controllable (process parameters) and uncontrollable (maybe environmental) factors, this theory is depicted schematically in Figure 2.38.

- A mathematical **model** of a process with high predictive capabilities can be generated to give a detailed understanding to a high degree of accuracy. These can take any number of forms but most engineering problems can be estimated by first- or second-order equations where regression analysis is used to determine the model coefficients. These can be used to establish a suitable operating window, find maxima/minima in a trend or identify the most efficient way to achieve a goal.

- **Optimisation** can then be achieved by use of a well-established and tested model. Optimisation may be achieved by maximising/minimising an output, hitting a target value repeatedly or reducing variation to establish a robust process.

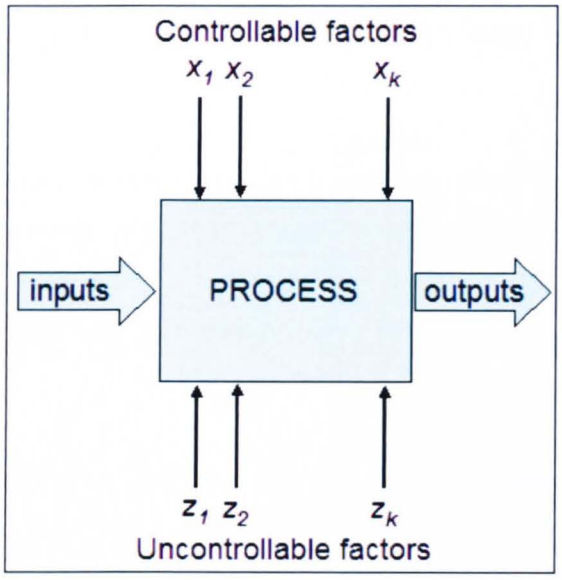

Figure 2.38 - black-box model (after Montgomery 1997)

The underpinning maths behind all stages of experimental design and analysis is well established and understood yet its heavy emphasis on quite involved statistics has lead partially to a lack of use in the field of engineering. This problem may be reduced as an increasing number of user-friendly software packages become available to assist in the design and analysis of experiments and the level of appreciation of DOE, if not mathematical understanding, improves. The use of an accurately modelled process is highly desirable to effectively use an existing process or to develop a less well understood one.

Many types of designed experiment exist, such as Robust Design (or Taguchi Design), Factorial and Fractional Factorial Design, and Response Surface Designs and all can be used to analyse the change in response for multiple factors.

Factorial Designs are commonly used for screening experiments and Response Surface Designs for process modelling. Factors under investigation can be continuous or discrete but responses are generally assumed to be continuous to enable them to be modelled mathematically where the data generated is fit to an empirical model which is an estimate of the true response surface, an example of a fitted Response Surface Diagram is given in Figure 2.39 for the expected yield of a process at various levels of Temperature and Pressure, this type of model can be used as a processing map to show the relationship between key process variables and an output. These types of statistically designed experiment can be used to predict the response of controllable factors (often equivalent to user defined processing parameters) or uncontrolled factors such as the environment (temperature, humidity) which may be incidental during processing but could be controlled during experimentation to establish their relevance.

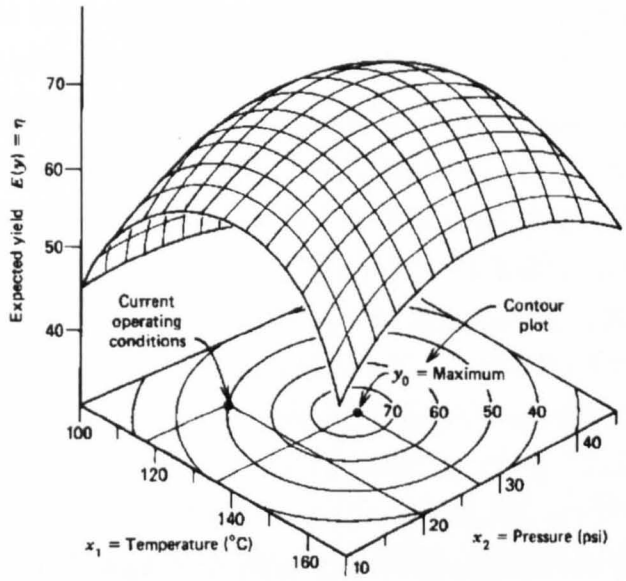

Figure 14–2. A contour plot of a response surface.

Figure 2.39 – Response surface and contour plot for a chemical process showing the effect of Temperature and Pressure (factors) on Yield (response). (Myers 2002)

There are several principles required to develop a process model which are of paramount importance when designing a statistical experiment;

- Enough data is required to estimate the coefficients of an assumed model (for example a quadratic model requires a minimum of three design points).
- Ideally, enough data should be gathered to test a higher order model than the one assumed which may not be the most appropriate (i.e. when expecting a linear response, three design points are desirable to be certain of no appreciable curvature).
- A design must have the ability to minimise the variation of the least-square coefficients during regression analysis.
- Data must be gathered and replicated where there is expected variation from noise or where a response has a high sensitivity to a change in factor (steep gradient).
- Replication of points should be used to test for lack-of-fit or signal to noise ratio.
- Data should be collected in a randomised order to minimise any bias caused by drift, wear, gain or loss. These may be a result of machine operation, operator changes, measurement error or changes in environment. The drift will be spread out over a curve in a randomised experiment which will make it possible to identify during diagnostics. (*NIST/SEMATECH e-Handbook of Statistical Methods).*

2.6.2 Factorial design

One type of experimental design is a Factorial Design (Myers 2002). This is used to investigate the joint effects of more than one factor, that is, the main effects of individual factors and the Interaction effects of multiple factors, it is not sufficient to vary one factor at a time and the effect one factor has on another must be considered (i.e. their interactions). A Factorial Design considers a number of factors at a given number of Levels (a level is the value attributed to the factor being scrutinised); for example the simplest Factorial design consists of two factors each tested at two levels (a high and a low level), giving 4 Trials. This is denoted as a 2^2 Factorial [(number of levels)$^{(\text{number of factors})}$], in general a two-level Factorial is often written as 'a 2^k-Factorial' where k is the number of factors being investigated and 2^k is the number of trails. This is depicted graphically in Figure 2.40, and is useful when evaluating the variation brought about by deliberate changes in experimental conditions.

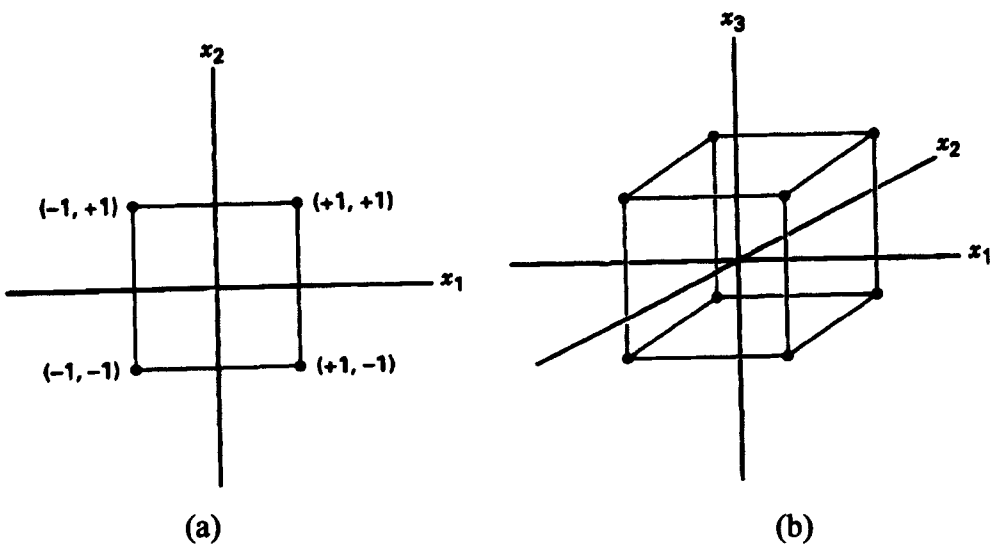

Figure 2.40 – (a) 2^2 factorial array, two factors x_1 and x_2 at two levels; -1 and +1, (b) 3^2 factorial array, three factors x_1, x_2 and x_3 at two levels (adapted from Myers 2002)

Factorial designs are used for different purposes such as; screening multiple factors, fitting first order response surfaces in order to ascertain what the next factor levels should be when investigating a large design space, and also as building-blocks for other Experimental Designs which are capable of modelling higher order response models. A Factorial Design with two levels has only two points so any plotted data will not be adequate to describe a high degree of curvature in the response surface, some curvature can be shown when there is an interaction between the two factors, i.e. when the effect of one factor is dependent on the level of another.

When a response has a significant amount of curvature, a higher-order polynomial is necessary to model the response. To fit a model to experimental data a general rule is that for every order of polynomial it is necessary to have one more level, i.e. to model a known linear function at least two levels are necessary, for a quadratic a minimum of three are needed, and so on. There are several Designs which allow for this; the simplest is to augment a 2^2 Factorial design by adding a centre-point, but a more in-depth design is known as a Central Composite Design (CCD) (Figure 2.40(b)) The CCD is the most commonly used design for fitting second order models. The Design consists of a 2^k Factorial, 2k axial or 'star' points and n_c centre-points (where n_c is the number of repeated trials at the centre of the design), which gives five Levels of each factor. For a two-factor experiment the CCD has 8 runs on the circumference of a circle with n_c centre points and a three-factor CCD has 14 runs on a common sphere plus the centre-points. This is discussed in more detail in Section 3.4.

2.6.3 DOE in practice

CCD and Factorial Designs can be used as part of Response Surface Methodology (RSM) which is a series of experiments used to make up a wider investigation of a system; simple factorial experiments can be used initially to explore a processes '*region of operability*' (the largest process window available), this is done to identify a '*region of interest*' which might include a minima or maxima or another desirable feature for optimising a process, this is shown schematically in Figure 2.41. Where minima or maxima exist, CCD is an appropriate Design to model the increased curvature in the *response surface.*

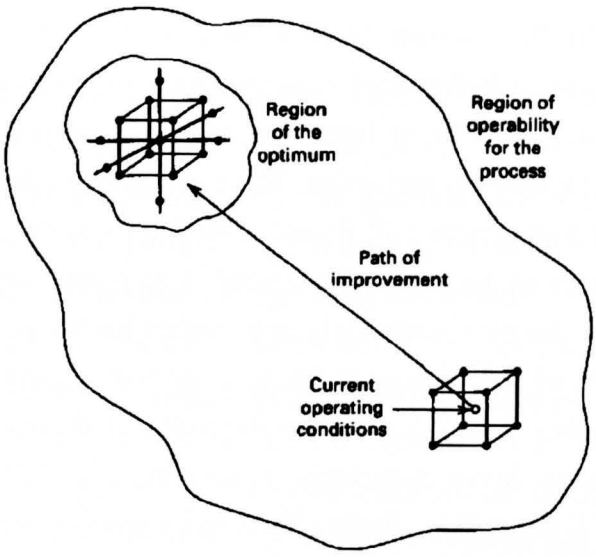

Figure 2.41 – Response Surface Methodology using multiple experiments (Montgomery 1997)

Branchu et al. (Branchu 1999) showed that 4-factor CCD as part of RSM was an efficient way to investigate the thermal stability of a model protein used in drug synthesis. Data was generated by high sensitivity Differential Scanning Calorimetry of samples produced by varying pH, and the concentrations of; sucrose, hydroxypropyl-β-cyclodextrin and protein. pH was identified as the most significant factor affecting thermal stability, the remaining factors all had a smaller but statistically significant effect.

Similarly, Gunaraj et al. (Gunaraj 1999) showed that a 4-factor CCD was successfully used to predict weld bead quality as a function of processing parameters (open-circuit voltage, wire feed rate, welding speed, and nozzle-to-plate distance) in submerged-arc-welding of carbon steel through the fitting of experimental data to empirical models. The CCD achieved statistically successful models for bead size, shape and dilution but it could be argued that the experiment was spread over a very wide range of parameters having established the operability limits and then setting the CCD to cover this whole area. A more common practise is the 'Method of Steepest Ascent' outlined by Myers and Montgomery (Myers 2002), which would test smaller areas in a screening procedure using a 2^2-Factorial to identify the locale of the Region of Operability near an optimum response before conducting a CCD, especially where a predictive model is generated, as this would normally produce a more accurate description of the true response in that area.

A special arrangement of CCD with the axial points on the face-centres of a 2^3-Factorial array as shown in Figure 2.42(a) was used by Ahmadi (Ahmadi 2005) to assess the removal of contaminants from wastewater in olive oil production. This type of design can be used to model second order responses but may be less accurate

because only three levels of each factor are tested as opposed to five in a standard CCD. The design also has less rotatability (in a totally rotatable array each trial is conducted at conditions that are the same distance from the centre point of the array) compared to a five level design which is important to ensure the variance is constant relative to the distance from the centre of the design. A study by Benyounis (Benyounis 2005a/b) used a Box-Behnken design, which is similar to a face-centred array but Design Points fall on the centre of the cubes edges (refer to Figure 2.42(b)), to investigate the effect of processing parameters on laser butt-welding bead characteristics to find parameter combinations to minimise the heat effected zone and heat input while maintaining a minimum penetration of half or full thickness. They also used software to develop processing maps to show windows of optimum conditions by numerical and graphical methods.

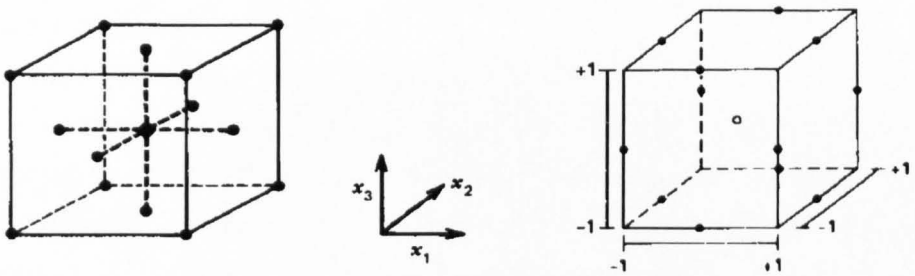

(a) (b)

Figure 2.42 – (a) Face-centred CCD and (b) Box-Behnken design (Montgomery 1997)

Work by Djoudi (Djoudi 2007) showed how CCD could be used to maximise yield in the cementation of Copper by Iron, and used existing theories to validate the relationships given by the empirical models fitted to the experimental data. Material flow rate was shown to be the most significant factor with a positive effect on yield and is consistent with theory that an increased mass transfer rate due to a reduced diffusion boundary layer thickness when the reaction is taking place. Similarly, pH, has a positive effect on yield which supports the theory that at lower pH levels (i.e. more acidic conditions) there is an increase in Hydrogen adsorption on the metal surface which reduces the number of sites available for the Cu/Fe reaction to take place. The models produced contain pure quadratic and interaction terms suggesting that there is a large degree of curvature in the response surface which implies that a design capable of fitting higher order models is necessary. They used a manual method of optimisation by plotting contour graphs of pH vs. Flow rate at three different Temperatures (Temperature also had a positive effect on yield by decreasing viscosity and hence increasing bulk diffusivity of Cu ions) as shown in Figure 2.43. Figure 2.43 show how the optimum conditions move with changing temperature and

how the maximum achievable yield changes, this makes it possible to either run the process at maximum output or at least predict the yield possible at a given temperature which may be lower than an optimum for economic reasons i.e. allowing a user to run a process cost-effectively.

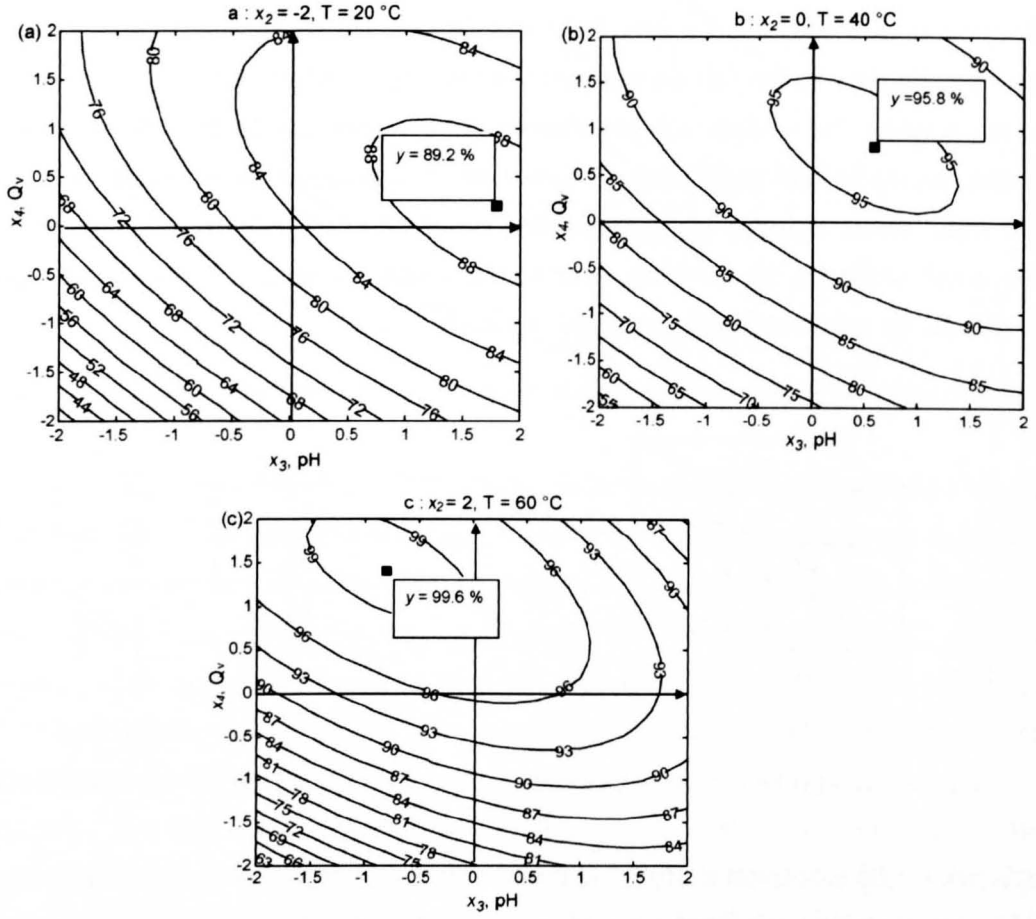

Figure 2.43 - Surface contour plots for copper cementation for different levels of temperature (*y* is Yield, *Qv* is mass flow rate, and *T* is temperature (Djoudi 2007)

Aslan (Aslan 2008) used a 3-factor CCD experiment to model the Chromite concentration and grade (a measure of quality) produced by the multi-gravity separator technique. The results of the experiment revealed that drum speed was the significant factor effecting both recovery and grade of Chromite. The remaining two factors (drum angle and wash water flow rate) are described as having a 'trivial' affect which might have been discovered earlier in a screening experiment to save on experimental effort. The drum speed had a positive effect on recovery but a negative effect on grade, which is counter-productive or conflicting as it is desirable to increase recovery rate and the grade. Therefore there is a trade-off between quality and quantity; as such the fitted model can be used to select processing conditions to optimise for one outcome while understanding and managing the negative effect on the other.

2.6.4 Key Phrases/terms

The following list of terms and phrases is intended as a guide for the reader, in the list they are highlighted in bold and given a brief definition and where these are used in the subsequent text they will be italicised for clarity;

- ***Study/Investigation*** – a collection of *experiments* used to examine a process or system.
- ***Experiment*** – a series of *trials* used to investigate a specific part of the *region of operability.*
- ***Trial/Design Point*** – a single test carried out in an experiment consisting of a specific combination of *factors* at specific *levels.*
- ***Design*** – the arrangement of the trials in a specific array dictated by the type of study being conducted.
- ***Design Space*** – the area covered by the Design array.
- ***Factor*** – a parameter or input varied to determine its effect on the outcome of the test. This can be controllable, i.e. a processing parameter used to control a process, or uncontrollable, i.e. an effect incidental to the process such as atmospheric conditions.
- ***Level*** – the specific setting or value of a given factor, e.g. laser power = 200W
- ***Treatment*** – the combination of factor levels describing a trial, i.e. the parameter set.
- ***Response*** – the output measured after a trial has taken place.
- ***Effects*** – the contribution of a factor to the Regression Model fitted to the responses across the Design Space. The Effects include the Main Effects of the factors, Interaction Effects of combined factors and where applicable the effects of higher order factors.
- ***Region of interest*** – the area of the design space where the response is of particular interest, for example, this may be an area which includes a maxima or minima at a specific combination of factors.
- ***Region of operability*** – the total area or range of parameters where experimentation is possible, i.e. that confined by the limits of the equipment used.
- ***Response surface*** – the collective, measured responses over the design space. The 'True response' is a complicated unknown function of the factors and the 'fitted response' is one described by a mathematical model that is fit to measured data to a specified level of confidence and is used to accurately predict the true response.

3 Experimental techniques

The experimental techniques used in the study are outlined in this chapter. Emphasis is placed on the two additive systems under investigations, particularly the definition of key processing parameters used to produce samples. The alloy of interest is described and the methods of characterisation used are briefly outlined.

The principals of statistical design of experiments are introduced and the methods of linear regression, analysis of variance (ANOVA) and residual diagnostics are outlined.

3.1 Additive layer manufacturing processes

Additive Manufacturing was described in Section 2.4. In this chapter the two processes used in this study are described in detail, the first is the EOS and the second is the Trumpf DMD505. The two systems are described in sections 3.1.1 and 3.1.2 respectively. Key processing parameters are defined and explained and the sample geometries produced to investigate the material response to these variables are described.

3.1.1 EOS M270 process description

3.1.1.1 Machine features

The EOS M270 (shown in Figure 3.1) uses a process described as Direct Metal Laser Sintering (DMLS) by the machine manufacturer (EOS GmbH). This name, though synonymous with the process, is not an accurate description of the mechanism being used to consolidate the metal powder feedstock. The metal powder is melted by a 200W Ytterbium-fibre laser and re-solidified rather than sintered; this is because the heating and cooling experienced by the powder is sufficient to melt it and too rapid to facilitate a significant level of sintering. The M270 is a so-called 'powder-bed' system which involves laying down a thin layer of powder across a work area then selectively melting an area corresponding to a cross-section of the final component geometry.

Figure 3.1 - EOS M270

A schematic of the M270 is shown in Figure 3.2 at three stages during the build process; (a) shows the starting position, three chambers can be seen; the right is the 'Dispenser' which holds the powder to be laid down, the middle chamber is the 'Build Platform' where the laser exposure takes place and the left is the 'Collector' which receives the excess powder. The Build Platform consists of a metal plate (usually mild steel for coat reasons unless the base plate will for part of the final component) onto which the powder is melted. On the right hand side there is a 'Recoater' which consists of a metal arm with a ceramic blade that scrapes the powder from the Dispenser across the build area and into the Collector, this can be seen in Figure 3.2(b) and (c). After a layer has been put down the laser selectively melts the relevant area (the 'Hatching technique' i.e. the path taken by the laser to melt the powder is important and described in section 3.1.1.2), once a layer is complete the build platform lowers and subsequent layers are laid down and melted to build a three-dimensional component. The layers of powder are laid down in a process known as 'recoating'.

The building process takes place under a controlled atmosphere. The machine used in this study uses a Nitrogen atmosphere but an extended machine is also available which uses Argon. The Nitrogen is produced from a supply of compressed air and is blown into the build chamber at a flow rate which can be altered depending on the material being processed. This flow of gas is necessary to remove particulates or 'condensate' from the build chamber which is produced during melting and are extracted through a filtration system, the amount and type of condensate produced is dependent on the material being melted. The exact composition of the condensate was not tested in this study but consists of spatter from the melt pool and a black soot-like substance.

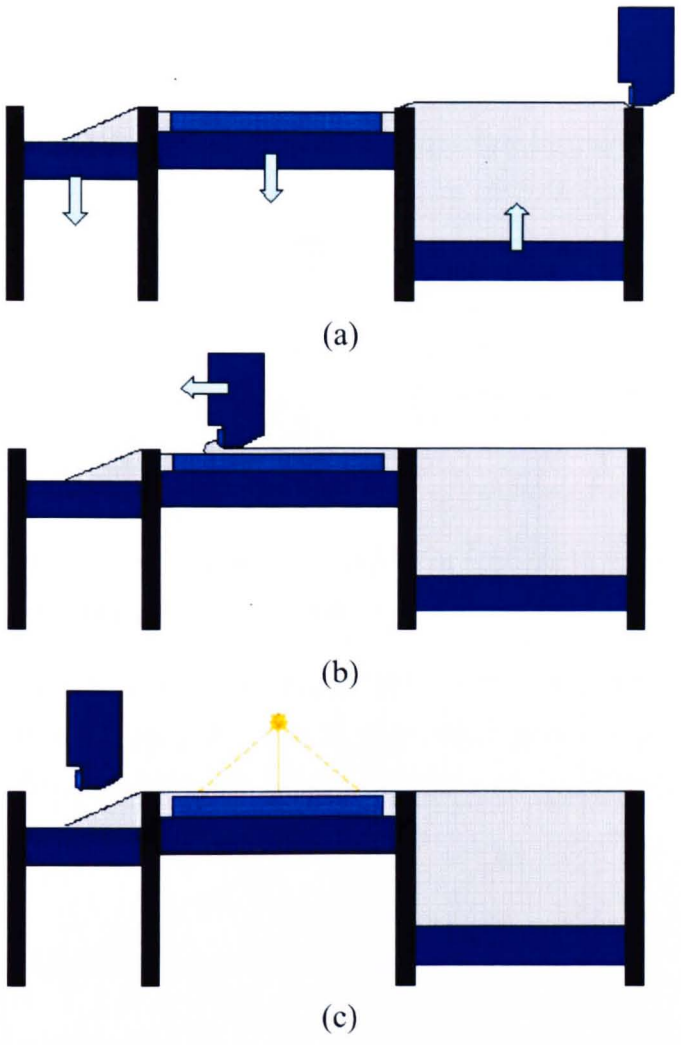

Figure 3.2 - Schematic of the EOS M270 showing different stages of the building process

3.1.1.2 Hatching technique

The hatching technique describes the different methods of melting an area of the powder layer. There are four definable regions shown in Figure 3.3 for a simple square cross-section of a cube. A single line is melted around the outside called the 'Pre-Contour', this defines the area to be melted. The 'Core' region inside the melt area is melted by the method shown in Figure 3.4 known as Squares or Checkerboard. The region is split into squares which have a pre-defined size typically 8mm, each square is melted by a rastering technique by melting lines side by side, adjacent squares are melted so that the laser scans 90° relative to each neighbour and squares are melted in an order shown in Figure 3.4. In the following layer the pattern is offset and rotated to ensure that the edges of the squares are not in line with the previous layer, this is to reduce the chance of stacking up any defects with are associated with these regions such as pores which may connect and form long voids through the height of a build.

The next area to be melted is the 'Skin' which has a definable thickness of typically 4mm. The Skin is melted in Stripes as shown in Figure 3.5, the width of these stripes can be changed and varies according to the material being melted.

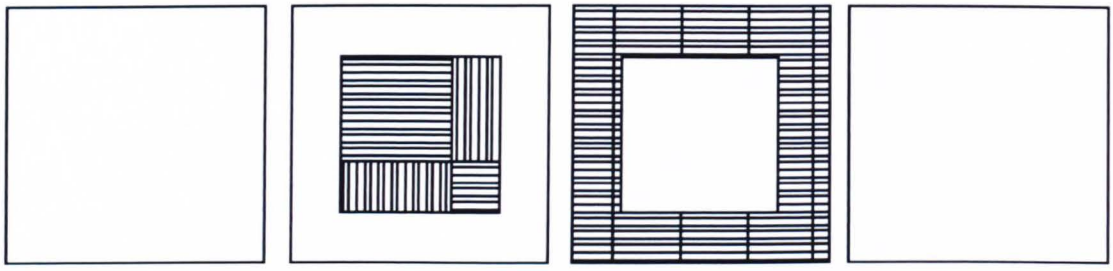

Figure 3.3 – Schematic of hatching technique (a) single line 'pre-contour' (b) Core hatching 'squares' (c) skin hatching 'stripes' (d) single line 'post-contour'.

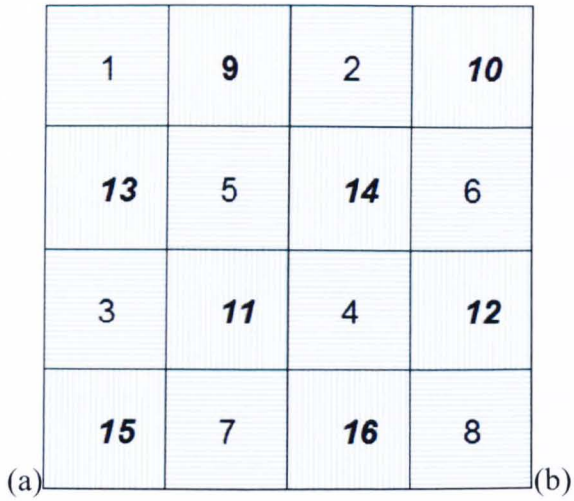

Figure 3.4 - The 'squares', checker-board hatching in the Core region (a) the blue lines indicate the hatching of the laser and the numbers show the order the squares are melted (b) the 'squares' pattern is rotated in subsequent layers.

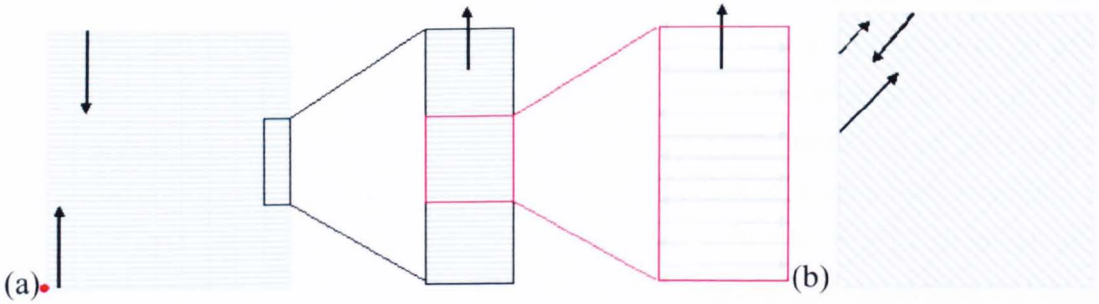

Figure 3.5 - The stripes hatching for the Skin region (a) blue lines indicate the path of the laser black lines indicate the progression of the melting along the stripe (b) hatching technique is rotated in subsequent layers.

3.1.1.3 Samples produced

To establish a suitable processing window, single line scans were used to produce a weld track on the surface of a bead blasted plate at different laser powers, beam velocities and beam diameters. After establishing a processing window, cubic samples measuring $20mm^3$ were built and cut into appropriate sections to examine the horizontal and vertical planes. Samples were built using the hatching techniques described above, the skin thickness and stripe width were 4mm, the squares in the core were $8mm^2$ and the hatching patterns were rotated for each layer relative to the previous by 7° to minimise the number of times the orientation of the hatching pattern is repeated. The beam diameter is determined by the beam expander which changes the height of the deflecting mirror and hence the focal distance of laser source from the work piece, the default is that the contour hatch uses a sharp focused beam and the interior hatching uses a wider defocused beam. This parameter is varied in the investigation (Chapter 4) along with the nominal laser power, beam velocity and the track offset (the distance between adjacent melted tracks. The layer thickness is nominally 20μm unless otherwise stated.

3.1.2 Trumpf DMD 505 process description

3.1.2.1 Machine features

The Trumpf DMD 505 shown in Figure 3.6 is based at TWI: The Welding Institute (South Yorkshire, UK). The system is a five-axis laser deposition system (Blown-powder) and is used for cladding, weld repair and component production or modification. It uses a coaxial nozzle to deliver powder from 360° into a molten pool created by a 2kW CO_2 laser on a substrate to build up a line of material, or a track. The nozzle array is shown in Figure 3.7; within the nozzle the laser beam passes through the centre and the powder is fed from 360° by a carrier gas into the melt pool allowing the assembly to be moved in any direction. The flow rate of the carrier gas is used to control the powder delivery rate to control the amount of material melted per unit volume and time. A shielding gas is used to minimise oxidation, in this study Argon is used but this can be substituted for Helium. The nozzle is moved on a single cantilever, five-axis Cartesian gantry with a process envelope of 2x1.1x0.75m and has a CNC control. The machine is equipped with optical cameras which monitor the molten pool and adjust the laser power when excessive heat is experienced, for example, when changing direction or with increasing distance from the substrate. The

cameras were not used in this study as the aim is a parametric investigation so constant levels of each variable are necessary throughout a build.

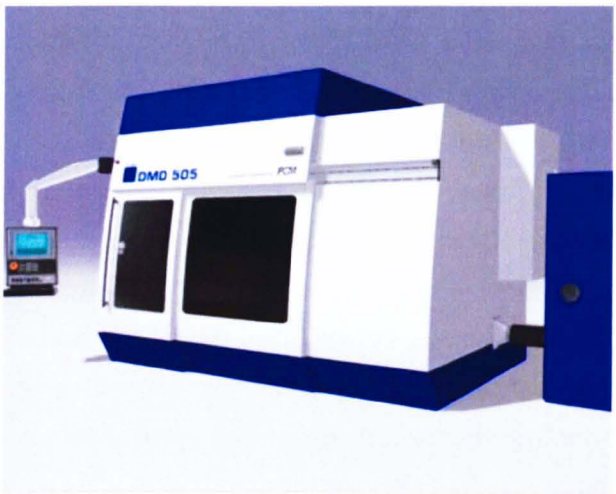

Figure 3.6 -Trumpf DMD 505 at TWI: The Welding Institute (South Yorkshire, UK)

3.1.2.2 Hatching technique

The DMD 505 follows a hatching pattern described by a CNC code; this pattern can be altered according to the type of deposition being done. In the current study simple backwards and forwards rastering patterns are used, for reference the nozzle assembly moves in the x direction (forwards is positive x and backwards is negative). The nozzle moves vertically in the z direction to deposit later layers of material to build up the 3-dimensional part, the distance the nozzle moves in z is referred to as the z-step (this is analogous to the layer thickness in powder-bed systems such as the EOS M270 described in the previous section) and can be adjusted to manipulate the height of a track and the depth that is melted back in the underlying material, both of these have implications on heat transfer and final microstructure.

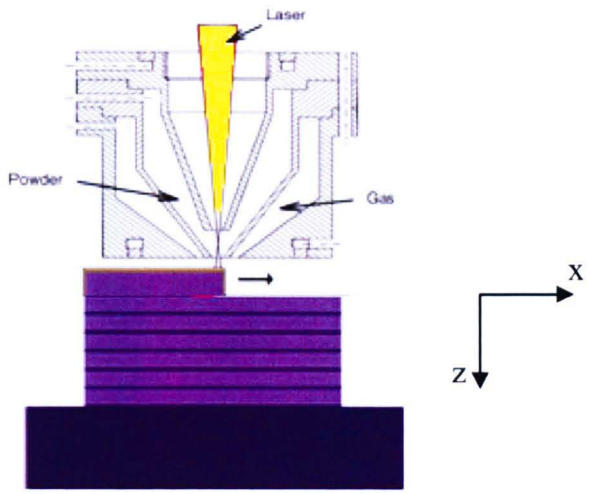

Figure 3.7 - Coaxial nozzle assembly showing path of laser, powder delivery and shielding gas delivery system

3.1.2.3 Samples produced

The samples produced for this investigation were 100mm in length and consisted of single clad tracks. Six layers were deposited to give a thin wall geometry. The powder feed rate, step height between layers and beam diameter were kept constant throughout and the substrate was allowed to cool between lines scans to reduced heat build-up. The individual walls are built up using a 'rastering' pattern, i.e. layer one is put down in a positive x-axis direction, layer two in a negative x-axis direction and so on.

3.1.3 Key process variables/terms

The following is a list of some of the key process variables and terms used when referring to the equipment and the experiments being conducted.

Laser Power – the power setting of the laser used to melt the material measured in Watts. The laser used on the EOS is a 200W Yb-fibre laser with a maximum nominal power of 195W.

Beam Velocity – the speed at which the laser spot is moved. This is controlled by a pivoting system of mirrors

Beam diameter – the size of the focussed laser beam at the work piece, this is controlled by the Beam Expander.

Beam Expander – the mechanism for controlling the Beam Diameter. This is the control setting on the machine on a scale of 0 to 10. The beam diameter varies from 100μm and 500μm but the scale is not continuous, intervals of 0.5 on the Beam Expander setting are possible. The change in beam diameter is brought about by changing the focal length of the beam by rising and lowering the deflecting mirror in the optics system. The beam is focussed by default for contour melting (beam expander setting 0) and is usually set to a wider beam for internal hatching to give a good surface finish and increase the melting rate for internal regions.

Layer thickness – the thickness of the powder layer put down across the build platform. This is controlled by the distance the platform is lowered between melting stages. The standard setting is typically 20μm but can be increased; this however results in a degradation of mechanical properties and will be investigated in the results chapter.

Weld/clad track – the line of material melted by a single pass of the laser

Track offset (OS) – the distance between the centreline of adjacent weld tracks

Hatching overlap – the distance/overlap between different regions of laser hatching

Theme – the combination of parameters used to process a material

3.2 Inconel 718

Inconel 718 is an iron-nickel-chrome based alloy which falls under the category of superalloy. Table 3.1 shows the composition of Inconel 718.

Table 3.1 Nominal alloy composition of Inconel 718 Ni-based superalloy

Alloying element	Cr	Fe	Nb	Mo	Al	Ti	C	Ni
Min Weight %	17	16	4.75	2.8	0.2	0.65	-	Balance
Max Weight %	21	20	5.5	3.3	0.8	1.15	0.08	

Inconel 718 was developed during the 1960's and is used in parts of aeroengines where operating temperatures are around 650°C. It is a precipitation hardenable alloy with good corrosion resistance, high strength and excellent weldability, including resistance to post-weld cracking. It also shows excellent creep rupture strength up to 700°C. Table 3.2 show some of the mechanical and physical properties of the alloy.

Table 3.2 thermal, physical and mechanical properties of Inconel 718 at room temperature and elevated temperature

Property	Room temperature	650°C
0.2% Yield strength/MPa	1030 – 1167	860 – 1000
UTS/MPa	1275 – 1400	1000 – 1200
% elongation	12 – 21	12 – 19
% reduction in area	15	15
Coefficient of thermal expansion/μm	13	-
Specific heat/ J/kgK	435	-
Thermal conductivity/ W/mK	11.4	-
Liquidus temperature/°C	1336	-
Solidus temperature/°C	1260	-
Density/kg/m^3	8190	-

Inconel 718 is composed of a face centred cubic (fcc) matrix, γ, which is strengthened by the addition of Cr that provides solid solution strengthening. Precipitation strengthening is achieved by stable intermetallics such as coherent, $L1_2$ γ', $Ni_3(Al, Ti)$, and incoherent, body centred tetragonal γ'', Ni_3Nb. It is these intermetallic phases that provide the superior high temperature properties, as ordering in the lattice reduces atomic mobility at elevated temperatures. Figure 3.8 shows a plot of phases present in Inconel 718 and their corresponding fractions as a function of temperature, this was calculated using the thermodynamic database in JmatPro software package (Sente Software, Guilford UK). It is clear from this that the main strengthening phases γ'+γ" show signs of dissolution as temperatures exceed ~650°C corresponding to degradation in mechanical properties above this temperature.

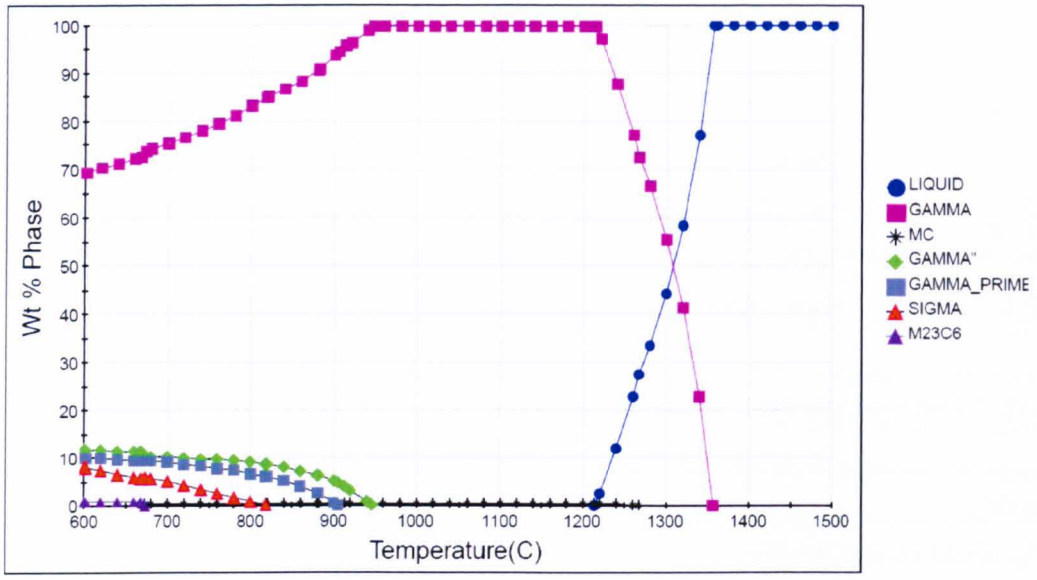

Figure 3.8 – Weight percentage of phases present vs. Temperature for Ni-based super alloy Inconel 718 calculated using JmatPro thermodynamic database.

The machines used in the project use metal alloy powder. The EOS M270 uses a particle size distribution of 15-45μm and the DMD 505 44-88μm. Both are argon gas atomised powders.

3.3 Characterisation

3.3.1 Light and electron microscopy

Light microscopy has been used for centuries in scientific investigation, however, the resolving power (resolution) is limited by the properties of the light used. For white light this limit is 0.2μm. For improved resolution, shorter wavelengths are necessary, but other forms of electromagnetic radiation such as X-rays cannot be focussed, this led to the development of the electron microscope (Grundy 1976). Electrons and other subatomic particles are known to have wave-like characteristics and hence an associated wavelength, for electrons this is acquired when they fall through a potential difference or an accelerating voltage is applied. The wavelength of an electron is given by Equation 3.1

$$\lambda = h/(2meV)^{½}$$

Equation 3.1

Where h is Plank's constant, m is the electron mass, e is the electron charge and V is the accelerating voltage. The resulting theoretical values of λ are now on the scale of picometres. This phenomenon combined with the capability to focus electron beams using magnetic fields made electron microscopy a common investigation tool today. Two types of electron microscopy are commonly used, Transmission (TEM) where the electrons pass through a samples and Scanning (SEM) where the electrons are scattered and analysed. The basic set up of the SEM is shown in Figure 3.9

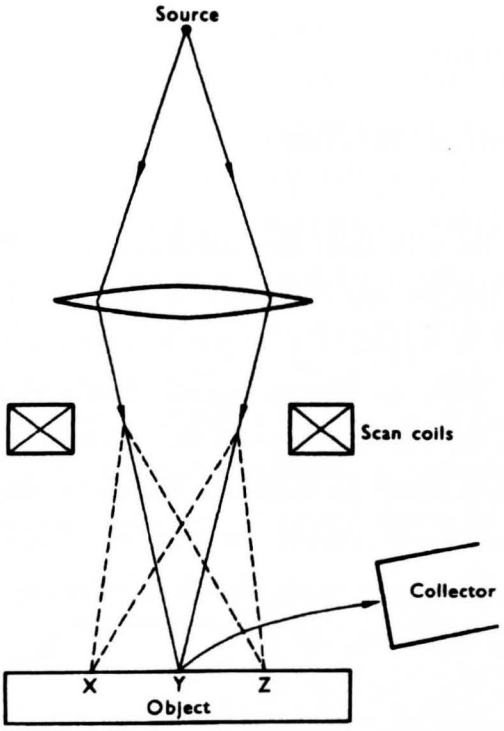

Figure 3.9 – Basic principle of the SEM (Grundy 1976).

SEM is used in this investigation and works as follows; a source of electrons is focused to a spot which is moved across the object to be observed, as the spot moves across a point on the target a number of responses are produced, it is these responses that are detected and collected sequentially to give an image. The responses are the emission of electrons and radiation from the surface which give a signal; it is this signal that is detected and converted to an image rather than a direct image being observed as is in light microscopy. The electrons directed onto the target interact with it and are scattered either elastically (with a change in direction but on loss of energy) or inelastically where energy is transferred to the internal degrees of freedom in the target atoms such as excitation of bound or free electrons and lattice vibrations (heating and radiation which cause damage to the target), it is this loss of energy which makes chemical analysis possible in SEM too as different atoms with different atomic weights absorb specific amount of energy.

The incident electrons are absorbed or reflected by bulk samples but in thin samples transmission also occurs. The types of responses which occur in electron microscopy are shown in Figure 3.10. The most important ones are Secondary electrons, Backscattered electrons and X-rays.

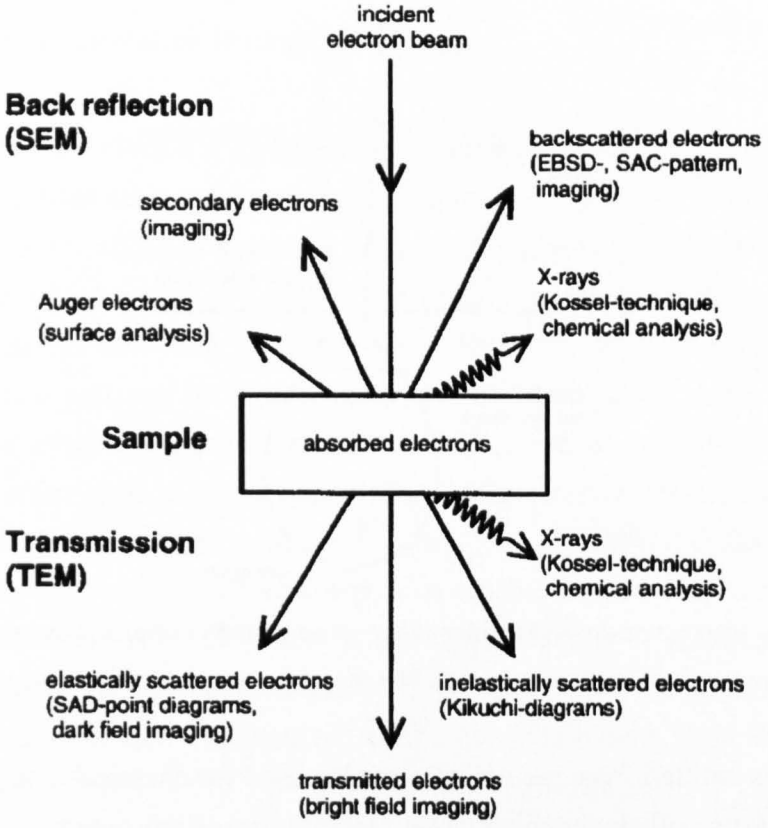

Figure 3.10 – Various responses obtained when electrons interact with the surface of a sample (Grundy 1976).

Secondary electrons are used for imaging; these are low energy electrons produced from inelastic scattering. They are excited and emitted from the sample when they acquire sufficient energy to overcome the work-function of the target material before being accelerated to the Fermi level. A positively biased grid is used to detect Secondary electrons and the intensity of these reaching the grid is a function of the incident angle, hence the topology of the target surface will provide variations in the angle the electron beam meets the surface providing variation in intensity which can be converted to an image. The surface topology can be a result of deliberate etching allowing specific microstructural features to be examined or an unetched surface can be observed to view surface profiles and pores which have been sectioned.

Backscattered electrons are used to detect changes in composition and orientation of the target's structure. Backscattered electrons are scattered by collisions with the nucleus of target atoms hence their intensity is a function of the atomic weight of the target i.e. heavier atoms scatter the electrons more efficiently to give an atomic number (Z) contrast which is used to produce an image. The interaction zone of the incident electrons and the regions which secondary and backscattered electrons originate are shown in Figure 3.11.

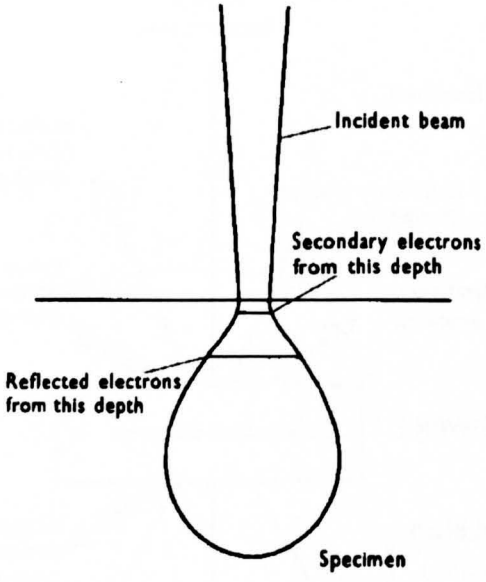

Figure 3.11 – Interaction zone of incident electrons on a bulk samples showing regions where secondary and backscattered (Reflected) electrons originate (Grundy 1976).

The X-rays emitted from the sample are also used for chemical analysis. They are a result of inelastic collisions which cause electron transitions between energy levels in the target and when detected the different energy associated with different elements can be used for Energy Dispersive Spectroscopy, this used for elemental analysis to give the relative amounts of each element at a given point on the target. X-ray emission occurs when the inner shell electrons in the target are excited by the incident beam and escape the host atom or moves into a higher, unoccupied level. The vacancy left by this process is filled by a higher energy electron from a higher energy level and x-rays are emitted to conserve energy. Each atomic element has a unique x-ray spectrum making identification of constituent elements in the target, and hence phases in the sample, possible.

In the present study, electron microscopy was undertaken using a JEOL JSM 6400 SEM with I-Scan image acquisition system, accelerating voltages of 15-20kV were used throughout. Samples were prepared by mechanical grinding in successive stages using silicon carbide abrasive papers starting with 250 down to 1200 grit size. After grinding the samples polished using 3μm and 1μm diamond pastes (ASM Specialty Handbook, 2000). This procedure was sufficient for observing porosity in samples, where the microstructure was observed the samples were etched using Schafmeister's reagent (50cc HNO_3, 500cc Hydrochloric Acid, and 500cc distilled water) or Kalling's reagent (40ml Distilled water, 2grams Copper chloride ($CuCl_2$), 40ml HCl, 40-80ml Ethanol or methanol) to reveal the dendritic solidification microstructure.

3.3.2 Electron Backscatter Diffraction (EBSD)

The backscattered electrons previously described can be used to obtain crystallographic orientation information about individual grains in a target material to provide information about a sample's texture. An EBSD pattern is formed when multiple planes of atoms act as a diffraction grating resulting in electron diffraction which gives patterns known as Kikuchi bands. These bands correspond to planes of atoms in a lattice and can be described by the Miller notation index (*hkl*) to give crystallographic orientation information. The orientation of crystals is important as materials properties such as stiffness and strength are texture specific, i.e. properties are a function of the average texture of a part (Randle 2000). Older methods for determining texture by x-ray diffraction give an overall texture or texture distribution of a bulk sample whereas EBSD allows specific grain data to be acquired. EBSD also allows information to be gathered about grain boundaries as these are detected through the misorientation between adjacent grains including high and low angle grain boundaries.

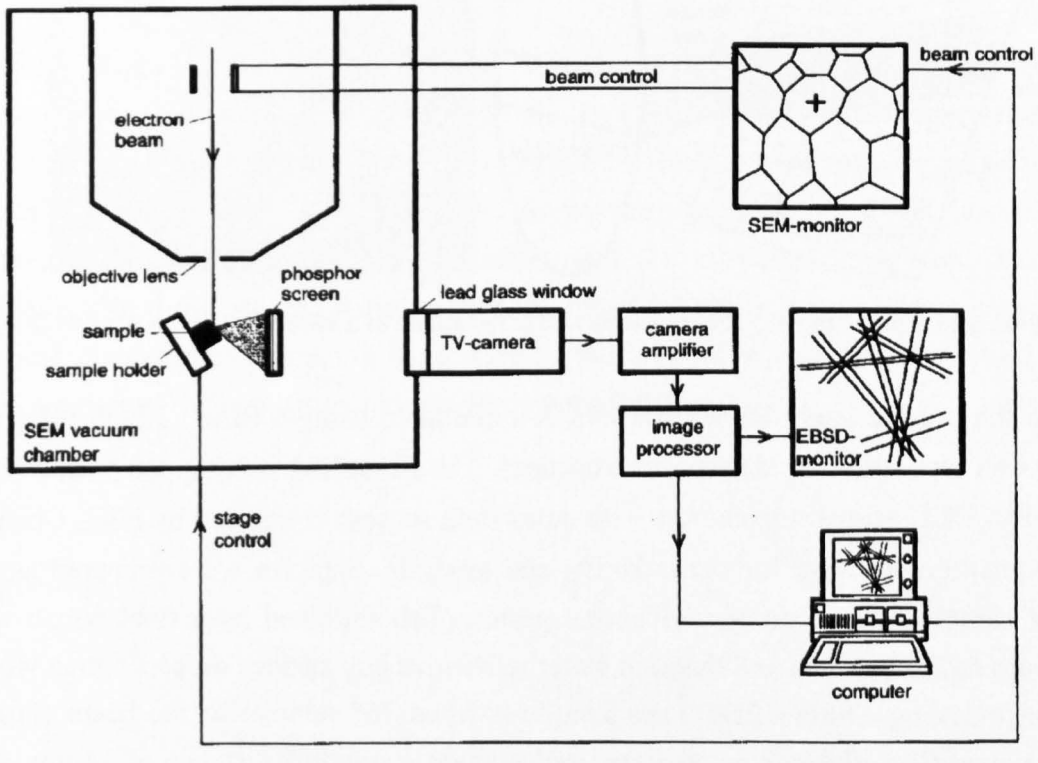

Figure 3.12 -EBSD equipment configuration (Randle 2000)

The set-up of EBSD analysis is shown schematically in Figure 3.12. The system detects the Kikuchi bands of the target sample using a phosphor screen and CDD

(Charge Coupled Device) camera, the bands are shown schematically and a real example is given in Figure 3.13. A Kikuchi pattern arises due to electron backscatter diffraction, as an electron enters a crystalline solid they are elastically scattered in all directions as previously described, some of these arrive at the Bragg angle for each lattice plane, these in turn undergo elastic scatter to give a reinforced beam relative to the scattered primary (incident) beam. The scattering source is between two planes hence two beams are produced (one for the upper and one for the lower plane) to give the typical band image, multiple bands are observed which represent each plane in the crystal and each band has a distinct width and corresponds to a particular orientation. A band is indexed by identifying the crystallographic indices of the bands and poles (where the bands intersect), the pattern has all the information about a crystal's unit cell's angular relationship relative to a known reference axis.

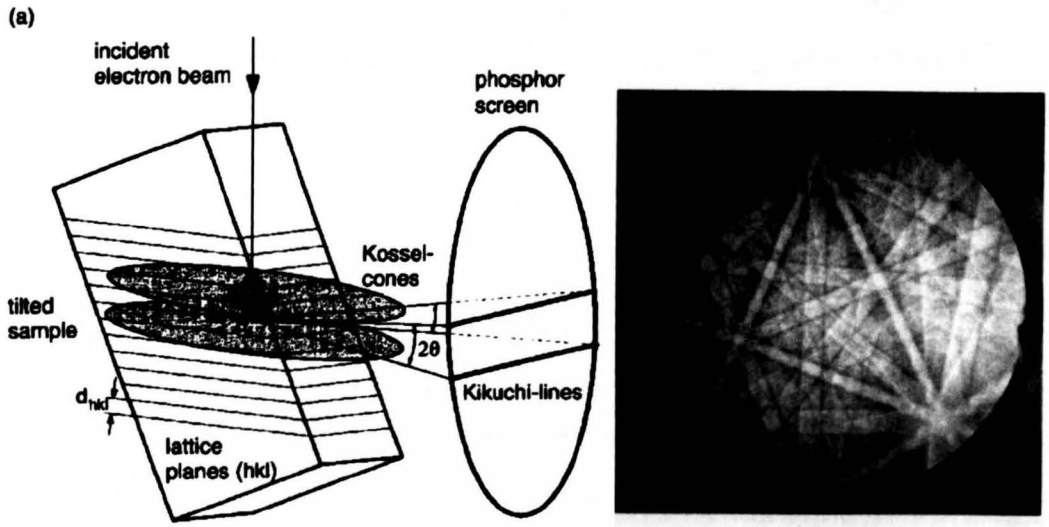

Figure 3.13 – (a) origin of Kikuchi bands and (b) example of a Kikuchi pattern (Randle 2000)

In the present study EBSD analysis is undertaken using a Sirion FEGSEM (field emission gun scanning electron microscope). The FEGSEM is equipped with a HKL Nordlys CCD acquisition camera with solid state sensors controlled by HKL Channel 5 acquisition software for the indexing and analysis. Samples were prepared as per SEM samples and up to 1μm diamond paste polish followed by a final polish with 0.25μm colloidal silica and distilled water to remove any surface defects which would affect indexing. During EBSD the sample is tilted 70° relative to the beam (Figure 3.13), as well as this the parameters used include a standoff distance of 14mm, spot size of 3 and an accelerating voltage of 20kV. The analysis uses automatic mapping by moving the stage platform to acquire Orientation Imaging Maps (OIM), step sizes range from 1 to 3μm depending on time restrictions and the area of the sample being

investigated, smaller steps would produce higher resolution images but grain structure is the primary feature being observed the mentioned step size is suitable.

3.3.3 Electron probe microanalysis (EPMA)

Figure 3.10 shows how x-rays are generated when an electron beam is incident on a surface. This technique is used in EPMA to non-destructively determine the chemical composition of small volumes of the target material. Characteristic X-rays are generated for specific elements in the specimen and the relative intensities of each are used to determine their concentrations and full chemical composition is found by comparison to known standards. Concentrations as low as 100 parts per million can be detected in volumes of material from 1-3μm in size.

In this investigation a CAMECA SX-51 Electron probe microanalyser was used, equipped with four wavelength dispersive spectrometers and able to perform automated line scans and elemental maps.

3.3.4 Surface profiling

Surface roughness is measured for the cube samples build using the EOS M270. Measurements were taken using a Surtronic 3+ (Taylor/Hobson Precision). Surface profiles are categorised simply as shown in Figure 3.14. A real surface has different forms of surface texture; the two basic forms are waviness and a roughness. The Surface Texture is quantified by parameters related to different characteristics, these are split into three groups; Amplitude, Spacing and Hybrid. Amplitude refers to the vertical displacement, Spacing is relative to the horizontal surface and Hybrid is a combination of the two. (Surtronic 3+ Operators Handbook)

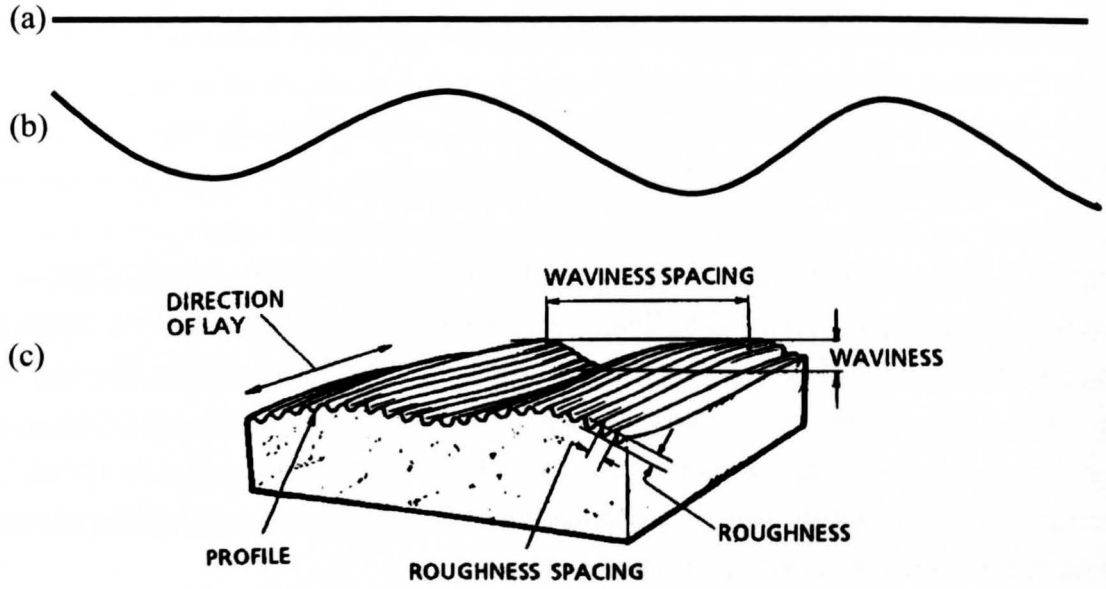

Figure 3.14 – (a) flat surface, (b) waviness, (c) 'real' surface

Different measurements are used in characterising surface roughness; it is common to reference the mean-line as shown in Figure 3.15, this is based on the least square method so that the area of the deviation above the line is equal to that below the line. The universally recognised parameter for roughness is the R_a value; this is the arithmetic mean of the departures of the profile from the mean line given by Equation 3.2.

$$R_a = 1/L\int|y(x)|dx$$

Equation 3.2

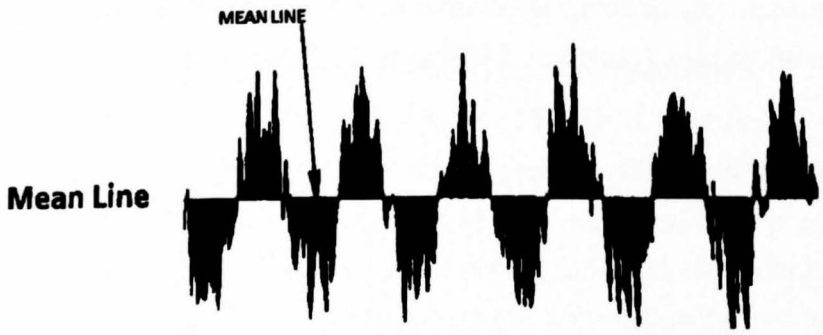

Figure 3.15 – representation of the meanline

Alternatively an R_q value can be used, this is the root mean squared corresponding to R_a. R_y is the maximum peak to trough distance, $R_z(DIN)$ is the average peak to valley and S_m is the mean spacing between peaks. For the purpose of this study the R_a value will be reported.

The Surtronic 3+ is a stylus device which scans a line on a surface and measures the surface, the set-up is shown schematically in Figure 3.16. The relevant parameters used are the cut-off length, L_c, or sampling length which is the length of the reference line used to characterise irregularities in the surface, this is set to 2.5mm. The Evaluation Length, L_n, which is composed of multiple L_c and is the length over which the surface is assessed, this is 4mm, and Traverse Length or Assessment Length, T_l, this is the complete length the pickup moves along the surface and this is longer than L_n so as to allow the ends of the scan to be neglected to eliminate any mechanical and electrical transients.

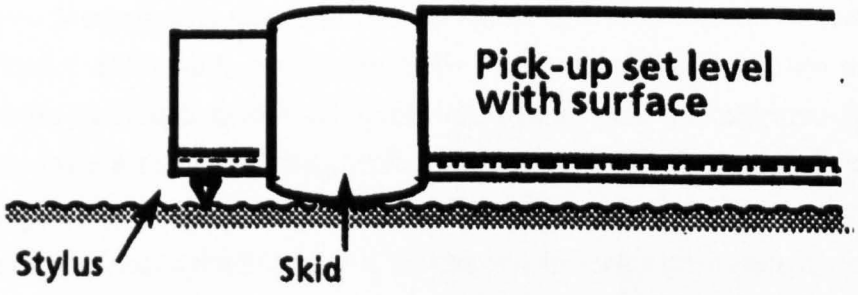

Figure 3.16 – Schematic of the stylus surface profiler.

3.4 Design of experiments (DOE)

A good experiment will provide the required information with the minimum experimental effort, this requires three things;

- Well defined questions to be answered
- A suitable method to acquire data accurately and with little risk
- A well-structured experimental 'pattern' or design to gather and analyse data

Statistical design of experiments deals with this third point (Davis 1978). Any set of experimental observations represents data in a certain arrangement corresponding to a known set of conditions, however when results are obtained in a haphazard way the arrangement can be unbalanced and irregular which can lead to errors or an incomplete insight into the subject being investigated. In such a case, there is still information to be gained, but a well-designed or more appropriate arrangement could yield clearer results with fewer observations. If more observations are made than are necessary then this represents wasted effort or if too few are made then false or incomplete conclusions can be made.

Experimental design was introduced in Section 2.6 where several methods were mentioned for generating a response surface, the most frequently used is based around the Box-Wilson central composite design (CCD); this type of experiment will be used in Chapters 4 and 5 to investigate two ALM processes. CCD can be used to examine 2-5 factors with relatively few tests compared to 'one-factor-at-a-time' experiments and even simple Factorial Designs whilst allowing the detection and modelling of higher order polynomials when estimating the Response Surface (5 levels for each factor).

The specific details of the CCD used in this investigation are described for each experiment in Chapters 4 and 5; the following is intended to provide a general overview of how CCD experiments are used. Commercially available software, Stat-Ease Design-Expert Version 6.0 (Stat-Ease Inc. Minneapolis, US), was used in the planning and analysis of the experiments, the following text will also describe some of the mathematical background to how a CCD computes a Response Model and the significance tests performed to quantify the model's relevance and accuracy.

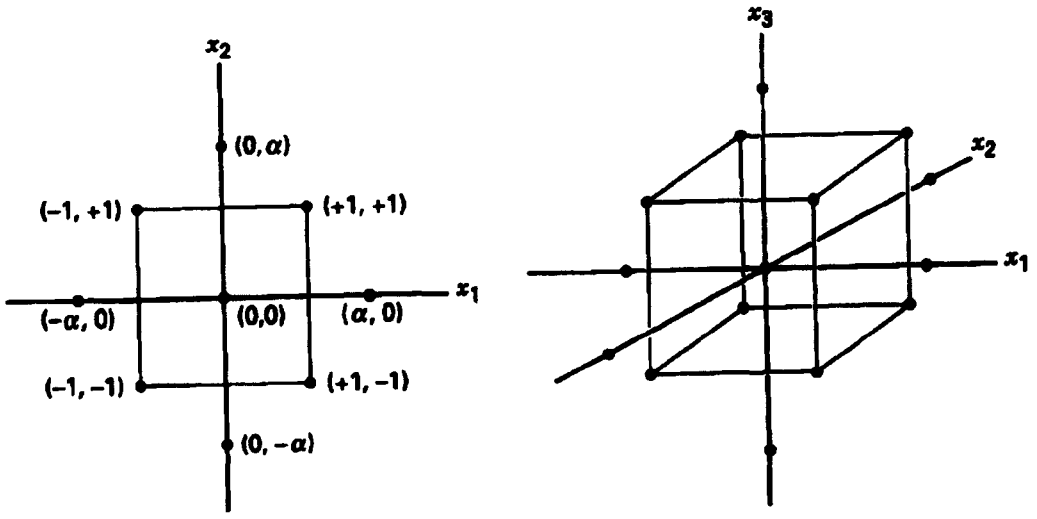

Figure 3.17 – 2 and 3 factor CCD (Montgomery 1997)

2- and 3-factor CCD's are easily represented graphically as shown in Figure 3.17. They are composed of 4 and 8 Factorial points respectively as well as 4 and 6 'axial' points and centre points. It is common practice to repeat the centre point a number of times to provide an indication of the scatter in measurements so that the model's signal to noise ratio can be checked, a large ratio is necessary to adequately describe a response. The non-centre points fall on the surface of a circle and sphere in two- and three-level CCD so that in coded factors (coded factors are discussed in the following section) are *1* and *-1* for the Factorial points and α and $-\alpha$ for the axial points, where $\alpha=\sqrt{k}$ and k is the number of factors.

An experiment is tabulated in a 'Design Matrix' which lists the parameter combinations for each Trial of the experiment; an example of a two-level CCD is shown in Table 3.3. Trials 1-4 represent the Factorial points, 5-8 are axial point and 9 is the centre point. The reader should note the difference between the 'Standard order' and the 'Run order' the former is used when listing the trials and the latter is a randomisation of the trials which determines the order in which they were conducted. Randomisation is necessary to mitigate any sequence-related phenomena which would bias the measured responses; an example would be the accumulation of heat in a system. The DX6 software produces the Design Matrix and the randomised Run Order after the user enters 'high' and 'low' levels for the natural factors (i.e. real values of a given parameter under investigation, such as laser power).

Table 3.3 - Design matrix for a two-factor CCD (CP = centre point)

Standard order	Run order	Natural factors		Coded factors		Response
		Z_1	Z_2	x_1	x_2	y_i
1		low	low	-1	-1	y_1
2		low	high	-1	+1	y_2
3		high	low	+1	-1	y_3
4	random	high	high	+1	+1	y_4
5		-axial	CP	$-\alpha$	0	y_5
6		axial	CP	0	α	y_6
7		CP	-axial	0	$-\alpha$	y_7
8		CP	axial	0	α	y_8
9		CP	CP	0	0	y_9

3.4.1 Mathematically building a Response Model – linear regression

The trials in the Design Matrix are performed and the responses under investigation are measured in each case, the measured values are the true response but this includes errors from the experiments and measurements. The next stage is to fit a Response Model to the raw data, this takes the form of a mathematical equation, commonly a high order polynomial. To do this linear regression is used.

The general relationship between a response, y, and the input factors of a process can be defined by Equation 3.3;

$$y = f(Z_1, Z_2, \ldots Z_k) + \varepsilon$$

Equation 3.3

Where f is the unknown function of the true response in terms of natural factors, Z, which may be highly complex and/or based on some physical mechanism. ε is the error not accounted for by f which may be caused by measurement inaccuracies, background noise or other unknown variables. The error is assumed to have a normal distribution with a mean of zero and a constant variance across the design space (i.e. is independent of processing parameters).

The general model (Equation 3.4) can be reduced to a function based on coded factors, x, which are dimensionless with a mean of zero and a constant standard deviation, coded factors are obtained using Equation 3.5. Coded values of a factor usually include 'high' and 'low' levels which are assigned values of +1 and -1 (the

most basic example forms a 2-level factorial), with midpoint levels having a value of Zero.

$$\eta = f(x_1, x_2, \ldots x_k)$$

Equation 3.4

$$x_i = \frac{Z_i - a}{b}$$

Equation 3.5

where

$$a = \frac{Z_{High} + Z_{Low}}{2}$$

Equation 3.6

$$b = \frac{Z_{High} - Z_{Low}}{2}$$

Equation 3.7

The true response is estimated by empirical models and is commonly fit to first or second order polynomials. Higher order equations are possible but once interaction terms are considered the equations become increasingly complicated for little or no improvement in model accuracy. For this reason, in engineering applications, it is accepted that two-factor interactions and single quadratic terms are sufficient to estimate the true response; examples of the types of polynomial commonly used are given in Equation 3.8 to Equation 3.10, these are likely to be used in the models produced in the present study.

First order model (linear):

$$y = b_0 + b_1 x_1 + b_2 x_2 + \ldots + b_k x_k$$

Equation 3.8

First order model with interaction terms (two factor interactions, 2FI), this type of model is used when some curvature in a Response Model exists:

$$y = b_0 + b_1 x_1 + b_2 x_2 + b_{12} x_1 x_2$$

Equation 3.9

Second order model with interaction terms (quadratic), this type of Model will be used if there is a high level of curvature in the Response Surface:

$$y = b_0 + b_1x_1 + b_2x_2 + b_{12}x_1x_2 + b_{11}x_1^2 + b_{22}x_2^2$$

Equation 3.10

These can all be written in the general form:

$$y = b_0 + \sum_{i=1}^{k} b_i x_i + \sum_{\substack{i,j=1 \\ i \neq j}}^{k} b_{ij} x_i x_j + \sum_{i=1}^{k} b_{ii} x_i^2$$

Equation 3.11

The coefficients b_{ij} (where i and j are integers) in the preceding equations are unknown values at this stage and must be calculated in order for the model to best fit the measured data. These values are determined by linear regression analysis.

3.4.2 Regression model

The DX6 Software performs linear regression to find values for the Response Model coefficients, the appropriate values for each coefficient will result in the lowest sum of the squared error for the overall model, and this is achieved using a Regression Model.

The Regression Model is analogous to the Response Surface Model but always linear regardless of the complexity of the Response Model since known values of y and x are considered (measured responses and known factor levels). The Regression Model is given in Equation 3.12

$$y = \beta_0 + \beta_1X_1 + \beta_2X_2 + \ldots + \beta_kX_k$$

Equation 3.12

Where β_k are the regression coefficients to be found and X_k represents a term in the Response Model described previously i.e. $X_1=x_1$, $X_2=x_2$, $X_3=x_1x_2$, $X_4=x^2$ ... This is more easily referred to in vector notation by Equation 3.13 and tabulated in Table 3.4;

$$\mathbf{Y} = \mathbf{X}\boldsymbol{\beta} + \boldsymbol{\varepsilon}$$

Equation 3.13

Where **Y** is an (n x 1) column vector containing the observed/measured responses (n is number of tests performed), **X** is an (n x p) matrix of the factors' levels (p is the number of terms in the regression model), **β** is a (p x 1) column vector of the regression coefficients and **ε** is an (n x 1) column vector of the random errors.

Table 3.4 - Analysis matrix for linear regression using coded variables

Standard order	*Run order*	*Regression factors*						y_i
		$I(\beta_0)$	X_1	X_2	X_3	...	X_k	
		Equivalent term in Response Model						
		intercept	x_1	x_2	x_1x_2	...	k	
1	*random*	1	-1	-1	-1	...		y_1
2		1	-1	+1	-1	...		y_2
3		1	+1	-1	-1	...		y_3
4		1	+1	+1	+1	...		y_4

3.4.3 The Method of Least Squares

When measurements of the response are taken the only unknown quantities in Equation 3.13 are the column vector **β** and the error **ε**. The next step is to find the column vector of regression coefficients (β's) which gives the minimum value of the sum of the squared error, ε. If L is the sum of the squared error then Equation 3.14 is obtained in scalar and vector notation

$$L = \sum_{i=1}^{n} \varepsilon_i^2 = \boldsymbol{\varepsilon}^T\boldsymbol{\varepsilon}$$

Equation 3.14

Rearrangement and substitution of Equation 3.13 gives Equation 3.15

$$L = (\mathbf{Y} - \mathbf{X}\boldsymbol{\beta})^T(\mathbf{Y} - \mathbf{X}\boldsymbol{\beta})$$

Equation 3.15

This simplifies to give Equation 3.16;

$$\mathbf{b} = (\mathbf{X}^T\mathbf{X})^{-1}(\mathbf{X}^T\mathbf{Y})$$

Equation 3.16

Where **b** is the column vector of coefficients which result in the minimum value of *L*.

The fitted estimate of the response surface model is now given by Equation 3.17 in vector notation and Equation 3.18 in scalar;

$$\hat{\mathbf{y}} = \mathbf{Xb}$$

Equation 3.17

$$\hat{y}_i = b_0 + \sum_{i=1}^{k} b_i x_{iu}$$

Equation 3.18

i=1, 2... n, u=1, 2... k, where *n* is the number of observations and *k* is the number of terms whose coefficients were estimated during regression analysis. So from Equation 3.17 the values in vector **b** can be calculated and substituted into a Response Model such as Equation 3.10. The final stage is to determine the validity of the model and which terms are necessary to accurately describe the response. This is done using Analysis of Variance (ANOVA) and Residual Analysis.

3.4.4 Analysis of Variance (ANOVA) and Residuals

Once a model is obtained it must undergo what is termed a 'Statistical test of Significance'. The most common way is based on the 'null-hypothesis', this is to assume there is no effect i.e. based on this, can the observed variation in data be attributed to chance? If the probability of seeing this variation is small (there is a low probability of there being no effect) then the null-hypothesis is considered disproved and the effect of the experiment is 'Statistically Significant', this indicates that the effects of the experiment are real compared to experimental error. If the opposite is true then it is not necessarily 'insignificant' but it can be said that there is insufficient evidence to confidently show that the effect caused by the change in experimental conditions exists.

The test statistic used by the DX6 software is known as the F-value, F_0. To obtain this it is necessary to obtain the values of 'sum of squares' for the regression model and errors, the errors used are known as 'Residuals' (the difference between the observed value and the modelled value for a specific trial). These are computed in DX6 and presented in an ANOVA table; a general example is given in Table 3.5.

The null-hypothesis is that all regression coefficients are zero; to reject this implies that at least one of the regressor variables contributes significantly to the model. To

test this the total sum of squares ($SS_T = \Sigma(y_{measured}-y_{average})^2$) is partitioned into the sum of squares due to the model or regression and due to the residuals or error ($SS_T = SS_R + SS_E$). To test the null Hypothesis F_0 is calculated as shown in Table 3.5, it is rejected when F_0 is greater than a value corresponding to $F_{\alpha, k, n-k-1}$ where α is a confidence level or level of significance (usually taken as 95% confidence i.e. α = 0.05), k is the number of terms in the model and n is total number of observations. This implies that when there is a large difference between the Mean Square for the regression (the Treatments) and the Error the treatments do have a significant effect on the response.

Another approach is the *P*-value statistic, this is the probability that the test statistic will take on a value at least as extreme as the observed value when the null hypothesis is true i.e. the null hypothesis is rejected if the *P*-value for F_0 is less than α.

Table 3.5 – ANOVA Table in the general form, k is the number of terms in the model and n is total number of observations

Source of Variation	*Sum of Squares*	*Degrees of freedom*	*Mean Square*	*F-value (F_0)*
Regression (Model)	SS_R	k	$(SS_R/k) = MS_R$	MS_R/MS_E
Errors (Residuals)	SS_E	$n-k-1$	$(SS_E/n-k-1) = MS_E$	-
Total	SS_T	$n-1$	-	-

The coefficient of multiple determination, R^2, is also used to test the adequacy of the model, this is given by $R^2 = SS_R/SS_T$ or $1-(SS_E/SS_T)$. However, additional terms in the model will always increase the R^2 value whether or not they are significant. To overcome this, the adjusted- R^2 value is used:

$$AdjustedR^2 = 1 - \frac{\left[\frac{SS_E}{(n-p)}\right]}{\left[\frac{SS_T}{(n-1)}\right]} = \left[\frac{1-(n-1)}{p-1}\right]\left(1-R^2\right)$$

Equation 3.19

This does not always increase when additional terms are included and will decrease when a term is used which is not statistically significant.

4 Results and Discussion - EOS

At the start of this study there were no processing parameters (processing 'theme') available for Inconel 718 on the EOS M270. The first experiment established a processing window over which subsequent trials could be carried out to analyse the material response to the processing parameters. In Sections 4.1.1 and 4.1.2 the surface of an Inconel 718 plate is melted using the laser's hatching technique over a range of processing parameters, the depth of melting was used as an indicator as to what parameters are then suitable to build simple cubic samples using Inconel 718 powder. Cubic samples are then built and analysed in Section 4.2.

To determine a suitable set of starting parameters to begin experimenting, the properties of Inconel 718 were compared to those of a commonly used material available on the EOS M270, CoCrMo. The parameters used to process this material were suitable to process Inconel 718 but were not necessarily the most appropriate so the first experiment was performed around these. This procedure is discussed in greater detail in Chapter 6.

The processing parameters and materials in question were defined in Chapter 3 along with the theory behind the Central Composite Design of Experiments (CCDOE) used to plan the experiments and analyse the material response. The response is initially presented as the geometry of single melted tracks on a flat plate to avoid unnecessary use of alloy powder which is costly. This was then expanded to consider 3 dimensional parts built from powder and empirical model building is used to fit the measured data. Processing maps are then presented relating track geometry to key processing parameters and show how these can be used to control porosity and surface roughness.

The geometries of the melt tracks were used with an analytical heat transfer model to calculate the size and shape of the solidification front and the local solidification conditions (cooling rate, temperature gradient and isotherm velocity). These were compared to the as-deposited grain structures of the parts built across the processing window of the two systems with the view to developing microstructure selection maps.

4.1 Determining a processing window for Inconel 718

Prior to designing an experiment the process limits were established for beam velocity when the laser is operating at the maximum nominal power of 195W by melting single tracks of a 20μm Inconel 718 powder layer onto a mild steel substrate. The results are shown in Figure 4.1 which shows that continuous tracks are successfully melted at velocities of 50mm/s to 1400mm/s. The tracks melted at 1600 and 1800mm/s show some loss of consistency and above this significant balling of the melted powder occurs. The range of values from 50 to 1800mm/s is deemed the *Region of Interest* as opposed to the *Region of Operability* which would be 50mm/s to 7000mm/s (the machine's limits). The other *factors* of interest will not influence the melting characteristics of a single track and so can be altered without giving a non-result, when an incomplete set of results are obtained the accuracy of fitted models obtained by regression analysis is diminished.

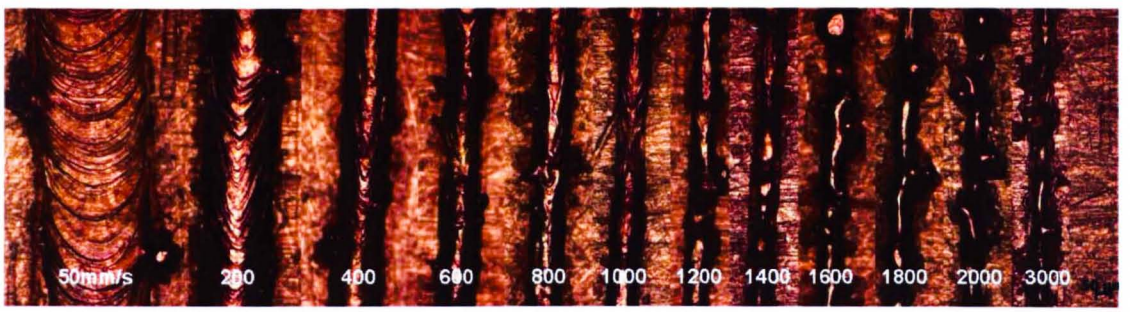

Figure 4.1 – Single line-scans of 20μm layer of Inconel 718 powder (laser power 195W, beam velocity indicated) showing the loss of track integrity and the onset of balling at velocities greater than 1400mm/s.

4.1.1 Effect of Beam velocity, track offset and stripe width

All materials respond differently when exposed to a heat source as a result of their differing thermo-physical properties. For instance, alloys with higher melting temperatures and high thermal conductivity require more thermal energy to melt and alloys with a higher thermal expansion coefficient experience greater distortion when heated unevenly which results in higher thermally induced stresses. With this in mind, it is necessary to establish a set of optimum processing parameters (a '*theme*') or a range of parameters over which a specific alloy can be melted consistently ('process window'). Machine manufacturers will only spend time and money developing a material processing theme if there is sufficient demand for a particular alloy and as previously discussed low demand is one reason for the faltering drive in development

of additive manufacturing. This means that material theme development is in the hands of individuals and mostly takes place behind closed doors.

When considering a new material for ALM which has no optimised theme, there are several process variables which can be manipulated to optimise a build. How an 'optimum' theme is measured also needs to be defined; the resulting parts need to be appropriately dense, the surface finish must be adequate, and a suitable microstructure achieved. It is also desirable to maximise the build speed or deposition rate. For structural parts, pore-free, fully dense material is necessary before we consider the microstructure. To achieve this it is necessary to consider an individual melted track and how this track is formed and manipulated by the heat input parameters the shape of a melted track and how it is overlapped with adjacent tracks to form a coherent layer is important in controlling porosity.

Statistical design of experiments was used in a circumscribed central composite design (CCD) to investigate the effect of three processing parameters (laser scanning velocity, inter-track spacing and stripe width) on track geometry and overlap. Experiments were designed and analysed using Stat-Ease Design-Expert Version 6 software which was described in detail in Chapter 3.5. Laser exposure was carried out in an EOS M270 DMLS system in an inert nitrogen atmosphere onto a flat, 6mm thick, Inconel 718 plate which had been bead blasted with steel shot. The laser power was kept at a nominal 195W, the machine maximum, as to allow for higher scanning velocities to be used; paramount to maximising deposition rate. The beam diameter was also kept constant; the machine setting for this variable is described in terms of a beam expander, zero being fully focused at 100μm and 10 being defocused to 500μm. A beam expander setting of 'one' (140μm, see Figure 4.7) was used to build the bulk material and the default setting of 'zero' being used for the contour hatch.

The measured response deemed critical to the control of porosity was defined as the depth achieved in the overlapping region between adjacent tracks as indicated by the red triangle in Figure 4.2. To obtain these measurements the laser was scanned across the surface of the Inconel 718 plate in a horizontal rastering pattern to give a melted area of single tracks side-by-side. These melted regions were sectioned perpendicular to the direction of the rastering and etched to reveal the cross-section of the meltpools, the depth in the overlapping region between adjacent tracks was measured using optical microscopy and an average value from 10 measurements for each trial was used to model the response.

As a secondary consideration, it is desirable to maximise the area melted in a given time (i.e. the width of the triangle in Figure 4.2) in order to reduce processing time whilst at all times maintaining a suitable melt depth. The area melted can be parameterised in terms of the processing variables by combining the scanning velocity

of the laser and the inter track spacing or offset; the product of the two giving the area melted in mm^2 per second.

Figure 4.2 illustrates the experiments performed to investigate this particular aspect of the process and is composed of a 2^3-factorial design (3 factors each at 2 levels); 6 axial points and 5 replicates at the centre-point. The latter sets of data points in addition to the factorial design allow the response to be modelled to a second order polynomial taking into account curvature of the response surface. The repeat tests are used to estimate the experimental or 'pure' error.

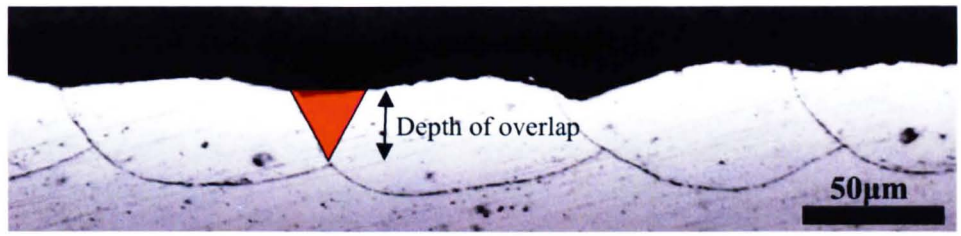

Figure 4.2 –Transverse cross-section of weld tracks from the hatching region

The measured overlap depths for the matrix experiments are listed in Table 4.1. Direct analysis of these results yields no clear trends because of the non-sequential nature of the CCD and the altering of multiple factors simultaneously. The results do however make it possible to perform linear regression analysis to fit a response model to the data points to acquire a response surface. The resultant data were used to test a second order model including two-factor interactions, each term and the final reduced model is checked for its significance using the Fisher Variance Ratio (F-value) and the corresponding Prob>F value (p-value); a low p-value indicating statistical significance for a stated confidence level - 95% in this study. This stage of regression analysis is known as 'analysis of variance' (ANOVA) and the results can be found in Table 4.2 where it may be seen that the significant terms in the model are velocity, velocity squared, track offset, and track offset squared. The stripe width and the interaction terms are not found to have any statistical significance from this series of experiments. The reduced, four-term model is hence deemed to be significant with $p<0.0001$. The response model is given by Equation 4.1 and Equation 4.2 for coded and actual variables and the response surface plotted as a contour map in Figure 4.2. Further indication that the model accurately describes the true response surface is given by the R^2 and adjusted R^2 (values of 94% and 92% respectively). Analysis of residuals (difference between measured and calculated depths) is shown to follow an approximately normal distribution and is shown in Figure 4.4 with a plot of the measured values of depth compared to the estimates calculated by the fitted model showing very good agreement.

Table 4.1- Experimental design table showing list of experiments conducted, the order in which experimentation took place and the measured overlap depth

order		*Natural values of parameters*			*Coded values of parameters*				V_b *	*overlap melt*
Std	*run*	*Beam veloity* mm/s	*track offset* mm	*stripe width* mm	x_0	x_1	x_2	x_3	*offset* mm^2/s	*depth* μm
1	7	400	0.05	4	1	-1	-1	-1	20	75.63
2	2	1400	0.05	4	1	1	-1	-1	70	39.07
3	15	400	0.15	4	1	-1	1	-1	60	52.73
4	12	1400	0.15	4	1	1	1	-1	210	0.00
5	4	400	0.05	10	1	-1	-1	1	20	60.02
6	11	1400	0.05	10	1	1	-1	1	70	30.22
7	14	400	0.15	10	1	-1	1	1	60	47.65
8	18	1400	0.15	10	1	1	1	1	210	8.56
9	9	59	0.1	7	1	-1.68	0	0	5.9	126.32
10	13	1741	0.1	7	1	1.68	0	0	174.1	25.08
11	5	900	0.02	7	1	0	-1.68	0	18	40.29
12	8	900	0.18	7	1	0	1.68	0	162	3.77
13	10	900	0.1	2	1	0	0	-1.68	90	42.98
14	19	900	0.1	12	1	0	0	1.68	90	36.19
15	17	900	0.1	7	1	0	0	0	90	33.46
16	3	900	0.1	7	1	0	0	0	90	26.82
17	20	900	0.1	7	1	0	0	0	90	33.09
18	6	900	0.1	7	1	0	0	0	90	29.50
19	1	900	0.1	7	1	0	0	0	90	32.61

From the contour plot of overlap depth it is possible to deduce a processing map to choose parameters which will allow a desired depth to be achieved consistently. It is shown that the overlap depth decreases with increasing values of beam velocity and track offset. It is known from Porter et al. (Porter 1988) that weld track depths and widths decrease with increasing beam velocity since the interaction time of the heat source is reduced and, hence the faster the beam moves the smaller the track offset must be to achieve a minimum melt depth in the overlapping region. These are conflicting measures when the processing time is considered; as previously outlined increasing V_b and offset will increase the area melted by each pass of the laser per unit time.

Coded parameters:

$$depth = 32.7 - 24.05x_1 - 11.5x_2 + 13.98x_1^2 - x_2^2$$

Equation 4.1

Actual parameters:

$$depth = 124.3 - 0.15V_b + 169.3offset + 5.6x10^{-5}V_b^2 - 1999offset^2$$

Equation 4.2

Table 4.2 - Analysis of variance (ANOVA) table for the fitted response model for the effect of laser scanning velocity, x_1, track offset, x_2, and stripe width, x_3, on the overlap melt depth.

Source of variation	*Sum of Squares*	*Degrees of Freedom*	*Mean Square*	*F-Value*	*Prob > F (p-value)*	** see below*
Model	13131.740	4	3282.934	54.207	< 0.0001	*
x_1	*7899.207*	*1*	*7899.207*	*137.379*	*< 0.0001*	*
x_2	*1814.181*	*1*	*1814.181*	*31.551*	*0.0002*	*
x_3	*76.836*	*1*	*76.836*	*1.336*	*0.2746*	
x_1^2	*2869.088*	*1*	*2869.088*	*49.898*	*< 0.0001*	*
x_2^2	*341.075*	*1*	*341.075*	*5.932*	*0.0351*	*
x_3^2	*25.958*	*1*	*25.958*	*0.451*	*0.5169*	
$x_1 x_2$	*81.080*	*1*	*81.080*	*1.410*	*0.2625*	
$x_1 x_3$	*52.041*	*1*	*52.041*	*0.905*	*0.3639*	
$x_2 x_3$	*97.528*	*1*	*97.528*	*1.696*	*0.2220*	
Residual	908.438	15	60.563			
Pure Error	34.880	5	6.976			
Total	14040.17	19				

***R-Squared** 0.9353, **Adj R-Squared** 0.9180,* [*] indicates that the source of variation is significant by the F-test at the 5% confidence level. The Model is deemed statistically significant and the four regression terms for the reduced model are highlighted (terms are rejected when p-value is >0.1).

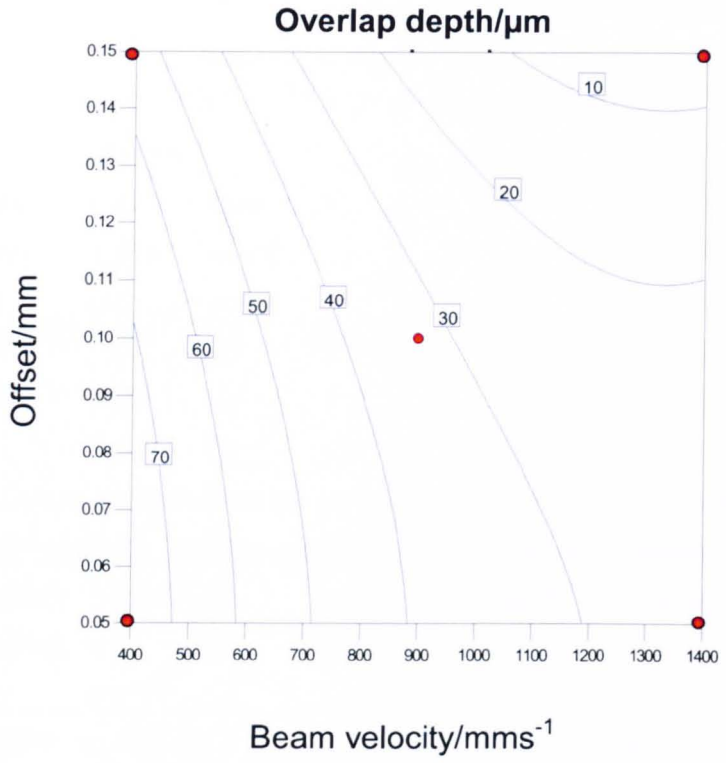

Figure 4.3 - Response surface contour plot of overlap depth (µm) as a function of beam velocity (mm/s) and track offset (mm). Red spot indicates the design points in the given region of the design space.

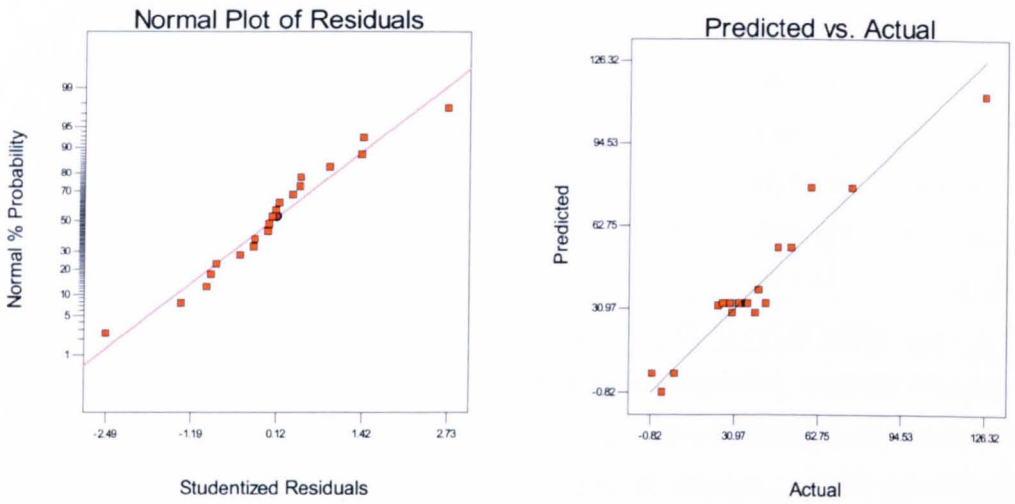

Figure 4.4 - normal probability plot of residuals and graph of measured depths vs. values predicted by the regression model (µm)

Standard practise during processing is to melt 20µm layers as recommended by the machine manufacturer (EOS GmbH). It would be desirable to melt thicker layers to reduce build time, however, doing so results in increased porosity as detailed in section 4.1.3.2. A minimum melted depth equal to 25µm is necessary based on a

nominal layer thickness of 20μm plus an allowance for the scattering effect of a powder layer in the true set-up of the system (Fischer 2003). When a plot of V_b multiplied by Offset is produced (Figure 4.5) it is possible to plot an overlay contour map to define processing parameter sets where the desired melt depth is not achieved and this region is shaded grey in Figure 4.6; the grey area to the right of the red line indicates parameter sets which do not result in the required 25μm overlap depth, and the area to the left represents decreasing melting rates. The arrow in Figure 4.6 indicates to reduction in processing speed so to optimise a theme it is necessary to build as fast as possible but maintain sufficient melt depth to produce a fully dense part. This is achieved with parameters in the range; beam velocity 950-1100mm/s and track offset 0.10-0.12mm.

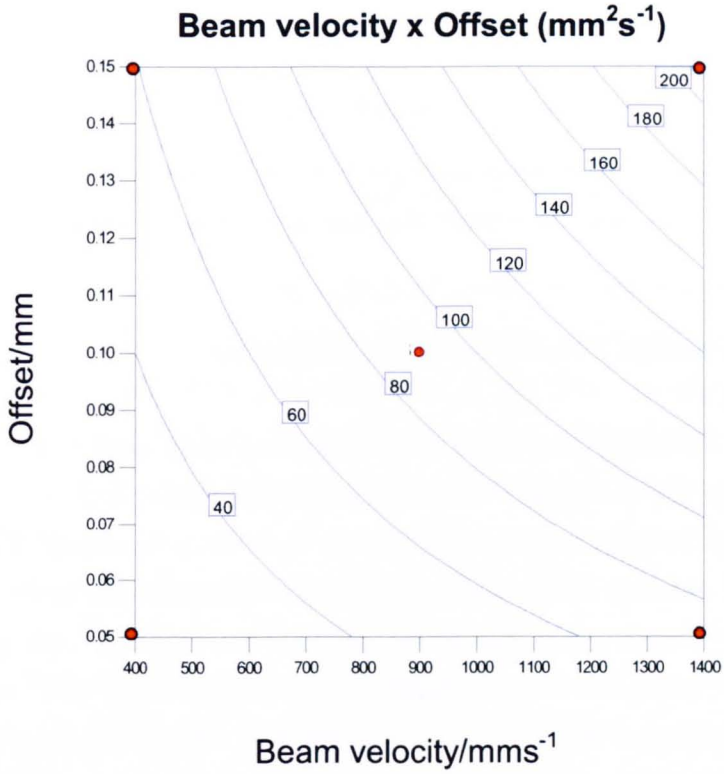

Figure 4.5 contour map of V_b*offset showing contours of equal area melted per unit time (mm^2/s)

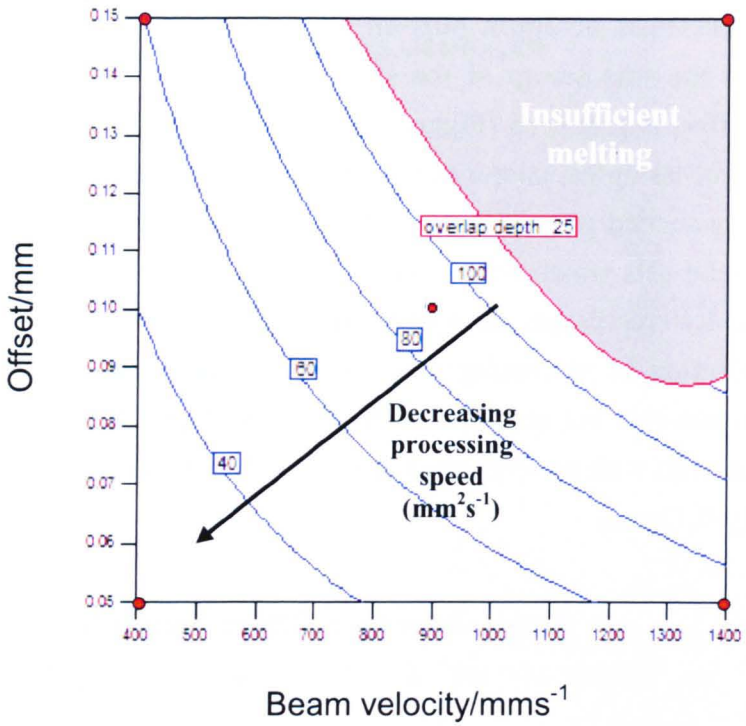

Figure 4.6 – Overlay plot of overlap depth (μm) and area melted per unit time (mm^2/s) as a function of V_b (mm/s) and offset (mm). Red line indicates minimum overlap depth (μm)

4.1.2 Effect of Power, Velocity and Beam Diameter

One technique commonly employed to reduce processing time and improve surface finish is to change the laser beam diameter. On contour hatching, the beam is focused to approximately 100μm to give finer detail and when hatching the interior of a melted layer the beam is defocused. No accurate values for the beam diameter were measured in the present work, instead we consider the machine setting known as the 'beam expander', a focused contour hatch has a beam expander (BE) setting of 'zero' which can be increased up to a value of 10 for a completely defocused beam in increments of 0.5. EOS standard materials are usually processed at a BE setting of 'one' or 'two' for interior hatching. To establish the diameter of the beam at different beam expander settings the known diameter of the focused and defocused beam was extrapolated in Figure 4.7. This shows that 'one' and 'two' correspond to real values of 140 and 180μm respectively. Also plotted in Figure 4.7 is the measured diameter of a weld track melted at 195W, 800mm/s at varying beam diameters on Inconel 718 plate. The tracks are shown to increase in width with increasing beam diameter up to a diameter of 230μm (beam expander setting 'six'), after this the energy density of the incident laser is reduced to such an extent that the weld track width decreases.

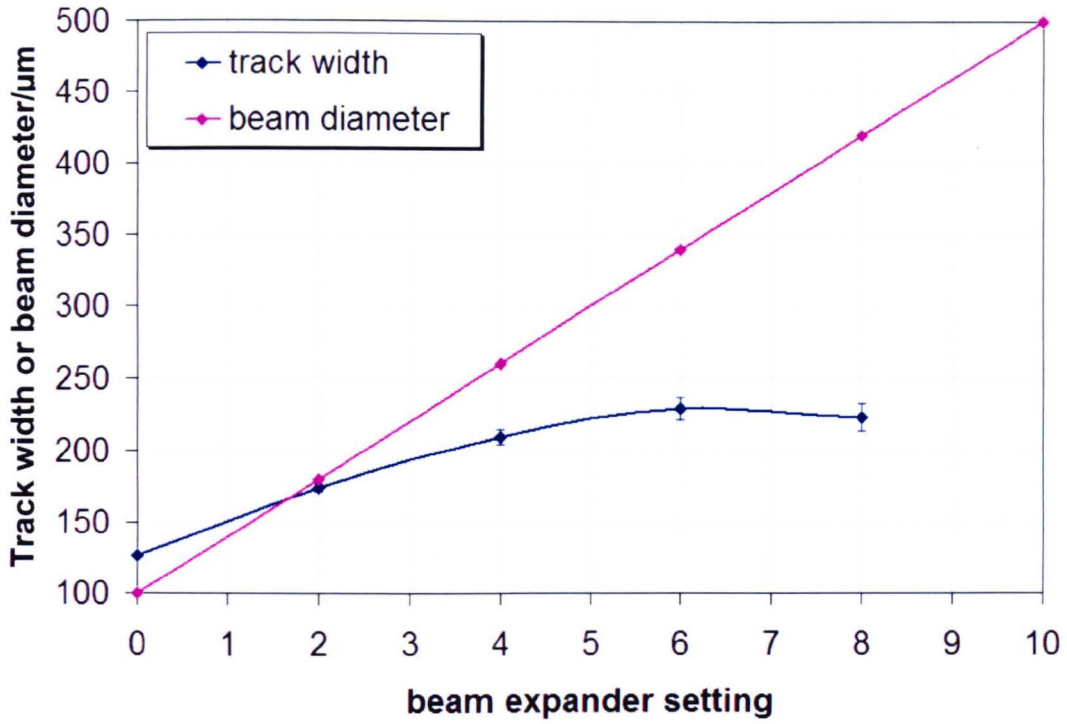

Figure 4.7 – Width of melted track as a function of beam diameter or beam expander setting

In this section of the study, single weld tracks were melted onto a flat Inconel 718 plate with no powder layer. Laser power and velocity are investigated again with a third variable (factor), the beam expander setting, this factor is categorical (i.e. non-continuous) as we are limited to discrete levels of 0.5. This results in a three-factor CCD but rather than a single experiment like in the earlier section looking at Vb, offset and stripe width, we conduct two two-factor experiments collectively termed a 'blocked experiment' the first 'block' is a two-factor CCD with the BE equal to zero and the second is a repeat with BE equal to 2. The two numerical factors considered are Power and Velocity with values identical to those in the previous section. These are summarised in Table 4.3 together with the measured depths and widths of individual tracks.

Figure 4.8 shows the cross-section of the tracks melted at BE=0 and the raw data of the measured widths and depths is plotted in Figure 4.9. Scrutiny of these results shows several interesting features; the defocused beam yields shallower, wider tracks compared to the focused beam as the incident energy involved in melting is spread over a larger area i.e. the energy density is reduced. The depth shows a strong linear correlation to the line energy input (P/V_b, in J/mm) and the width likewise to a 'P over square-root V_b' relationship which is consistent with results reported by Olivera et al. (Olivera 2005). There are some notable discrepancies in the data for the focused beam width measurements which correspond to the high power, low velocity samples (upper left section of the CCD array); from Figure 4.8 we note a change in pool shape

in these two examples from a semi-elliptical cross-section to a pool with exaggerated width at the top surface. This effect indicates the increasing significance of Marangoni convection in the weld pool compared to normal conduction of the heat. As the pools become wider than the beam diameter Marangoni effects will dominate because of an increase in the temperature difference on the top surface from the pool centre to its edge causing a surface tension differential on the top surface which transports heat outwards from the centre of the pool (Drezet 2004, Limmaneevichitr 2000). For this reason the two values and data sets highlighted in yellow in Table 4.3 are not used in the regression analysis which is used to plot contour maps of the responses measured as a function of the three factors.

Table 4.3 - 3 factor CCDOE showing effect of Power, Vb and beam expander on depth and width of weld tracks. Note that the Beam Expander value is not continuous and so the 'high' and 'low' values represent two blocks each containing a 2-factor central composite array.

standard order	*run order*	*block*	V_b *mm/s*	*Power W*	*C:BE*	x_0	x_1	x_2	x_3	*depth μm*	*width μm*
1	4	1	600	95	0	1	-1	-1	-1	52.44	127.60
2	12	1	800	95	0	1	1	-1	-1	50.40	108.13
3*	22	1	600	175	0	1	-1	1	-1	146.86	146.67
4	8	1	800	175	0	1	1	1	-1	99.72	142.88
5*	23	1	558	135	0	1	-1	0	-1	137.27	189.10
6	17	1	841	135	0	1	1	0	-1	66.03	96.80
7	26	1	700	78	0	1	0	-1	-1	43.08	115.04
8	13	1	700	192	0	1	0	1	-1	133.54	141.27
9	14	1	700	135	0	1	0	0	-1	66.01	117.06
10	10	1	700	135	0	1	0	0	-1	77.05	124.91
11	7	1	700	135	0	1	0	0	-1	88.71	127.30
12	21	1	700	135	0	1	0	0	-1	74.63	114.00
13	16	1	700	135	0	1	0	0	-1	75.02	113.35
14	5	2	600	95	2	1	-1	-1	1	42.03	121.16
15	9	2	800	95	2	1	1	-1	1	30.15	125.15
16	20	2	600	175	2	1	-1	1	1	66.23	174.51
17	2	2	800	175	2	1	1	1	1	55.83	165.53
18	3	2	559	135	2	1	-1	0	1	53.96	145.95
19	24	2	841	135	2	1	1	0	1	44.75	144.90
20	25	2	700	78	2	1	0	-1	1	30.40	102.33
21	15	2	700	192	2	1	0	1	1	53.67	193.08
22	6	2	700	135	2	1	0	0	1	43.19	148.41
23	18	2	700	135	2	1	0	0	1	49.57	153.93
24	1	2	700	135	2	1	0	0	1	49.50	147.98
25	19	2	700	135	2	1	0	0	1	55.81	146.86
26	11	2	700	135	2	1	0	0	1	42.73	154.08

Trials marked * were not used in the regression model as convection effects in the pool begin to skew the measurements.

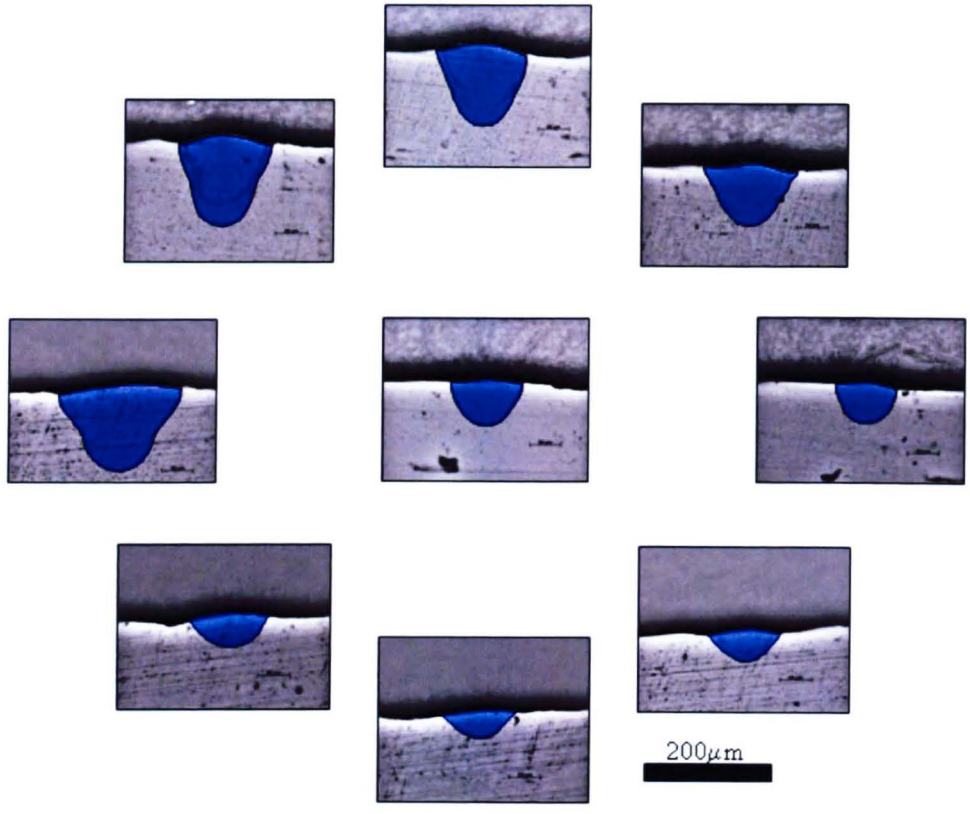

Figure 4.8 - Cross-section of weld tracks highlighted in blue for BE=0 set out in the CCD array

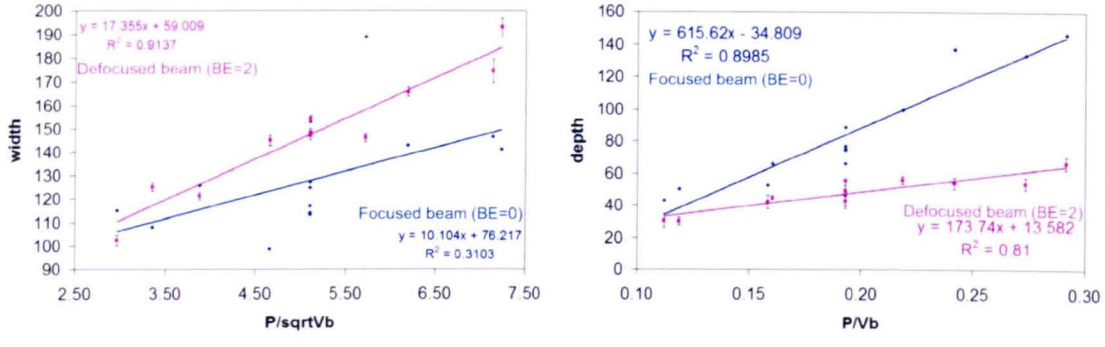

Figure 4.9 - Scatter plots of measured widths and depths for focused and defocused beam (BE=0 'focused' and BE=2 'defocused')

Linear regression was used to fit an empirical model to the measured responses, the ANOVA results are given in Table 4.4 From the analysis it is shown that a linear relationship is observed with the linear models for width and depth having p-values <0.0001. R-squared and adjusted R-squared values in excess of 90% indicate good fit of the regression model to the data which is supported by the diagnostic plots in Figure 4.10. Equation 4.3 to Equation 4.6 and the contour maps in Figure 4.11 show the relationships between power/velocity and width/depth at different levels of beam expander setting. The equations cannot include a term for beam expander due to the inputs being non-continuous (categorical) as mentioned previously, instead, different models for the different beam expander settings are generated.

Figure 4.11 and Equation 4.3 to Equation 4.6 suggest several trends, notably that the effect or contribution of power and velocity is not consistent for increasing beam diameter. The contour map for track width at BE=0 cannot be considered accurate at low velocity/high power combinations as Marangoni convection starts to dominate and track widths are exaggerated relative to purely conduction driven heat transfer, the approximate limit being a width in excess of 130μm. A defocused beam yields wider, shallower pools as previously noted but there is also a very much diminished effect of velocity on width.

If the required depth could be maintained then a larger beam diameter (higher BE) could be used to hatch the interior of a melt region and hence a larger offset could be used and melting rate would increase. This may require higher nominal laser powers so in the case of the EOS M270 the 200W Yb fibre laser may be a limiting factor in this regard.

To recall the issues relating to surface roughness; since a focused beam is used for contour melting, the cross-sections observed in Figure 4.8 suggest that high power levels are beneficial but at velocities high enough to avoid Marangoni effects in order to maximise the radius of the pool edge.

Table 4.4 - ANOVA table for track widths and depths

Source	*Sum of Squares*	*DF*	*Mean Square*	*F Value*	*Prob > F (p-value)*
Width Model	12052.39	5	2410.48	61.68	< 0.0001
x_1	546.87	1	546.87	13.99	0.0016
x_2	4100.95	1	4100.95	104.93	< 0.0001
x_3	3550.19	1	3550.19	90.84	< 0.0001
Residual	664.39	17	39.08		
Pure Error	212.20	8	26.52		
R^2 0.9478	*Adj.* R^2 0.9324				
Depth Model	9886.11	4	2471.528	55.36998	< 0.0001
x_1	260.1796	1	260.1796	5.828841	0.0266
x_2	5540.835	1	5540.835	124.1321	< 0.0001
x_3	5493.474	1	5493.474	123.0711	< 0.0001
Residual	803.4587	18	44.6366		
Pure Error	381.3727	8	47.67159		
R^2 0.9248	*Adj.* R^2 0.9081				

$$width_{BE=0} = 193 - 0.14V_b + 0.2P$$

Equation 4.3

$$width_{BE=2} = 60 - 0.01V_b + 0.7P$$

Equation 4.4

$$depth_{BE=0} = 8.8 - 0.05V_b + 0.77P$$

Equation 4.5

$$depth_{BE=2} = 45.5 - 0.05V_b + 0.26P$$

Equation 4.6

(a) Width

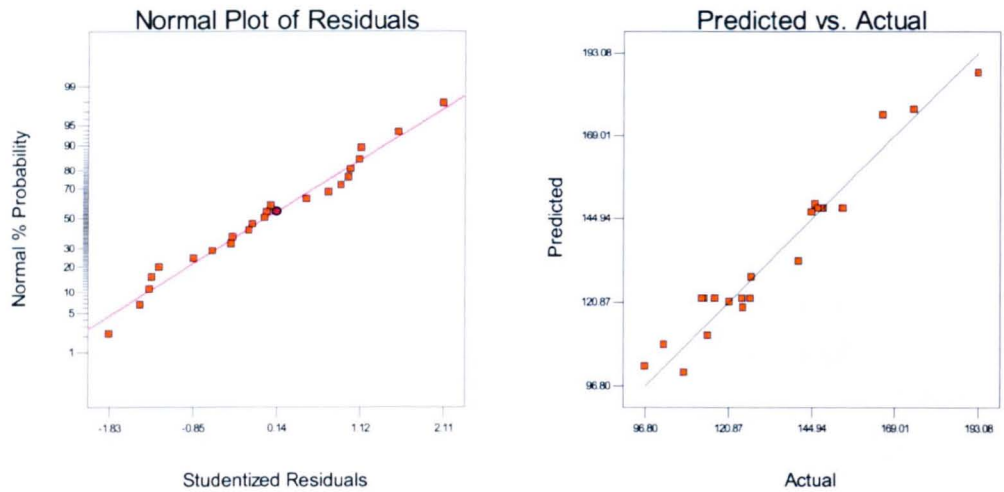

(b) Depth

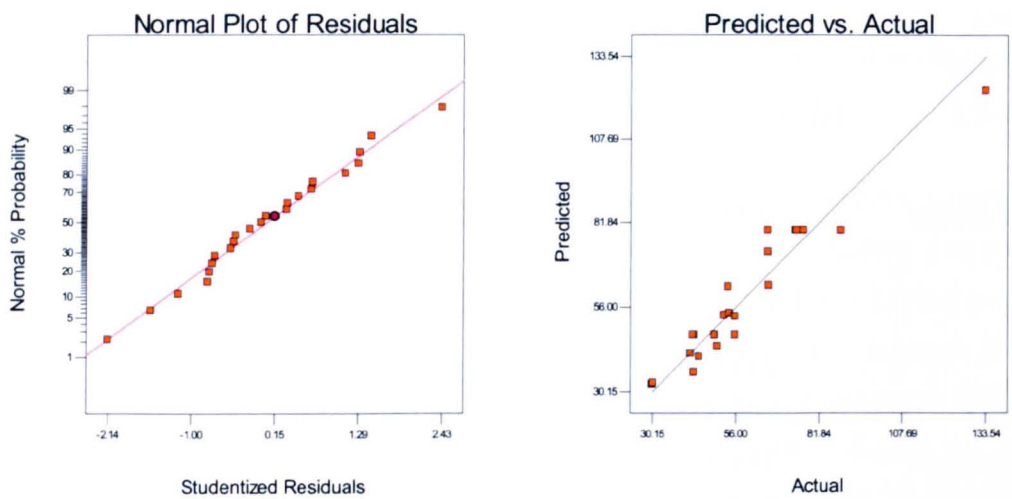

Figure 4.10 - Diagnostic plots for the fitted (a) width and (b) depth measurements

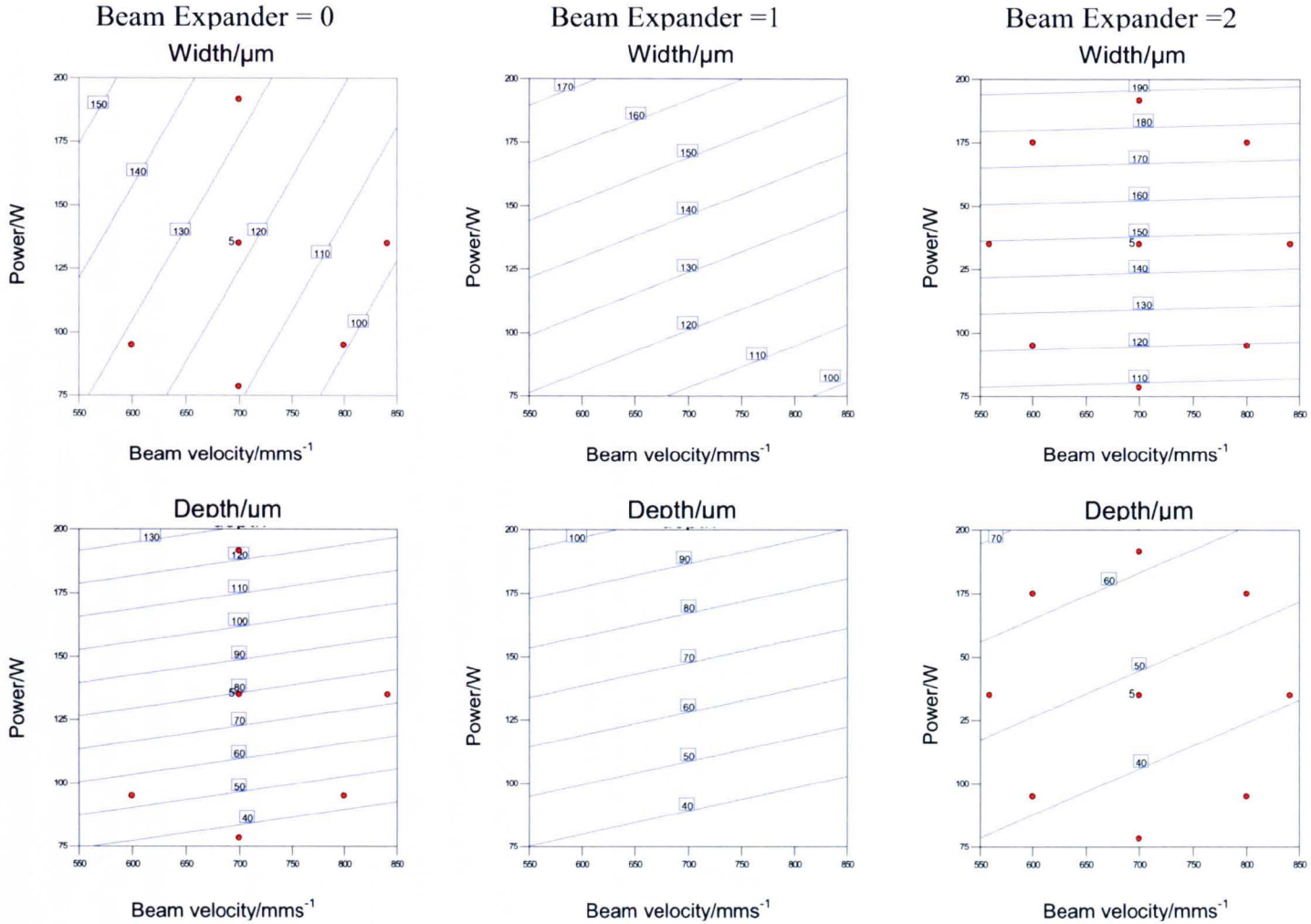

Figure 4.11 - Contour plots for width and depth as a function of Power (W) and Velocity (mm/s). graphs from left to right show increasing beam expander setting (0, 1, 2) i.e. increasing beam diameter. The models for a beam expander value of 1 are extrapolated based on the models obtained for values of 0 and 2.

4.2 Building simple 3-Dimensional parts

The processing window established in Figure 4.6 was used as a basis to build cubic samples on the EOS M270. The track offset and beam expander were held constant at 0.1mm and 1 (140μm beam diameter) in the experiment and beam velocity and power were varied according to Table 4.5. The building process and sample are shown in Figure 4.12.

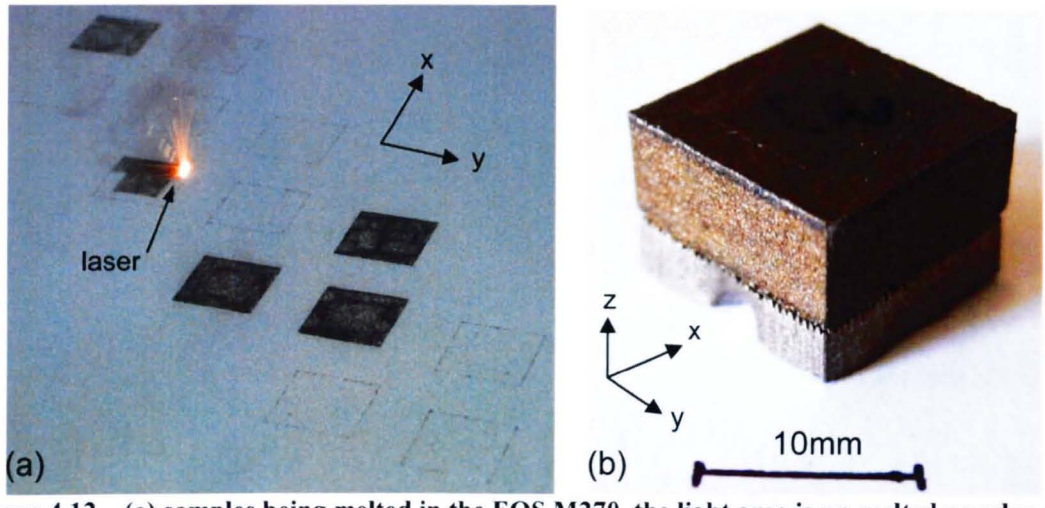

Figure 4.12 – (a) samples being melted in the EOS M270, the light area is un-melted powder and the dark is melted cross-section of the samples. (b) on of the cubic samples after removal from the machine. The lighter band at the bottom is support structures to fix the sample to the base plate and the dark upper region is the sample itself.

The following sections will consider the surface roughness and porosity in the samples produced and then modelling of the weld pools and solidification conditions will be carried out. The microstructures are observed and hardness measurements are also reported.

4.2.1 Surface roughness

Having established a suitable processing window based on laser melting of Inconel 718 plate it was possible to further the study into part production. 15mm cubic samples were built using Inconel 718 powder supplied by LPW Technologies Ltd with a powder specification of 20-40μm particle size in line with powders supplied by EOS GmbH in other materials (EOS718 was not available at the time). This would enable the analysis of porosity (to assess the feasibility of the initial part of the study) as well as issues relating to surface roughness and microstructure. Having established previously that track offset and stripe width do not contribute to the heat input, i.e. do

not influence the size and shape of the weld pool significantly, that these would not be investigated in the following section. Instead, a second design of experiments was carried out, a two factor CCD, considering laser power and beam velocity. Both are known to influence the weld pool and therefore may have some impact on surface roughness and microstructure. A two-factor CCD comprises a 2^2 factorial square arrangement and 4 axial points and 5 repeats at the centre were used in the present case.

In the Section 4.1.1, power was kept at a nominal maximum of 195W therefore in this section it is only possible to reduce the power and it follows that to maintain a fully dense part it is necessary to build using lower beam velocities as can be seen in the overlay plot in Figure 4.6. To build the samples in this section the track offset was maintained at 0.1mm.

Surface roughness is important in part production and is one of the first problems encountered when using ALM. The relatively small layer thickness of 20μm on the EOS M270 helps to reduce the surface roughness of as deposited parts to an approximate 10μm reported by the machine manufacturer. The surface roughness will dictate the finishing procedures required in part production but will also have to be accounted for to optimise geometrical accuracy, therefore minimising surface roughness in as-deposited parts is crucial.

Table 4.5 - Design matrix for CCDOE investigation of beam velocity and laser power showing the results of surface roughness measurements. Samples are referred to by their 'standard order'.

standard order	*run order*	*A: Power W*	*B: V_b mm/s*	x_0	x_1	x_2	R_a μm
A	12	95	600	1	-1	-1	12.90
B	3	175	600	1	1	-1	9.96
C	7	95	800	1	-1	1	11.84
D	8	175	800	1	1	1	10.90
E	2	78	700	1	-1.41	0	11.36
F	6	192	700	1	1.41	0	8.58
G	5	135	559	1	0	-1.41	9.26
H	9	135	841	1	0	1.41	11.22
I	1	135	700	1	0	0	10.04
J	4	135	700	1	0	0	12.04
K	13	135	700	1	0	0	10.08
L	11	135	700	1	0	0	10.14
M	10	135	700	1	0	0	10.98

Surface roughness was measured in the z direction on the horizontal sides of 15mm cubes built according to the CCD described in Table 4.5. Measurements were made using Surtronic 3+ (Taylor/Hobson Pneumo) stylus profile-meter to plot line profiles and measure R_a values of the surface of interest (for the R_a values 10 measurements were made and an average reported, the error is shown in Figure 4.17 and discussed in the following paragraphs), a sample was also observed using an Olympus laser confocal microscope to plot a profile of the same side-wall surface. Line and surface plots are shown in Figure 4.13 and Figure 4.14 and indicate the sporadic undulations in the as-deposited surface but these do not allude to any quantitative trends. R_a values of the 13 blocks built were analysed using the Stat-Ease software and are reported in Table 4.5. As with the previous study, it was possible to perform linear regression analysis to fit an empirical model to the measured data. The model is linear and plotted as a contour map in Figure 4.15 showing that there is an improvement in surface finish as power increases and velocity decreases; this is likely a result of an increasing size of track cross-section (i.e. radius) with increasing heat input and interaction time. This is depicted schematically in Figure 4.16.

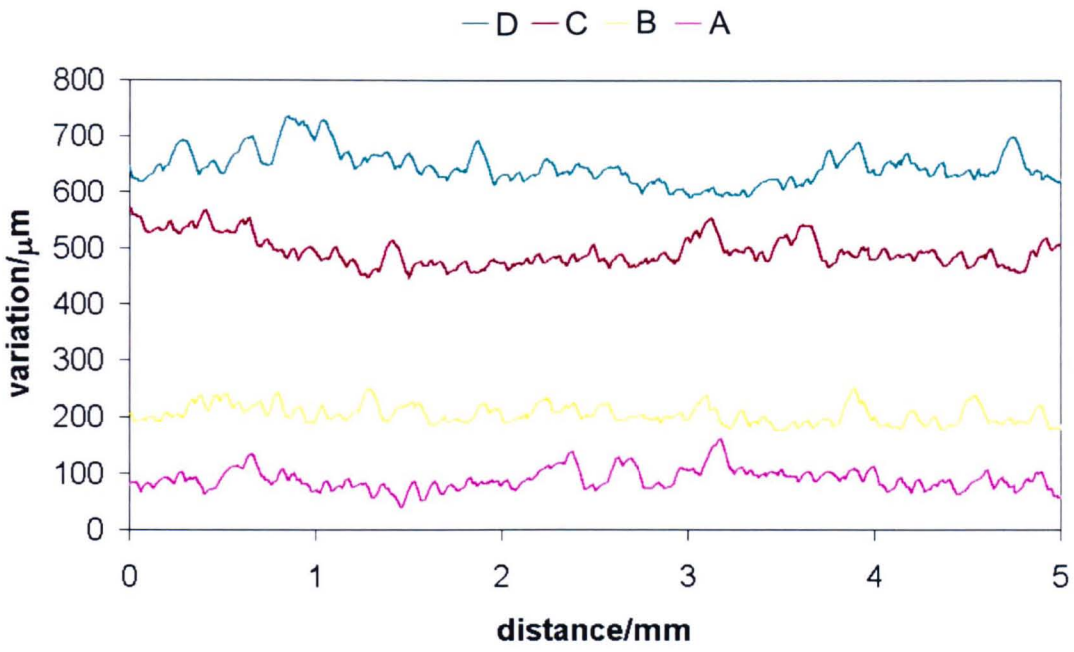

Figure 4.13 - line-plots of side-wall surface profile in the z direction for the factorial point samples built in the CCDOE

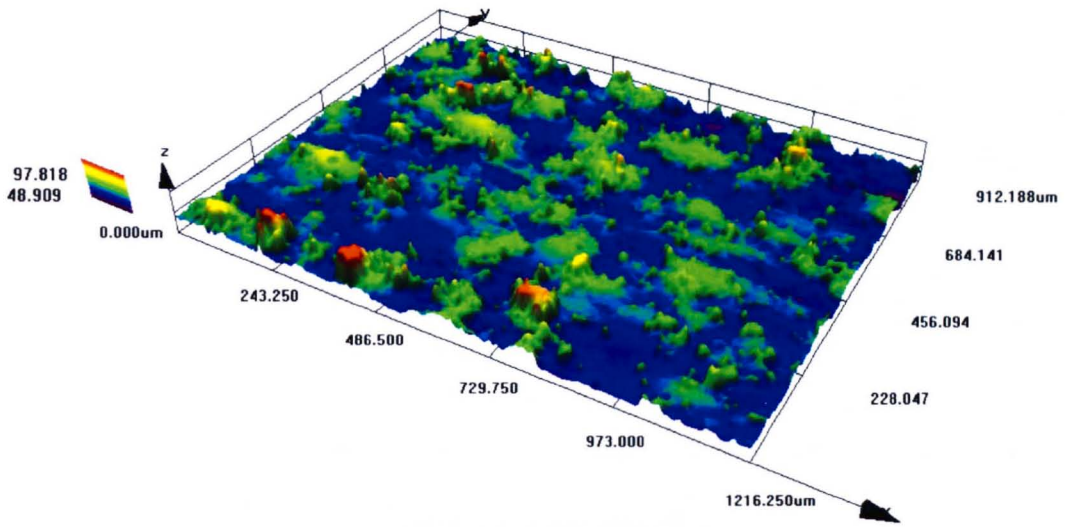

Figure 4.14 - Surface profile taken using confocal microscope of the side wall of sample E built in the centre of the CCDOE (y axis indicates the build direction normal to the layers (y axis indicates build direction)

The model while showing a rational trend must be treated with caution however; if we consider the ANOVA data in Table 4.6 we see that the model is statistically significant by the F-test at a 5% confidence level yet the p-value is not as small as one would hope. This is reflected in the R^2 and adjusted R^2 values of 50% and 40% respectively, the reason for this is seen when you consider the mean-square value for the pure error. This is an indication of the scatter observed in the repeated

experiments at the centre point and in this case is not small compared to the model mean-square value. The point is better made if we consider all measurements taken since the values used in the DOE analysis are averages taken from ten measurements on each sample cube. Figure 4.17 shows this raw data against the 95% confidence intervals for the measurements taken and indicates that the scatter in the data is of a similar order of magnitude to the true response, i.e. the signal to noise ratio is low. The scatter in the data is most likely a result of the different sources of roughness (such as powder particle size, layer thickness, machine instability) combined with inaccuracies associated with using a stylus profile meter. The different sources of surface roughness include the layered nature of the process, the stability of the heat source to hatch a straight and smooth line, the partial melting of powder on the surface and the hatching technique which may cause periodic hotspots at the surface causing excess powder to be melted locally.

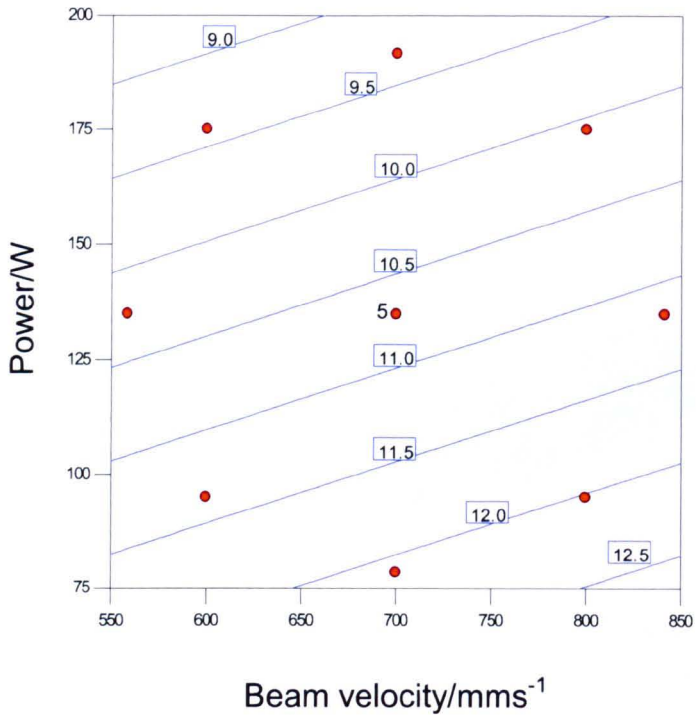

Figure 4.15 - Contour plot of surface roughness (µm) as a function of processing parameters, Power (W) and velocity (mm/s)

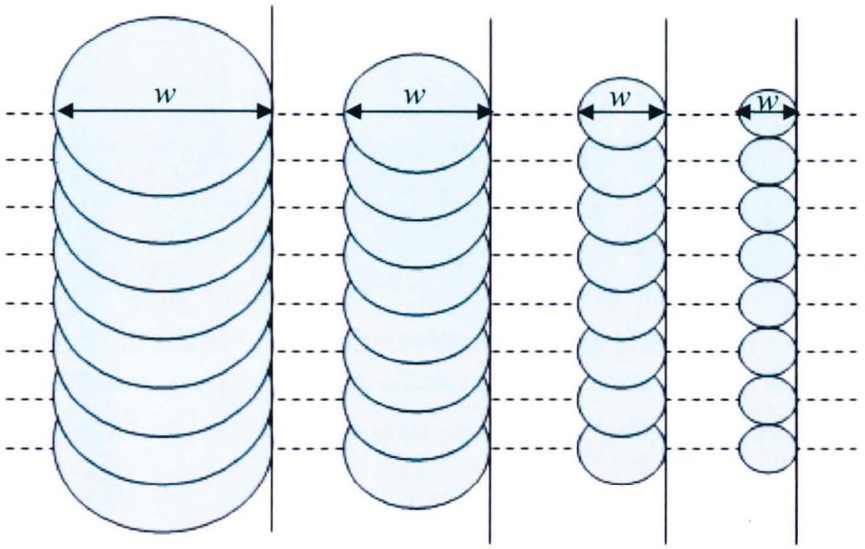

Figure 4.16 - Schematic representation of clad tracks as cross-section al area increases. A consistant step height is shown by the dotted lines and the vertical solid line depicts the outer surface of an ideal smooth wall (*w* is track width).

Table 4.6 - ANOVA table for the results of surface roughness measurements

Source	*Sum of Squares*	*DF*	*Mean Square*	*F Value*	*Prob > F (p-value)*
Model	8.507	2	4.253	5.004	0.0312
x_1	*7.627*	*1*	*7.627*	*8.974*	*0.0134*
x_2	*0.879*	*1*	*0.879*	*1.034*	*0.3331*
Residual	8.499	10	0.850		
Pure Error	2.998	4	0.749		
Total	17.006	12			

R-Squared *0.50,* ***Adj R-Squared*** *0.40*

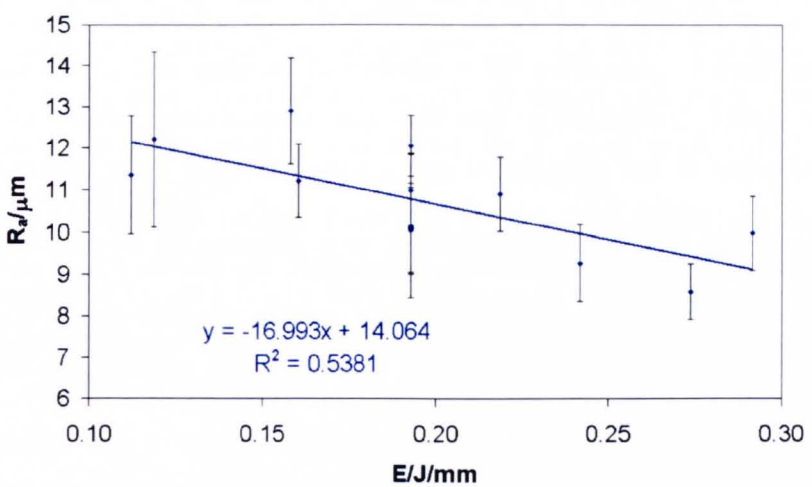

Figure 4.17 - Graph of surface roughness vs. line-energy (P/Vb). Error bars represent 95% confidence interval

4.2.2 Sources of porosity

There are many other sources of porosity to be found during additive manufacturing, all of which are manageable through the use of appropriate corrective measures. When developing a new material theme there are numerous settings to be manipulated beyond the relative few discussed in the previous sections, these settings vary from system to system but several are discussed relative to the EOS M270 in the following section.

4.2.2.1 Hatching technique

There are numerous sources of porosity relating to hatching technique and all are controllable by altering so-called 'overlap' and 'offset' parameters. Figure 4.18 shows three examples of porosity which results from hatching mismatch in the 15mm cube samples build according to the CCDOE described in Table 4.5, the first image is an optical micrograph of subsurface porosity associated with poor alignment of the contour and the 'outer skin' region of the hatching (detail of the hatching techniques and terminology can be found in Chapter 3.1 - experimental techniques). This was observed in all the samples built in the experiment and would require a decrease in the parameter 'beam offset', the distance between the end of a hatching tracks and the nominal path of a contour.

Similarly, in all samples, porosity was present in the region where the 'outer skin' hatching and the 'inner core' region meet. The second and third images in Figure 4.18 show skin/core interface porosity, the size and morphology of these and the contour pores suggest they are a result of the hatching mismatch rather than pores retained from the powder feedstock which are smaller than a powder particle (<40)μm. The skin/core interface is controlled by a number of overlap and offset settings on the machine but further investigation into this was deemed unnecessary as the skin/core hatching technique is not considered appropriate for bulk parts, instead hatching in stripes across the whole melt area is preferred and so the overlap between stripes becomes the most relevant controllable parameter. No porosity was observed which could be attributed to this and so the stripe overlap used (0.1mm) was considered appropriate, this may not be the ideal, however, as minimising the overlap is beneficial to reduce melting time.

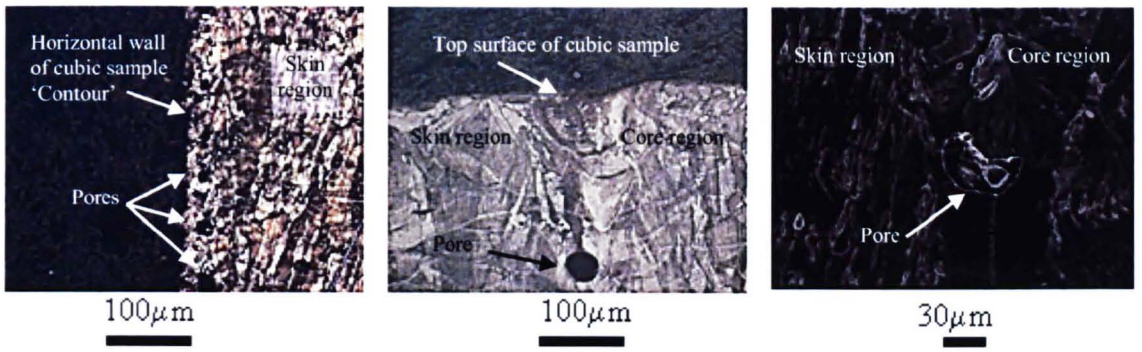

Figure 4.18 - Different sources of porosity relating to hatching mismatch in the contour region and the skin/core interface

4.2.2.2 Layer thickness

As alluded to previously, the layer thickness is an attractive parameter to increase in order to greatly reduce build times. Indeed, compared to the EOS M270 which typically builds in 20μm layers, there are a number of ALM systems which build using thicker layers (O'Neill 1999, Morgan 2002). To examine the influence of layer thickness an initial examination at two different power/velocity combinations was undertaken, the results of which are shown in Figure 4.19 and Figure 4.20.

At 20μm there is some porosity which is a result of the use of non-optimised parameters but the increase in porosity with increasing layer thickness can clearly be seen. Both of the parameter sets chosen represent a line energy of 0.2J/mm with 'A' consisting of a nominally high power and high velocity and 'B' the converse. Despite this there is a difference in the level of porosity observed at a constant layer thickness; at 20μm the difference is slight which suggests that at this level there is a certain amount of process 'robustness', but ultimately the results support the findings of Section 4.1.2 with the suggestion that power has a more significant effect on the depth of melt. Considering Figure 4.11, it can be seen that at a beam expander setting of 1 the parameter combinations used (A and B), the expected melt track cross-section is smaller at low power/low velocity and hence for a given track offset the critical overlap depth will be smaller.

The increasing level of porosity with increased powder layer thickness may be a result of a number of factors; firstly there will be more free 'space' between powder-particles in a thicker layer since the packing density of the powder is less than 100%. This 'space' which will be composed of whatever gas is used in the controlled atmosphere represents a certain degree of porosity in the un-melted powder layer which will not have time to escape a meltpool due to the very rapid nature of laser melting and re-solidification. Also, when observing the build process the loose powder appeared to be physically displaced as the heat source traversed which results

in partially formed weld tracks and ultimately will lead to thicker regions of powder than the nominal layer thickness.

Having conducted the builds to varying degrees of success, one positive outcome was that the samples were built in their entirety. There was concern that the larger layer thicknesses would result in balling-up of the weld tracks which would cause a recoater collision and stop the build. With this in mind the results represent the early stages of study into controlled porosity structures, if there is the ability to tolerate or indeed utilise porosity in a final application then increasing layer thickness has a much greater effect on reducing build times. One possible application is the use of large solid support structures.

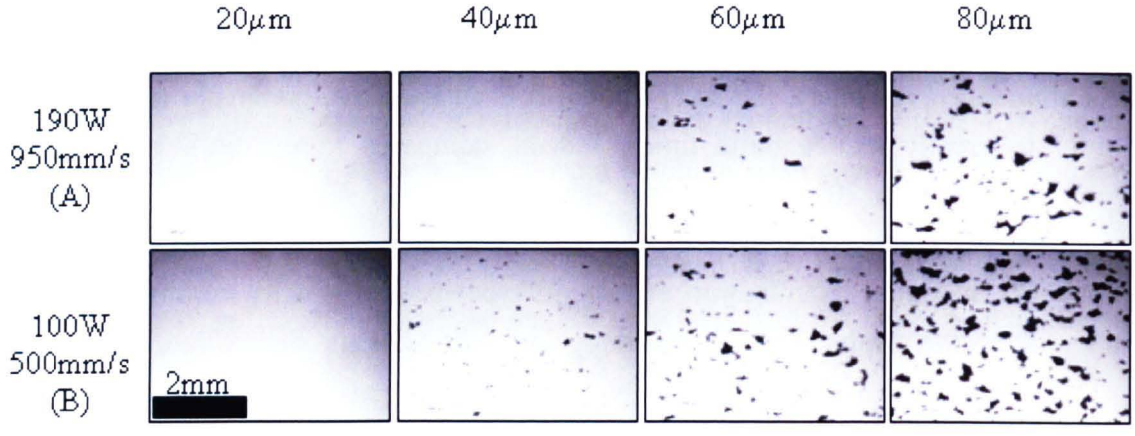

Figure 4.19 - Effect of layer thickness on porosity for two power/velocity combinations.

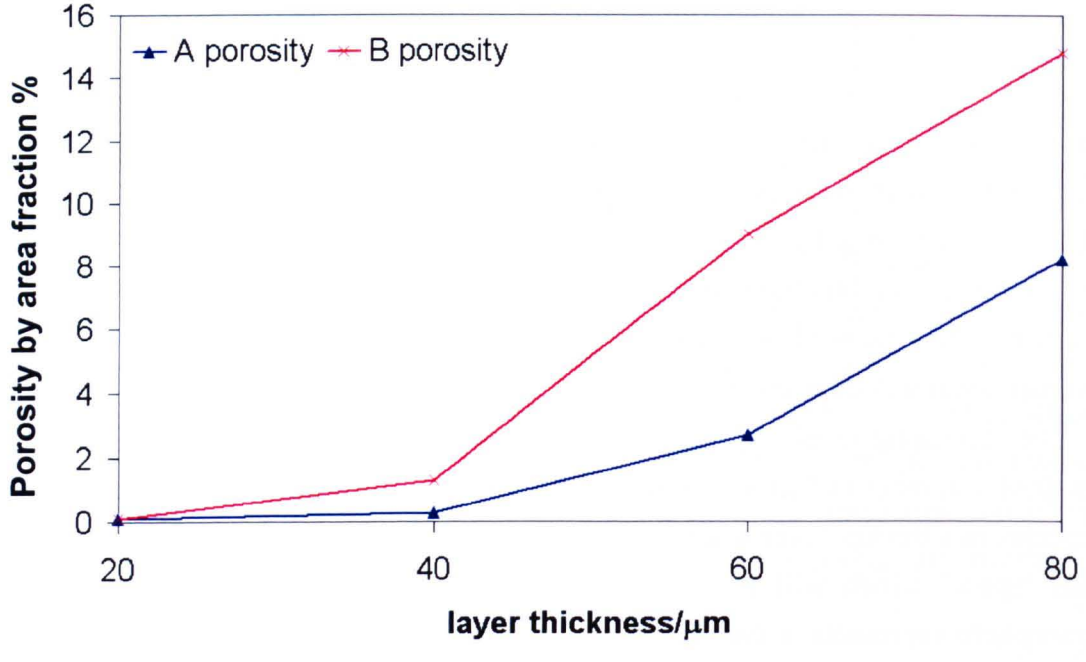

Figure 4.20 - Effect of layer thickness on porosity for two parameter sets (A: 190W, 950mms^{-1} and B: 100W, 500mms^{-1})

4.3 Analytical modelling of solidification front

From the Rosenthal solution Equation 4.7 it has been possible to determine the size and shapes of the melt-pools by graphical intercept methods equating the heat transfer equation with the liquidus temperature of Inconel 718. This was carried out for the experiment involving the EOS M270 over the range of parameters described in Table 4.5.

$$T = T_0 + \frac{\alpha Q}{2\pi k r} e^{\frac{-v_b(x+r)}{2D}}$$

Equation 4.7

Equation 4.7 has been shown to be a good approximation for heat transfer modelling of laser welding and deposition processes (Dye 2001, Vasinonta 2001), however, values of α are not readily available or easily measured. α is the absorption coefficient in Rosenthal's original work and is a characteristic of individual materials and a function of temperature and the wavelength of the heat source used. In this study α is adjusted to fit the calculated values to the measured data obtained experimentally and as such is employed as a fitting parameter rather than a physical property of the system. This term can be used to account for thermal losses through inefficient absorption of the incident energy due to a materials absorption characteristics and the scattering of energy by un-melted particles as well as radiative and convective losses. These losses can be seen to be more significant as deposited tracks decrease in size. In turn, α varies with changing parameter sets as the surface area for radiative loss and the super-heating of the molten metal changes. After the walls were deposited, curve fitting was used to establish accurate values for α based on the known processing parameters and the measured track heights and widths.

The values of α determined for the melted tracks were analysed using Stat-Ease DOE software to produce the contour map given in Figure 4.21. α is seen to increase for tracks melted at high power/low velocity combinations but at lower powers is insensitive to velocity, the diagnostic graphs in Figure 4.22 along with the R-squared and Adjusted R-squared values of 0.9999 imply an excellent fit of the data and the F- and p-values of 19735 and <0.0001 indicate the model is valid. It is also apparent that the values of α increase rapidly and in some cases exceed unity; this would suggest that the coupling efficiency of the heat source increases at higher powers and lower velocity parameter sets. This is misleading as the model fitted to the data is not physically based, it is merely a fit to the observed data, and in this investigation the term 'α' cannot accurately describe the absorption coefficient. The tracks melted at

higher powers and lower velocities were seen to experience a shape change attributed to convective effects in the meltpool as discussed in Section 4.1.2. The values of α obtained are shown to be an accurate fitting parameter but cannot be assumed to describe the physical mechanisms taking place in the meltpool.

$$\alpha = -1.64 + 0.016P + 0.003V_b + \left(6.7 \times 10^{-6}\right)P^2 - \left(1.3 \times 10^{-6}\right)V_b^{\ 2} - \left(1.4 \times 10^{-5}\right)PV_b$$

Equation 4.8

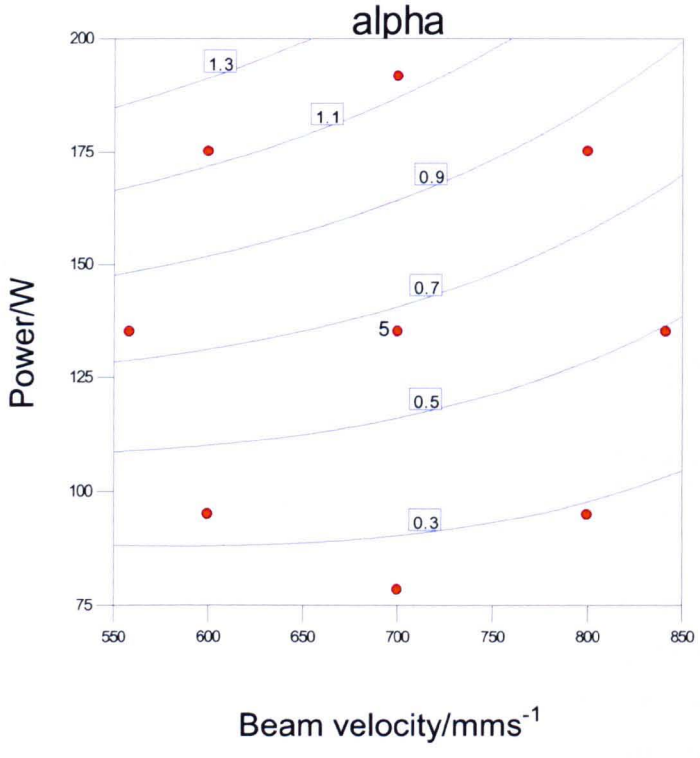

Figure 4.21 - Contour plot of α as a function of laser power and velocity for tracks melted on Inconel 718 plate using EOS M270

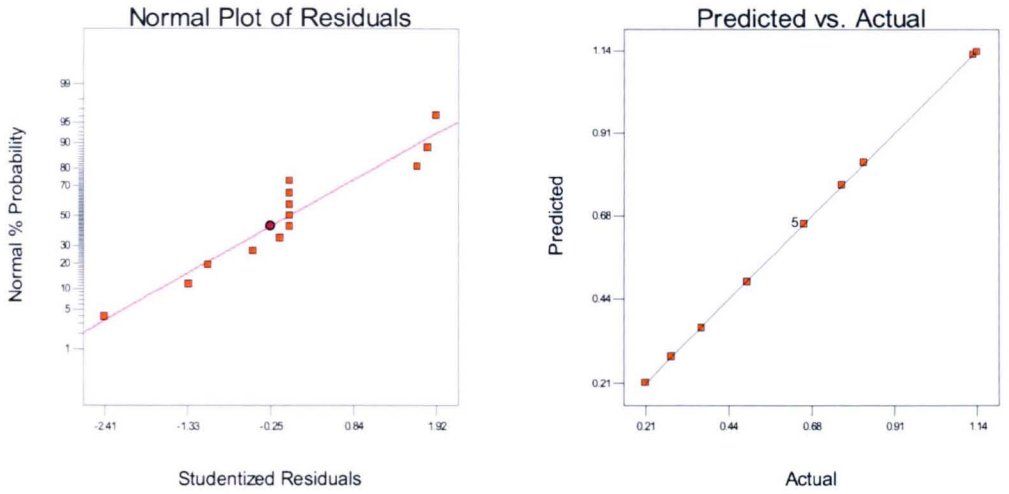

Figure 4.22 - Diagnostic graphs for the model describing alpha as a function of laser power and velocity

Knowing accurate fitting parameters, α, and the meltpool widths and depths it was possible to calculate the solidification isotherms for the parameter sets used in the CCD, these are shown in Figure 4.23. Power has a greater effect on the meltpool size than velocity as the higher powers produce larger pools, in particular the power is seen if greatly increase pool length, increasing velocity reduces pool length and depth but not to the same extent as a change in power over the range of parameters used.

(a)

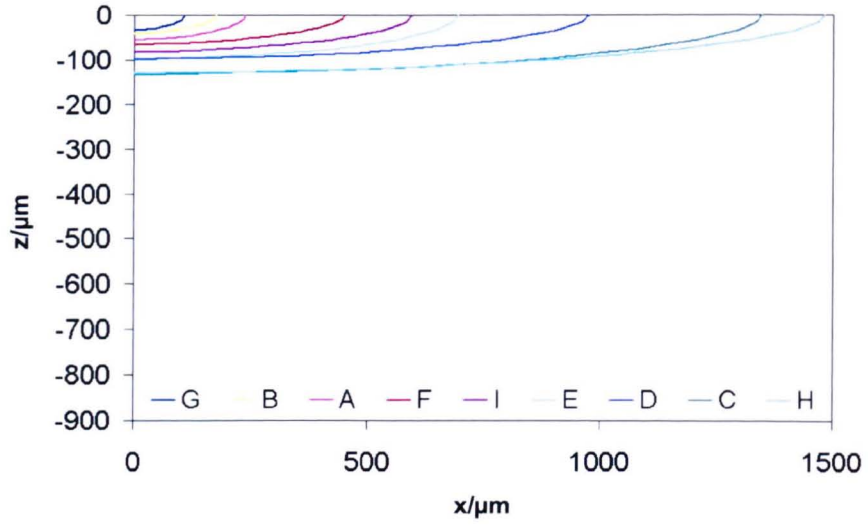

(b)

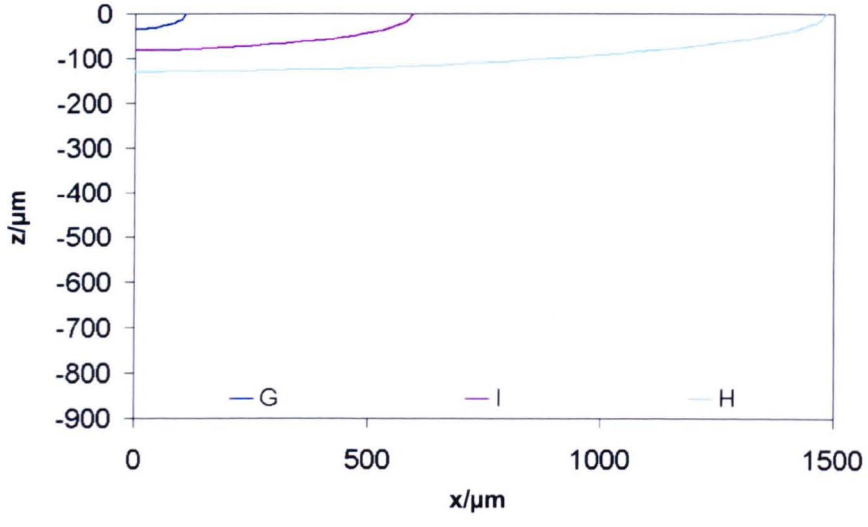

(c)

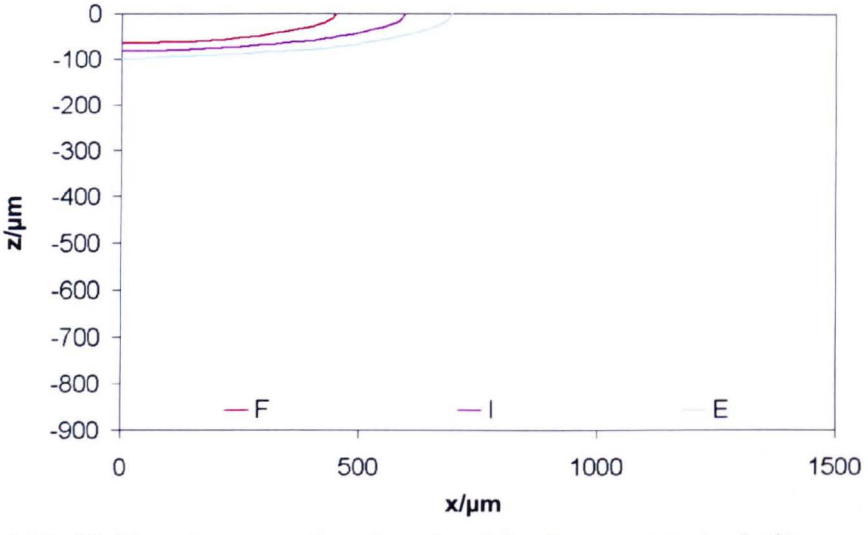

Figure 4.23 - Weld pool cross-sections (x-z plane) for the power and velocity experiment performed using EOS M270. The effect of Power at constant Vb (b) and velocity at constant Power (c) are highlighted. The axes are scaled so that the true aspect ratio is seen. Weld pools are identified by the letters described in Table 4.5.

All of the calculated melt pools have a large length to depth ratio, i.e. the solidification isotherms are flat. This is apparent in Figure 4.24 where it can be seen that the angle between the isotherm and the z-axis slowly decreases to the rear of the pool before a sudden drop to zero at the end of the pool, when the bottom 20μm of the pool is considered (the height of one layer during optimum building) the pools all have an incline relative to the z-axis that is greater than 75°.

(a)

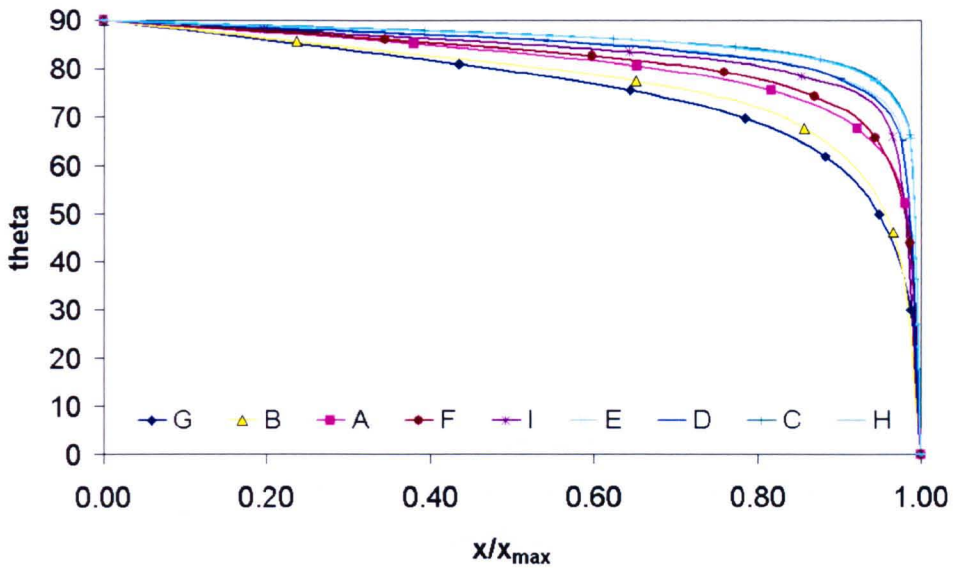

(b)

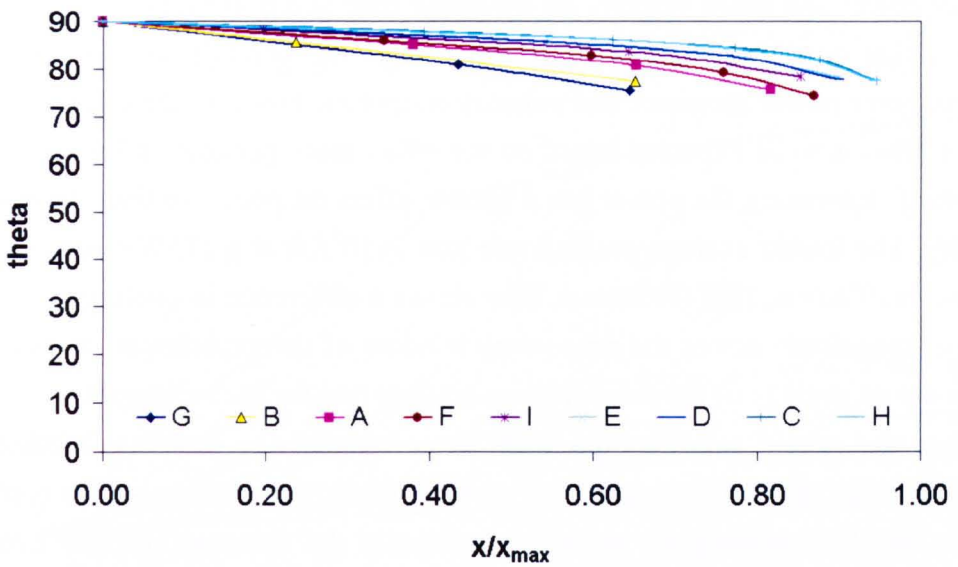

Figure 4.24 – Angle, θ, in degrees of the solidification isotherm along the length if the meltpool. Total pool (a) bottom 20μm of the pool (b)

4.4 Analytical modelling of solidification conditions

Having previously established meltpool geometries and fitting parameters for the parameter sets used to melt the single tracks it is possible to calculate the solidification conditions for the experiments. The cooling rate, temperature gradient and isotherm velocity were obtained using Equation 4.9, Equation 4.10 and Equation 4.11 (from Bontha 2006a described in Section 2.5).

$$\frac{\partial T}{\partial t} = \left(\frac{\alpha Q v_b^2}{4\pi D k r}\right) e^{\frac{-v_b(x+r)}{2D}} \left(1 + \frac{x}{r} + \frac{2xD}{v_b r^2}\right)$$

Equation 4.9

$$|\nabla T| = \left(\frac{\alpha Q v_b^2}{4\pi D^2 k}\right) \sqrt{G_x + G_y + G_z}$$

Equation 4.10

$$V_{iso} = \frac{\left(\frac{\partial T}{\partial t}\right)}{|\nabla T|}$$

Equation 4.11

The average cooling rates calculated for the experiments are plotted as a function of laser power and beam velocity on a contour map given in Figure 4.25. Here it can be seen that over the range of parameters tested the cooling rate decreases as the nominal laser power increases and velocity decreases, however the effect of power is greater. This is to be expected based on the effect these parameters have on the weld pool sizes; increasing the power has a greater effect on pool size than decreasing the velocity. The lowest average cooling rate was $3x10^5$K/s at a 175W-600mm/s and the highest $4x10^6$K/s at 78W-700mm/s. This shows a difference in cooling rate over one order of magnitude across the processing window of the experiment, however, these values are an average of the solidification cooling rate for each example.

When the whole solidification front is considered the problem becomes more complex as can be seen in Figure 4.26. At the bottom of the weld pool the cooling rate is zero which represents the point where locally the material changes from being heated and melted to the solidifying region behind the heat source. The cooling rate rapidly increases along the solidification front towards the rear of the pool where the maximum cooling rate is seen, hence there exists a large variation in the local solidification conditions within the solidifying region.

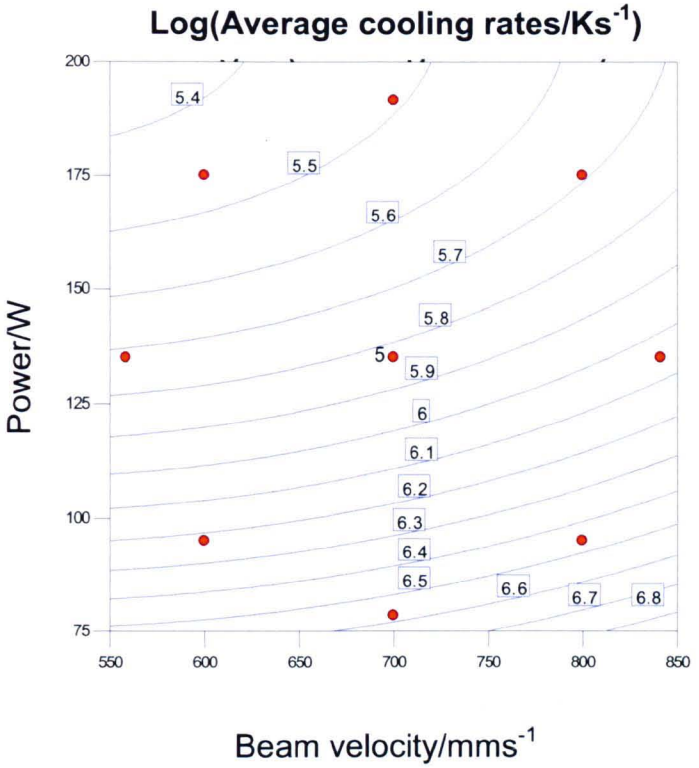

Figure 4.25 – Average cooling rates (log scale) calculated at various power and velocity combinations. Cooling rate decreases as power increases and velocity decrease but power has a greater effect.

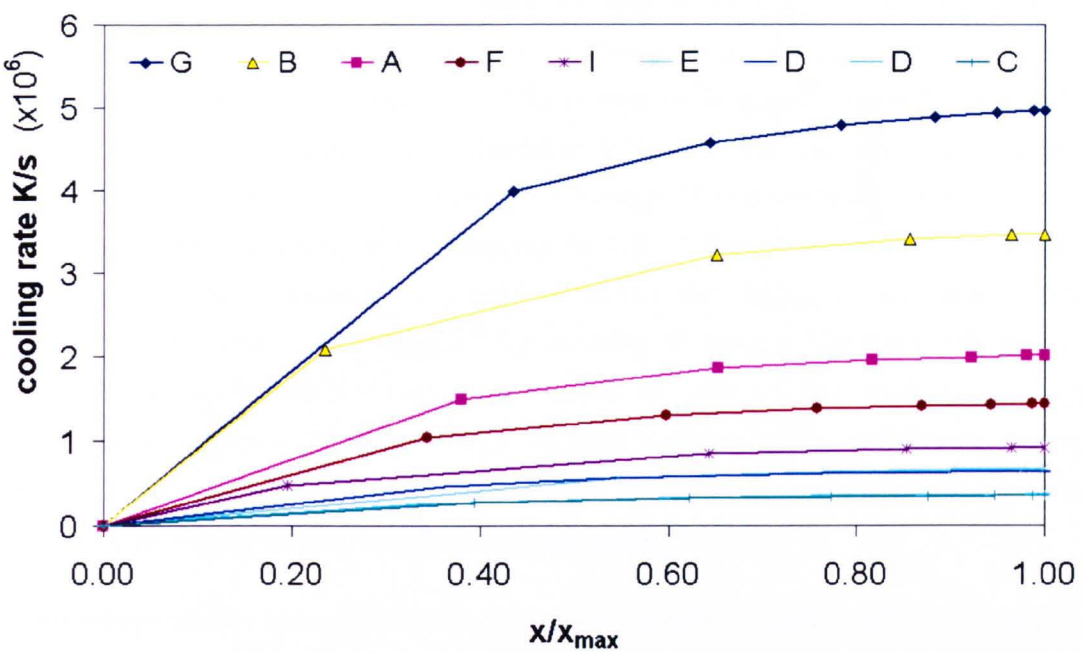

Figure 4.26 - Cooling rates along solidification front from the bottom to the rear of the melt pools

The temperature gradients calculated are shown in Figure 4.27 and Figure 4.28. The temperature gradients across the experiments range from $6.5x10^6$ to $2.4x10^7$K/m with the lowest occurring for tracks melted at high powers and slower beam velocities and lower gradients for tracks with low powers and high velocities. This clearly coincides with the high-energy parameter sets producing larger melt pools. The high values of temperature gradient observed over the experiment window are indicative of additive manufacturing systems which use a localised heat source combined with a substrate which acts as a very efficient heat sink.

The temperature gradient is highest at the bottom of the melt pool and decreases along the solidification front to the rear of the pool. This represents an increasing distance from the heat source. The smaller pools associated with the low energy input parameter sets show a greater rate of change in temperature gradient from the bottom of the melt pool to the rear, this represents the increased curvature of the pool compared to the high energy input parameters which produce not only larger but flatter pools with a more unidirectional transfer of heat.

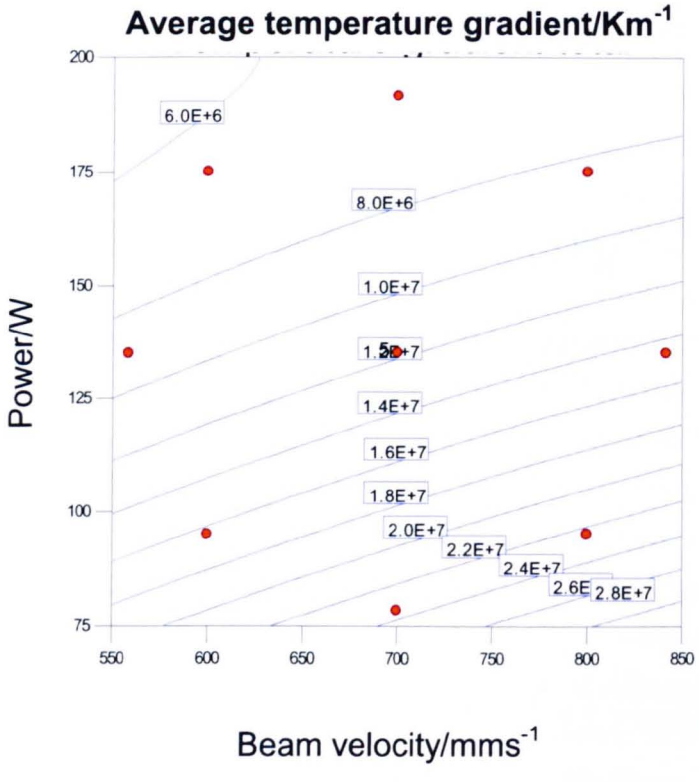

Figure 4.27 - Temperature gradients calculated at various power and velocity combinations

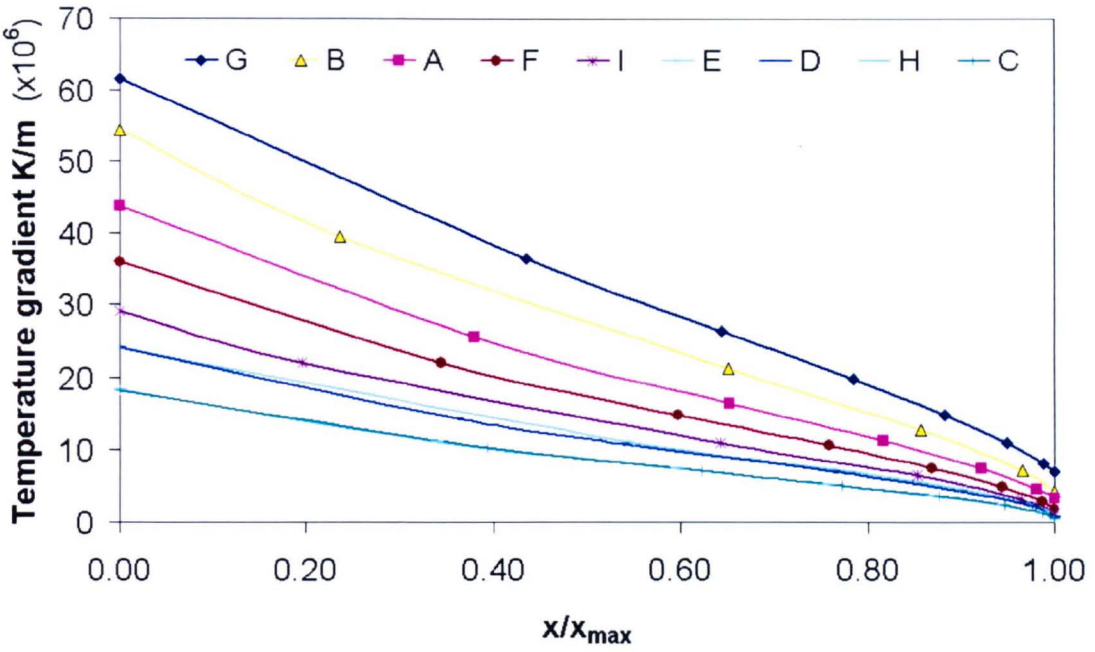

Figure 4.28 - Temperature gradients along solidification front from the bottom to the rear of the melt pools

The isotherm velocity completes the conditions necessary to describe solidification. The velocity is not solely defined by the velocity of the heat source so it is important to distinguish between the two. This is shown in Figure 4.29 where it can be seen that the laser power also affects to the average isotherm velocity; at a constant beam velocity the isotherm velocity decreases with increasing power. This is due to the changing shape of the pools across the different parameter sets. The larger pools are longer and flatter so the direction of heat transfer is greatly altered compared to the beam travel direction, this was highlighted in the previous section where the angle of the solid liquid interface was compared to the axis of motion of the laser.

The calculated isotherm velocities range from 0.15 to 0.31m/s which are as low as a quarter of the beam velocity. Figure 4.30 shows the change in isotherm velocity along the solidification front and makes it possible to see that the flat pools result in relatively slow isotherm velocity for a large section of the melt pool. Layer thicknesses are typically 20μm so only a very small region of the solidifying material is retained after melting of the following layer. This region coincides with the very slow isotherm velocities and very high temperature gradients.

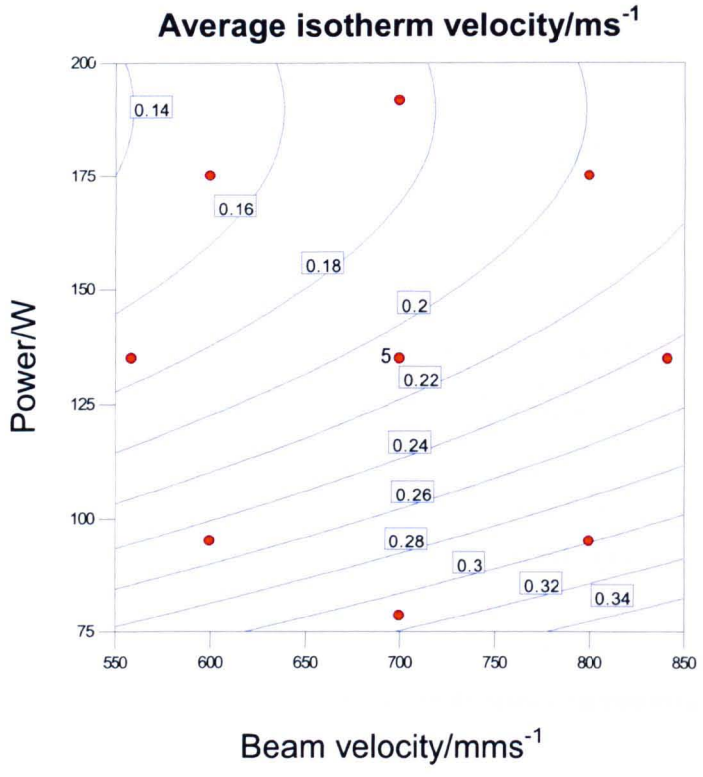

Figure 4.29 - Isotherm velocity calculated at various power and velocity combinations

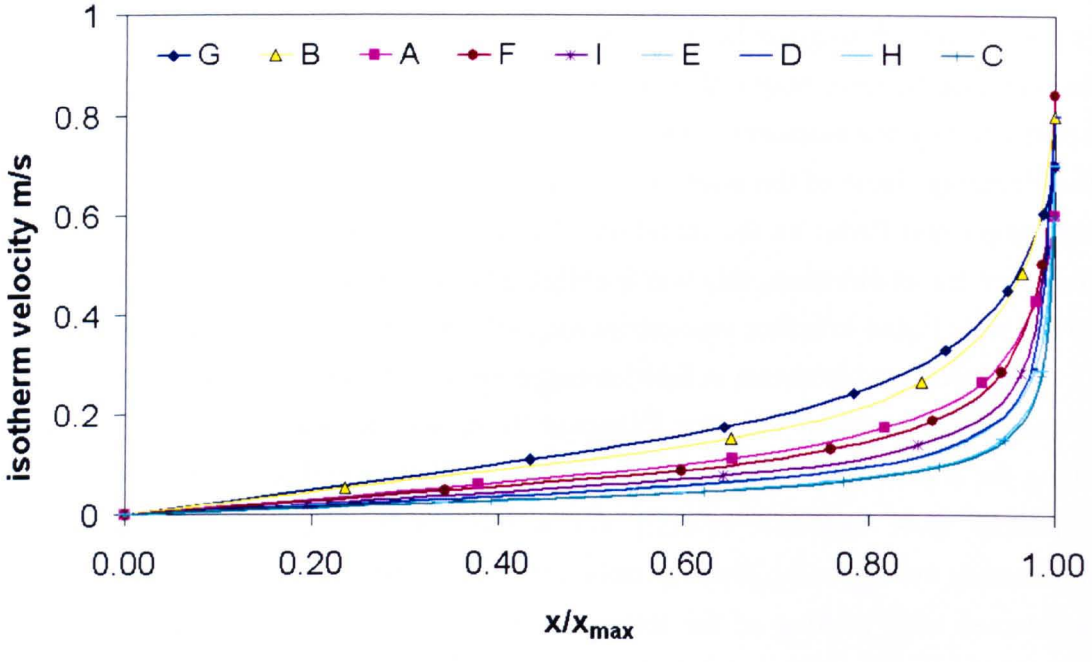

Figure 4.30 - Isotherm velocity along solidification front from the bottom to the rear of the melt pools

Having calculated the solidification conditions it is possible to plot these against the columnar to equiaxed transition (CET) criteria described in Section 2.2.3

(Gäumann 1999a, Kurz 2001) to give a microstructure selection map. This is shown in Figure 4.31 where the calculated solidification conditions across the experimental window are plotted for different positions along the solidification front. The calculated solidification conditions bridge CET with the bottom of the melt pools appearing in the columnar regime and the rear of the pool in the mixed or equiaxed regime. The high energy input parameters (high power, low velocity) are closer to the mixed/equiaxed regime compared to the smaller pools produced at lower heat input.

The effect of increasing power is to move the solidification conditions down and left on the map in Figure 4.31 and has a greater effect than decreasing the beam velocity. However, it can be seen that the limits of the columnar to equiaxed transition also slope down and to the left which would suggest that a large decrease in temperature gradient is the most effective way to achieve a change in the solidification conditions. The most effective way to affect such a change is shown to be an increase in laser power in Figure 4.27; however this is also shown to reduce the isotherm velocity, especially when just the bottom section of the pool is considered.

The effect that these processing parameters have on the as-deposited metal microstructure is dealt with in the next section.

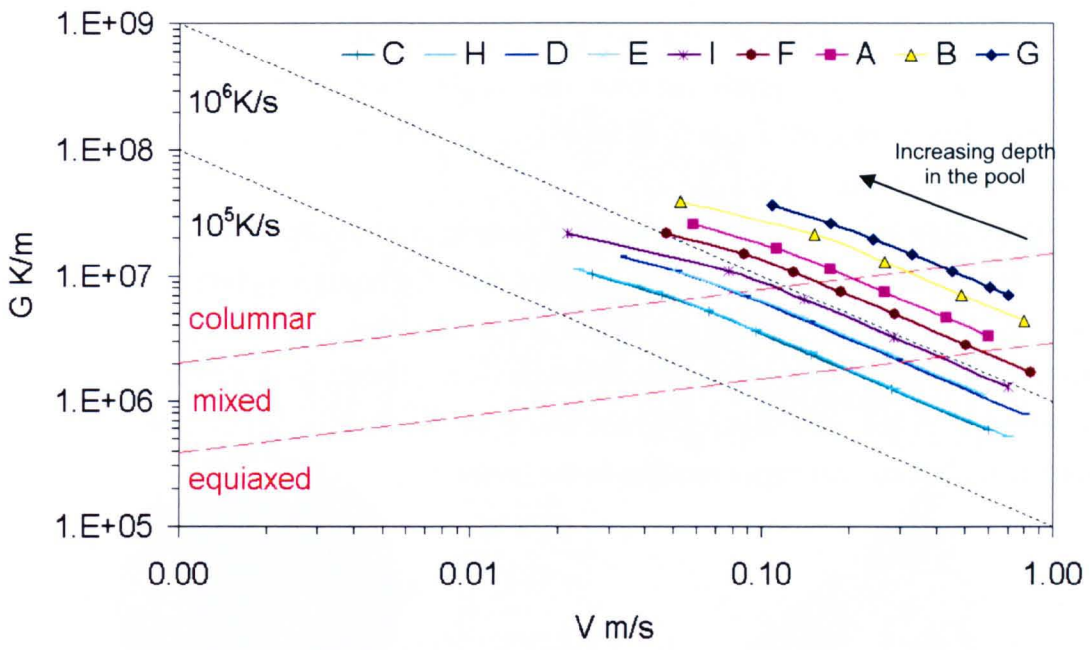

Figure 4.31 - Temperature gradient vs. isotherm velocity along the solidification front for the laser power and beam velocity combinations tested. Red dashed lines represent columnar to equiaxed transition and black dotted lines show iso-cooling rates.

4.5 As-deposited metal microstructures

The as-deposited microstructures were investigated by Electron Backscatter Diffraction (EBSD) to determine the grain structure of the Inconel 718 cubes built over the range of parameters described in Table 4.5. EBSD was necessary to reveal the grain structure as the rapid solidification which takes place means that segregation is restricted to the inter-dendritic region which makes chemical etching and SEM backscattered imaging ineffective.

No observable difference was seen across the samples, with all showing similar structures with fine grains which are elongated in the vertical direction (or the 'z' or build direction).

Figure 4.32 shows an Orientation Imaging Map (OIM) of the vertical section of sample F. The OIM colouring shows that the grains are strongly orientated in the (001) direction, this is confirmed by the pole figure and the Multiple of Uniform Distribution (MUD) value of 6.23 times random. The side wall of the cube was also sectioned as can be seen in Figure 4.32, in this region there are very fine grains on the outer edge which are a result of contact with the surrounding powder in the bed which provides nucleation sites. Moving away from the sidewall into the contour region of the material there appears to be a a very large single grain. The grain boundary image reveals that this large grain contains low angle grain boundaries (LAGB) which suggests that it may be a group of finer grains with very similar orientations rather than one large grain.

Figure 4.33 shows a similar section of sample B at the bottom of the cube where the support structures (seen as the protrusion from the bottom surface) meet the down-facing surface. In this 250μm region the grains are more randomly orientated before the faster growing (001) grains start to dominate to give the bulk a strong texture. This is reflected in the pole figures which show an increase in MUD from 3.17 at the bottom surface to 7.01 times random in the bulk.

4.5.1 Vertical Plane

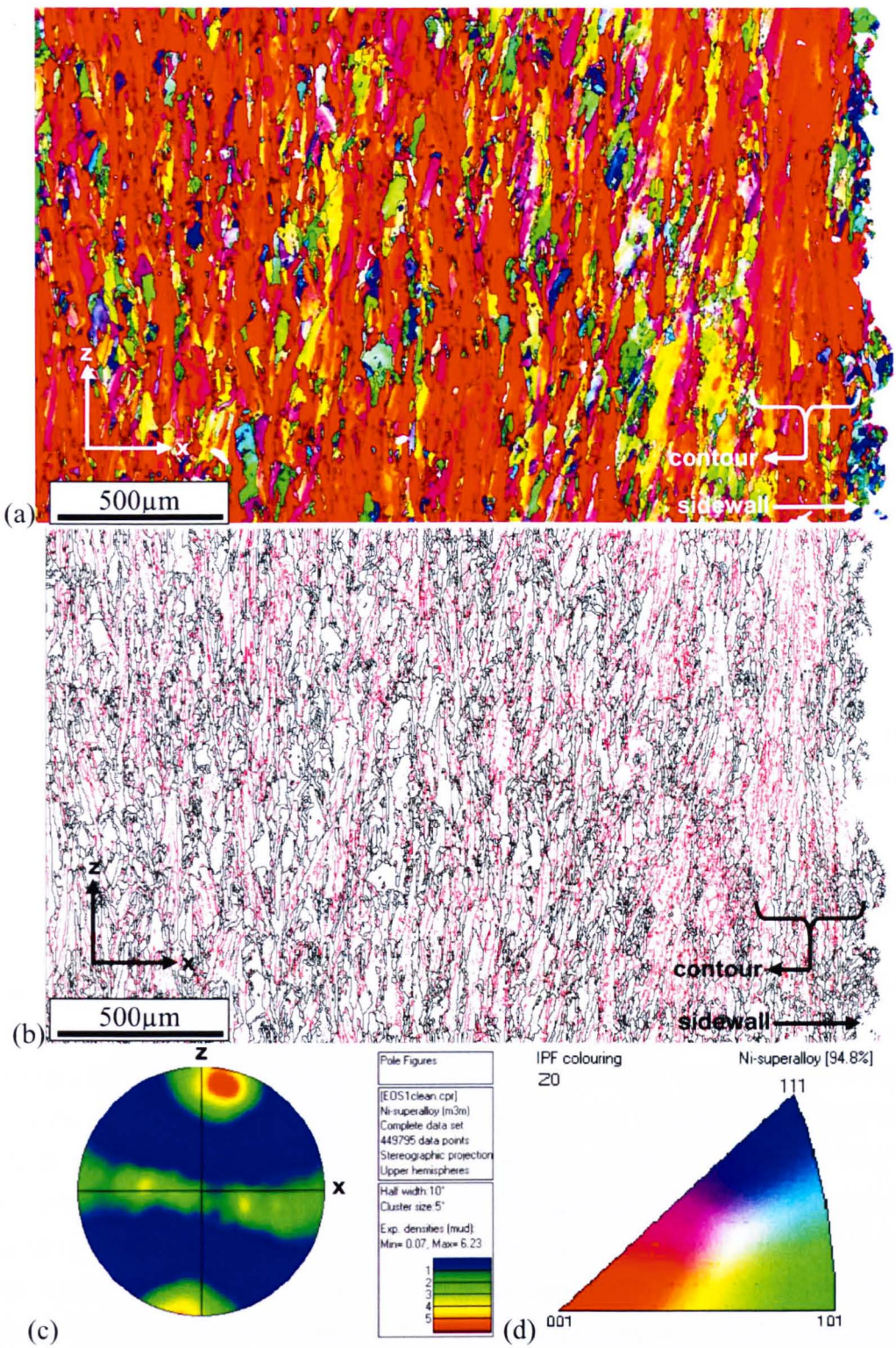

Figure 4.32 - Vertical section of sample F (a) OIM (b) grain structure showing high (black) and low (red) angle grain boundaries (c) (001) pole figure showing strong texture in the z direction (build direction perpendicular to powder layers) (d) IPF colouring in z for OIM, 94.8% is the amount of successful indexing across the observed area.

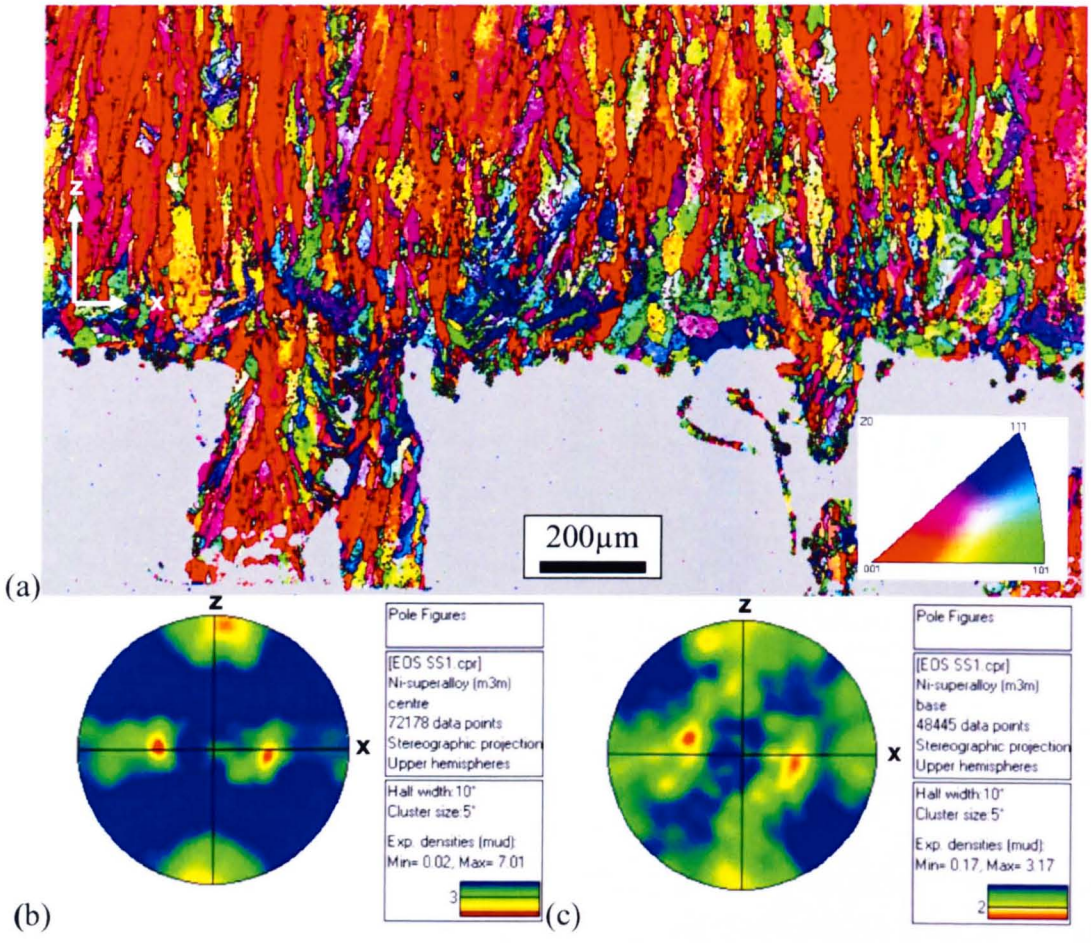

Figure 4.33 – Vertical section of sample B including downward facing edge and support structure (a) and (001) pole figures for the bulk (b) and bottom surface (c).

Sample I is shown in Figure 4.34 having been sectioned in the horizontal plane (xy). In this plane the grains are round as opposed to the long columnar grains observed in the vertical section. The sample has a strong (001) texture indicated by the red colouring, this is also shown by the pole figure which does not show any evidence of a preferred rotation of the directional grains. Two regions are highlighted in the horizontal sections shown in Figure 4.34; A and B. A is in the area of the skin/core interface which is a region where the laser changes direction during hatching, in this area the local heat input is greater than in the steady state region because of the increased interaction time of the laser. Here the melt pool will be larger than normal (Hofmeister 1999) and the direction of heat transfer will change so that the direction of grain growth can be altered. This can be seen in region A where the (001) texture is disrupted in a 200µm wide band, which may have implications for mechanical properties as such a regular microstructural abnormality could provide a continuous weakened path for cracks to propagate. The highlighted region B shows a fine grain structure where the contour hatching occurs.

4.5.2 Horizontal plane

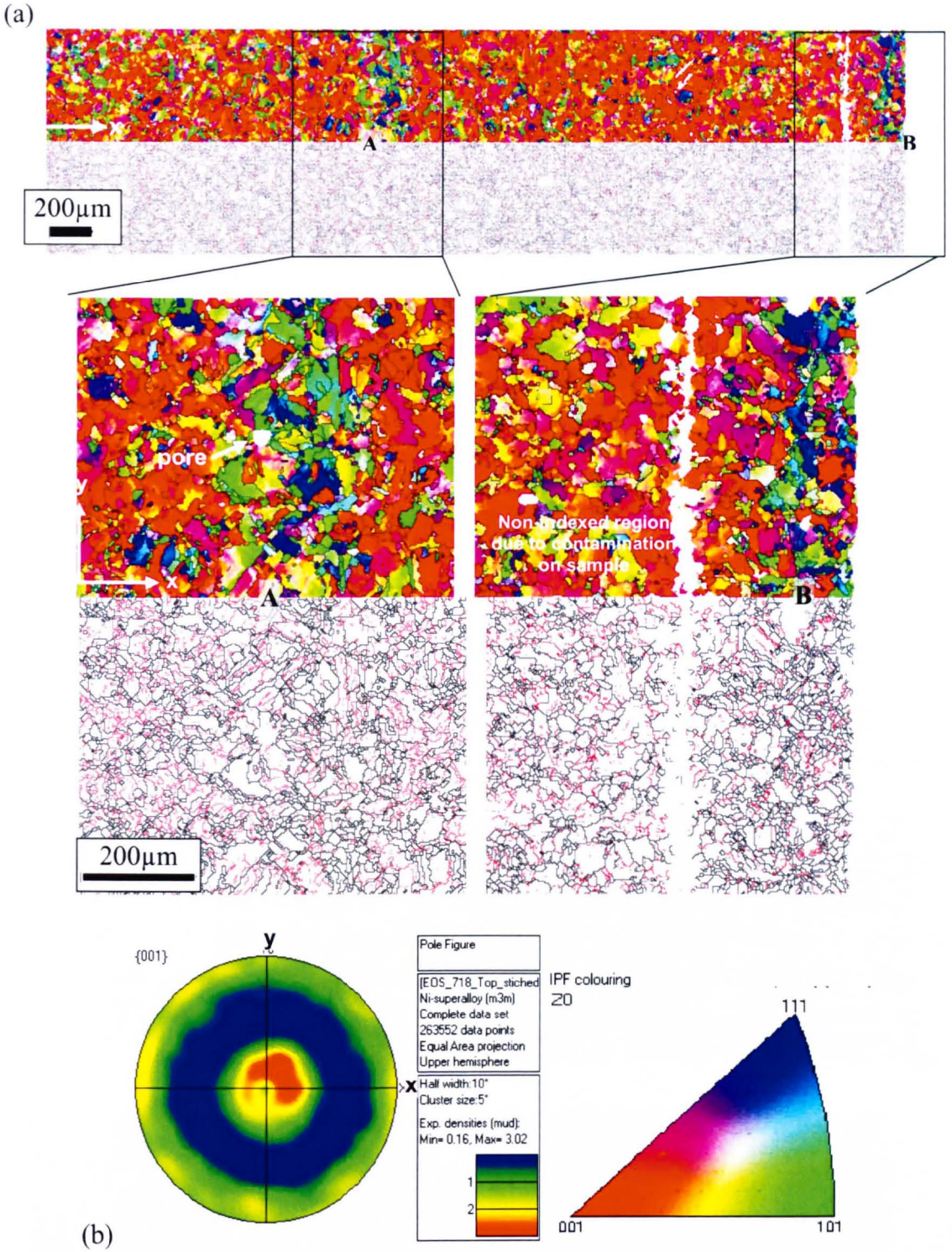

Figure 4.34 – (a) Sample I in the horizontal section regions A and B are highlighted to show changing in orientation caused by the changing direction of the beam (A) and the contour hatching (B). (b) Pole figure for the horizontal plane across the whole sample showing strong (001) texture.

4.5.3 Grain structure

The typical grain structure observed across the range of samples built is shown in Figure 4.35 where high angle grain boundaries (HAGB) are shown as black lines and low angle grain boundaries (LAGB) as red lines. The grains appear mostly very fine in the horizontal section with some larger grains whereas in the vertical section the grains show a high aspect ratio with elongation in the build direction. Within the larger grains there is often a network of LAGB which suggests that they could be individual grains with very similar rotational orientation.

The columnar-type grains suggest the modelled melt-pools in Section 4.2 are accurate as the flat pools would result in almost unidirectional heat transfer to the underlying material and hence the direction of grain growth in the molten pool would be vertical. Since the liquid metal is the same composition as the base material, there will be good wetting between the solid and liquid regions. This implies that there will be little if any nucleation barrier on solidification and hence little undercooling, this will lead to solidification occurring epitaxially, and atoms at the solid-liquid interface will be arranged in the orientation of the underlying grains at the interface (Porter 1988). These observations also support the microstructure selection map in Figure 4.31 which predicts that the solidification conditions at the bottom of the melt pool will lie in a columnar regime.

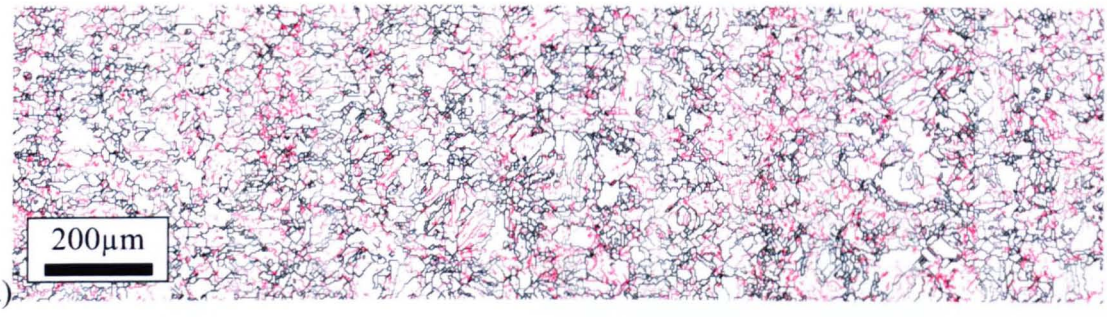

(a)

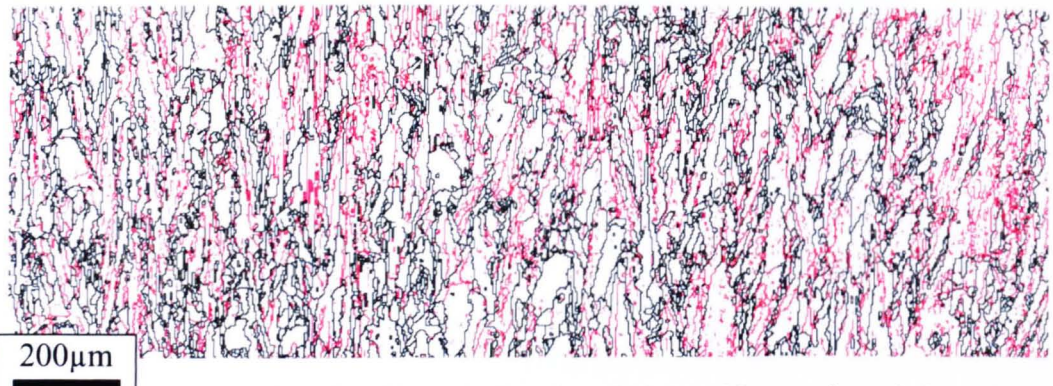

(b)

Figure 4.35 – (a) horizontal section (b) vertical section of high and low angle grain boundaries

4.5.4 EOS chemical analysis

Electron-Probe Microanalysis (EPMA) was used to produce elemental maps (Figure 4.36) and elemental line scans (Figure 4.37) of the samples to test for segregation of key elements.

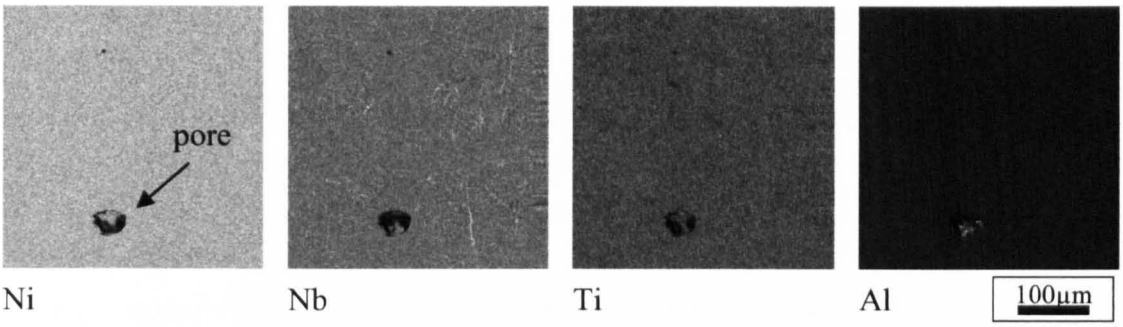

Figure 4.36 – Elemental maps of Ni, Nb, Ti and Al for Sample I. The round, dark defect is a pore in the skin/core interface region of the block built.

The elemental maps in Figure 4.36 show no clear segregation of Nb, Ti or Al at the resolution of the maps. No elemental segregation was observed at grain boundaries nor was there any evidence of higher concentration of the three elements to suggest the formation of γ' or γ" precipitates greater than the resolution of the equipment used. There is also no evidence of segregation in inter-dendritic regions which is possibly the reason for the difficulty in chemical etching, the degree of etching observed suggested that there is some inter-dendritic segregation but this was not detected by EPMA suggesting the sensitivity was insufficient.

The line scans in Figure 4.37 show there is no obvious difference in element concentration in the total cross-section of the laser deposited block and that the element weight percentages are in line with those for Inconel 718 listed in Table 3.1.

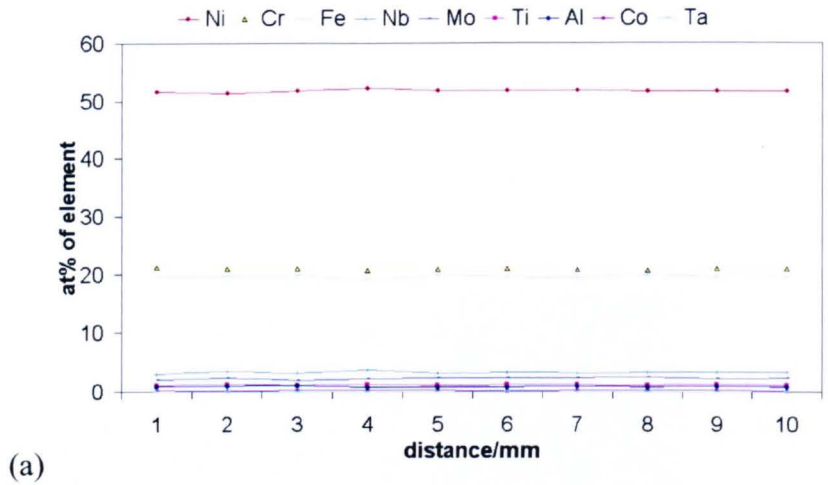

(a)

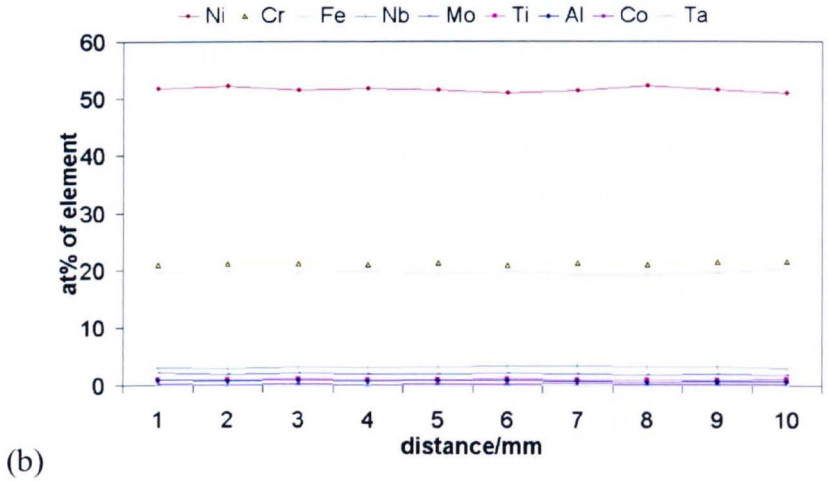

(b)

Figure 4.37 - Line scans (a) centre to edge of cube (b) bottom to top of cube

4.6 Hardness

Vickers hardness measurements were carried out on the Inconel 718 samples built in the EOS M270. The hardness did not vary appreciably across the experimental window with hardness values of 350±10Hv. The results for Samples G and H are shown in Figure 4.38 and compared to values of wrought Inconel 718 given in the CES Selector 2008 database (Granta Design, Cambridge, UK). The values for the as-deposited Inconel 718 built on the EOS M270 are approaching the lower end of the reported wrought values before receiving a solution heat treatment and precipitation aging. Further work is necessary to test the response to aging heat treatments of the laser deposited materials and also to investigate the effect, if any, of the Nitrogen atmosphere during building but this was beyond the scope of this investigation.

Figure 4.38 also shows hardness values of laser deposited Inconel 625 (Ni 58% min, Cr 20-23%, Fe 5% max, Mo 8-10%, Nb+Ta 3.15-4.15%) which was built using the EOS M270 as part of a student project at The University of Sheffield (the author acknowledges Martyn Jones, Masters student under the supervision of Dr Iain Todd for this work). These hardness values were shown to be consistent across the horizontal cross-section of the sample geometry and were in excess of the reported values from the CES 2008 database.

Inconel 625 is a Nickel-Chromium alloy with high strength and corrosion resistance It is solution strengthened by additions of Molybdenum and Niobium (Special Metals 2006) as opposed to a precipitation strengthened alloy like Inconel 718 and so no aging treatment is usually practised. The increased hardness compared to the reported wrought values indicates that there may be cause to further investigate the microstructure of such alloys to identify the reasons behind this, which could be residual stresses in the parts, an effect of the Nitrogen atmosphere or potentially a microstructural effect from the rapid solidification experienced from the laser melting process.

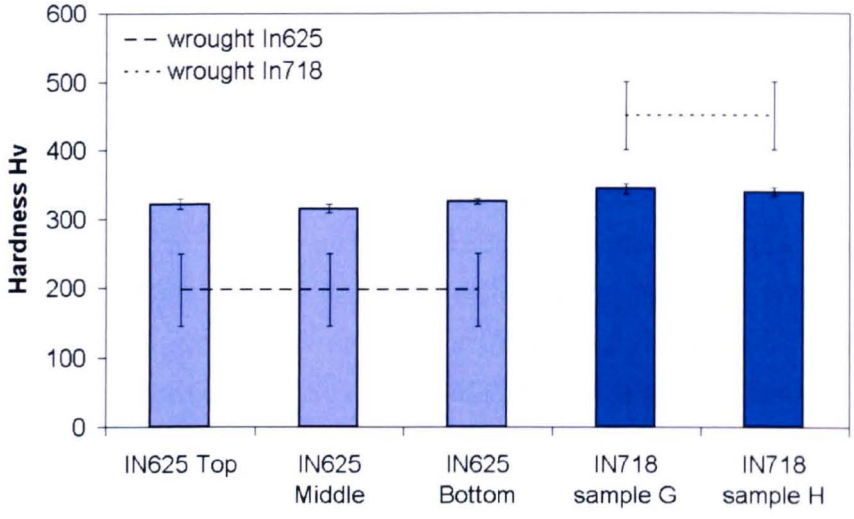

Figure 4.38 - Average Vickers hardness values for laser deposited Inconel 625 and Inconel 718 in the as-deposited state. Dotted and dashed lines show average wrought values for the alloys and error bars show the range. The error bars on the measured hardness values show the 95% confidence interval.

4.7 Chapter summary

A processing parameter theme was developed and an investigation into several Key Process Variables was carried out on laser melting of Inconel 718 Nickel-Iron-Chrome superalloy using an EOS M270. The effect of processing parameters on the geometry of individual weld tracks was investigated to determine an operating window. The weld tracks were considered as the building blocks of 3D parts in ALM so understanding the effect of processing parameters on tracks is crucial when developing a new material theme. A processing window was defined to successfully build simple geometries in Figure 4.6 which shows it is possible to build over a range of parameter combinations. However, the fastest processing parameters to use (in terms of area melted per second) while maintaining a sufficient melt depth are; laser power 195W, beam velocity between 950 and 1100mm/s and a track offset between 0.1 and 0.12mm.

Power, velocity and beam diameter were shown to be most important for determining the track geometry; high power and low beam velocity produce wider pools for small beam diameters but velocity has little effect on width when the beam diameter increases to be larger than the pool width. When the pool is larger than the beam diameter a temperature gradient on the top surface is produced which provides a driving force for a surface tension differential which drives Marangoni convection. When Marangoni convection takes place the width of a weld pool is exaggerated when compared to a pool in which conduction is the dominant heat transfer mechanism. The depth of the melt tracks is dependent on power and velocity in a similar fashion but at larger beam expander settings i.e. larger beam diameters, the effect of power is reduced.

Knowing the effect of heat input on track geometry then allows the inter-track distance or track offset to be set so that a consistent melt depth in a layer can be achieved. This forms the basis of a theme to build simple geometries using an ALM system.

The thickness of the powder layer used and the overlap of adjacent hatching regions are most important for removing porosity. The porosity increases with layer thickness but for a given thickness high power/high velocity parameter sets were shown to reduce the porosity, if a higher power laser was used there may be scope to use thicker layers than the optimum 20μm typically used on an EOS M270. It would be favourable to use thicker layers to reduce build time, to put this into perspective; 20μm is roughly one fifth the thickness of a sheet of printer paper.

Statistically designed experiments were used in the form of two and three factor Central Composite Designs. This was successful in accurately fitting empirical (first, second and interaction) models relating weld track geometries and surface roughness to key process parameters. From these models it was possible to produce processing maps to select parameters suitable to build fully dense parts as well as maximise build speed. DOE has been shown to be an efficient way to conduct experiments by extracting lots of information from relatively few trials.

Analytical heat transfer models were used to model the solidification front by fitting the models to the experimental measurements; all of the modelled pools were seen to have a high aspect ratio being shallow and long. The models were extended to the solidification conditions (cooling rate, temperature gradient and isotherm velocity) to establish how these vary along the solidification front and with processing parameters; it was shown that high power/low velocity parameter sets result in lower cooling rates, lower temperature gradients and lower isotherm velocities. The models were used to plot processing maps and also compared to existing columnar to equiaxed transition criteria to give a microstructure selection map as a function of laser power and velocity.

The microstructure of the as deposited metal samples were analysed by EBSD to reveal the grain structure, sub-structure and texture. The samples' grain structure did not vary over the region of interest in the process window, all showing a highly directional columnar structure with a strong (001) orientation. If it is desirable to avoid columnar structures then alternative measures need to be considered such as higher powder lasers or a heated build chamber to generate larger melt pools and reduce temperature gradients. EPMA showed no discernible segregation in the samples but chemical etching did show a dendritic solidification structure which suggests that some degree of microsegregation that was not detectable at the resolution of the EPMA.

Vickers hardness values were consistent across the samples built during the experiment and lower than values reported for wrought processes. This combined with the EPMA results suggests that a super-saturated solid-solution is produced by the EOS M270 due to the rapid solidification rate of the process and segregation of elements to form secondary phases such as strengthening precipitates is avoided. Post-process heat treatments are necessary to precipitation harden the as-deposited Inconel 718 to obtain optimum strength, this was not tested as part of the investigation.

The consistent hardness values and observed microstructures show that the ALM process is very robust when operating within parameters which produce fully dense parts. The speed at which an area is melted is limited by the need to avoid porosity as maintaining a consistent melt depth requires either slowing down the beam velocity to

use a wider beam offset or reducing the beam offset to increase the beam velocity; these counter-act each other. What this robustness does mean is that changing parameters to control other issues such as residual stresses should not affect the as-deposited microstructure or compromise properties.

5 Results and discussion – DMD

The work in this section focuses on the DMD 505 blown powder laser deposition system and was carried out at TWI: The Welding institute. The work centres on thin walled structures which are used in the repair of aerospace components to extend their life cycle. To this end, the approach used in this section differs slightly from that used in Chapter 4 on the powder bed EOS M270 system as there is no need to develop starting parameters for a processing theme; this information was previously established at TWI.

Blown powder systems have, to date, been more widely used to for their potential in 'freeform' processing as the deposition process is controlled by a five-axis system as opposed to a pre-placed powder layer method. This has meant considerable work has been carried out using these systems for weld-repair or cladding application for which freeform fabrication of whole parts forms a logical extension. The effect of processing parameters on track overlap and melt depth is applicable to bulk (3D) part production, but single track thin walls have no such overlapping features so in this section the focus is on those processing parameters influencing individual track geometry.

5.1 Melting response to Key Process Variables – track geometry

The process parameters under investigation are laser power and velocity; other parameters which may affect track geometry are the flow rate of the powder and the beam diameter. Flow rate and beam diameter were kept constant and are not considered in this study as the aim if the next stage of the investigation was to consider simple analytical heat transfer models which involve only the absorbed laser power and velocity to model the solidification conditions and form the basis of a microstructural investigation.

Statistical design of experiments was used in the investigation in the form of a two-factor central composite design (CCD) comprising a 2^2 full factorial with four axial points and 5 centre point repeats. The design matrix for the experiment is given in Table 5.1 along with the measured track widths and the walls can be seen in Figure 5.1. Widths were measured by sectioning the walls in the xz-plane and observed under optical microscopy; an average of 10 measurements is reported. The wall samples built are referred to in this chapter by their respective 'standard order' number indicated in Table 5.1.

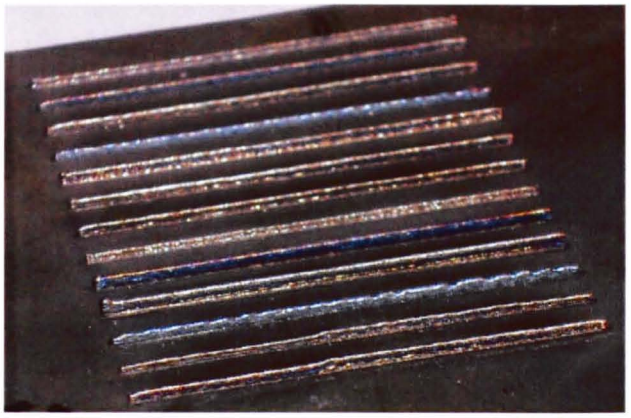

Figure 5.1 – thin wall samples producedon DMD 505.

The raw data is plotted in Figure 5.2, the track width exhibits a strong power divided by square-root velocity relationship in line with results reported by Olivera et al. and Meacock et al. (Olivera 2005, Meacock 2008). Table 5.2 shows the ANOVA data for the fitted model after linear regression was performed by the Stat-Ease Design-Expert v6. The data were fitted to a two-factor interaction (2FI) model and the p-value of <0.0001 indicates the model is significant by the F-test at the 5% confidence level. The R-squared and adjusted R-squared values of 0.98 and 0.97 respectively, and the diagnostic plots given in Figure 5.3 confirm the model is accurate and appropriate to describe the track width in terms of the laser power and beam velocity.

Table 5.1 - Experimental design matrix showing the processing parameter window studied and the results of the measured track width. Samples are referred to by their 'standard order'.

standard order	*run order*	V_b *mm/s*	*P W*	x_0	x_1	x_2	*measured width μm*
1	5	13	150	1	-1	-1	296.0
2	1	25	150	1	1	-1	242.5
3	9	13	350	1	-1	1	547.0
4	4	25	350	1	1	1	392.5
5	10	11	250	1	-1.41	0	425.0
6	12	27	250	1	1.41	0	309.0
7	8	19	109	1	0	-1.41	212.0
8	11	19	391	1	0	1.41	525.0
9	7	19	250	1	0	0	337.5
10	6	19	250	1	0	0	343.5
11	13	19	250	1	0	0	376.0
12	2	19	250	1	0	0	342.0
13	3	19	250	1	0	0	351.0

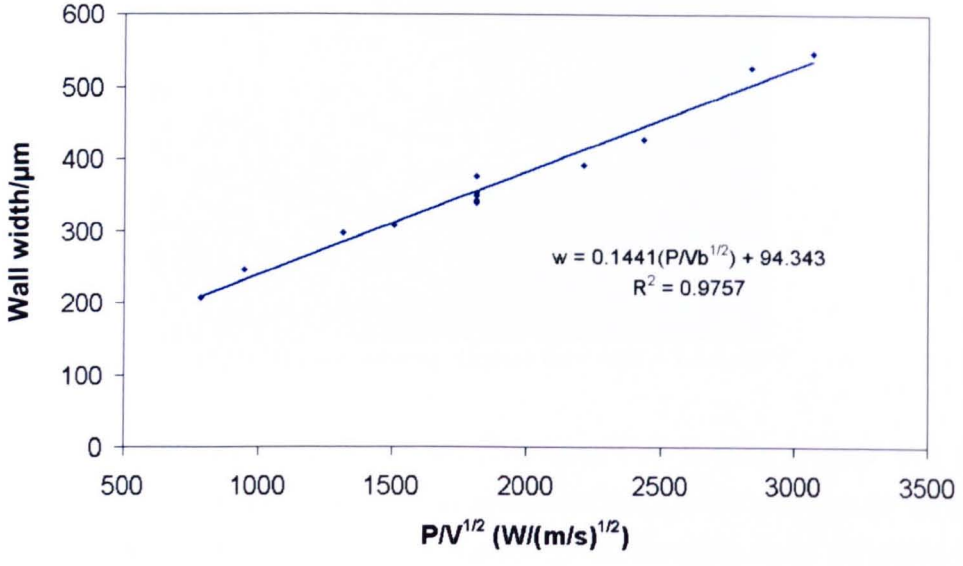

Figure 5.2 - Track width as a function of P and V_b

Table 5.2 - ANOVA table for two-factor interaction model describing track width as a function of P and V_b

Source	*Sum of Squares*	*Degrees of Freedom*	*Mean Square*	*F Value*	*Prob > F (p-value)*
Model	108820.70	3	36273.57	131.98	< 0.0001
x_1	17302.54	1	17302.54	62.96	< 0.0001
x_2	88967.92	1	88967.92	323.71	< 0.0001
$x_1 x_2$	2550.25	1	2550.25	9.28	0.0139
Residual	2473.52	9	274.84		
Pure Error	939.50	4	234.88		

R-squared *0.9778,* ***adjusted R-squared*** *0.9704*

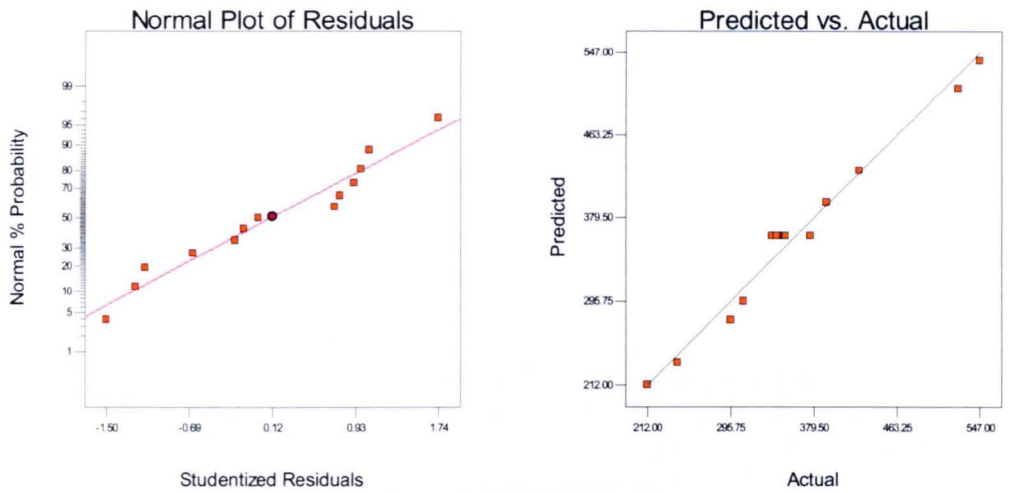

Figure 5.3 - Diagnostic plots for 2FI model describing track width

Equation 5.1 which is plotted as a contour map in Figure 5.4 suggests a strong dependence of width on power and velocity as well as a significant interaction term to account for curvature in the Response Surface. The tracks deposited ranged from 200μm to 550μm ±15μm based on the pure error, wider tracks were observed at the high power low, velocity parameter sets as the energy input and interaction time of the heat source increase and more powder is delivered into the melt pool per unit time. Such a contour map is useful in understanding how different parameter combinations can give a track of equal width, which makes it possible to alter laser power to account for decreasing velocity as the beam changes direction during processing. As discussed in the following sections of this study there may be consequences relating to the metal microstructure when different parameter sets are used which is vital when such a feedback loop is used to maintain consistent track geometries. This must be fully understood and detailed on processing maps so that the microstructure can be

accounted for throughout the building of a component, especially when we consider properties which are grain size and grain boundary orientation sensitive such as high temperature creep.

$$width = 45.2 + 2.8V_b + 1.9P - 0.04V_bP$$

Equation 5.1

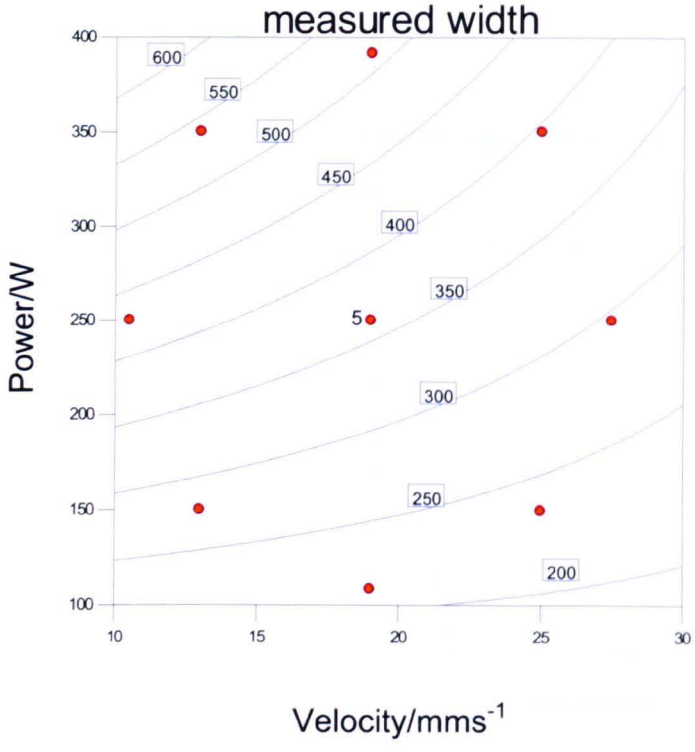

Figure 5.4 - Maps of wall width (μm) as a function of laser power and beam velocity (red spots indicate design points of the central composite experimental design, R-squared=98%)

Assuming circular track geometry, the cross-sectional area of an individual track was calculated based on the width ($width=2r$) measurements taken previously ($area=\pi r^2$). This allowed the melting efficiency of the delivered powder to be determined as a function of processing parameters. These results are given as a contour map in Figure 5.5. The highest melting efficiency was seen to be at higher powers and faster velocities (80 to 90%). Under such conditions the tracks melted do not have the largest cross-section as the powder delivered per unit time is less. The melting efficiency during laser welding of different metals and alloys was reported by Zhao et al. (Zhao 1999) to increase with Rykalin number, Ry. Ry is a dimensionless number used to relate melting efficiency (energy required to melt vs. energy applied) to processing parameters in welding and is proportional to the absorbed power multiplied by the welding velocity; this is shown in Equation 5.2.

$$Ry = V_b r_\infty / 2\alpha$$

Equation 5.2

Where V_b is welding speed in m/s, r_∞ is the steady state pool diameter in m for a given power and α is thermal diffusivity in m^2/s. (Bertram 1996, Elsen 2008)

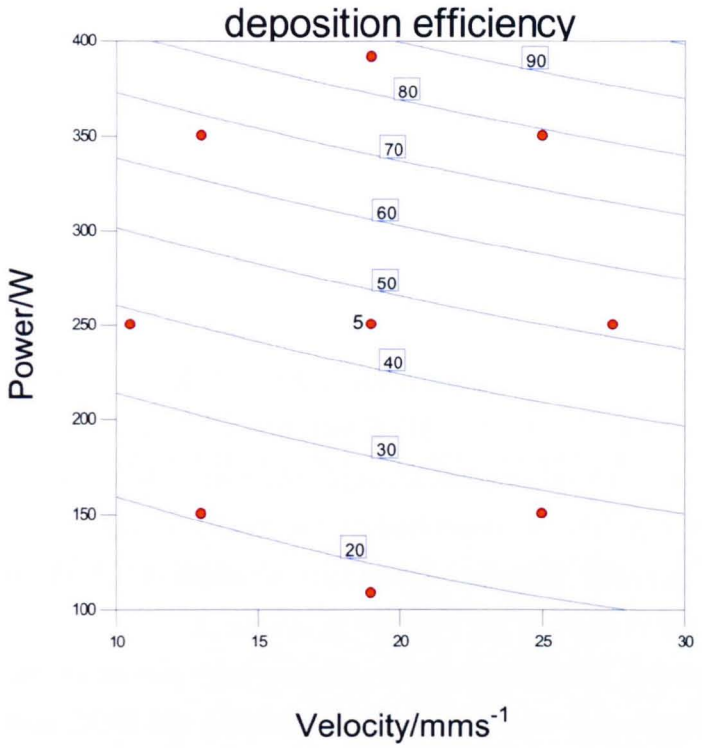

Figure 5.5 - Contour map of melting efficiency (%) as a function of laser power and beam velocity (red spots indicate design points of the central composite experimental design)

Knowledge of how track geometry is affected by imposed processing parameters is important for two key reasons: the size and shape of individual tracks must be understood when developing a deposition theme for bulk samples as the offsets and overlaps used in the hatching technique will control such issues as porosity in bulk components as well as the surface finish in the same manner as previously reported in section 4.1.4 for ALM powder bed deposition. Also, the geometry of a track is needed to calculate solidification conditions and weld pool geometries in order to predict the resulting microstructures; this is discussed further in a later section in context with the observed microstructures.

5.2 Analytical modelling of solidification front

From the Rosenthal solution Equation 5.3 it has been possible to determine the size and shapes of the melt-pools by graphical intercept methods equating the heat transfer equation with the liquidus temperature of Inconel 718.

$$T = T_0 + \frac{\alpha Q}{\pi k b} e^{\frac{-v_b x}{2D}} K_0\left(\frac{v_b r}{2D}\right)$$

Equation 5.3

Equation 5.3 has been shown to be a good approximation for heat transfer modelling of deposition processes; however, as wall thickness decreases to less than 1mm the equation becomes less accurate and over estimates the size of the molten zone. This is based on values of α (the absorption coefficient) reported in the literature to be between 0.15 and 0.2 (Vasinonta 2001, Pinkerton 2006). As previously discussed in Section 4.2 where the 3D Rosenthal solution was used, α is used as a fitting parameter and so takes into account alternative sources of heat loss to the purely conduction heat transfer described by the model. Using α as a fitting parameter also takes into account material dependant absorption which is a function of temperature and wavelength of the incident heat source.

Values for α ranged from 0.09 to 0.13 and vary with power and beam velocity, this can be seen in Figure 5.6 which was obtained using the DOE software to plot the fitted values of α as a function of laser power and velocity. The model is seen to be valid from the diagnostic graphs in Figure 5.7 along with a model p-value of <0.0001 and R-squared and Adjusted R-squared values of 0.995 and 0.994 respectively. A is shown to increase with increasing power and velocity according to Equation 5.4 in a similar way to deposition efficiency (Figure 5.5) which suggests better coupling of the heat source as mentioned previously.

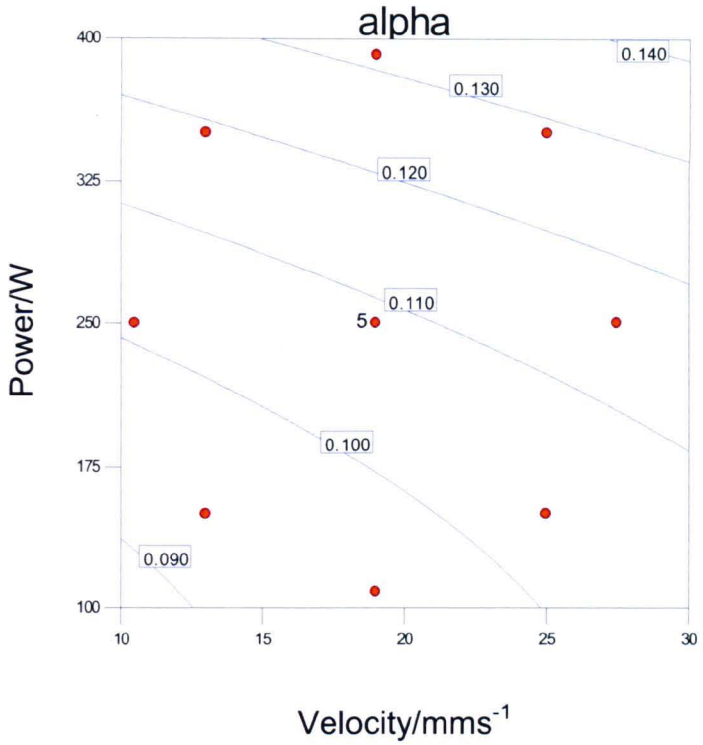

Figure 5.6 - α as a function of laser power and velocity

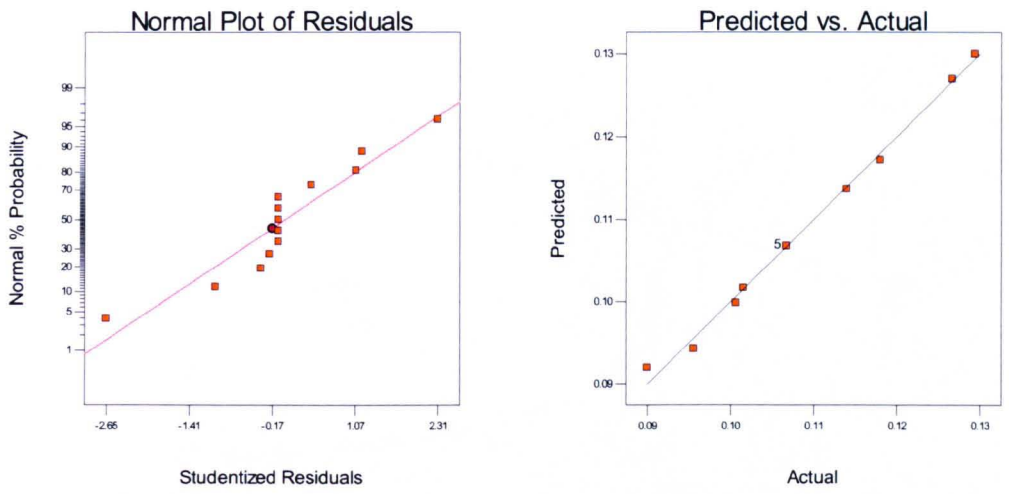

Figure 5.7 - Diagnostic graphs for the model fitted to the values of α obtained

$$\alpha = 0.08 + 0.8\text{x}10^{-3}\, V_b - 7.1\text{x}10^{-7}\, P + 2.68\text{x}10^{-7}\, P^2$$

Equation 5.4

The model derived for α (Equation 5.4) and that for track width determined in section 5.1 can be substituted into the Rosenthal solution (Rosenthal 1946) to determine the solidification front shape and reveal the effect of processing parameters.

It is understood from welding technologies that the shape of a weld pool directly influences grain morphology; flatter pools with straighter isotherms exhibit grain growth in a more unidirectional manner and yield long columnar structures whereas pools which are rounder with curved solidification fronts can break up columnar growth as the grains are forced to change growth direction. A similar theory can be applied to laser deposition, the effect of laser power and beam velocity on the solidification front shape is illustrated in Figure 5.8. Fast speeds and higher powers result in pools with larger aspect ratios, i.e. long solidification fronts relative to the depth, conversely low power/slower speeds give pools with lower aspect ratios. When Energy input is high but interaction time is low, the penetration of the weld pool into the underlying material is reduced.

Figure 5.9 shows the effect of laser power and velocity independently, Power is shown to have a large effect on both pool depth and length whereas velocity has relatively little effect on the pool length but does influence the depth. The interaction effects are not apparent from these observations however.

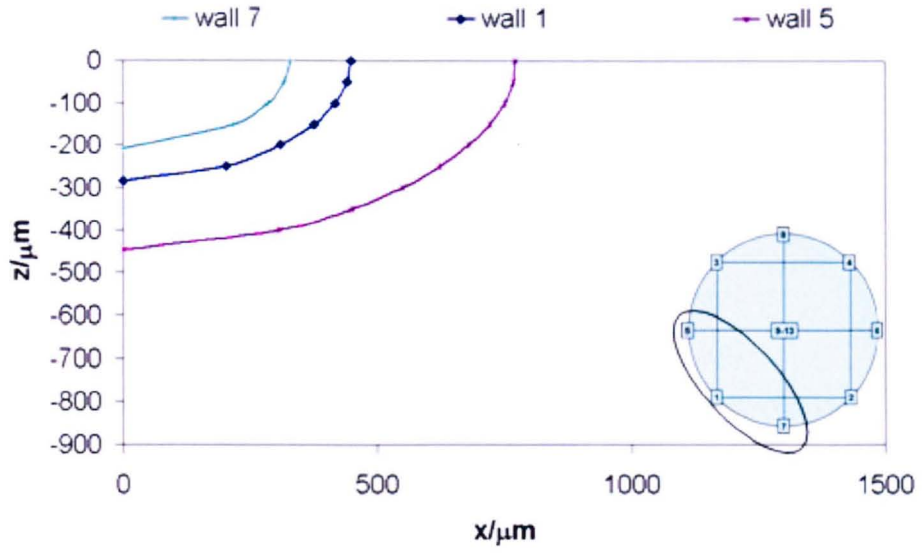

(a)

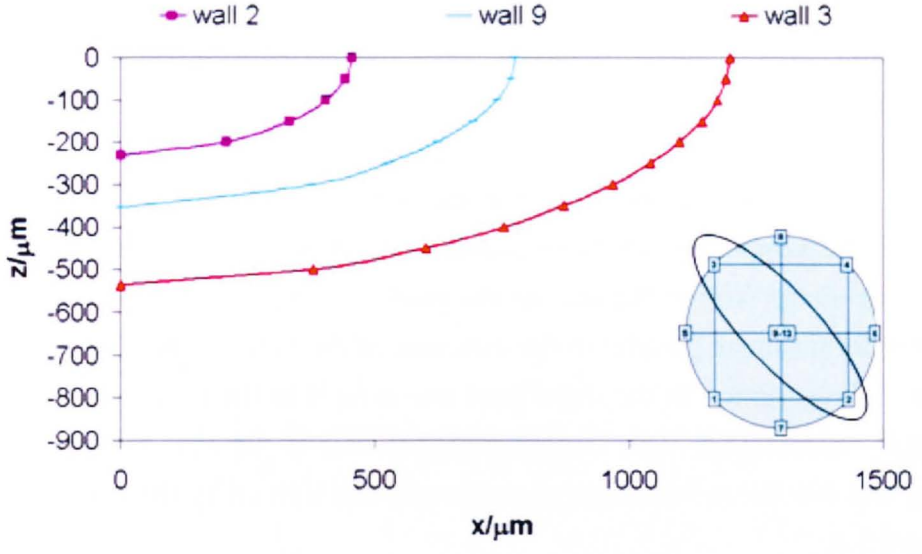

(b)

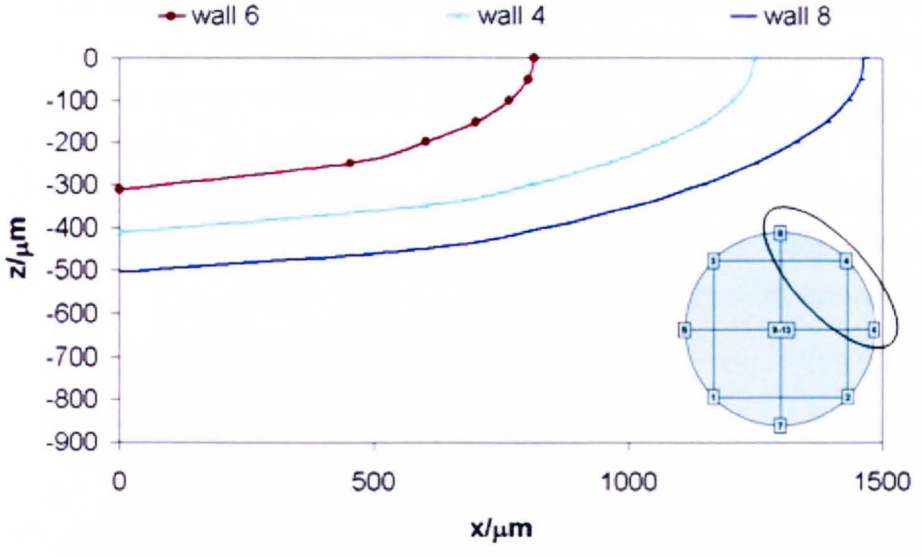

(c)

Figure 5.8 - Solidification front geometries obtained using the Rosenthal solution

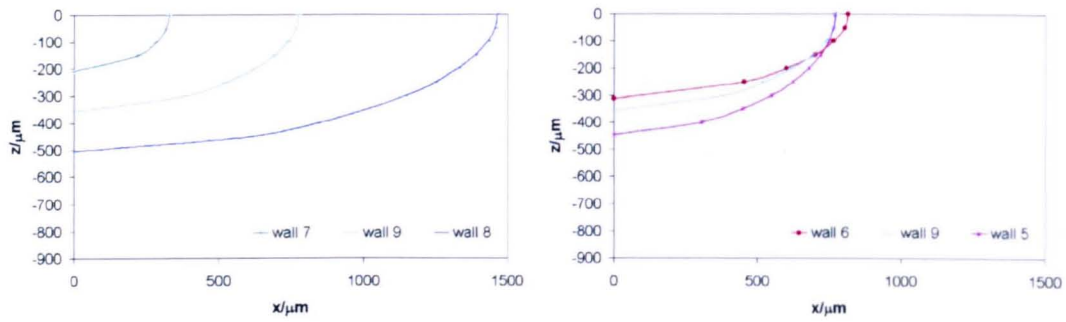

(a) (b)

Figure 5.9 - Effect of Power (a) and Velocity (b) on calculated weld pool shapes

An important measurable feature of the solidification isotherms is its angle relative to the z-axis, i.e. at the bottom of the melt pool this angle is 90° and at the rear it is 0° (cf. Figure 4.24), as this will influence the direction of heat transfer and hence the growth direction of solidifying grains. Since the isotherms are curved it is difficult to quantify them by an absolute value and hence they cannot easily be plot as contour maps, for this reason Figure 5.10 shows the angle of the solidification isotherm and how this varies from the bottom to the rear of the pool. The first graph in Figure 5.10 shows all the samples in the experiment; the first point of note is the shape of these curves, the sharp drop at the rear of the pool indicates that the pool the direction of heat transfer becomes parallel to the direction of the heat source. The next noteworthy feature is the variation in the slope from one sample to the next; a steeper gradient on the graph represents a more curved meltpool, this is the case for samples with low powers and low beam velocities as previously highlighted by the calculated melt pool in Figure 5.8.

The second and third images in Figure 5.10 show the same data without the sharp change in curvature associated with the rear of the pool, this was done by ignoring the region of the solidification front in the first 100μm from the top surface. If the rear of the pool is neglected as an area likely to be remelted the remaining region of the solidification front will be that which determines the as-deposited microstructures. The implications of these findings will be discussed in relation to the observed microstructures in section 5.4.1

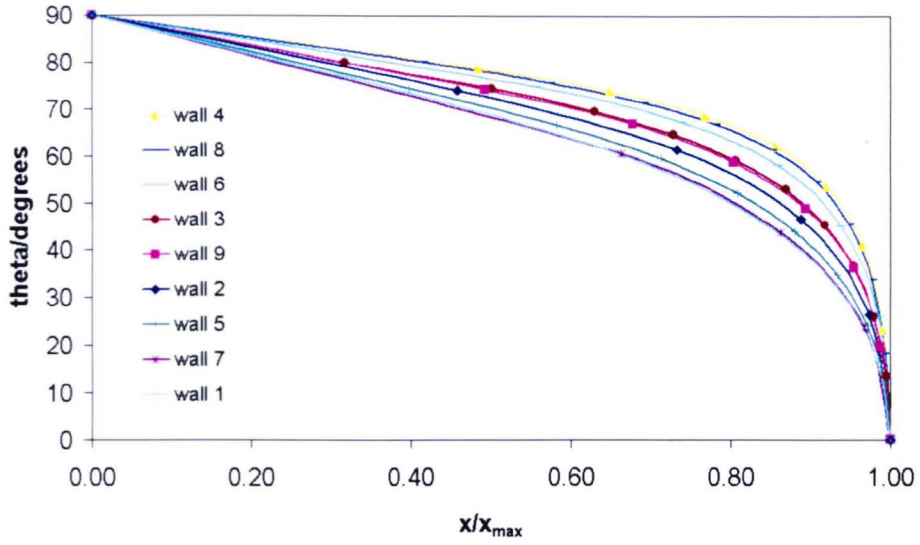

(a)

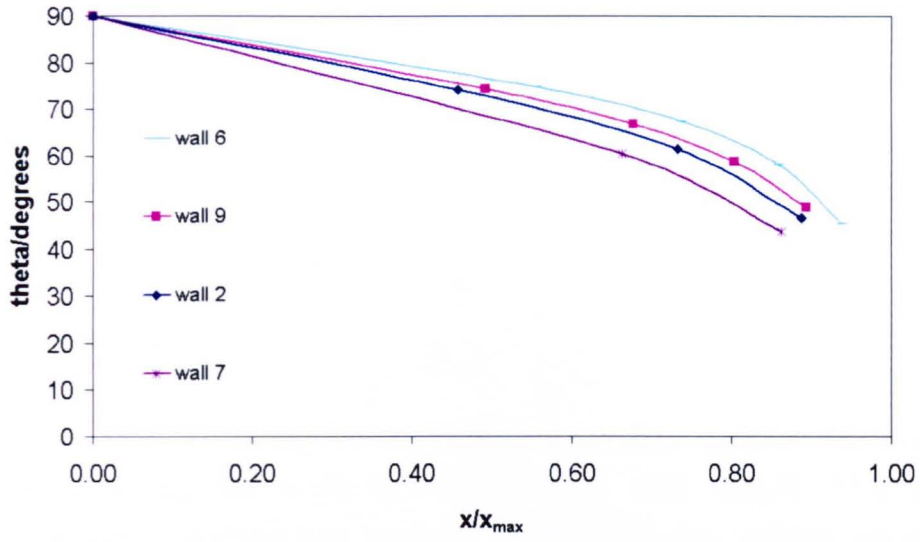

(b)

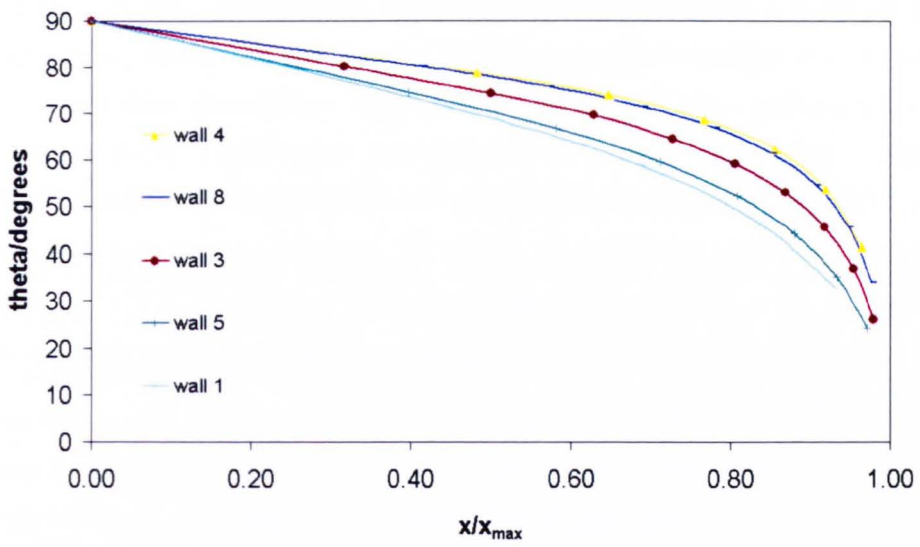

(c)

Figure 5.10 – Angle of the solidification isotherm relative to the z-axis as a function of distance along the solidification front

5.3 Analytical modelling of solidification conditions

Having obtained the co-ordinates of the solidification fronts in Section 5.2 it is possible to calculate the solidification cooling rates at the various parameter sets using Equation 5.5 these were compared to cooling rates determined by measuring dendrite arm spacing and applying Equation 5.8 in Section 5.6.

$$\frac{\partial T}{\partial t} = \left(\frac{\alpha Q v_b^2}{2\pi D k b}\right) e^{\frac{-v_b x}{2D}} \left(\frac{x}{r} \cdot K_1\left(\frac{v_b r}{2D}\right) + K_0\left(\frac{v_b r}{2D}\right)\right)$$

Equation 5.5

$$|\nabla T| = \left(\frac{\alpha Q v_b}{2\pi D k b}\right) \sqrt{G_x + G_z}$$

Equation 5.6

$$V_{iso} = \frac{\left(\frac{\partial T}{\partial t}\right)}{|\nabla T|}$$

Equation 5.7

Calculated cooling rates ranged from 4000K/s (wall 3) to 21,000K/s (wall 7). Figure 5.11, Figure 5.12 and Figure 5.13 show the calculated solidification conditions; cooling rate, temperature gradient and isotherm velocity respectively. Figure 5.11b is a contour map of the average cooling rates determined by Equation 5.5 shows how higher energy input (high power, low velocity) parameter sets yield the slower cooling rates, this is due to the larger weld tracks with lower surface area to volume ratio and hence a lower induced temperature gradient. Dendrite arm spacing, DAS, measurements put cooling rates at values of the order 10^4K/s which are in agreement with the model in terms of magnitude and certainly well within experimental error, DAS is discussed in Section 5.6. Figure 5.11a show the cooling rate to vary along the solidification front from zero at the bottom to a maximum at the rear of the pool.

(a)

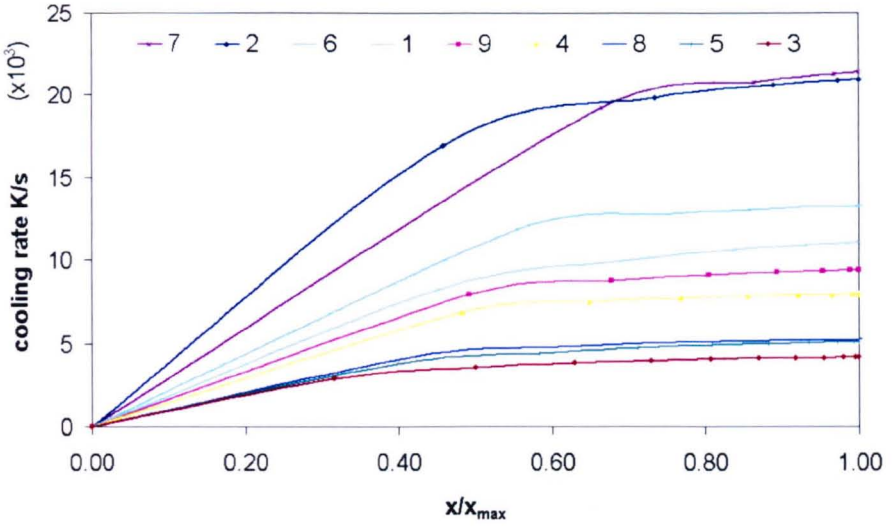

(b)

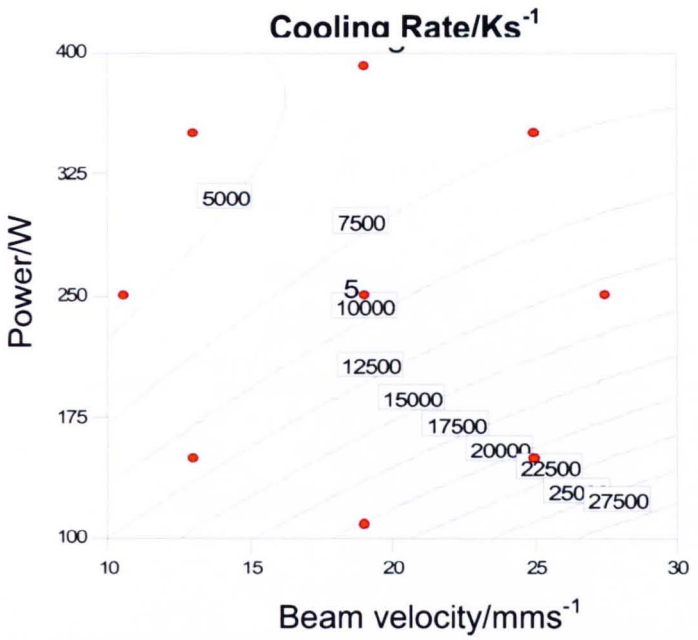

Figure 5.11 - Cooling rates calculated across the design space of the experiment

Temperature gradients were calculated using Equation 5.6 the results along the solidification-front range from $7.5x10^5$ to $2.0x10^6$ K/m and are shown in Figure 5.12. The temperature gradient is highest at the bottom of the pool and decreases a linearly towards the rear at the top (Figure 5.12a). The gradient profile is steeper along the solidification front for walls with low P/V_b (low linear energy input) reflecting the increased curvature of the weld pools and the lower gradients were calculated for the larger pools in line with the lower cooling rates, this is shown as a contour map in Figure 5.12b.

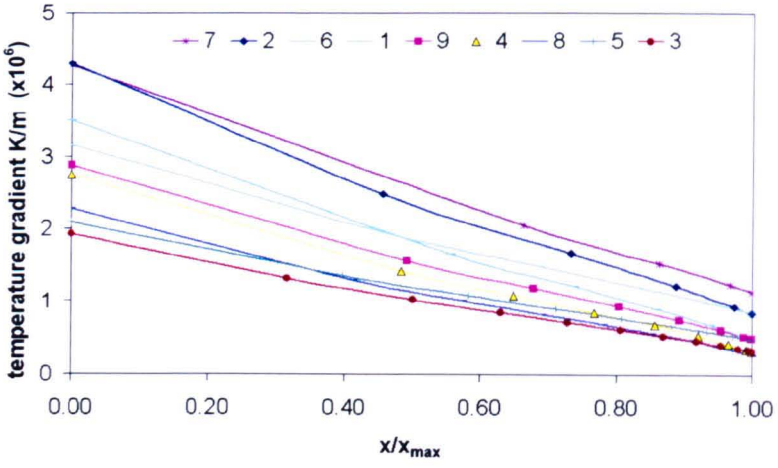

(a)

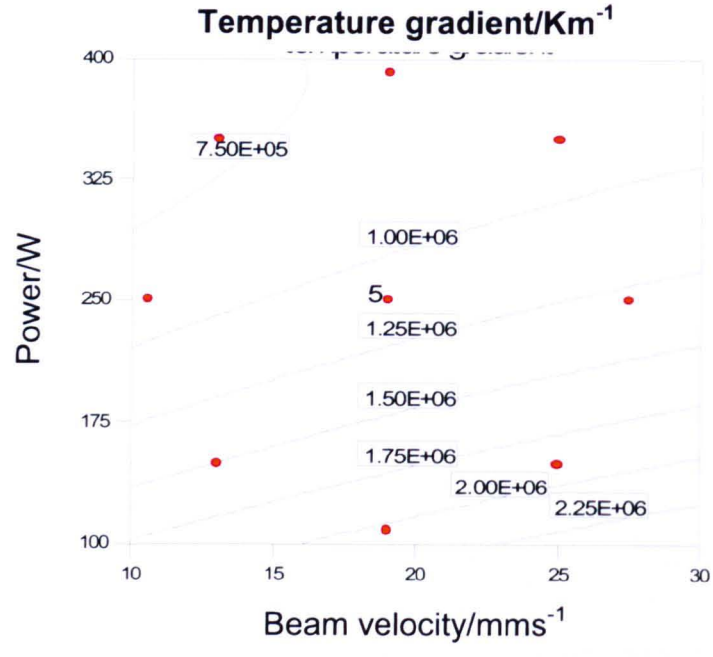

(b)

Figure 5.12 - Temperature gradients calculated across the design space

The isothermal velocities were calculated using the cooling rates and temperatures obtained previously using Equation 5.7, the results range from 0.007 to 0.015mm/s and are given in Figure 5.13. The average velocity is plotted in a contour map (Figure 5.13b) and interestingly shows that power can independently be altered to elicit a change in the isotherm velocity if only over a short range of velocities. It is also shown that velocity is zero at the bottom of the pool and increases to V_b at the rear with a sharp increase occurring in the final 20% of the solidifying region, these two regions may have great implications when determining the retained grain structure. The first region exhibits slow velocity and a relatively flat isotherm and thus would favour a columnar microstructure maintaining epitaxy with previous layers across the

whole layer height. Considering the rear-end of the pool, a CET occurs due to the increased velocity, decreasing gradient and the rapid change in direction of the heat flow which is also influenced by heat lost the upper surface through radiation. This will result in a solidified track consisting of a lower region with a columnar structure and an upper region where epitaxy is lost as grains first change their growth angle and at the top surface new grains can nucleate as a result of an increase in nucleation sites provided by the impinging powder on the top surface and the rapid heat loss through radiation in the opposite direction to conductive heat flow.

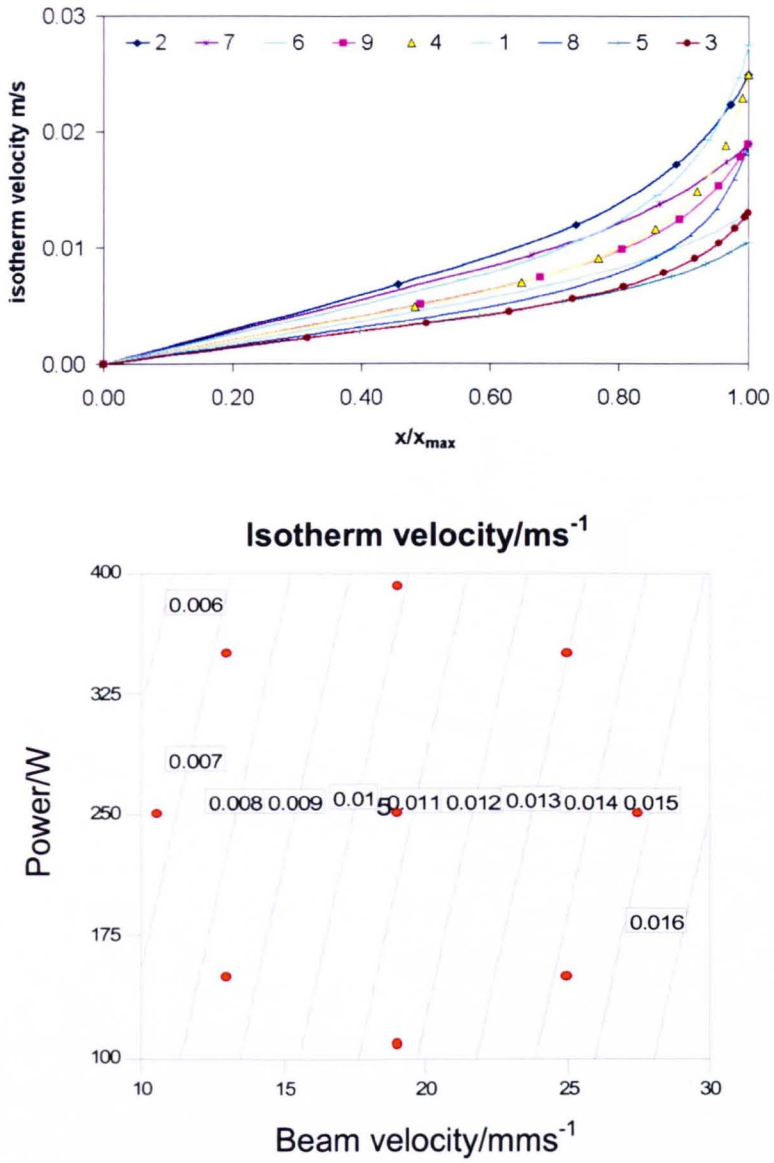

Figure 5.13 - Isotherm velocity calculated across the design space

Considering the columnar to equiaxed transition criteria described in Sections 2.2 and 4.3 it is possible to plot the calculated solidification conditions for the experiment against the Gäumann (Gäumann 1999a) criteria. Figure 5.14 shows the results from this study compared to this limit and it is apparent that all processing parameters reside mostly in the 'mixed' regime, moving from columnar at the bottom of the pool towards the equiaxed at the rear as G decreases and V_{iso} increases. This will be discussed in relation to the as-deposited microstructures in the following sections.

(a)

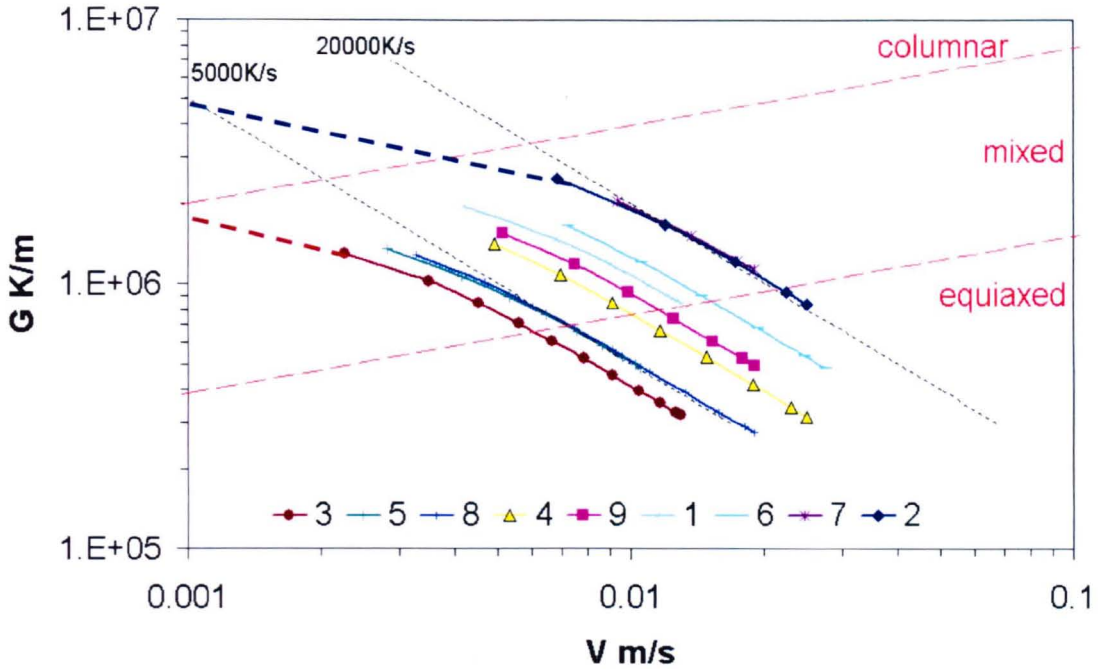

(b)

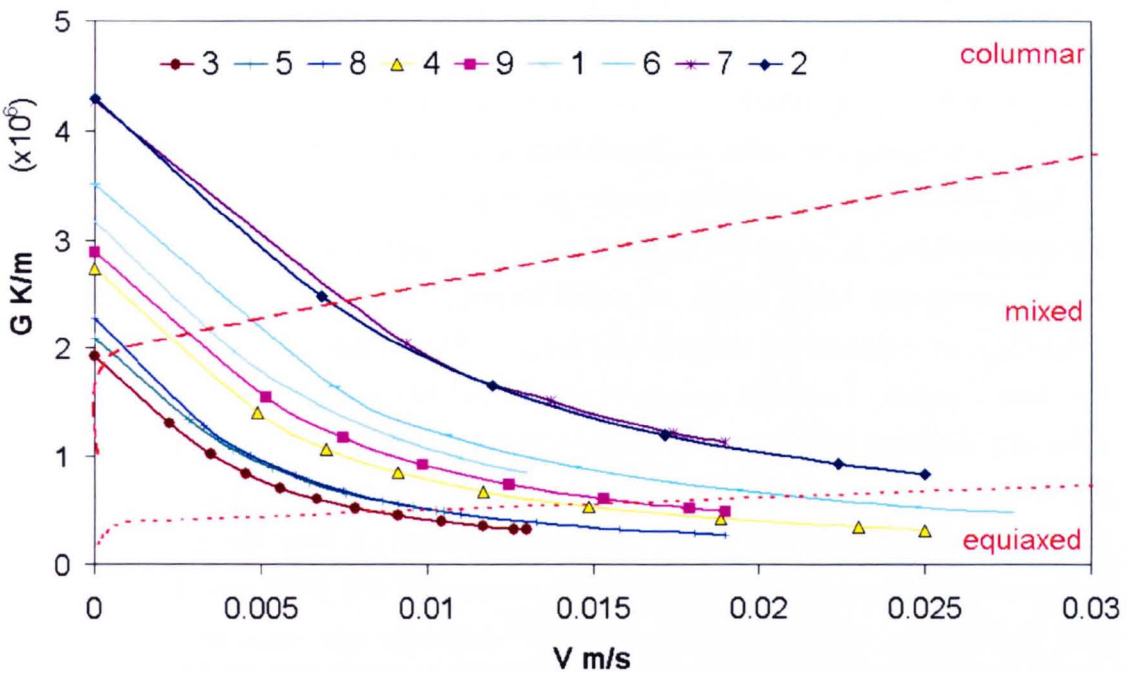

Figure 5.14 - Temperatrure gradient vs. isotherm velocity showing CET acording to Gäumann (Gäumann 1999a) (Red Dashed lines), (a) log scale, (b) linear scale. The plotted lines representing the various build condtions of the DOE represent the distance along the solidification front.

The red contour in Figure 5.15a indicates the mixed/equiaxed limit and indicates how the processing parameters might be altered to push the solidification conditions into a region necessary to form equiaxed grains, in this instance further reducing beam

velocity and increasing the power with power being the most significant. The most efficient way is to reduce the temperature gradient which has a greater response than reducing velocity; this would ultimately increase the size of the pool. Other measures to achieve this might include increasing the substrate temperature, this was not within the scope of this study but can be simulated using the governing heat transfer equations outlined and was looked at in detail by Gäumann (Gäumann 1999a). Figure 5.15b shows that the value of $G^{3.4}/V$ change along the solidification front and that the CET occurs along this region. The bottom of the molten pool shows calculated solidification conditions which would favour a columnar structure and hence epitaxial grain growth, whereas at the rear of the pool the conditions would favour equiaxed grain growth with a mixed region in the middle portion.

The solidification conditions calculated are idealised to the conditions at the centreline of the weld pool as the original heat transfer model does not account for radiative and convective surface losses. When these are considered, the temperature gradient at the outer region of the wall would indeed be lower on account of the atmosphere being a less efficient heat sink than the underlying metal. The CET derived by Gäumann assumes nucleation undercooling is negligible since nucleation is dominated by nuclei density at high temperature gradients. With this in mind, the fine equiaxed region observed in the walls occurs in the pool where G is lowest; hence it is possible that undercooling is becoming more pronounced.

The solidification conditions across the whole range of parameters studied vary within individual pools to the extent that, in all cases, a CET would be expected to occur during the latter stages of solidification. What can be manipulated is the proportion of the pool i.e. the physical length of the solidification front which lies in the three regimes described: columnar, mixed and equiaxed. Knowing this would then make it possible to select a z-step height which would remelt upper part of the track to the extent necessary. For instance, if long continuous grains are required (such as in the repair or deposition of single crystal components) a long flat pool is beneficial with a small z-step to ensure directional heat transfer and grain growth is maintained and any grains which begin to change direction are remelted. Alternatively, discontinuous grains are more likely when a highly curved pool is present as changes in the grain growth direction are induced. Ultimately there exits a paradox/conflict for development of equiaxed grains where low temperature gradients are necessary, i.e. large pools, but high solidification velocities, which are achieved by high beam velocities and hence smaller pools. This is the reason for the trend seen in Figure 5.14 and Figure 5.15 where the solidification conditions for all parameter sets cross the three defined regimes of columnar, mixed and equiaxed growth.

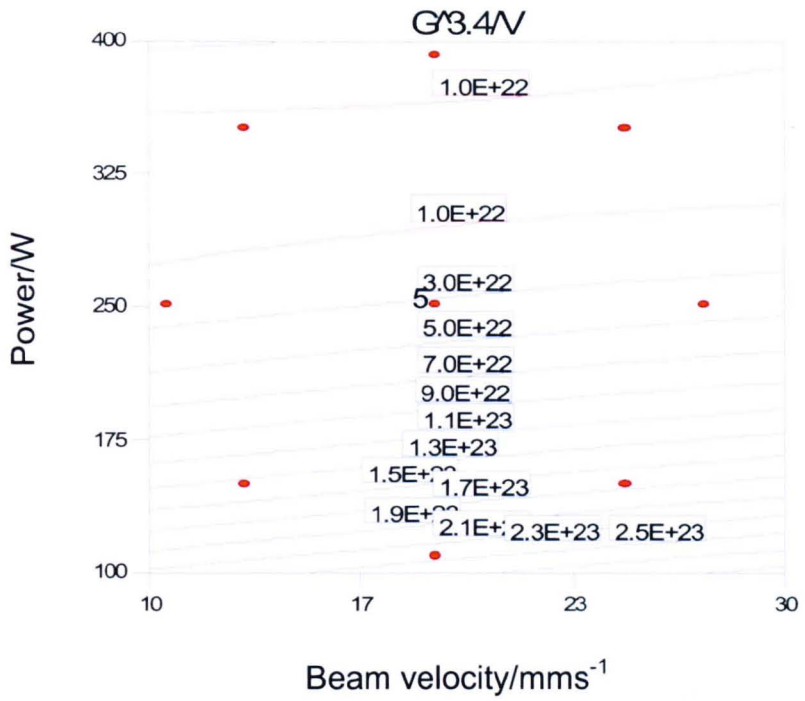

(a)

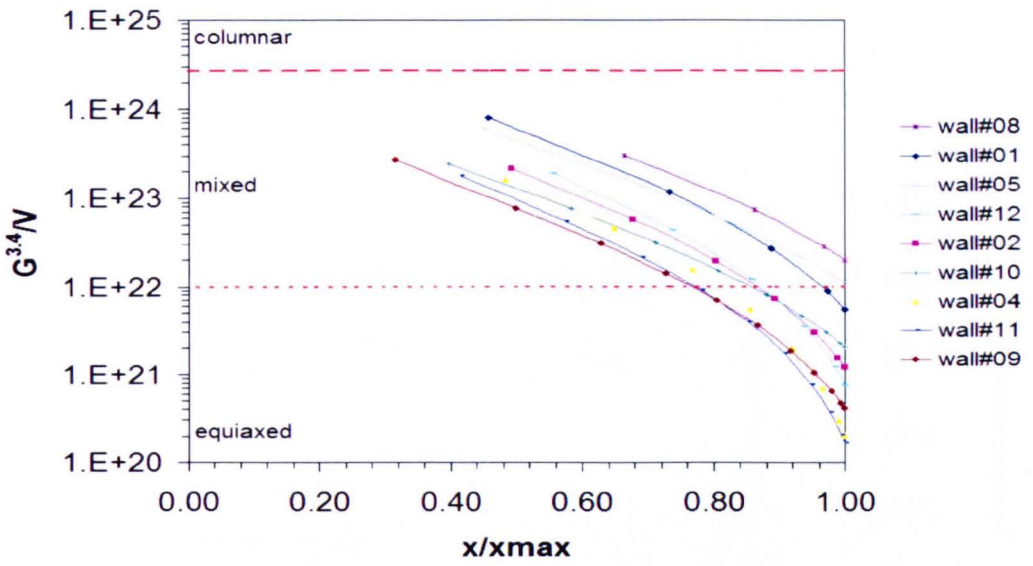

(b)

Figure 5.15 - CET criterion plotted as a function of process parameters (a) and position along solidification front (b). Note the absence of the data from the early stages of the solidification front; this is due to the anomaly caused by the velocity approaching zero and hence $G^{3.4}/V$ tending to infinity.

Inconel 718 derives its properties through precipitation strengthening, primarily the formation of coherent γ" (Ni_3Nb) and γ' $Ni_3(Al,Ti)$. The time-temperature-transformation (TTT) curve for Inconel 718 is considered in Figure 5.16. The calculated cooling rates are compared to the curves representing the formation of these strengthening phases and it is apparent that solidification is sufficiently rapid to avoid this. Wang et al. (Wang 2008) used FE to model the LENS process for steel and showed that subsequent passes of the beam reheat lower layers to temperatures where precipitation is possible, but due to the rapid cooling achieved by conduction to the metal substrate acting as an effective heat sink, the cooling rate is still sufficiently high to avoid this. Calculations of the temperature and cooling rate beneath the weld pool at 50μm intervals are shown in Figure 5.17 for wall 3 in this study which experiences the highest temperature and slowest cooling rates. The time spent at temperatures high enough to cause precipitation is seen to be too low even up to 300μm below the melt pool; beyond this depth the calculations show the temperature is not sufficiently high. This suggests that optimum properties are not achieved through deposition alone and post-process heat treatments are necessary, this would have implications where the technique was used for repairing components as it is likely the whole component would require solution treatment and aging if localised treatment is not feasible.

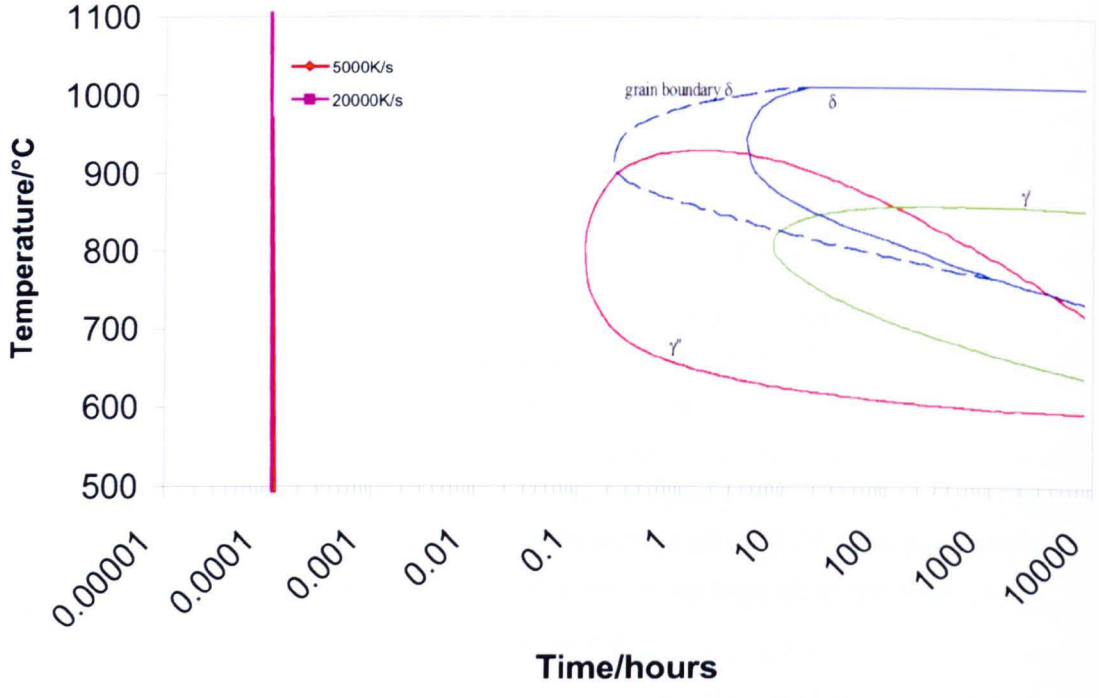

Figure 5.16 – TTT diagram for Inconel 718 after Cambridge University micrograph library (University of Cambridge, DoITPoMs Micrograph Library). The lines showing cooling rates of 5000K/s and 20000K/s are shown almost overlapping on the

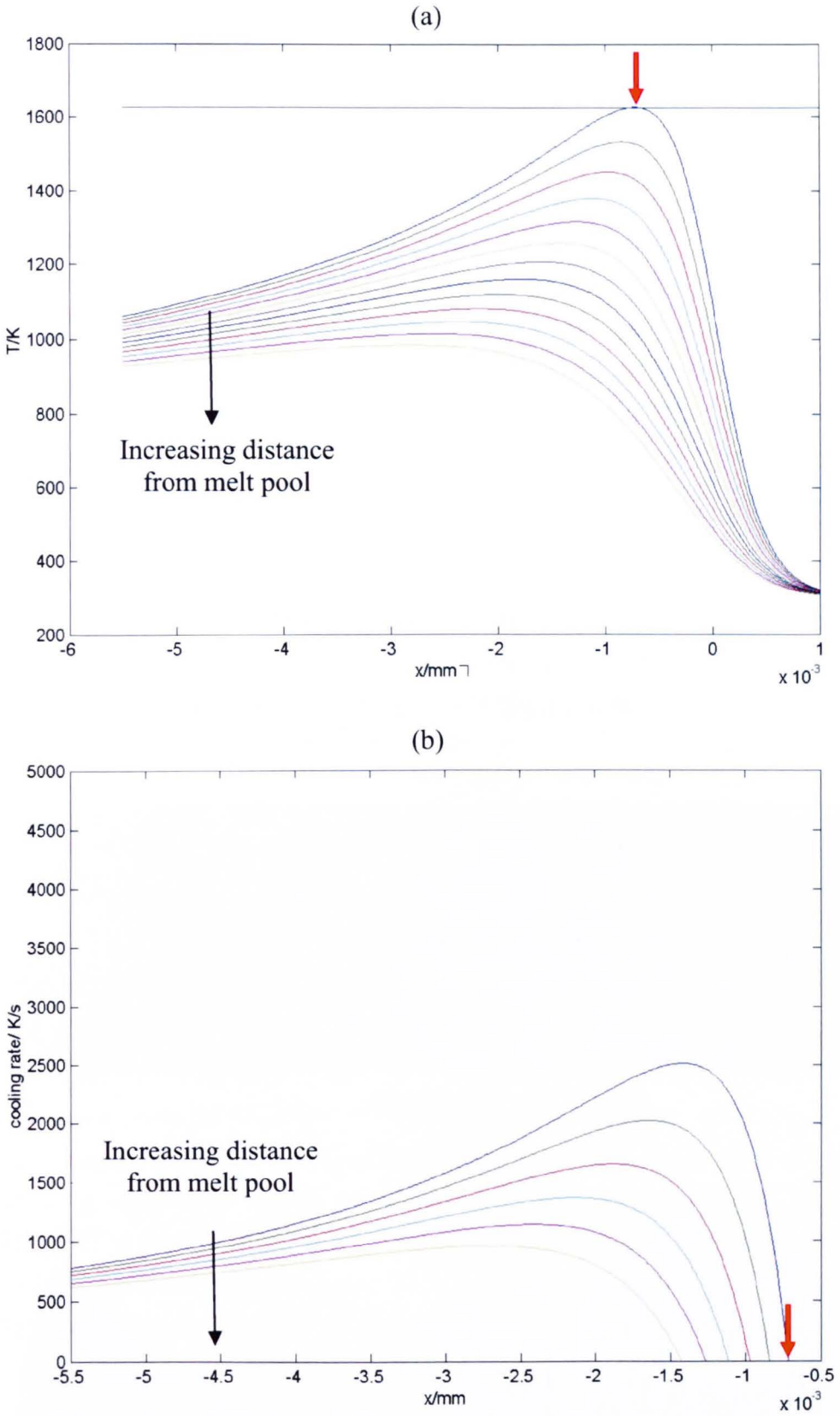

Figure 5.17 – (a) Temperature and (b) cooling rate profiles for wall 3 in the quasi-stationary state. Red arrow indicates bottom of melt pool, *x=0* is the position of the laser. Lines plotted show profile at 50μm intervals beneath the melt pool.

5.4 As-deposited microstructures

5.4.1 DMD grain structure

The walls built across the design space displayed a variety of grain structures and the size and shape of the grains varied within the individual walls themselves making quantitative comparisons difficult. The final grain structures in all the deposited walls were investigated using EBSD to obtain Orientation Imaging Map (OIM) and pole figures. All of the walls differ greatly from the substrate material which is represented in Figure 5.18 as an OIM. The substrate used is a 6mm Inconel 718 plate consists of near-random orientated equiaxed grains with an average grain size of 25μm +/- 5μm; the random orientation is confirmed by the pole figure which shows a weak texture quantified by a low 'Multiple of Uniform Distribution' (MUD) value of 1.6 times random.

The black lines in Figure 5.18 and in subsequent OIMs represent high angle grain boundaries (HAGB) with a misorientation <15° any low angle grain boundaries (LAGB) with a misorientation angle of <5° appear as grey lines.

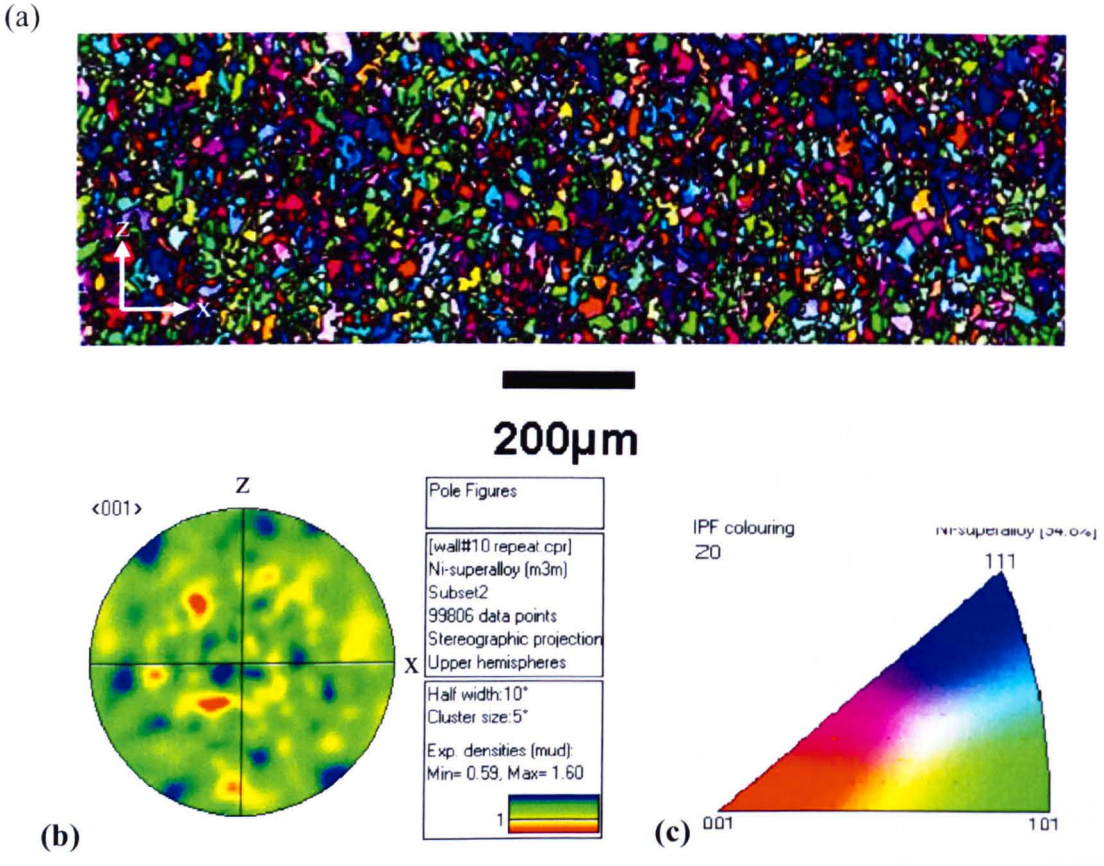

Figure 5.18 - EBSD OIM of Inconel 718 substrate and corresponding (001) pole figure showing random grain orientation and equiaxed grain structure

5.4.1.1 Walls at the CCD centre point

Two examples of the walls build at parameters described by the centre point of the CCD (Power 250W, velocity 19mm/s) are shown in Figure 5.19. The longitudinal section and transverse section are observed and were seen to be consistent for all the repeated builds.

The transverse section (yz plane) (Figure 5.19b) reveals a region of very fine, randomly orientated grains at the outer surface and relatively large grains in the centre which are continuous across layer boundaries, this is also seen in the longitudinal sections (xz) at the top surface where there is a distinct layer approximately 60μm thick. The origin of this outer equiaxed region is alluded to in Section 5.2 and 5.3 and is a combination of the sudden change in heat transfer direction caused by the shape of the rear of the pool and the effect of radiation, combined with the lower temperature gradient, faster isotherm velocity and increased number of nucleation sites available due to the impingement of the blown powder particles at the pool surface.

The longitudinal observations (Figure 5.19a and c) reveal a 'zigzag' grain structure which is a result of the back and forth rastering technique used to build the walls as the direction of grain growth is determined by the direction of heat flow i.e. the grains follow the direction of the moving laser. There is a region of competitive growth in the lower regions of the wall which quickly becomes dominated by the faster growing (001) grains (indicated by the red colouring on the OIM). A strong texture is evident and is shown by the (001) pole figures and corresponding MUD values of 7.19 and 12.25 times random. The pole figures suggest that the (001) grains are rotated by approximately 45° relative to the x-axis. The grains are continuous across multiple layers suggesting that epitaxy, rather than nucleation and growth, is the dominant solidification process that will favour a directional grain morphology.

The two longitudinal views in Figure 5.19 differ slightly; Figure 5.19(c) has some similar long continuous grains but appears to have smaller grains which are discontinuous at the layer boundaries too. These are a result of misalignment during sample preparation as the wall was not sectioned accurately along the centreline; the discontinuous grains are part of the outer region of the wall where grains become smaller and more equiaxed closer to the outer surface because of increasing growth velocity and lower temperature gradients. The implication of this is that the observed microstructure is not representative of the centre of the wall.

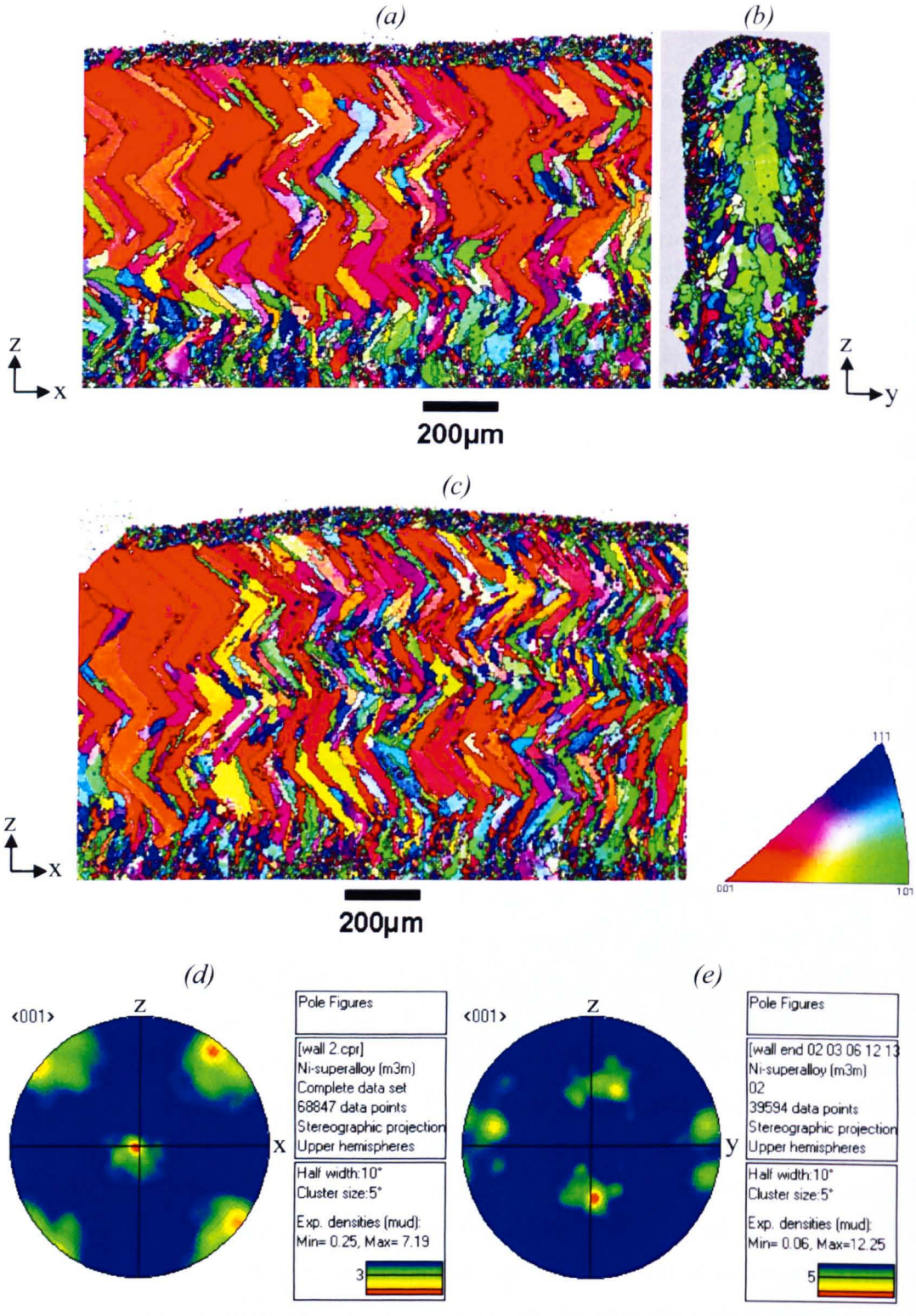

Figure 5.19 – OIM showing longitudinal sections (xz) of Walls 9 (a) and 10 (c) with IPF Colouring in 'y'and transverse section (yz) of Wall 12 (b) with IPF Colouring in 'x' built at the centre point of the CCD. (d ,e) show <001> pole figures for longitudinal and transverse sections respectively.

5.4.1.2 Walls built at low power and velocity

Figure 5.20 shows the EBSD data collected for Walls 5 and 7 which represent two of the axial points of the CCD with the lowest beam velocity (10.5mm/s) and lowest laser power (109W) respectively. The transverse sections (yz) of both walls (Figure 5.20b and d)) have different grain structures than those observed in Figure 5.19. There is a region at the outer surface composed of fine equiaxed grains, however the interior regions do not exhibit the same large continuous grains observed in Wall 12. The interior have a discontinuous, equiaxed morphology. This is not a complete picture of the grain structure however; when we consider the longitudinal sections it becomes apparent that 'equiaxed' is not an appropriate description. In both there is a zigzag arrangement as a result of the rastering heat source, Wall 7 shows some areas of continuous grains similar to those seen in Figure 5.19 but on a finer scale; these finer grains, which are again tilted relative to the x-axis, are sectioned during sample preparation in the wall's transverse orientation and so appear to be round grains as opposed to elongated in one direction. The textures obtained are weaker than those found in the walls built at the centre point of the CCD shown in Figure 5.19 but are still greater than the substrate being 4.46 and 4.43 times random for the transverse and longitudinal respectively. The weaker texture and the less obvious continuous grains in Wall 7 result from the thinner wall produced at the low power setting as the fine grains seen in the outer regions of the walls are a larger proportion of the cross-section limiting the size of the interior region and hence time for solidification and making longitudinal sectioning of the walls difficult to execute accurately.

The longitudinal section of wall 5 (Figure 5.20a) shows that the apparent round grains observed in the transverse orientation are again a result of the sectioning of grains elongated in the x-direction. In the lower region of the wall these are, in some cases, almost horizontal and parallel to the x-axis, but are closer to a 45° inclination on the upper wall. There is evidence that there is some epitaxy at layer boundaries but this does not appear to be maintained over the layer height and does not result in continuous grains over the wall's total height. There are also regions of finer grains observed at layer interfaces, these are likely present because of insufficient material being removed during sectioning and are remnants of the outer fine grained region. The texture of the wall is again weaker, especially in the transverse with an MUD value of 2.07 times random and 4.14 in the longitudinal orientation. The pole figure for the transverse also shows that the <001> grains are tending to tilt towards the centreline of the wall, growing at an angle close to 45°; this is not the case in Walls 7 (Figure 5.20) and Walls 9 and 10 (Figure 5.19) which suggests that the melt pool isotherms in these cases are flatter in the yz plane.

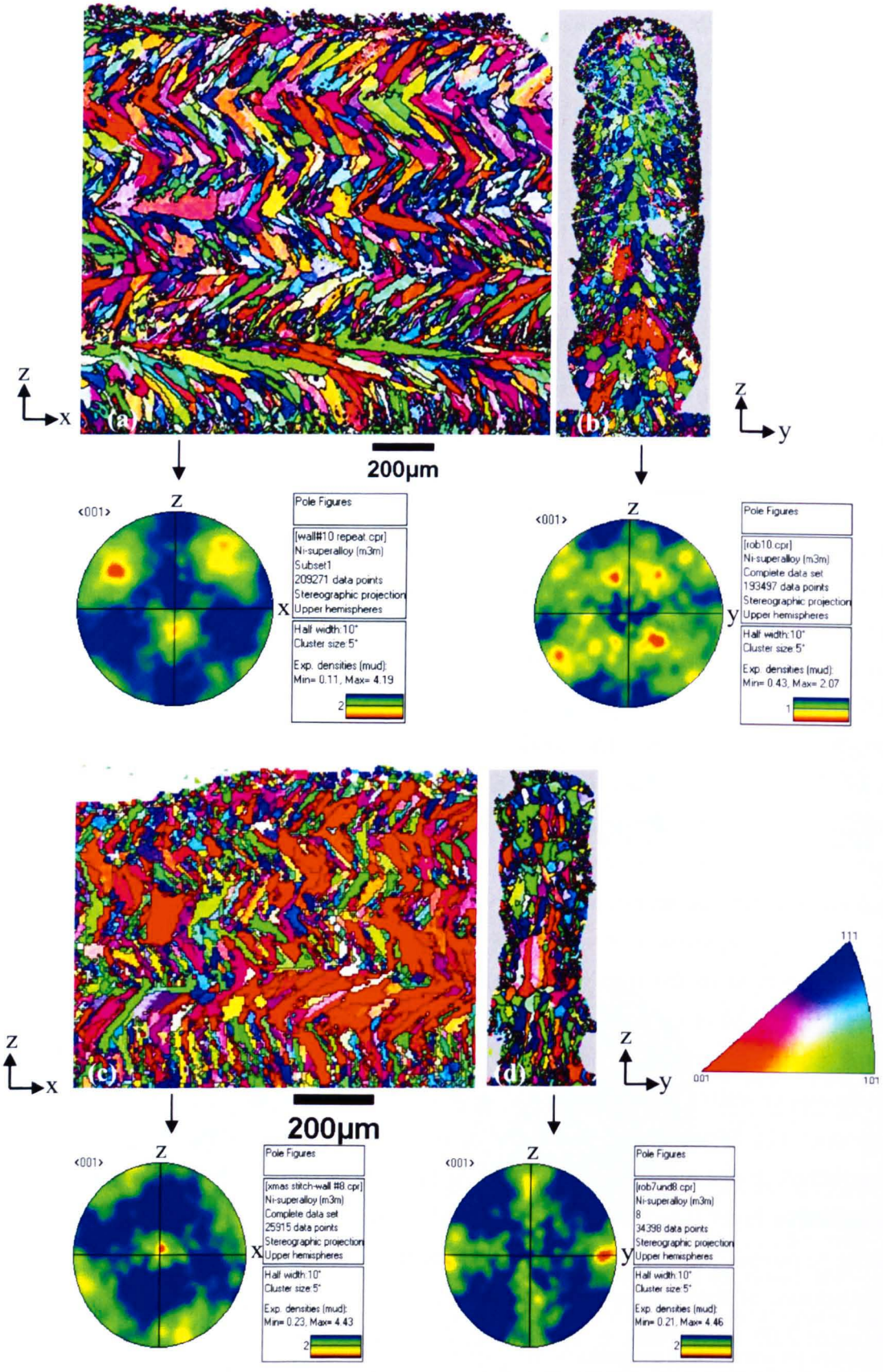

Figure 5.20 - OIMs and (001) pole figures of longitudinal (xz) and transverse (yz) sections of Walls 5 (a, b) and 7 (c, d) built at 250W/11mm/s and 109W/19mm/s respectively. IPF colouring in longitudinal samples is 'y' and in transvers samples is 'x'.

5.4.1.3 Pools with microstructure anomalies

Figure 5.21 and Figure 5.22 show the OIM and (001) pole figures for Walls 4 and 8, which show grain structures differing from those in Figure 5.19 and Figure 5.20. The microstructure observed in the longitudinal section (xz) of Wall 4 has three regions which differ largely from each other (labelled (a), (b) and (c) in Figure 5.21). To the left of the image (a) there is evidence of the same zigzag structure spanning the entire wall height as seen in Figure 5.19 but on a larger scale where an 800μm section of wall is composed of just 3 large grains (I, II, III in Figure 5.21) which appear to have been seeded from lower layers or the substrate. The centre of the image (b) shows very thin grains which begin in the substrate and stretch straight to the top surface of the wall but do not follow a zigzag pattern similar to the microstructures observed for the laser deposited samples produced on the EOS M270 described in Section 4.3. Finally, the right hand side of the image (c) shows a region of zigzagging grains which have some evidence of epitaxy at layer boundaries but which are not continuous across the total wall height. The textures in these regions also differ in the three regions highlighted; (a) has a strong texture of 19.85 times random due to the dominance of three very large grains, (b) is strongly textured (MUD 11.42) with the pole figure showing alignment with the z-axis but no preferred rotation about that axis, and (c) has a weaker texture of 8.08 times random. The transverse OIM shows a tendency for the grains to 'lean' towards the centreline and in the upper region grains are continuous across multiple layers, the texture is again weaker in this orientation at 4.5 times random.

Wall 8 again shows inconsistencies in the observed grain structure on the longitudinal section, Figure 5.22a bares a likeness to previous grains with continuous zigzag shaped grains over multiple layers, whereas Figure 5.22b shows smaller discontinuous grains in the lower layers and larger grains in the top layer. This may be caused by insufficient material removal of the wall during sample preparation. The transverse section Figure 5.22c again shows grains leaning towards the centreline of the wall.

These varying regions appear to coincide with undulations on the top surface of the wall. Walls 4 and 8 were the only walls which displayed this melt pool instability on the top surface but both maintained a relatively consistent width. An unstable pool results in non-uniform microstructures which will have implications on the mechanical properties of parts produced by DMD so understanding the origin of such anomalies is advantageous.

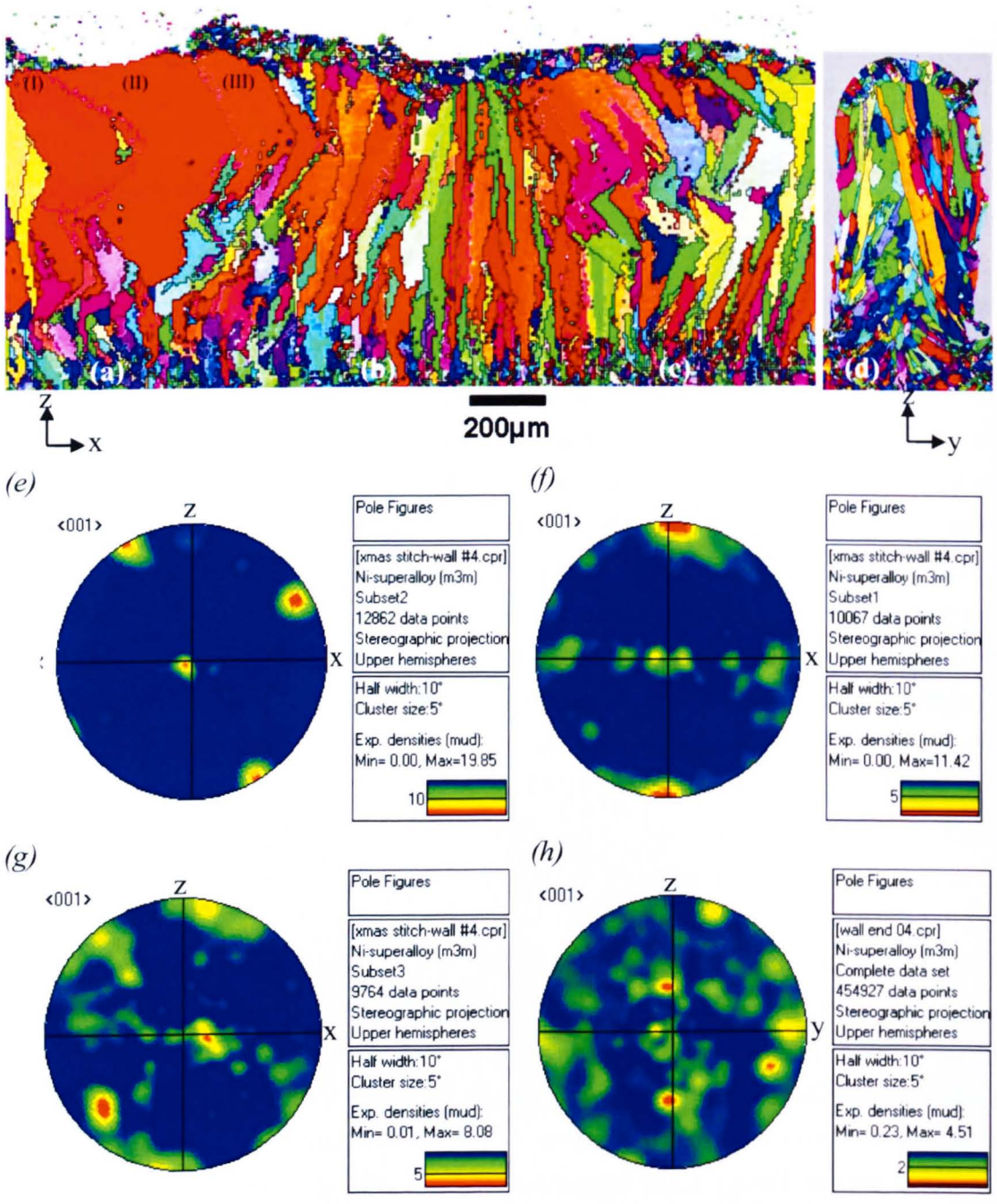

Figure 5.21 – EBSD OIM and <001> pole figures for Wall 4 build at 350W/25mm/s. Longitudinal section is split into three regions of interest (a, b, c), transverse section labelled (d), the corresponding pole figures to (a, b, c, d) are given in (e, f, g, h) respectively. IPF colouring is as described in Figure 5.20.

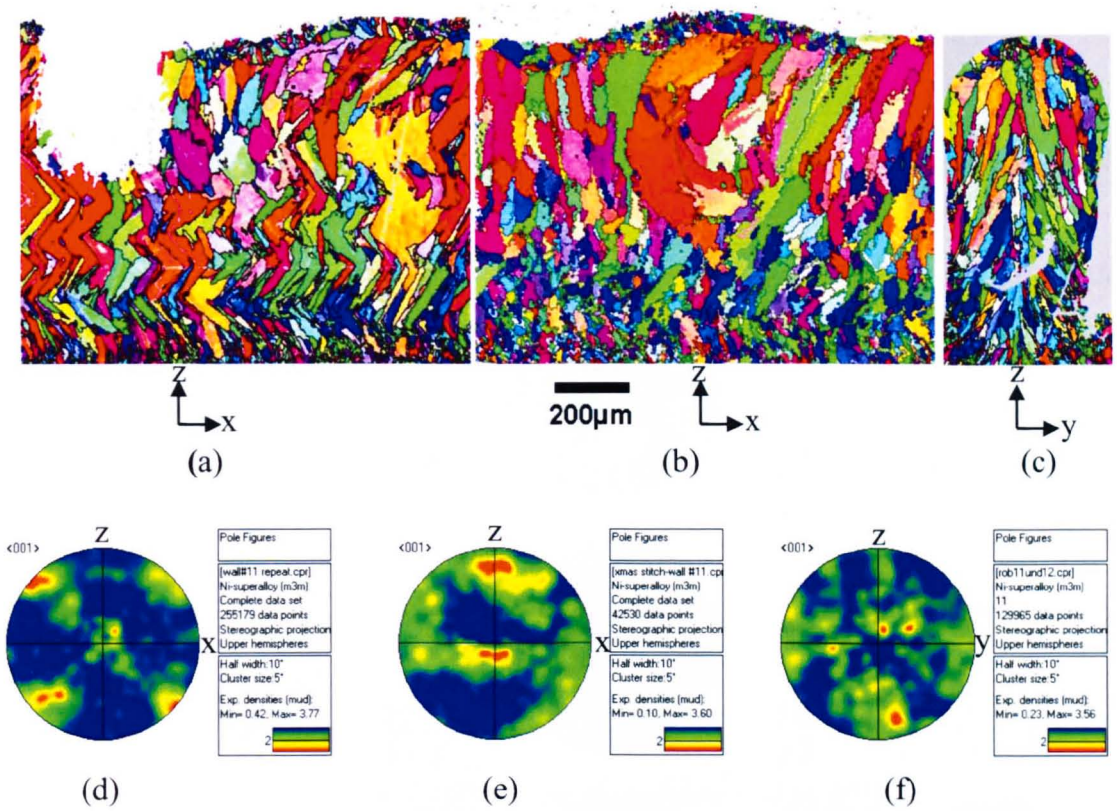

Figure 5.22 - EBSD OIM and <001> pole figures for Wall 8 built at 390.42W/19mm/s. Two longitudinal sections are analysed (a) and (b) and transverse section (c) the corresponding pole figures are (d, e, f) respectively. IPF colouring is as described in Figure 5.20.

5.4.1.4 Effect of distance from substrate

The texture of the walls has been shown to be greater in the deposits than the substrate material and can be attributed to the highly directional heat transfer from the molten pool into the underlying metal which acts as a heat sink. Figure 5.24 shows how the overall texture of a wall is developed as subsequent layers are deposited. The substrate material has a low MUD value but this increases in layers towards the top of the wall (Figure 5.23) as the faster growing <001> orientated grains dominate through competitive growth. The strong texture is lost at the top surface where the equiaxed grains which have been previously discussed are present.

Wall 9 is seen to have the highest MUD and this is apparent in the grain structure shown in Figure 5.19a, Wall 2 has a stronger texture than Wall 5 but this may be stronger than the MUD values suggest as sectioning Wall 2 was not as successful in finding the centreline than in Wall 9 due to it being thinner.

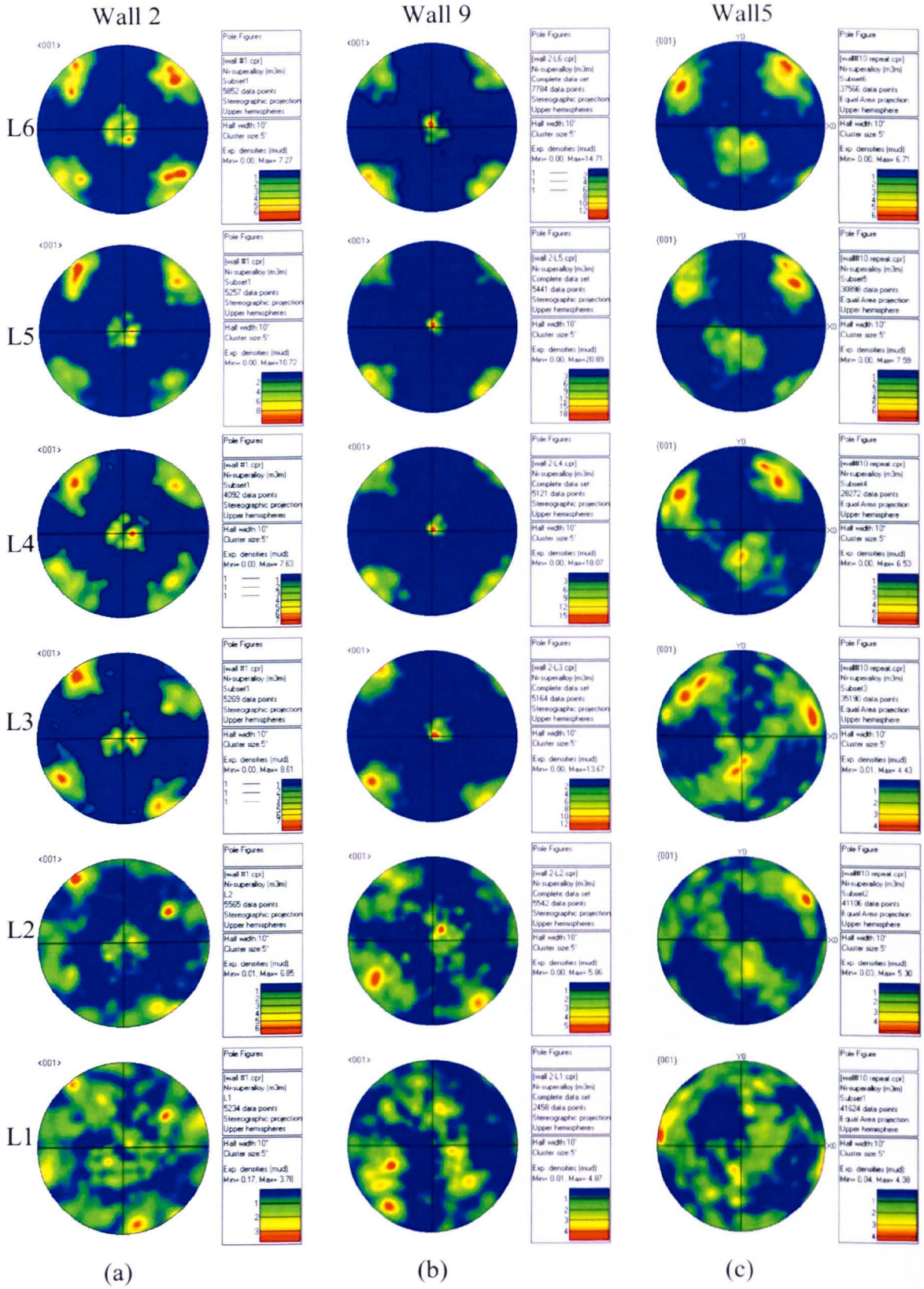

Figure 5.23 – Pole figures of the individual layers (L1 to L6) of Walls 2, 9 and 5 (a, b, c) showing the development of texture

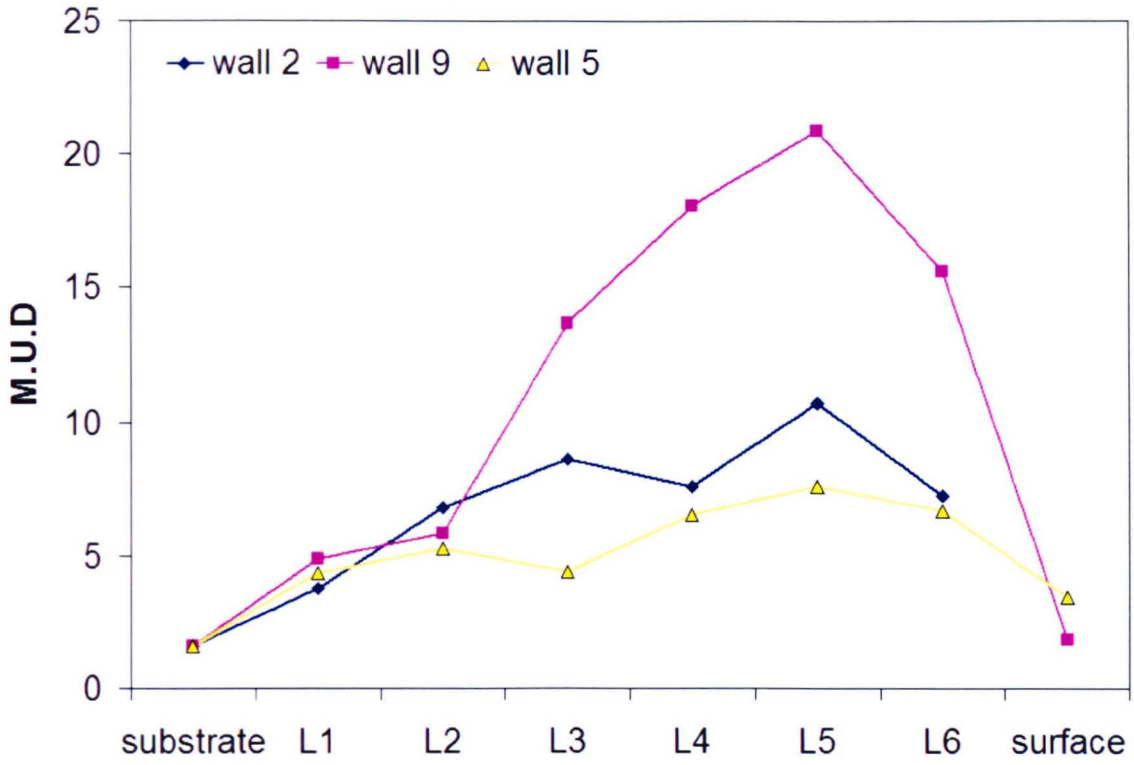

Figure 5.24 – Plot of Multiples of Uniform Distribution in the substrate material, individual layers and the top surface of Walls 2, 5 and 9

5.4.1.5 Overall effect across the design space

Having discussed individual walls and specific microstructural features observed in sample walls built across the Design Space it is now useful to consider the effect of parameters across the entire Experiment and note the global effects on the as-deposited grain structures. Figure 5.25 shows the complete CCD array with longitudinal and transverse images obtained by EBSD.

The transverse sections show that walls built at faster beam velocities have long grains which are continuous across multiple layers whereas at slower velocities the grains appear rounder and do not extend through the wall's height. As previously established one orientation of the grain structure is insufficient to draw conclusions. The longitudinal sections reveal that the 'round' grains may be, in fact, the cross-section of tilted, elongated grains which are a result of the direction of the moving heat source.

The two walls with high power and high velocity settings (Walls 4 and 8) have varying microstructures as a result of melt pool instability. The bottom right quadrant of the Design Space contains Walls 2, 6, 7 and 9-13; these have a distinct grain structure with long grains which zigzag according to the rastering pattern of the laser

and grow epitaxially through the layers of the wall. The remaining walls (1, 3 and 5) have grain structures which do not contain grains like the bottom right quadrant; these walls are built at the lowest beam velocities and have elongated grains resulting from the direction of heat transfer from the moving laser but the effect is not sufficiently dominant as to provide a driving force for their growth through multiple layers as epitaxy is lost in the mid-region of each individual layer. These grains are finer than the larger continuous grains but are not equiaxed. The reason for this may be the shape of the isotherms in the transverse (yz) cross-section which have not been considered. The lower beam velocity increases the interaction time of the heat source and hence the penetration depth is increased, this results in a rounder melt pool in this plane. The resulting grains will grow towards the centre of a wall; this is supported by the pole figure for Wall 5 (Figure 5.20) in which it is seen that the grains are tilted in this fashion, meaning that as grains reach the centreline of the wall they impinge on each other.

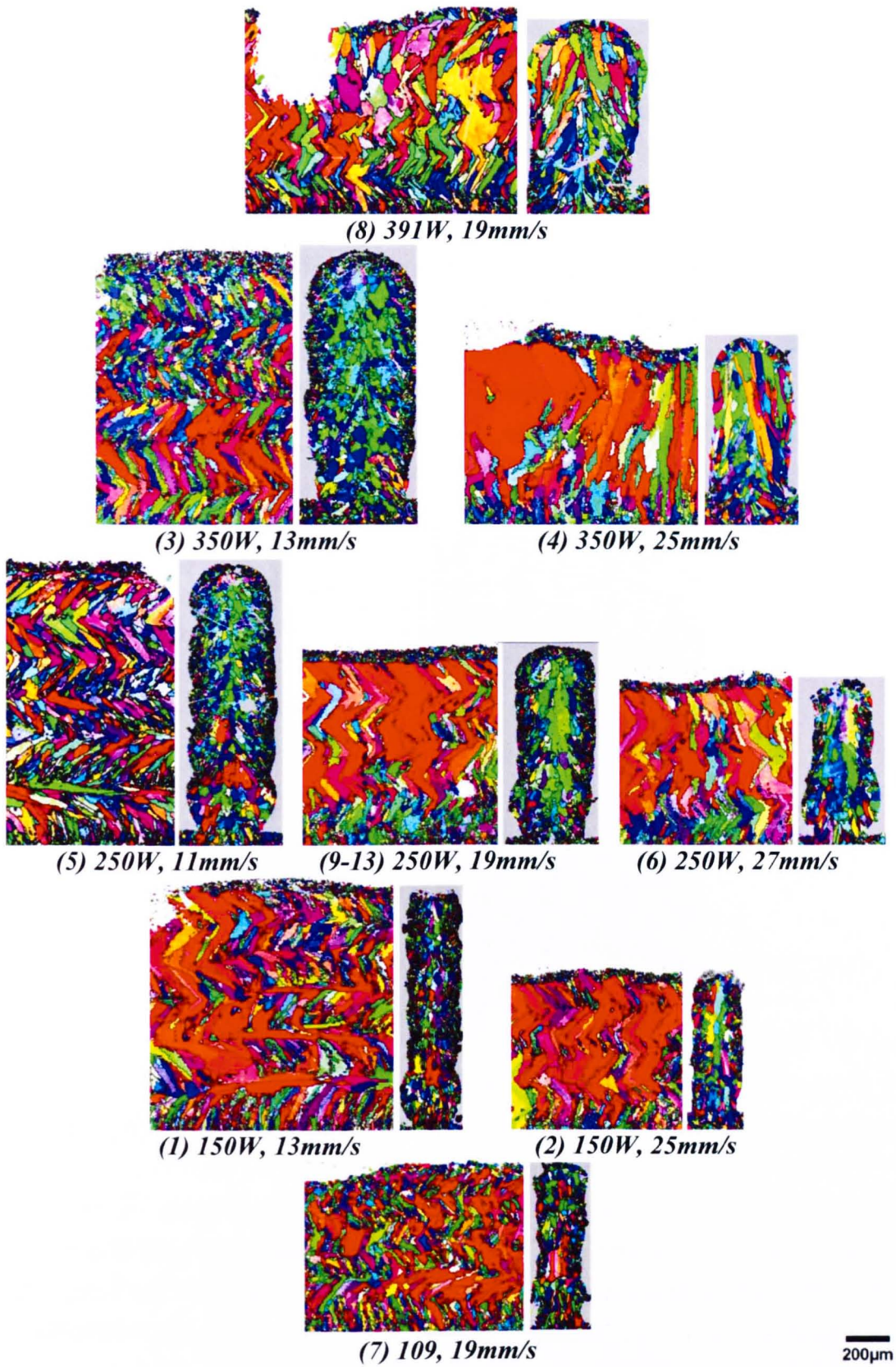

Figure 5.25 – Longitudinal and transverse sections of all walls built in the CCDOE. Images are displayed in a central composite array with laser power on the vertical axis and beam velocity the horizontal. 200µm scale bar is true for all images. IPF colouring is as described in Figure 5.19 to Figure 5.22.

The discontinuous grains are analogous to those reported by Tin et al. (Tin 2005) who modelled the Vacuum Arc Remelting (VAR) process of Inconel 718 for turbine disc applications. The modelled and observed grain structures bare resemblance to those observed in the present study deposited at lower beam velocities albeit on a larger size scale. The remelted ingot of Tin et al. (Tin 2005) (Figure 5.26) displays a region at the surface where grains are nucleated followed by competitive growth where long (001) grains dominate and follow the direction of the moving pool before a region in the centre is reached where equiaxed grains are retained. This was also discussed by Hunziker et al. and Dye et al. (Hunziker 2000, Dye 2001) in relation to centreline grain boundary formation in laser welding of Inconel 718 who attributed the change in grain structure to the angle at the rear of the pool and the increase undercooling where the isotherm velocity is highest.

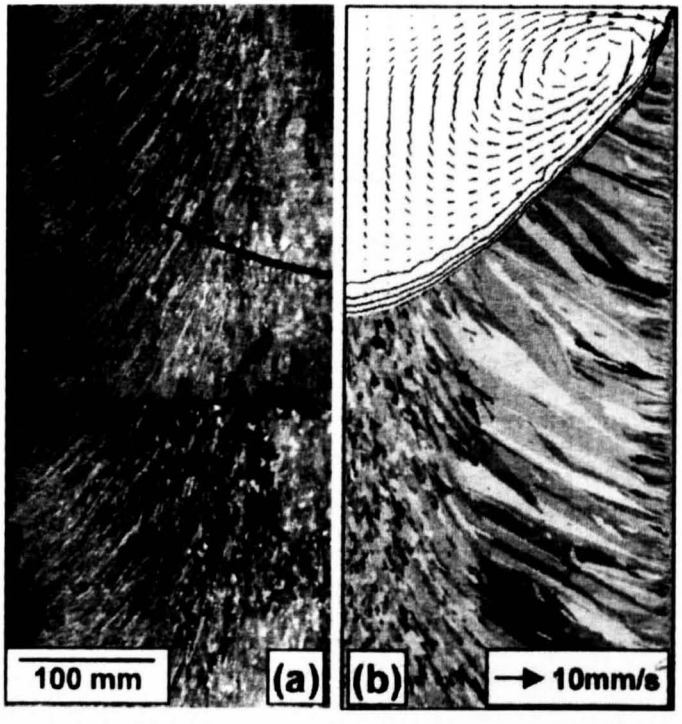

Figure 5.26 - VAR ingot of Inconel 718 (a) observed and (b) modelled microstructure (Tin 2005)

The walls with long, continuous grains have flatter weld pools and hence heat transfer is, generally speaking, vertically downwards towards the base plate which in turn means that grains can grow vertically to the full height of the layer and be continuous through the wall height. Porter and Easterling (Porter 1988) described the high and low velocity welds as having two distinct melt pool shapes; these are shown schematically in Figure 5.27. Low velocities have curved solidification fronts so grain growth has the opportunity to change direction to follow the direction of heat transfer whereas the faster velocities follow a flatter isotherm to give continuous grains growing to the centreline. The latter is observed in this study at faster beam

velocities for the DMD and also for the EOS M270 in Chapter 4. This leads to the conclusion that, overall, a CET cannot be brought about truly by manipulation of processing parameters, it is experienced along the solidification front towards the rear of a melt pool regardless of processing conditions as the bottom of a pool always favours epitaxial and columnar growth due to low isotherm velocity and higher temperature gradient, as the velocity increases to the rear of the pool, only here is the degree of undercooling sufficient for equiaxed grains to be retained. This is particularly important when we consider the EOS where the retained grain structure is determined by the bottom 20μm of the pool where the growth velocity is slow; this effect could be reproduced with the DMD with smaller z-step heights to melt back more of the previous layer.

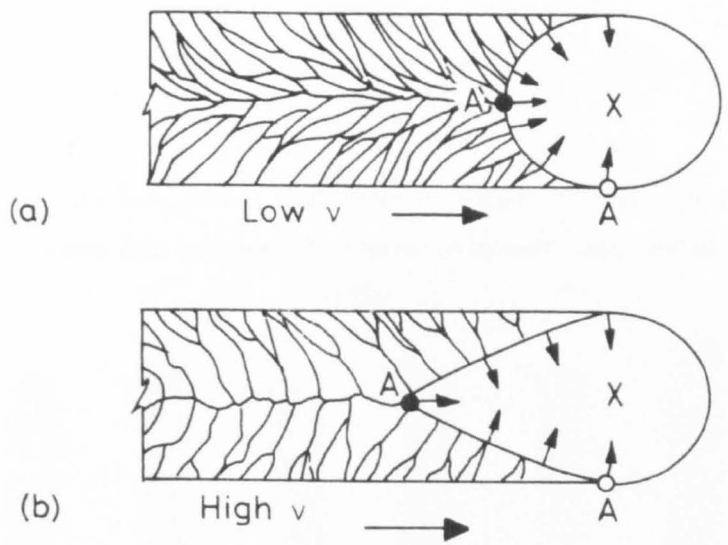

Figure 5.27 – Shapes of weld pools at high and low welding speeds (after Porter 1988)

Liu et al. (Lui 2004) showed by modelling the melt pool geometry of laser remelted single crystal superalloys that the geometry is important in determining the direction of dendrite growth. They showed that for similar pool cross-sections at different beam velocities the direction of dendrite growth can also change as shown in Figure 5.28. This suggests that velocity is a key process variable in breaking up long continuous grains rather than reducing temperature gradient as is key in classic CET maps used by Bontha et al. (Bontha 2006a) which do not take into account pool geometry.

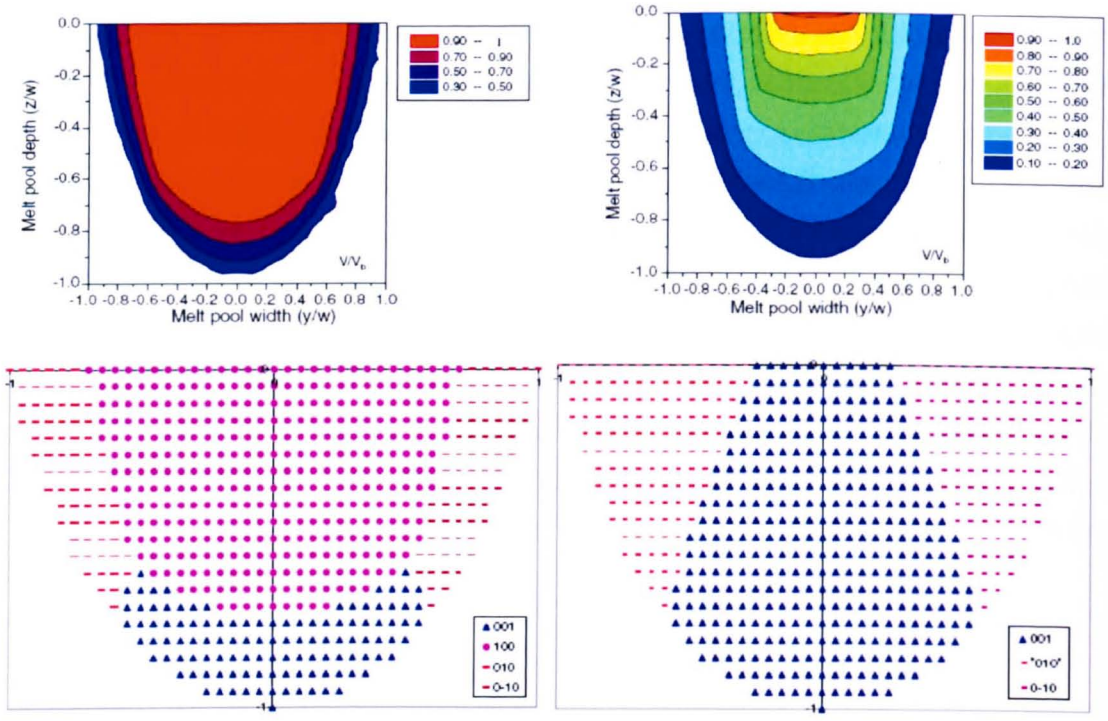

(a) (b)

Figure 5.28 – dendrite growth velocities and directions on melt pool interface (a) highly curved pool analogous to low beam velocity (b) flatter pool associated with faster velocities (Liu et al. 2004)

5.5 Hardness

Vickers microhardness values of the Walls built at the factorial points on the CCD (Walls 1, 2, 3, 4) and the substrate material are plotted in Figure 5.29. The hardness was roughly 300±20H_v which is slightly lower than the measured values for material made on the EOS M270 reported in Section 4.4; this may be a result of the Nitrogen atmosphere used on the EOS compared to the Argon shielding gas used on the DMD or the use of an alternate machine to take the hardness measurements. The values are lower than the equivalent wrought material values in the CES database which are 450±50H_v but this is most likely a result of the laser deposited samples not receiving an ageing heat treatment to produce the precipitation strengthening phase γ".

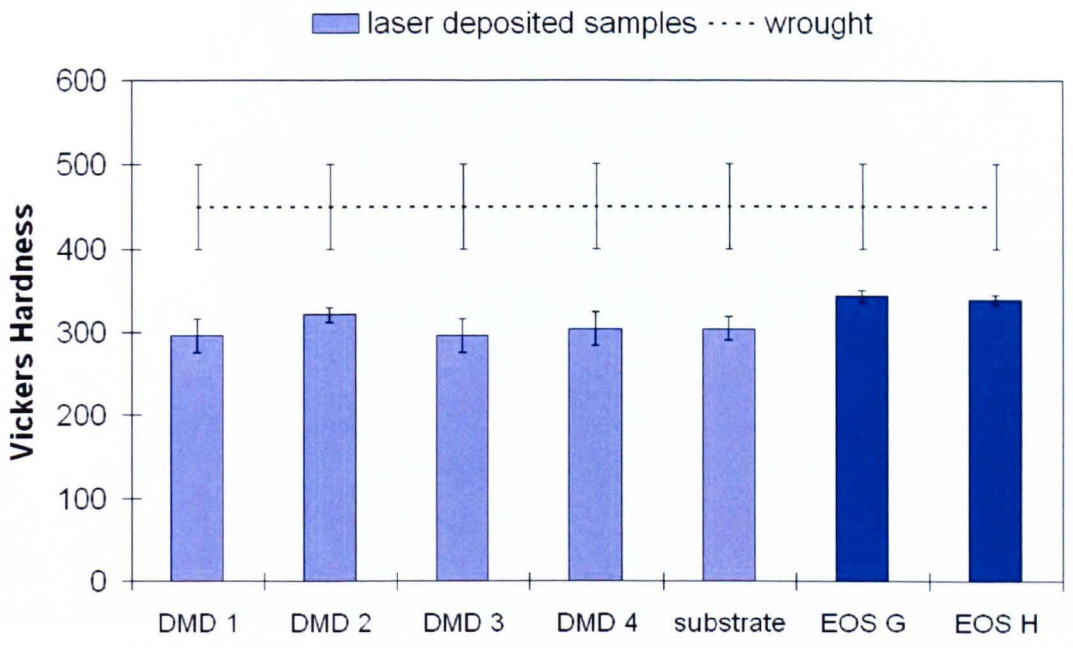

Figure 5.29 -Vickers hardness values for laser deposited Inconel 718 compared to wrought values

5.6 Dendrite arm spacing

Cooling rate has been modelled in Chapters 4.2.2 and 5.3 using analytical heat transfer models. The calculated values were fit to measured meltpools and deposits but the model still requires validation. To support the modelled cooling rates a comparison is made to calculated values based on dendrite arm spacing (DAS). The spacing between primary and secondary dendrite arms varies according to the solidification cooling rate of alloys as previously discussed in Chapter 2.2.

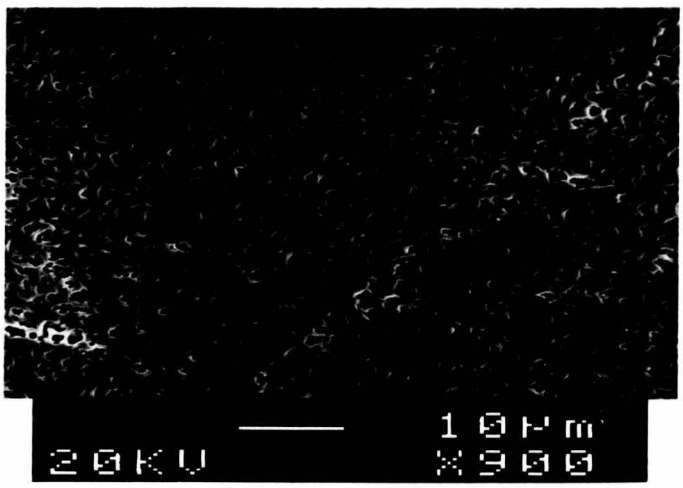

Figure 5.30 - Section of EOS sample I in the XY plane etched to reveal dendritic structure

The as-deposited microstructure is seen to be cellular-dendritic as shown in Figure 5.30 and Figure 5.31 for Inconel 718 deposited using the EOS M270 and DMD 505 respectively. Figure 5.31 shows how the change in scan direction during deposition using the DMD 505 results in primary dendrite arms being melted back and seeding the primary arms in the new layer which take on the growth direction of the secondary arms in the previous layer with an approximately 90° angle between primary arms in adjacent layers.

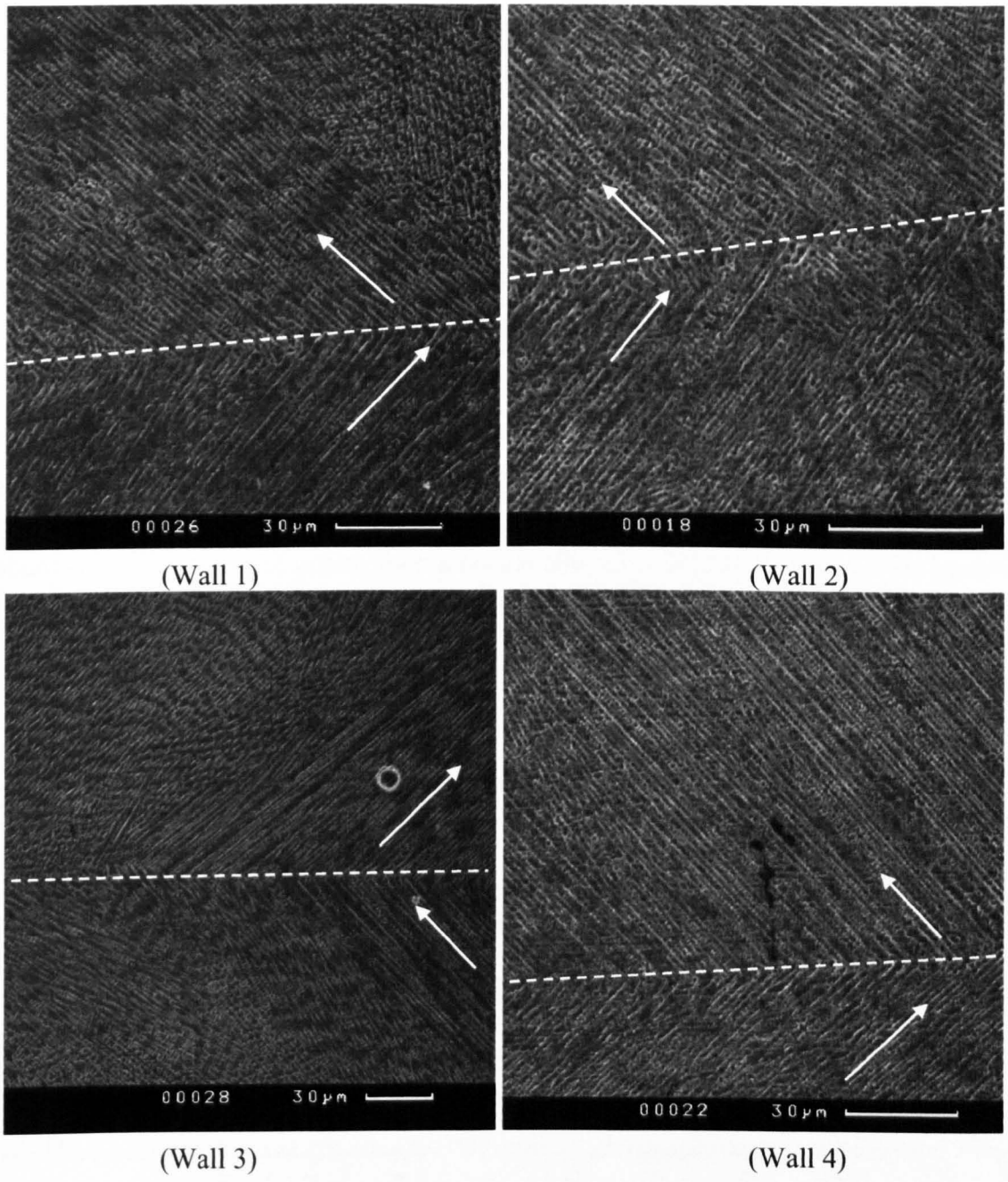

Figure 5.31 – Longitudinal section of the Walls built at the factorial point of the DOE (Walls 1 to 4) using the DMD 505. Dotted lines indicate a layer boundary and arrows the growth direction of primary dendrites.

Several studies have looked at the relationship between DAS and cooling rate specifically for Inconel 718 (Davies 1980, Antonsson 2006). Davies et al. (Davies 1980) compared the microstructures derived from rapidly-solidified, melt-spun Inconel 718 ribbon to those obtained by more conventional processes with slower cooling rates. A relationship linking DAS to cooling rate was devised by comparing and extrapolating rapid solidification DAS to conventionally cast microstructures. The

relationship is given by the following equations for primary (λ_1) and secondary (λ_2) DAS;

$$\lambda_1 = 97 \pm 5\left(\frac{\partial T}{\partial t}\right)^{-0.36\pm0.01}$$

Equation 5.8

$$\lambda_2 = 25 \pm 5\left(\frac{\partial T}{\partial t}\right)^{-0.29\pm0.03}$$

Equation 5.9

The relationship devised by Davies is reproduced in Figure 5.32 where it is seen that dendrite arm spacing becomes increasingly sensitive to experimental error as cooling rates increase. In particular, secondary DAS is very sensitive when cooling rates are in excess of 1000K/s, for this reason a comparison to primary DAS is made for samples produced using the EOS M270 and DMD505 in this study.

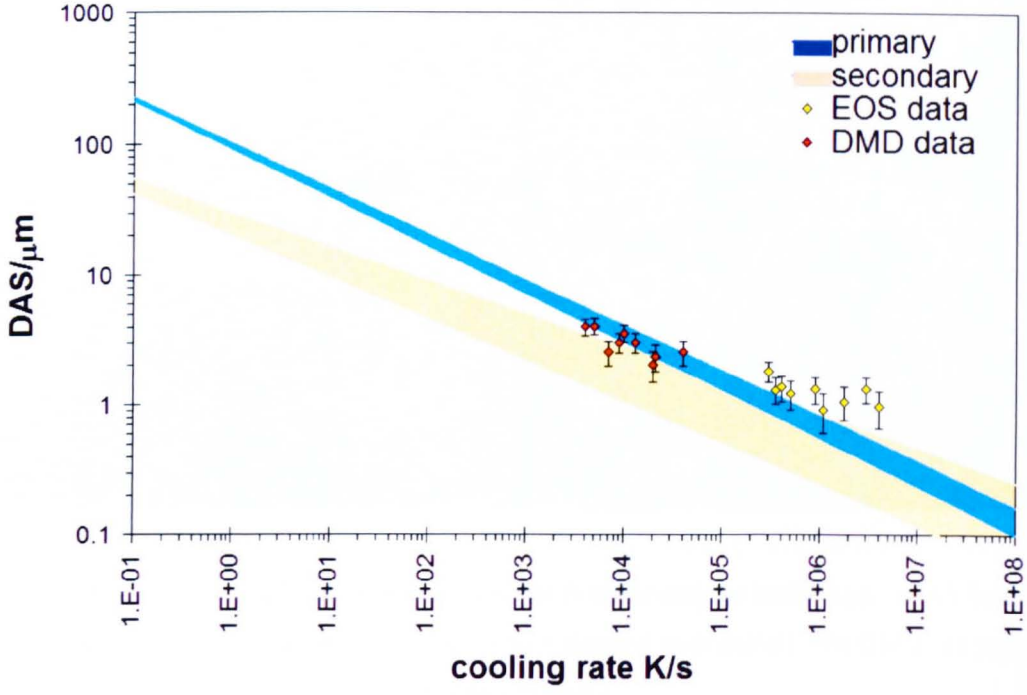

Figure 5.32 – Primary and secondary dendrite arm spacing vs. cooling rate based on Equation 5.8 and Equation 5.9 after Davies et al. Primary DAS is compared to measured values from laser deposited samples produced using EOS M270 and DMD505. Error bars show 95% confidence interval over 10 measurements.

Primary DAS was measured for the Inconel 718 samples produced using the EOS M270 and DMD505, these data were plotted against cooling rates determined using the analytical models presented in Chapters 4.2.2 and 5.3 and are compared to the

expected values of cooling rate from the Davies relationship in Figure 5.32. The measured DAS for the EOS samples were of the order 1-2μm and for the DMD 2-4μm, despite the seemingly small difference between these values the effect on the associated cooling rate is large. The DMD samples show close agreement with the Davies model, the EOS samples which experienced higher cooling rates have slightly higher DAS than expected from the modelled cooling rates but also show larger scatter.

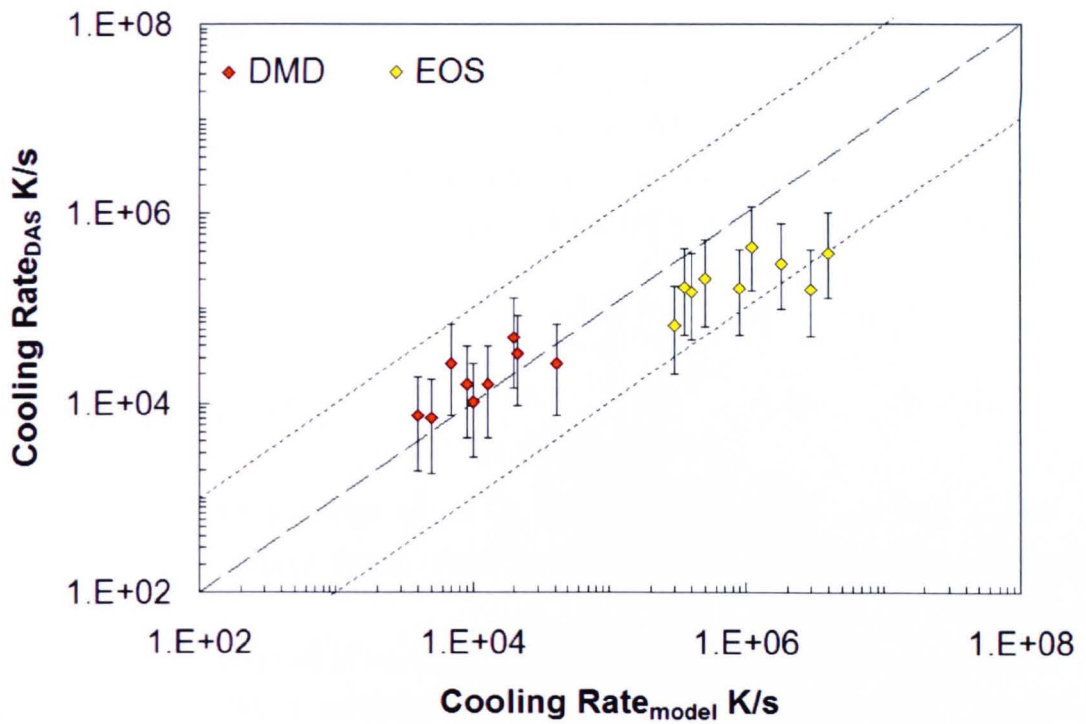

Figure 5.33 - Comparison of cooling rates determined by analyitical model and experimentally determined dendrite arm spacing using the *relationship derived by Davies* et al. Error bars represent the limits shown in Equation 5.8, dashed line indicates agreement between cooling rates obtained by the two methods and dotted lines show +/- one order of magnitude (10%).

There does not appear to be a clear relationship between cooling rate and processing parameters for the experiments carried out on the two processes as the experimental scatter is large compared to the response. The scatter is a result of difficulty in identifying primary arms as well as their different orientations and fine scale which is insensitive to large differences in cooling rate, i.e. an order of magnitude increase in cooling rate would result in a DAS decrease of only 1-2μm at rapid cooling rates.

Figure 5.33 shows the difference between the modelled cooling rates from Chapters 4.2.2 and 5.3 compared to the expected cooling rates determined from measured DAS according to Equation 5.8. It is confirmed that there is good

agreement between the two models for the samples produced by DMD but there is a discrepancy for the EOS samples which experience higher cooling rates, the model tends to overestimate the cooling rate compared those calculated using DAS.

The error in the modelled values of cooling rate for the EOS samples is in some cases an order of magnitude higher than cooling rates calculated using DAS which suggests a significant error in the model. An explanation for this is the use of 80°C as a substrate temperature, T_0, in reality this value is likely to be higher because of the fast rastering of the laser which causes local increases in temperature in the vicinity of the melt pool. This is not a problem for tracks deposited using DMD since the samples produced had a dwell time between layers to allow them to cool to room temperature before the following layers were deposited. Consider the case of a stationary point heat source, i.e. the laser velocity is zero; the temperature gradient at the liquidus isotherm is given by Equation 5.10:

$$G = \frac{dT}{dr} = \frac{-2\pi k(T_l - T_0)^2}{\alpha Q}$$

Equation 5.10

Where T_l is the liquidus temperature, T_0 is the substrate temperature, k is the thermal conductivity, Q is the absorbed laser power and α is the absorption coefficient.

It is seen that temperature gradient, G, decreases as T_0 increases, this is quantified in Figure 5.34 for Inconel 718 with incident laser powers of 78W and 192W which correspond to the upper and lower limits used in the investigation. As T_0 increases by a few hundred degrees, G decreases by a factor of two. There is clearly a greater decrease at lower powers which correspond to higher cooling rates during processing, these samples show the greatest error in Figure 5.32 and Figure 5.33. Adjusting these values to take into account the increase in local temperature caused by the rastering laser would have the effect of reducing the cooling rates bringing them in line with the values calculated using DAS. Figure 5.34 also shows that as T_0 increases the temperature gradients associated with the different power settings converge so that the processing parameters have a less significant effect on the gradient. This will limit further the level of control a user has on the solidification conditions.

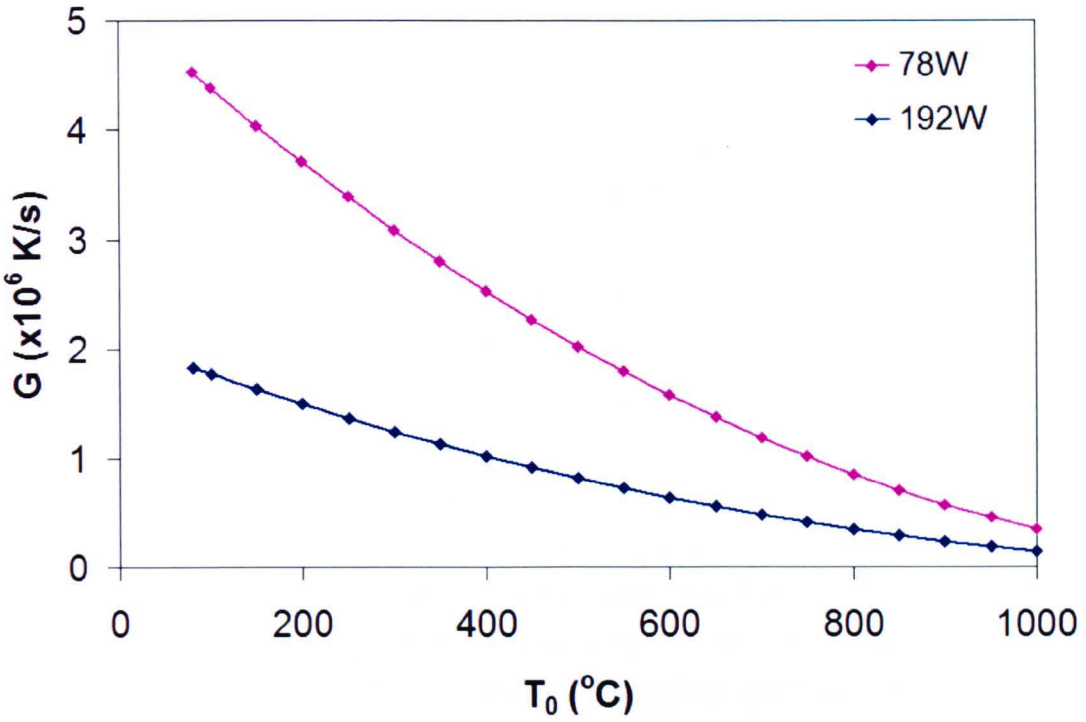

Figure 5.34 – Effect of T_0 on temperature gradient for a stationary point heat source at nominal laser powders of 78W and 192W.

5.7 Chapter summary

A study of the Direct Metal Deposition process was carried out to observe the influence of laser power and beam velocity on the deposit geometry and microstructure.

Single tracks were deposited layer by layer to produce thin wall structures consisting of single tracks deposited one on top of another. The width of the tracks was shown to increase at high laser power and low beam velocities due to the increased energy input and the deposition efficiency increased with higher powers and high beam velocities since the amount of powder delivered to the pool per unit time decreases.

A statistical Design of Experiment in the form of a Central Composite Array was used to investigate the process and was successful in generating an accurate empirical model to describe the track width as a function of laser power and beam velocity, this model was then used in conjunction with a model for a fitting parameter to calculate melt pool geometries and solidification conditions from established analytical heat transfer equations. These were compared to CET maps reported in the literature.

The solidification conditions were used to explain the resulting as-deposited microstructures which varied across the experiment. Grain structures were analysed by EBSD to show how they change with processing parameters and were shown to have three distinct types of microstructure; a mixed structure at high powers and high beam velocities caused by melt pool fluctuations, long zigzag grains which are continuous across multiple layers at beam velocities between 1927mm/s and elongated but non-continuous grains at beam velocities between 11-19mm/s. The choice of parameters is thus dependent on the desired grain structure.

The reasons for the latter two types of microstructures appear to be the transverse shape of the melt pool. At slower beam velocities the pool is more convex towards the substrate which means grains will grow towards the centreline of the wall preventing them from growing epitaxially into the subsequent layers. Under these conditions the longitudinal section of the pool is also more curved which makes it necessary, in some cases, for the grains to become discontinuous within the layer as they are forced to change direction to follow the direction of heat transfer. Where the beam velocity is faster the transverse isotherms are flatter, which allows heat transfer and grain growth to be close to vertical in the central region of the wall with resulting grains being able to grow epitaxially through layer boundaries.

There is also a columnar to equiaxed transition within the deposited track's cross-section; this is limited to a region roughly 50μm thick at the top surface where the combination of high isotherm velocity, low temperature gradient as well as radiative

heat loss make the solidification conditions favourable to give equiaxed grains. In the lower region of the solidifying pool there is good contact between the solid substrate and the melt where conduction dominates and epitaxy is possible making the resulting grains elongated and orientated according to the underlying material which gives rise to a strong texture in the walls.

In order to compare the results for the EOS M270 and the DMD 505, the solidification conditions for both are plotted in Figure 5.35 along with the criteria for CET. It should be noted that the two processes use different lasers sources (DMD CO_2 laser and EOS Yb-fibre) and so the absorption characteristics are not necessarily comparable, however, since the solidification conditions were calculated using a model fitted to the experimental data this difference can be disregarded. The higher power and slower beam velocities of the DMD samples result in lower temperature gradients and isotherm velocities but the difference is not sufficient to put the samples into a purely equiaxed regime, and the solidification conditions are actually similar relative to the CET with the lower region of the solidification front having columnar conditions and the rear moving towards more equiaxed conditions.

The resulting microstructures from the two processes were markedly different. The reason for this is the layer thickness; at 20μm in the EOS only the very bottom of the solidifying region avoids being re-melted, whereas the DMD has a layer thickness of 200μm so a larger proportion of the track is retained during the re-melting stage including those parts of the layer experiencing conditions associated with formation of a mixed microstructure. Also the calculated melt pools show that the EOS pools are longer and flatter than the DMD meaning that more of the solidification front experiences conditions conducive to the formation of columnar grains.

Since both processes show epitaxy between the newly deposited material and the re-melted material underneath, forming equiaxed grains is unlikely in this region for Inconel 718 over the parameters studied here. Significantly reducing temperature gradient with higher laser powers or higher substrate temperatures could move the solidification conditions into the equiaxed regime but this requires practical investigation. Other alloy systems may undergo recrystalisation or phase transformations to produce an equiaxed structure.

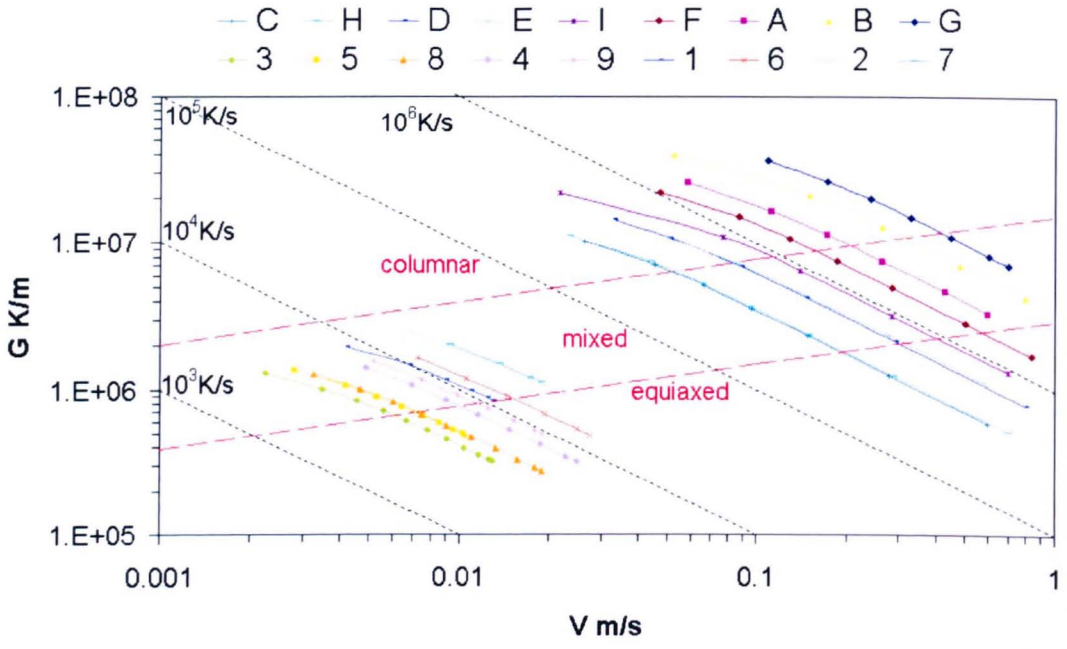

Figure 5.35 - Comparison of EOS M270 (data points on the right) and DMD505 (data points on the left) solidification conditions

6 Materials issues and theme development for Additive Layer Manufacturing

As mentioned at the beginning of Chapter 4, it has been necessary to develop the processing parameters for a new material (Inconel 718) for use on the EOS M270, and that initial experiments were performed after consideration of the material properties and known processing theme of a commonly used material on the same machine (CoCrMo). This procedure is described in more detail in the current chapter and is expended to consider many other materials by plotting performance indicators of alloys and alloy groups on material selection charts. This will aid the development of new materials for the process and show how consideration of candidate alloys for ALM can be undertaken in a more efficient way by considering an alloys thermo-physical properties and how problem alloys can be identified in advance and what might be done in terms of process, equipment and alloy modification to accommodate these issues rather than discovering problems through costly or ineffective experimentation. Emphasis is placed on considering and identifying trends and tendencies in material properties of alloys not absolute values.

Powder-bed type systems are given more emphasis since these are more commonly used to manufacturing components directly, compared to blown-powder systems which are mostly used for cladding and repair.

6.1 Issues in additive layer manufacturing

Additive Layer Manufacturing is not widespread as a manufacturing process compared to standard techniques such as casting and machining, this is due to several factors;

- It is a relatively new technology.
- Poor knowledge of the process by organisations that could utilise it. This means that ALM requires continued promotion throughout the engineering and manufacturing world.
- It is associated with Rapid Prototyping and other such applications which do not extend into structural part production.
- There are relatively few alloys which can be processed at present, i.e. alloys which have tried and tested processing *themes* to produce fully dense parts consistently.
- It is not currently suitable for production of very large parts.

The latter is discussed in this section with a view to identifying ways to expedite the development of new materials through consideration of material properties and their expected response to processing conditions.

Due to the high production costs associated with additive manufacturing methods (which arise due to the high cost of machines and raw materials) its applications to date have centred around products with high added value, i.e. products made from materials which cannot be easily cast or machined, or products which can benefit from the design freedoms associated with ALM. Examples of these are; the cobalt-chrome-molybdenum alloys which work-harden during machining and have long freezing ranges making them inappropriate for casting, or tool/maraging steels used for injection moulding and die-casting tools which can take full advantage of conformal cooling channels to improve productivity and justify higher manufacturing costs.

The benefits of ALM will only be fully exploited when it has been accepted as a manufacturing route and is considered in the design of a component and when alloys exist which are specifically tailored for additive processing. Until such time, ALM processes will have to process existing alloys and build existing components which are not necessarily optimised for the process.

To minimise the risks taken when developing a parameter *theme* for a new alloy and establish starting parameters for experimentation it is useful to consider materials

which are already successfully in ALM processes (such as CoCr, stainless steels and maraging steel), their tried and tested processing parameters and their thermo-physical properties. This is attempted in this chapter using Cambridge Engineering Selector 2008 (CES Selector 2008 Software, Granta Design Ltd., Cambridge, UK 2008) to plot charts comparing some properties of different alloys and alloy classes making it possible to reverse engineer the themes used to process existing ALM materials.

6.2 Theme development rationale based on material properties

6.2.1 Consideration of melting

It was shown in Chapters 4 that the basis for a material *theme* for powder-bed ALM systems can, in part, be developed using efficient experimentation and process modelling in order to minimise effort. Before starting costly experiments it is useful to consider the material properties of an alloy, how these would affect the melting characteristics during laser melting and how processing parameters can be manipulated to change these. Doing this would make it possible to identify alloys which may be problematic for ALM processing and make necessary adjustments to the process before experiments begin, such as alloys which are difficult to weld and require pre-heating or surface treatment. With time, the number of alloys available to ALM will increase and a better understanding of how different materials respond during processing will make it possible to accurately select processing parameters prior to experimenting, or at least narrow the window to provide starting parameters to then optimise. This procedure is discussed in this Chapter by highlighting key material properties to consider.

A minimum melt depth is necessary to build a fully dense part and the size of a melt pool is related to several materials properties; the thermal conductivity, k, the absorptivity, η, and the melting temperature, T_m. For a given heat input:

- A highly conductive material will have a smaller melt pool as the heat is dissipated away from the heat source faster.
- A material with low absorptivity (or high reflectivity) will have a smaller pool as the coupling efficiency of the incident laser is lower.
- A higher melting point alloy requires more energy to melt.

These effects are apparent when the special case of a stationary point heat source on a surface is considered as described in Figure 6.1 and Equation 6.1 where it is seen that for a given power input and substrate temperature, the radius of the isotherms

decreases directly with absorptivity and inversely with conductivity and melting temperature.

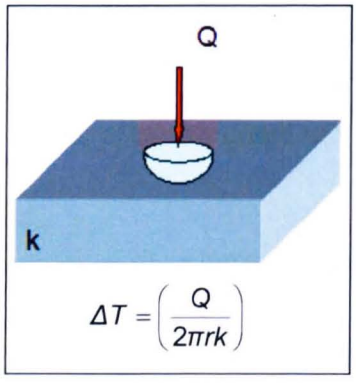

Figure 6.1 – Heat transfer for a stationary point heat source and governing equation

$$r = \left(\frac{\eta Q}{2\pi k\left(T_l - T_0\right)}\right)$$

Equation 6.1

Where r is the distance of the melting isotherm from the point source, η is absorptivity, Q is laser power, k is thermal conductivity, T_l is liquidus temperature and T_0 is the far-field or substrate temperature.

Materials with high conductivity, high melting temperatures and low absorptivity will have a lower maximum deposition rate, i.e. on a design space such as that in Figure 6.2 the red contour (which indicates the limit of processing speed to maintain a part's integrity) will be moved to the left, the converse being true for alloys with low conductivity, low melting temperature and high absorptivity. It follows that materials in the former category require higher powers, lower beam velocities or smaller track offsets to achieve the same melt depth and, as shown in Figure 6.2, this is at the expense of processing speed which is indicated by the black arrow.

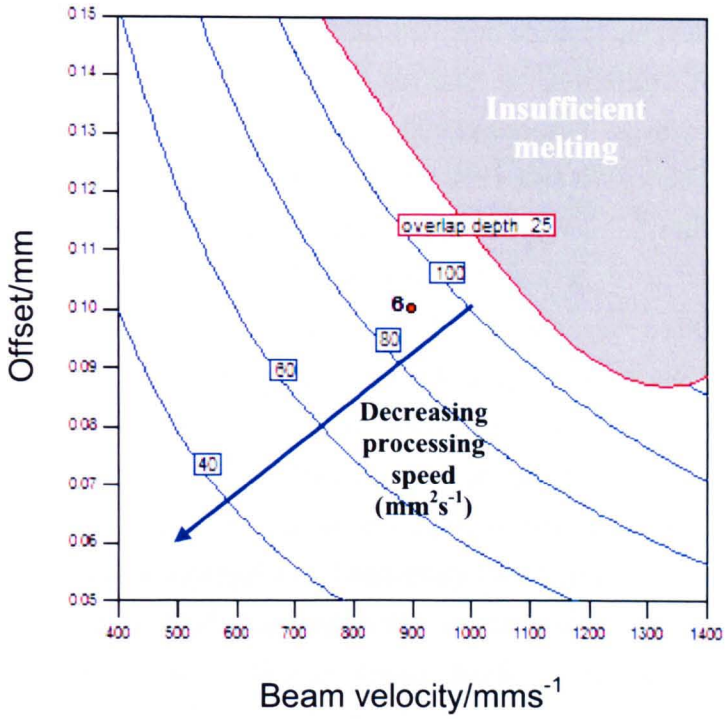

Figure 6.2 - Overlay plot showing the effect of beam velocity and track offset on processing speed and melt depth in the region where adjacent tracks overlap (μm, outlined in red). Also highlighted is the limit where melting is not sufficient to produce fully dense parts. Blue arrow indicates the effect of beam velocity and track offset on overall processing speed

Figure 6.3 shows a bubble chart produced using CES 2008 in which a comparison of melting range and absorptivity for different alloy classes is made. A number of engineering alloys are highlighted including several which are commonly processed by ALM. It is seen that several alloy types (including Nickel-based and Steels) fall in a small window on the chart having similar properties with the obvious exceptions being Ti and Al alloys, the former having higher melting temperatures and higher absorptivity and the converse being true for Al. The absorptivity was calculated using the Bramson Formula (Equation 6.2) which was discussed in Section 2.3 and plotted in Figure 6.3(a) and (b) for different wavelengths of radiation corresponding to CO_2 and Fibre lasers (10.6μm and 1.06μm respectively);

$$\eta_\lambda(T) = 0.365\sqrt{\frac{\rho(T)}{\lambda}} - 0.0667\left(\frac{\rho(T)}{\lambda}\right) + 0.006\sqrt{\left(\frac{\rho(T)}{\lambda}\right)^3}$$

Equation 6.2

Where $\eta_\lambda(T)$ is absorptivity at a given temperature and wavelength (λ) and $\rho(T)$ is electrical resistivity at the given temperature.

There is a clear difference between the absorptivity of alloys when using different wavelengths of radiation, at shorter wavelengths indicative of fibre lasers the absorptivity increases. The calculated absorptivity for Inconel 718 at a wavelength of 10.6μm is between 11% and 12% which is similar to the values of fitting parameter, α, used in Section 5.2.2 where values in the range 10% and 13% were used to fit an analytical model to experimental data. Similarly, for absorptivity of radiation with wavelength 1.06μm the calculated values for Inconel 718 were between 31% and 32%, this is similar to the values of α used in Section 4.2.1 for experiments conducted at lower laser powers. As the power increases this value of α increases due to convection being more dominant in larger melt pools, resulting in a change in size and shape which is not in line with pools where conduction is dominant. It can be concluded that the fitting parameters used in Chapters 4 and 5 are analogous to the absorptivity when conduction is the dominant heat transfer mechanism in the meltpool.

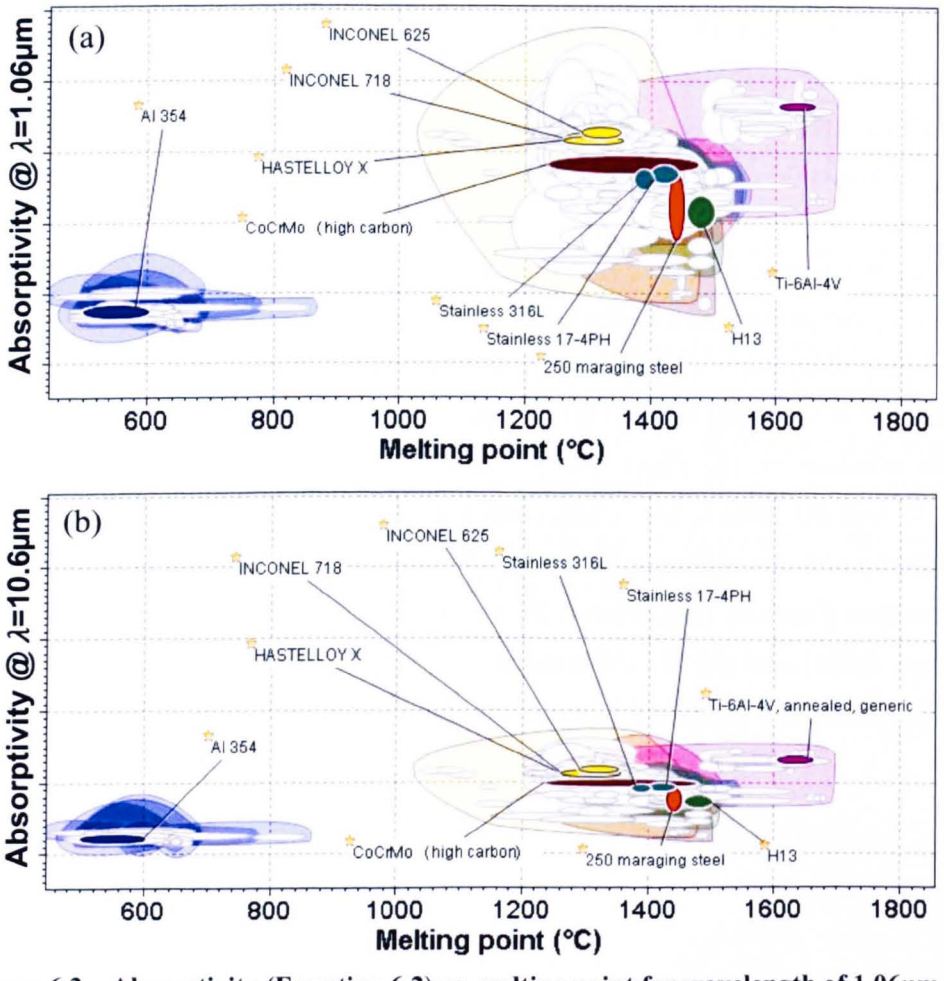

Figure 6.3 – Absorptivity (Equation 6.2) vs. melting point for wavelength of 1.06μm corresponding to fibre lasers (a) and 10.6μm (b) corresponding to CO_2 lasers. [Alloy classes: blue = Al, yellow = Ni, brown = CoCr, pink = Ti, red = high alloy steels, green = tool steels, teal = stainless steels]

Two alloys of particular interest are Inconel 718 and CoCrMo, Inconel 718 is shown to have slightly higher absorptivity and lower liquidus temperature which implies that less energy is required to melt it.

The key materials properties are also shown in Figure 6.4 and Figure 6.5, it is seen that within an alloy class there is considerable variation in Absorptivity and Thermal Conductivity but less in Melting temperature. It should also be noted that many engineering alloys have similar melting temperatures, indeed Nickel alloys, Cobalt based and Steels all have similar melting temperatures but vary more in terms of conductivity and absorptivity. Ti and Al alloys have relatively high and low melting temperatures respectively, this might suggest that Al would be easier to melt then Ti, but Al also has high reflectivity and conductivity, which would make it difficult to melt using a laser. Figure 6.4 shows a strong inverse relationship between Absorptivity and Conductivity, this is a result of the link between electrical and thermal conduction in solids being related to electronic effects. This is described by Equation 6.3 which is known as the Wiedemann-Franz Law (Mahan 1999):

$$K_e = L_0 \sigma T \left(\frac{k_B}{e} \right)^2$$

Equation 6.3

Where K_e is the thermal conductivity of electrons, L_0 is a dimensionless constant equal to $\pi^2/3$ for metals, σ is thermal conductivity, T is temperature, k_B is Boltzmann's constant and e is the electron charge.

This means that the absorptivity is intrinsically linked to thermal conductivity due to Equation 6.3 as electrical resistivity is equal to reciprocal conductivity. It follows that metal such as aluminium which has a high density of free electrons is a good reflector since electrons at the surface hinder coupling of the incident energy (Zhao 1999) and also has a high thermal and electrical conductivity.

Using the charts in Figure 6.3, Figure 6.4 and Figure 6.5 it is possible to see that despite Al having a low melting temperature, it will still be difficult to melt using a laser, and conversely, Ti, has a high melting temperature but low conductivity/high absorptivity and so may not be as difficult to melt as might be expected. Other engineering alloys which are of interest in ALM are highlighted in Figure 6.3 to Figure 6.5, these include Inconel 718 which has been extensively studied in this investigation, two other Ni-base high temperature alloys, Inconel 625 and Hastelloy-X, CoCrMo which is a commonly used in ALM and 316 and 17-4 Stainless steel which are also often used in ALM. All of these alloys are shown to have similar melting temperatures but vary in absorptivity and thermal conductivity. The Ni alloys have higher absorptivity and lower conductivity than the others, CoCrMo is

intermediate in both and the stainless alloys have low absorptivity/high conductivity. For these reasons it can be speculated that the Ni alloys can be processed with faster beam velocities (or at lower powers, but in the interest of minimising build times this would not be beneficial), it follows that CoCrMo requires lower speeds and the stainless steel alloys lower still to sufficiently melt a consistent depth of material without reducing track offset and counteracting the increase in melting rate caused by the faster beam velocity.

This approach is based on the melting response of a material only and so is not a complete description of all the relevant mechanisms which are taking place during laser melting. Further to this, the rapid thermal cycling and the large temperature gradients associated result in complex thermal histories and the generation of large stresses. This is a crucial consideration when processing any material by ALM and is discussed in the following section.

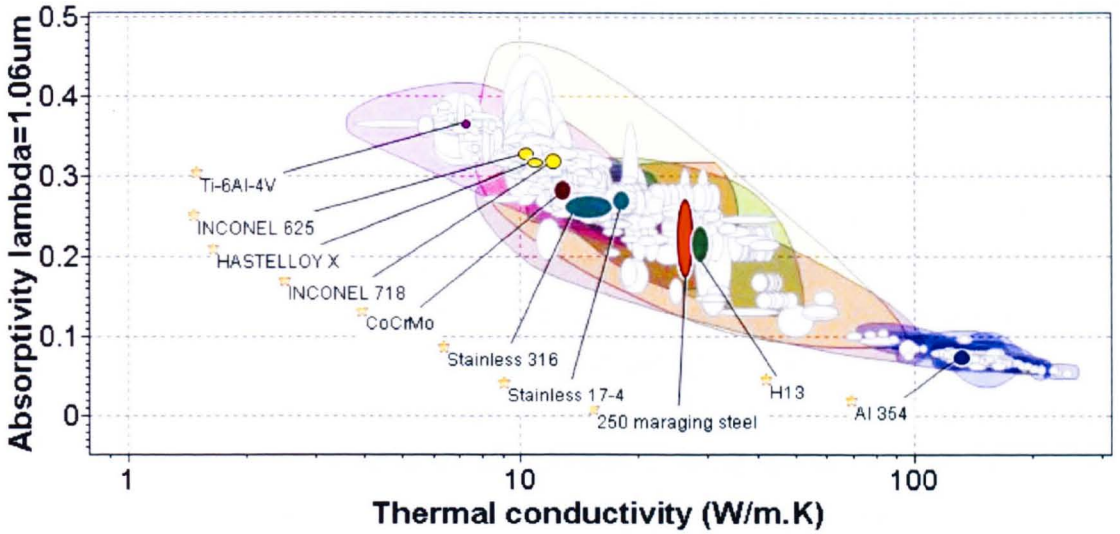

Figure 6.4 - Absorptivity (Equation 6.2) at 1.06μm vs. thermal conductivity [Alloy classes: blue = Al, yellow = Ni, brown = CoCr, pink = Ti, red = high alloy steels, green = tool steels, teal = stainless steels]

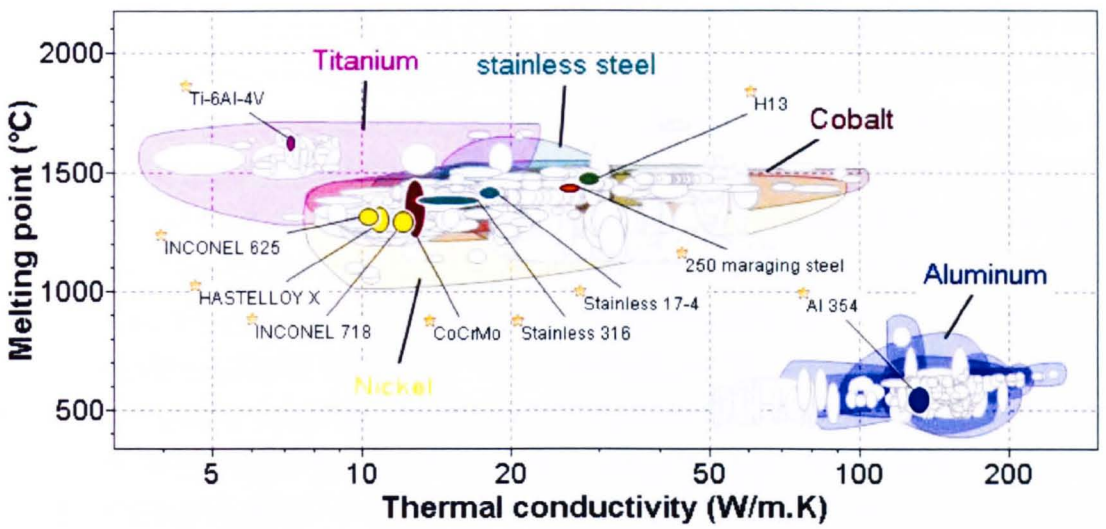

Figure 6.5 – Melting point vs. thermal conductivity [Alloy classes: blue = Al, yellow = Ni, brown = CoCr, pink = Ti, red = high alloy steels, green = tool steels, teal = stainless steels]

6.2.2 Consideration of residual stress

One area not yet discussed is the relevance of residual stresses caused by the heating and cooling during the laser heating/melting process used in ALM.

Residual stresses combine with in-service stress and when these act in the same direction they combine so that a component experiences a higher stress than expected form service (Withers 2001 part I and II). Thermally induced stresses arise due to thermal mismatch or sharp temperature gradients. Three types of stress exist and are defined according to the length scale they are applied; Type-I are macro-stresses which span large distances on the scale of a components size and vary continuously, Type-II and –III are micro stresses, the former act over the scale of grains or across different phases in a material and the latter act on the sub-grain or atomic scale. In ALM Type-I stresses are most relevant. The relaxation of stresses can take place in several ways, for example, plastic flow (when the residual stress exceeds the materials' yield stress), creep (at elevated temperatures) and micro-cracking (when the fracture stress is exceeded.

Residual stress in ALM has been reviewed in a number of studies; Matsumoto et al. (Matsumoto 2002) considered the role of residual stress when melting an unsupported overhanging layer where melting occurs on to the loose powder-bed (no solid material underneath) for a Ni-Cr-Fe alloy. The problem faced was the deflection of the melted layer vertically upwards which prevents melting of subsequent layers and even causes cracks due to the stresses generated. The scanning pattern was modelled as a simple back and forth raster in the x direction which results in a striped stress state of tensile and compressive stresses perpendicular to the scan direction with magnitudes of 275MPa and -100MPa. The processing conditions were as follows; power = 1kW, beam velocity = 4mm/s, beam diameter = 0.75mm. The model showed that the defection of the melted layer was reduced when the scan length was reduced and the authors suggest segmenting the melt area into small squares with reduced scan lengths to minimise the overall distortion of the layer. Similar conclusions were draw by Mercelis et al. (Mercelis 2006) and Kruth et al. (Kruth 2004) the former used an analytical model and experiment to consider several factors which influence stress in Selective Laser Melting of 316L stainless steel and the latter melted a single layer of Fe-base alloys onto 1mm steel plate and measured the deflection of the plate caused by the stresses generated. Mercelis et al. showed that a stress distribution exists from the top to the bottom of a part built by ALM; the top has a small region of tensile stress (as high as 120MPa), the middle is under compression at ~50MPa and the bottom region is again under tension. This was measured for samples built at parameters of; power = 100W, V_b = 400mm/s, for a layer thickness of 30μm. The

authors also used XRD to measure residual stresses as high as 200-300MPa with a 100MPa difference between stresses in the x and y directions when scanning was in a single direction, similar to Matsumoto, they suggest segmented scanning and showed that this would reduce the maximum stress and the anisotropy.

Kruth et al. and Mercelis et al. (Kruth 2004, Mercelis 2006) attribute the stresses generated in ALM to the Temperature Gradient Mechanism (TGM) which is the phenomenon which causes the displacement during laser forming of sheet metal that causes it to bend (Watkins 2001, Cheng 2000, Cheng 2001). The TGM results in a bending moment being produced in unconstrained material or a stress in constrained, it also explains the deflection observed in thin section butt welds. In ALM the underlying material acts to constrain the upper layers which want to bend towards the laser, this is caused by the steep temperature gradient imposed by the heat source across a thickness of material which causes a differential thermal expansion through the thickness. The upper surface is heated which results in a reduction in strength, material beneath the source expands but is constrained by the surrounding cooler material. This places the heated material in compression, when this compressive stress exceeds the heated material's yield stress it is plastically deformed so that on cooling to ambient temperature the upper layer is effectively shorter than when it started and hence puts the upper surface in tension which causes bending towards the laser in unconstrained sheet or residual stress in bulk samples like in ALM.

The thermal history of a part built on a powder-bed ALM system is very complex and difficult to describe in detail but ultimately there exists a stress state in any part after it is built unless the temperature of the build chamber is sufficient to allow recovery mechanisms to take place. If the temperature is not high enough the stress will remain until a stress relieving heat treatment is carried out on the part or if the magnitude of the stress is greater than the material's yield strength it will cause the part to distort or crack.

The EOS M270 used in this project operates with a build chamber temperature of 80°C which equates to homologous temperatures between 0.18 and $0.22T_m$ for the alloys highlighted in the previous section. This is not sufficient for any stress relieving to take place through recovery or diffusion creep, for this to happen a homologous temperature of at least $0.5T_m$ is necessary for some alloys, but high temperature alloys used in the aerospace industry are specifically designed to resist these processes so temperatures in excess of $0.7T_m$ would be necessary for several hours. In the case of Inconel 718 the recommended stress relieving heat treatment is equivalent to a full anneal at 955°C for 1 hour per 1 inch section (Chandler 2006), similarly Hastelloy X requires 1175°C for the same time. Since the ALM process involves melting it is only at temperatures below the solidus that stresses are induced. There will be a minimum

temperature where thermal expansion is negligible for each alloy and it is this temperature range which is critical for the formation of stresses.

Attempting to model the stress is outside the scope of this project but it is possible to consider the factors influencing the magnitude of the thermal stresses generated as a function of material properties. Equation 6.4 shows how thermal stress is proportional to Young's modulus (E), thermal expansion coefficient (α_{CTE}) and the temperature difference (ΔT) imposed on the surface being heated, the first two factors are material specific properties whereas the latter is governed by the processing parameters.

Thermally induced strain: $\varepsilon_T = \alpha_{CTE}\Delta T$, (Barber 1971, Yoshimoto 1999) so in a biaxial system where material is constrained the induced thermal stress is:

$$\sigma = \left(\frac{E\alpha}{2(1-\nu)}\right)\Delta T$$

Equation 6.4

The temperature range is itself a function of the power used to heat the target (Q), the thermal conductivity (k) of the alloy and a shape function, F. Figure 6.6 shows how different heating methods have different shape factors, (a) is planar heat transfer, (b) is a stationary point heat source and (c) is a moving point heat source as described by the Rosenthal solution (Rosenthal 1946). The relevant processing parameters in laser heating/melting are laser power and beam velocity which are important in determining the shape factor of the isotherms and hence the distance over which the thermal stresses are relevant.

$$\Delta T = f\left(\frac{Q}{k}\cdot F\right)$$

Equation 6.5

From Equation 6.4 and Equation 6.5 it is clear that the materials properties most important in determining the magnitude of thermal stresses are; thermal expansion coefficient, Young's modulus and thermal conductivity. These can be expressed as a *Stress Performance Index* (Equation 6.6) which incorporates all of the relevant material dependant properties to give an indication of their contribution to the magnitude of the thermally induced stress.

$$\sigma_{PI} = \left(\frac{E\alpha}{2k(1-\nu)} \right)$$

Equation 6.6

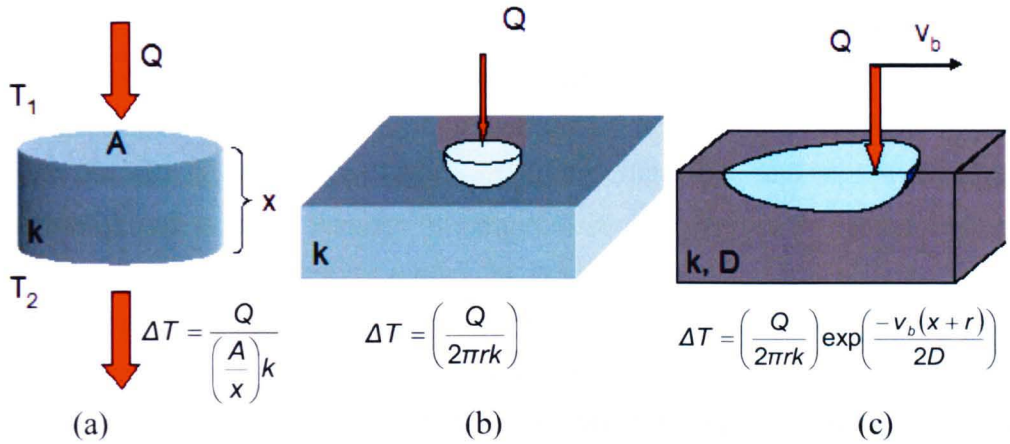

Figure 6.6 – Governing equations determining shape of isotherms for the conditions; (a) planar heat transfer, (b) a point heat source and (c) a moving point heat source (Rosenthal 1946).

Performance Indices make it possible to compare the material response of different alloy classes to heating and cooling cycles associated with ALM. A *Performance Index* (PI, also known as a Material Index) is used in the design of a component where the design is specified by three requirements; functional requirements (*F*, such as load baring capability, heat transfer, and energy storage), geometry (*G*) and materials properties (*M*). The performance can be measured in a general form by Equation 6.7:

$$P=f(F, G, M)$$

Equation 6.7

Where *P* is an aspect of performance of a component to be optimised and *f* is an unknown function. A design can be optimised by selecting a material or geometry to maximise or minimise a given aspect of performance based on imposed constraints to describe a real situation. This process can also be used to compare the performance of different materials under the same conditions for a standard geometry.

The CES Software has pre-defined *Performance Indices* and two examples which may be of interest are *Thermal Stability* and *Thermal Shock Resistance* (*TSR*), the former gives an indication of how much a given material will deflect for a given geometry and heat input and is a key consideration in laser forming of sheet materials (Watkins 2001). Watkins et al. showed that Ti-6Al-4V and AA2024 T3 alloys have different responses to the same conditions because Al has a higher thermal

conductivity than Ti which results in a lower temperature gradient through the sheet thickness. *Thermal Shock Resistance* is an indication of how a material resists cracking due to increasing temperature for a known heat input and geometry. Yoshimoto et al. (Yoshimoto 1999) carried out quench tests on brittle materials (cemented carbide, Cermet, Si nitride SN-220) and medium carbon steel (JIS45C) to investigate *TSR*. *TSR* is related to a critical temperature difference ($\Delta T_c = T_{furnace} - T_{quench}$); for a material which experiences ΔT_c there is an abrupt decrease in bend strength due to the formation of thermal cracks which form to accommodate the thermal stress generated by the temperature gradient, the larger the ΔT_c that can be tolerated before this loss in bend strength the greater a materials *TSR*. Yoshimoto showed that the stress generated was proportional to the thermal expansion coefficient (α_{CTE}), Young's Modulus (E) and the temperature difference experienced (ΔT).

Assuming dimensional stability is desirable i.e. there is little movement induced by the heating process, the performance of a material can be measured by maximising the thermal conductivity and minimising (α_{CTE}), i.e. maximising the performance indicator k/α_{CTE}. For good thermal shock resistance it is necessary to maximise the performance indicator $\sigma_{YS}/(E \cdot \alpha_{CTE})$, where E is Young's Modulus. Again a low α_{CTE} is desirable and a material must be strong but low in stiffness. These are plotted on a material selection chart in Figure 6.7 and Figure 6.8, the former shows some common alloy classes (Ni, Ti, Stainless Steel, Co, Al) and the latter highlights some alloys used in ALM and other common engineering applications as previously indicated in Figure 6.3, Figure 6.4 and Figure 6.5.

Figure 6.7 shows that Aluminium alloys typically have good dimensional stability despite their high CTE because of their high thermal conductivity but they have low and moderate resistance to cracking because of their relatively low Yield Strength. Aluminium alloys also have relatively low stiffness which means that the thermal stresses generated should be relatively low (Equation 6.6). It has previously been shown in Figure 6.3 that Aluminium alloys have very low absorptivity of infrared radiation so despite their good stress performance index they are still potentially difficult to process by ALM even though they have relatively low melting temperatures.

Figure 6.7 also shows that some Titanium alloys exhibit good thermal shock resistance because of their high strength but relatively poor dimensional stability because of their low thermal conductivity despite also having low α_{CTE}. Other engineering alloys such as Nickel, Cobalt-Chrome and Stainless Steel alloys lie in between Aluminium and Titanium with some exceptions in the problematic region of low thermal stability and low shock resistance. Tool steels and Maraging steels appear to have good values for each of the performance indices but two alloys which stand

out are Nickel alloys in the top right corner of the diagram, these are INVAR alloys, Ni-Fe based alloys in the cold worked and annealed conditions. Their performance indicators suggest that they are likely to have low thermal distortion and good resistance to cracking which is attributable to their very low α_{CTE} of 1.25-2 μstrain/°C (CES 2008).

Figure 6.8 highlights some specific alloys including the alloys discussed in Section 6.2. At the lower end of the *Performance Indices* are some useful engineering alloys such as Inconel 625 and Hastelloy-X Ni-based alloys and Stainless Steel 316L. Their position on the material selection diagram (Figure 6.8) suggests that these alloys may be problematic with regards to their thermal stability and resistance to cracking on heating. This is not to say that they cannot be used for ALM but that consideration of the stress generated is necessary when choosing processing parameters.

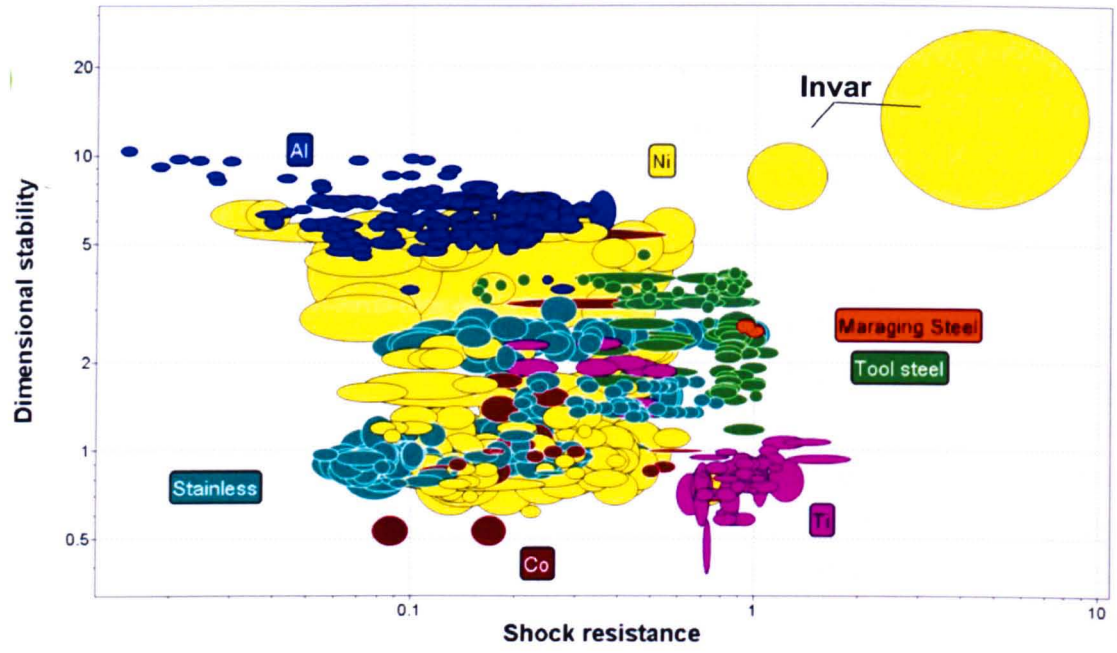

Figure 6.7 – Performance index plot of thermal shock resistance vs. dimensional stability [alloys classes: blue = Al, yellow = Ni, brown = CoCr, pink = Ti, red = high alloy steels, green = tool steels, teal = stainless steels]

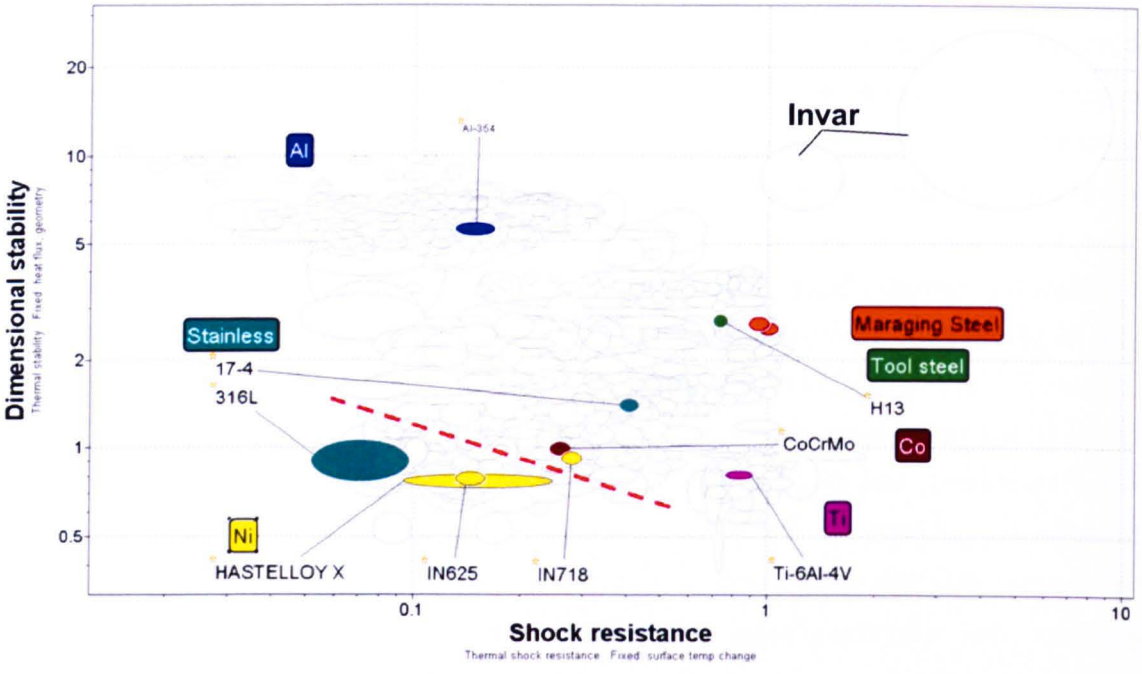

Figure 6.8 –Performance index plot of thermal shock resistance vs. dimensional stability [alloys classes: blue = Al, yellow = Ni, brown = CoCr, pink = Ti, red = high alloy steels, green = tool steels, teal = stainless steels]

Figure 6.9 and Figure 6.10 show material selection diagrams of the absorptivity (Equation 6.2) versus stress performance index (Equation 6.6), Figure 6.9 shows the different alloy groups and Figure 6.10 highlights some alloys of interest to ALM and other engineering applications. It is generally seen that alloys with a low stress performance index have a low absorptivity to infrared radiation on account of the material's electronic structure, i.e. a low stress performance can be attributed to a high thermal conductivity and, in metals, a high thermal conductivity is synonymous with high electrical conductivity. The free electrons in metals at the surface hinder the coupling of energy, indeed, as the density of these free electrons increases the coupling is further reduced, as a result, metals such as Aluminium have high conductivity and low absorptivity as shown in Figure 6.3 and Figure 6.9. This phenomenon also supports Equation 6.2 which describes absorptivity as proportional to electrical resistivity i.e. reciprocal conductivity. It follows that there is a conflict as high conductivity means a low stress performance but poor absorptivity, in order to maintain low stresses and higher absorptivity the key material properties are α_{CTE} and Young's Modulus.

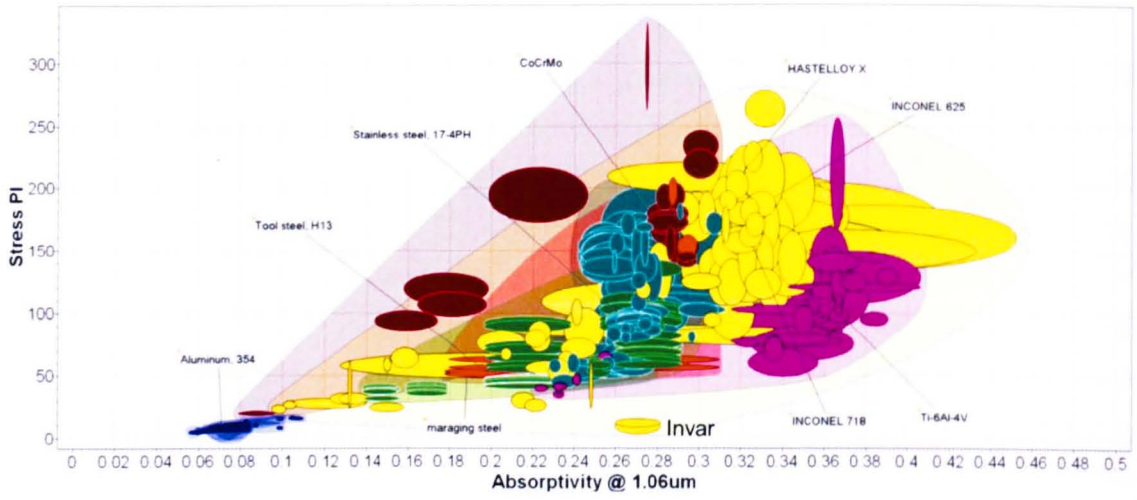

Figure 6.9 –Absorptivity (Equation 6.2) vs. stress performance index (Equation 6.6) [alloys classes: blue = Al, yellow = Ni, brown = CoCr, pink = Ti, red = high alloy steels, green = tool steels, teal = stainless steels]

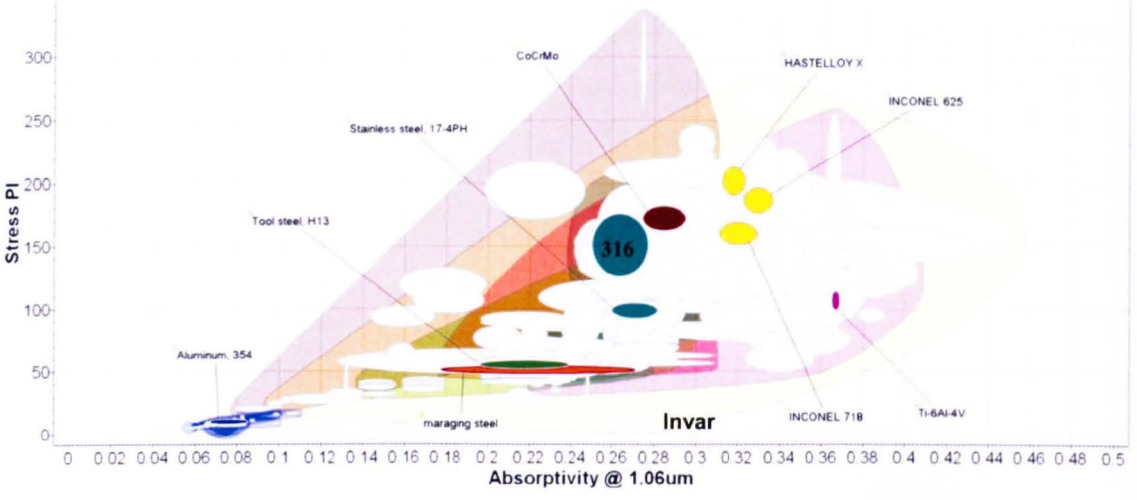

Figure 6.10 –Absorptivity (Equation 6.2) vs. stress performance index (Equation 6.6) [alloys classes: blue = Al, yellow = Ni, brown = CoCr, pink = Ti, red = high alloy steels, green = tool steels, teal = stainless steels]

On-going work at the Universities of Sheffield and Manchester has shown that the magnitude of residual stress in CoCrMo samples built using an EOS M270 is as high as 900MPa when measured by The Contour Method (Moat 2009) (this is shown in Figure 6.11 (the residual stress measurements and analysis were carried out by Dr Wufei Zhang at the University of Sheffield courtesy of Dr Iain Todd and Dr Richard Moat at the University of Manchester courtesy of Professor Michael Preuss). There is a tensile stress at the parts edges and a compressive stress towards the centre which increases towards the top of the part. The part is a 20mm square cross-section, 40mm in length built with the longest dimension in the z-axis and a layer thickness of 20µm, with laser parameters of 195W, 800mm/s. The scanning pattern consists of 4mm stripes as described in Chapter 3.1.1.2. Similar parts were subjected to a stress relieving heat treatment which did not completely remove the residual stress but reduced it significantly. This work is part of an on-going study to compare different alloys built using the EOS M270.

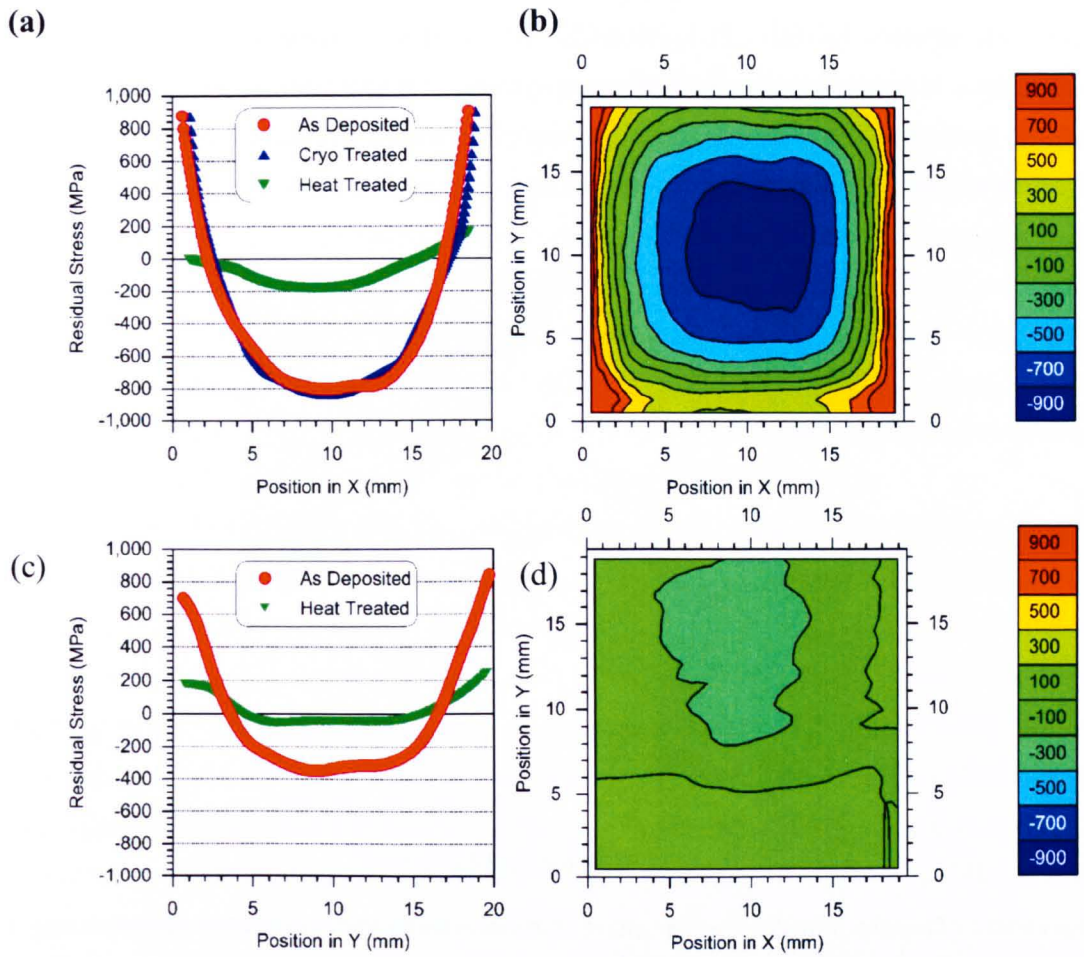

Figure 6.11 – Residual stress measured using The Contour Method for EOS CoCr built using EOS M270. (a) stress profile in 10mm form top surface (b) contour map of residual stresses (MPa) (c) stress profile 10mm for the bottom of the part (d) contour map after heat treatment at 850°C for 2 hours.

6.2.3 Effect of processing on residual stress

Further to material properties, the processing conditions used when stresses are induced is relevant, namely the temperature range, ΔT, which is relevant to stress formation and the distance over which this is applied. The geometry and size of this region is determined by the processing parameters according to the equations in Figure 6.6 and this contributes to the magnitude of the thermally induced stress according to Equation 6.6. Increasing the absorbed power (by increasing the nominal power of the heat source or using a material with higher absorptivity) and reducing the beam velocity have the effect of increasing the penetration depth of the thermal energy which increases melt depth and hence the distance between the isotherms which represent the critical ΔT to generate thermal stress. This was shown previously in Chapters 4 and 5 for laser melting of Inconel 718. Increasing the penetration depth was shown to reduce the temperature gradient which in turn reduces the magnitude of the residual stresses (Kruth 2004, Mercelis 2006). It was discussed in Section 6.2.1 that to reduce temperature gradient when operating at maximum power it is necessary to reduce beam velocity as indicated by the red arrow in Figure 6.12. It is clear that doing this will reduce the processing speed also.

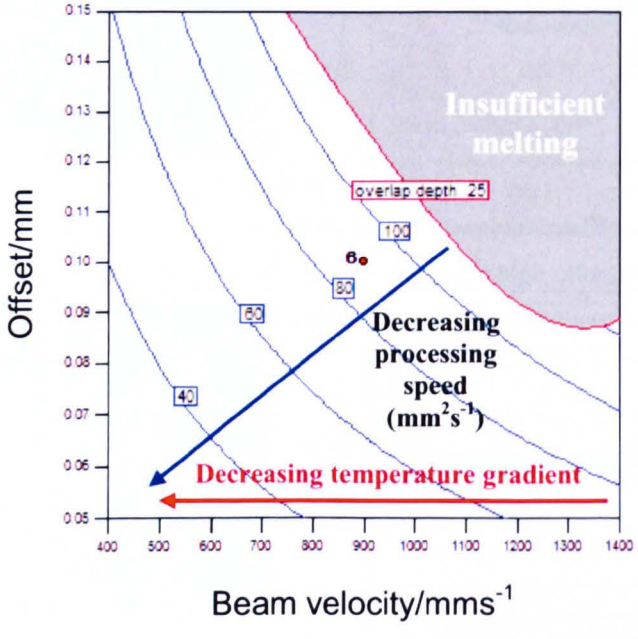

Figure 6.12 - Overlay plot showing the effect of beam velocity and track offset on processing speed and melt depth in the region where adjacent tracks overlap (μm, outlined in red). Also highlighted is the limit where melting is not sufficient to produce fully dense parts. Blue arrow indicates the effect of beam velocity and track offset on overall processing speed.

Another processing parameter which might be used to affect a change is increasing the substrate temperature, T_0, doing this is common practise for welding some metals to minimise distortion (processes such as TIG washing) and is inherent in some ALM systems such as Electron Beam Melting (EMB, Arcam AB) which require sintering of loose powder prior to melting. This is achieved by rapidly moving the defocused electron beam over the surface of the bed to increase the overall temperature without localised melting. An elevated T_0 temperature will reduce ΔT ($=T_{max}-T_0$) and hence lower the thermally induced stress according to Equation 6.4, if the temperature is sufficient then thermally activated recovery mechanism will also become relevant and stress relieving occurs in-situ. Increasing T_0 will also increase a materials absorptivity due to the increase in electrical resistivity. Absorptivity is also dependant on the wavelength of the radiation used as shown in Figure 6.3 and if an electron beam is used the issue of absorptivity is negligible as long as plasma formation is avoided. Increasing T_0 also has a pronounced effect on the thermal conditions during solidification, in particular on the temperature gradient which is greatly reduced and may expand the processing window of the systems used in this study to potentially manipulate microstructure and avoid epitaxy allowing the development of equiaxed grain structures. To incorporate T_0 as a processing parameter in ALM systems would not be straight forward as existing machines may not be constructed from suitable materials to operate at elevated temperatures. Also consideration is necessary of the operation and accuracy of optics and efficiency of heat sources which may require extra cooling considerations. Holding loose powder at elevated temperatures necessary to mitigate stresses may also induce solid-state sintering of particles which would potentially alter their morphology and cause them to be unusable in subsequent processing, and it may also increase the chance of oxide formation.

Material selection maps such as Figure 6.10 can be used to identify specific alloys' properties which are attractive or problematic for ALM. Figure 6.10 highlights some typical ALM alloys; Inconel 718 and CoCrMo have similar stress performance indicated by their properties but Inconel 718 has a higher absorptivity and lower melting point. This means it can be processed at a higher beam velocity. Stainless Steel alloy 17-4 and CoCrMo have comparable melting temperatures and absorptivity but significantly different stress performance index values, 17-4 having a significantly lower value; this means it can tolerate a higher temperature gradient and therefore can be processed using a higher beam velocity.

The materials selection maps can be used to compare the properties of alloys which are not yet used in ALM to those already in use to form a logical starting point for developing a theme. For example, stainless steel grade 316 has a similar absorptivity and melting temperature to 17-4 but a stress performance index value closer to that of

CoCrMo so this alloy may require processing with lower beam velocities to reduce the temperature gradient and hence the magnitude of the residual stress.

Other Nickel alloys which may be considered are Hastelloy X and Inconel 625; these have comparable absorptivities and melting temperatures to Inconel 718 but slightly higher stress performance index values and so would most likely require a lower beam velocity than Inconel 718 (or indeed a higher laser power and T_0 if this is possible). Similar behaviour is seen in the different alloy classes where differing compositions yield alloys with the same absorptivity but ones which would generate lower stresses during processing. Obviously, different alloys are designed for specific ranges of properties and other considerations are necessary to compare suitability for the final product not just for ease of processing. An alloy's chemistry includes allowable ranges for specific elements which means that there may be scope to manipulate an alloys chemistry to affect the stress response on solidification and cooling by reducing its α_{CTE}.

Some alloying elements contract on freezing; for example Aluminium and Nickel can shrink by 6.5%, Co by 5.5% and Fe 3.5% but others expand such as C, Si, Bi, Sb and In and it is common practise to use C to reduce solidification shrinkage in Fe and Steel and likewise Si in Al (Polmear 1995).

An alloy which exhibits suitable properties to minimise thermal stress will have a good absorptivity and low stress performance value, the Invar alloys labelled in Figure 6.10 are such examples. Conversely there are a number of CoCr alloys which appear to have properties which will result in high stresses and so would require measures during processing to reduce the magnitude of the stress.

The method described for selecting alloys based on their thermo-physical properties and assigning processing parameters based there-on does not take into account a number of other issues. Many alloys will not be suitable to ALM on the basis of price; this may be due to the cost of atomisation or simply that the economics of ALM are not suitable for the intended part. Some alloys will also undergo phase transformations during cooling which may have a volume change associated with them. Such a volume contraction or expansion could contribute to the stress induced by thermal contraction or indeed counteract the effect, in such cases it may be necessary to hold a processing temperature above a phase transformation temperature and conduct a more controlled cool down.

At the beginning of this chapter it was noted that current ALM alloys are not designed for use in ALM and that in the future, alloys would be designed or altered to suit the conditions experienced in ALM. Control of α_{CTE} has been discussed previously to minimise residual stresses which are inherent in ALM but further to this it has been shown in welding that it is possible to use alloys with low transformation

temperatures (known as *LTT* alloys) as weld filler material which undergoes a Martensitic phase transformation and has a net expansion on cooling so that the residual stress in the weld is actually compressive (Ohta 1999). These alloys were developed based on a Steel containing 10% each of Ni and Cr to give a Martensite-start (M_s) temperature of 180°C which is completed at room temperature; this is compared to the base metal which undergoes the phase transformation at 590°C. Ohta et al. used the alloys as weld filler to improve fatigue strength of box welds by removing the detrimental tensile residual stress which works against fatigue crack closure for a Ferrite-Pearlite steel welded by Gas Metal Arc Welding. The presence of a compressive residual stress is known to be beneficial to fatigue strength and is normally achieved by a post welding shot-peening procedure. The use of *LTT* alloys makes this possible without this secondary processing stage (Suzuki 2004). Bhadeshia (Bhadeshia 2004) discussed the mechanisms involved in *LTT* alloys in detail relative to shape deformation. It was further suggested that the remaining residual stress in the welds at ambient temperature is reduced for alloys with lower transformation temperatures, this phenomenon could be used in the next generation of ALM alloys which can be processed with zero residual stress. The *LTT* allows shape deformation to compensate for accumulated strains from thermal contraction by exploiting transformation plasticity; since the coefficient of thermal expansion for austenite (CTE_γ) is greater than that of Ferrite (CTE_α) the volume expansion due to the transformation is larger at lower temperatures. If the transformation is exhausted much before ambient temperature is reached then contraction of the Ferrite phase takes place in the final stages of cooling, this is shown in Figure 6.13. The Yield Strength of Ferrite is high so less of the contraction is accommodated by plastic relaxation; this contraction is what leads to the tensile residual stress in conventional alloys.

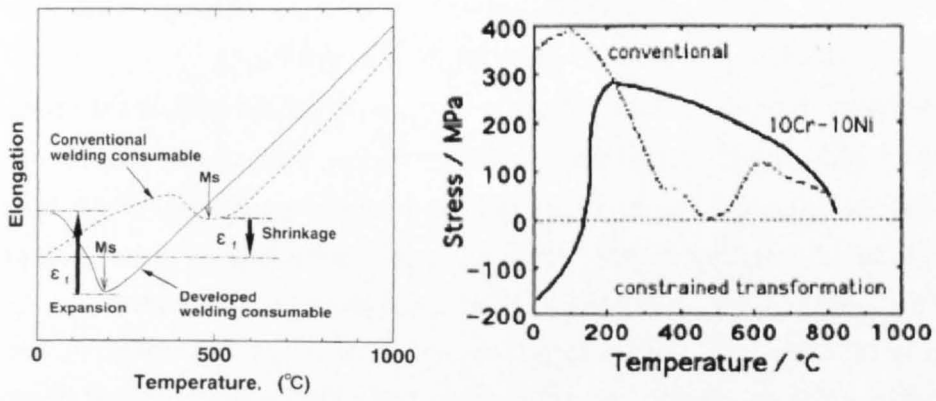

Figure 6.13 – (a) Expansion and contraction and (b) stress as a function of temperature for alloys undergoing Martensitic phase transformations.

6.3 Chapter summary

As discussed at the beginning of Chapter 4, no processing theme was available for Inconel 718 on the EOS M270 at the start of this project. To begin using this material, some thought was put into the initial parameters to be used; this involved comparing the theme for a commonly used alloy (CoCrMo) and its material properties to the properties of Inconel 718. Figure 6.3 shows that Inconel 718 has a higher absorptivity and lower liquidus temperature than CoCrMo, comparing the other properties plotted in Figure 6.4 to Figure 6.10 the two alloys are very similar and so can potentially be melted using the same laser power and beam velocity. Based on the lower melting temperature and higher absorptivity, Inconel 718 can potentially be melted using lower power or faster beam velocities, the latter making it possible to reduce processing time.

This Chapter has expanded this procedure to compare a number of alloys against key materials properties to consider for melting thus making it possible to identify alloys which may be difficult to process. These properties have been identified as the melting temperature (liquidus temperature), T_l, the thermal conductivity, k, and the absorptivity at a given temperature and wavelength, η. Conductivity and η are inversely related for most alloy so not all display the desirable *(high η)/(low k)* ratio, Ti alloys fulfil this criteria but Al does not and so may be difficult to process by laser melting.

Further to melting there must be consideration of residual stresses caused by volume change on heating/cooling. The key properties which contribute to this are Young's Modulus, E, thermal conductivity, k, and the coefficient of thermal expansion. An example alloy where these properties could be significant is the Ni-based alloy Hastelloy-X which has similar melting temperature and absorptivity to Inconel 718, but is prone to generating higher thermal stresses. This means it is necessary to reduce the temperature gradient during processing.

It was shown that manipulating processing parameters can reduce the magnitude of the stress by reducing the temperature gradient during heating and that an increase in the substrate temperature can in theory reduce the stress generated. If this is sufficient it can facilitate thermally activated recovery mechanisms and even be used to further manipulate solidification conditions to affect changes in microstructure.

Thermal conductivity and absorptivity are seen to be important in melting of alloys and in stress generation. To minimise stress a high conductivity is desirable but alloys with this trait are also more likely to have reduced absorptivity, this means that in order to maintain high absorption the α_{CTE} is key to minimise stress, so a lower α_{CTE} is desirable.

Performance Indices or *Indicators* are used to compare aspects of materials' response to processing by combining several material properties which may need to be maximised or minimised in order to avoid high residual stresses through alloy choice. These are used to further compare alloys and identify examples which may be good candidates for ALM or ones which may require special consideration to control stresses and manage heat input during processing.

7 Conclusions

The main findings of the current investigation are summarised in this section and conclusions drawn. As set out in the opening section the key areas addressed were; identification of key process variables, analysing the melting response to user defined variables, Analytical modelling of the melt pool geometry and the local solidification conditions, investigation of the as-deposited grain structure.

To summarise;

- Statistically designed experiments were used successfully to accurately fit empirical models relating weld track geometries and surface roughness to key process parameters. DOE was shown to be an efficient way to investigate as sufficient data was collected from relatively few *trials* and the resulting models are useful tools in *theme* development and microstructure selection.

7.1 Melting response

- Processing maps were developed to select parameters suitable to build fully dense parts as well as maximise build speed.

- Power, velocity and beam diameter were shown to be most important for determining the track geometry. Knowing the effect of heat input on track geometry allows *track offset* to be set so that a consistent melt depth in a layer can be achieved. This forms the basis of a *theme* to build simple geometries.

- It is apparent from the investigation that there are numerous combinations of parameters which can be used to produce fully dense parts. These will impact on the speed of the *hatching* process and ultimately the build speed.

- Thinner powder layers and sufficient overlap of adjacent *tracks* are most important for removing porosity.

7.2 Solidification

- Simple analytical heat transfer models are suitable to model the solidification front by fitting the models to experimental measurements. The models can be used qualitatively to compare the effect processing parameters (laser power and beam velocity) have on the size and shape of melt pools. This provides insight into the local heat transfer of individual pools which was shown to impact on the resulting microstructure.

- The models were used to calculate the local solidification conditions to establish how these vary along the solidification front and processing maps were produced to show variation with processing parameters. This makes it possible for an ALM user to choose processing parameters to select different microstructures, for example, temperature gradient and isotherm velocity can be manipulated to control grain morphology through the columnar to equiaxed transition, or cooling rate can be controlled to influence the size and shape or even suppress the formation of secondary phases.

7.3 Microstructure

- The heat transfer models are useful prediction tools and showed good agreement with the resulting metal microstructures. However the processing windows of the EOS and DMD impose limits on the range over which the model can be tested.

- The microstructure of the as deposited metal samples were analysed by EBSD to reveal the grain structure and orientation. Grain structure did not vary over the *region of interest* for the EOS and all samples show a highly directional columnar structure with a strong (001) orientation, this is because of the relatively flat meltpools but in particular the layer thickness used. The bottom 20μm of a meltpool is the region where the microstructure is retained and does not change in incline angle significantly, hence heat flow is almost uni-directional for all parameters used. The isotherm velocity in this region is relatively low and the temperature gradient is highest, these conditions favour epitaxial growth and columnar grains.

- Three distinct types of microstructure were observed in the DMD samples; a complicated mixed structure at high powers and high beam velocities caused by

melt pool fluctuations, long zigzag grains which are continuous across multiple layers at the higher beam velocity settings and elongated but non-continuous grains at slower beam velocities. The shape of the melt pool is critical in determining grain morphology; at slower beam velocities the pool is highly curved which means grains will grow towards the centreline of the wall and they are forced to change direction to follow the direction of heat transfer. At a faster beam velocity the weld pools are flatter, which allows heat transfer and grain growth to be close to vertical in the central region of the wall with resulting grains being able to grow epitaxially through layer boundaries. As with the EOS the layer thickness or *z-step* is important as this determines the amount of underlying material to be remelted. If the remelted zone is large, only the bottom of the melt pool is responsible for the retained microstructure so even large curved pools will produce long columnar grains in all but the very top of the deposit.

- There is a columnar to equiaxed transition close to the top surface where the combination of high isotherm velocity and low temperature gradient make conditions favourable for equiaxed grains. If this region is not completely remeted then the fine equiaxed grains are retained in the microstructure and the long continuous columnar grains are avoided, this was not observed in the present investigation but can explain the presence of some equiaxed grain structures from laser deposition reported in the literature. In this case the criteria for equiaxed growth may not be reached but the grains are elongated over the length of the weld track. The random orientation of the underlying equiaxed material mean that the deposit about is not a sufficient size for a preferred orientation to be achieved.

7.4 Other considerations

- Rationale for processing parameter selection based on comparisons between existing and potential ALM materials and their thermo-physical properties was made. Key materials properties to consider for melting are the melting temperature, the thermal conductivity, k, and the absorptivity at a given temperature. When plotted as a materials selection chart or bubble-chart, this makes it possible (along with initial metallurgical knowledge of an alloy system, for example, of phase transformations) to compare an alloy to other existing ALM materials and hence select appropriate starting parameters to achieve fully dense parts.

- Consideration of residual stresses caused by volume change on heating/cooling is made, key properties which contribute to this are Young's Modulus, thermal conductivity, and the coefficient of thermal expansion.

- Residual stress is shown to be high in ALM so controlling/minimising this is advantageous. Despite the apparent inability to significantly manipulate grain morphology, the fact that a range of processing parameters can achieve a fully dense part means that there is scope to manipulate other factors such as thermally induced stress by altering the heat input into the system.

- It was suggested that manipulating processing parameters can reduce the magnitude of the stress by reducing the temperature gradient and that an increase in the substrate temperature can, in theory, reduce the stress generated.

7.5 Further work

7.5.1 Heat treatment

- The work presented in this thesis has focussed on the as-deposited material. Post-process heat treatment is a vast subject which must be explored but was outside the scope of this project.

- ALM materials experience residual stress which is detrimental to performance in service and stress relieving heat treatments are documented for many alloys.

- For alloys such as Inconel 718 which is a precipitation strengthened alloy, the aging response must be investigated. The residual stress from AML must be removed as rafting of precipitates in the presence of stress can cause anisotropy or inferior properties.

7.5.2 Mechanical properties

- This study has only considered the hardness of the deposited samples; further detailed investigation is required to test the properties of ALM materials at a range of temperatures with the view to generating a database of ALM properties similar to other processes.

- In high-end applications static and dynamic testing is necessary; in particular in high temperature applications for Superalloys creep is of paramount importance. The highly directional nature of the microstructures (in particular the EOS structures) could be beneficial in this case when the grains are aligned with the principal stress axis.

- The effect of surface finish has an impact on properties such as fatigue performance so testing should take into account the as-deposited surface as well as various finishing techniques.

7.5.3 Other work

- Not all process variables were investigated in this study. As a result of the theoretical discussion in Chapter 6 the substrate temperature has been identified as having potential impact in several areas.

- The residual stress can be mitigated by increasing the build temperature and can affect the solidification conditions. This warrants further investigation as the potential to expand the processing window is attractive in controlling microstructure beyond current capabilities.

- More alloys are required to test some of the theories discussed in Chapter 6, in particular the effect of material properties on magnitude of residual stress and how the processing parameters should be altered to account for this. This will contribute to a database of alloys which will have accepted processing *themes* which can be used on a range of ALM systems.

- Manipulation of alloy composition is also of interest when minimising residual stress is the aim. This should be tested with existing and model alloys to assess whether the impact is significant.

8 References

Ahmadi M, Vahabzadeh F, Bonakdarpour B, Mofarrah E, Mehranian M. (2005), ***Application of the Central Composite Design and Response Surface Methodology to the Advanced Treatment of Olive Oil Wastewater using Fenton's Peroxidation***, Journal of Hazardous Materials B, **Volume 123**, Pages 187-195,

Akihiko O. (1999), ***Double Fatigue Strength of Box Welds by LTT Weld Wire***, Journal of Construction Steel, **Volume 7**, Pages 173-180.

Antonsson T, Fredriksson H. (2006), ***The Effect of Cooling Rate on the Solidification of INCONEL 718***, Metallurgican and Materials Transactions B, **Volume 36B**, Pages 85-96.

Armitage J R. (1991), ***Introduction of Glass Fibre Lasers and Amplifiers***, in France P W, ***Optical Fibre Lasers and Amplifiers***, Blackie & Sons, East Kilbride, Scotland.

Aslan N. (2008), ***Application of Response Surface Methodology and Central Composite Rotatable Design for Modelling and Optimisation of a Multi-gravity Separator for Chromite Concentration***, Powder Technology, **Volume 185**, Pages 80-86.

ASM Specialty Handbook. (2000), ***Nickel, Cobalt and Their Alloys***, Edited by Davis J R, AMS International, Ohio, US.

Barber J R. (1971), ***The Effect of Thermal Distortion on Constriction Resistance***, International Journal of Heat and Mass Transfer, **Volume 14**, Pages 751-766.

Baufeld B, van der Biest O. (2009), ***Mechanical properties of Ti-6Al-4V specimens produced by shaped metal deposition***, Science Technology of Advanced Materials, Volume 10, Pages 1-10.

Benyounis K Y, Olabi A G, Hashmi M S J. (2005a), ***Effect of Laser Wedling Parameters on the Heat Input and Weld-bead Profile***, Journal of Materials Processing Technology, **Volume 164-165**, Pages 978-985.

Benyounis K Y, Olabi A G, Hashmi M S J. (2005b), ***Optimising the Laser-welded Butt Joints of Medium Carbon Steel Using RSM***, Journal of Materials Processing Technology, **Volume 164-165**, Pages 986-989.

Bertram L A. (1996), ***A Digital Rykalin Function for Welding***, Sandia National Laboratories Report, Albuquerque NM, US, **Number SAND97-8225**, accessed at **http://www.osti.gov/bridge/servlets/purl/481611-o4OmZ/webviewable/481611.pdf** on 7/11/2009.

Bhadeshia H K D H. (2004), ***Developments in Martensitic and Bainitic steels: role of the shape deformation***, Materials Science and Engineering A, **Volume 378**, Pages 34–39.

Blackwell P L. (2005), ***The mechanical and microstructural characteristics of Laser-deposited Inconel 718***, Journal of Materials Processing Technology, **Volume 170**, Pages 240–246.

Bontha S. (2006a), ***The Effect of Process Variables on Microstructure in Laser-Deposited Materials***, PhD Thesis, Wright State University, Dayton, Ohio, US.

Bontha S, Klingbeil N W, Kobryn P A, Fraser H L. (2006b), ***Thermal process maps for predicting solidification microstructure in laser fabrication of thin-wall structures***, Journal of Materials Processing Technology, **Volume 178**, Issues 1-3, Pages 135-142.

Bramson M A. (1968), ***Infrared Radiation: A Handbook for Applications***, in ***Optical Physics and Engineering***, Plenum Press, New York, US.

Branchu S, Forbes R T, York P, Nyqvist H, ***A Central Composite Design to Investigate the Thermal Stabilization of Lysozyme***, Pharmaceutical Research, 1999, **Volume 16**, Issue 5, Pages 702-708.

CES Selector 2008 Software. (2008), Granta Design Ltd., Cambridge, UK.

Chandler H. (2006) ***Heat Treater's Guide: Practice and Procedures for Nonferrous Alloys***, ASM International, Ohio, US.

Cheng P J, Lin S C. (2000), ***Using neural networks to predict bending angle of sheet metal formed by laser***, International Journal of Machine Tools and Manufacture, **Volume 40**, Issue 8, Pages 1185-1197.

Cheng P J, Lin S C. (2001), ***An analytical model to estimate angle formed by laser, Journal of Materials Processing Technology***, **Volume 108**, Issue 3, Pages 314-319.

Choi D S, Lee S H, Shin B S, Whang K H, Song Y A, Park S H, Jee H S. (2001), ***Development of a direct metal freeform fabrication technique using CO_2 laser welding and milling technology***, Journal of Materials Processing Technology, **Volume 113**, Issues 1-3, Pages 273-279.

Clark D, Bache M R, Whittaker M T. (2008), ***Shaped metal deposition of a nickel alloy for aero engine applications***, Journal of Materials Processing Technology, **Volume 203**, Pages 439–448.

Cline H E, Anthony T R. (1977), ***Heat Treating and Melting Material With a Scanning Laser or Electron Beam***, Journal of Applied Physics, **Volume 48**, Issue 9, Pages 3895-3900.

Costa L, Vilar R, Reti T, Deus A M. (2005), ***Rapid Tooling by Laser Powder Deposition: Process Simulation Using Finite Element Analysis***, Acta Materialia, **Volume 53**, Pages 3987-3999.

Coulon. (2006), ICALEO 2006 – Congress Proceedings, Laser Materials Processing Conference, Paper Number 1803, Pages 888-897.

CVI Melles Groit, https://www.cvimellesgriot.com/products/Documents/TechnicalGuide/Basic_Laser_Principles.pdf, accessed on 18/10/2006.

David S A, Vitek J M. (1993), ***Analysis of Weld Metal Solidification and Microstructure***, in ***Mathematical Modelling of Weld Phenomena***, edited by Cerjal H, Easterling K E, Institute of Materials, University Press, Cambridge, UK.

Davies H A, Shohoji N, Warrington D H. (1980), ***The Structure of Rapidly Quenched Nickel-beased Superalloy Ribbons Produced by Melt Spinning***, in ***Rapid Solidification Processing: Principles and Technologies II, Proceedings of the 2nd International Conference on Rapid Solidification Processing***, Edited by Mehrabian R, Kear B H, Cohen M, 1980, Pages 153-164, Baton Rouge, Claitor's Publishing Division, US.

Davis O L. (1978), ***The Design and Analysis of Industrial Experiments***, 1978, Longman Group Limited, London, UK.

Dinda G P, Mazumder J, Song L. (2006), ***Microstructure and Mechanical Properties of Laser-deposited Ti-6Al-4V Scaffold***, ICALEO 2006 – Congress Proceedings, Laser Materials Processing Conference, Paper Number 1501, Pages 695-700.

Djoudi W, Aissani-Benissad F, Bourouina-Bacha S. (2007), ***Optimisation of Copper Cementation Process by Iron Using Central Composite Design Experiments***, Chemical Engineering Journal, **Volume 133**, Pages 1-6.

Donachie M J, Donachie S J. (2002), ***Superalloys: A Technical Guide, 2nd Ed.***, ASM International, Ohio, US.

Drezet J-M, Pellerin S, Bezencon C, Mokadem S. (2004), ***Modelling the Marangoni convection in laser heat treatment***, Journal de Physique IV, 2nd International Conference Thermal Process Modelling and Computer Simulation, Pages 1-8.

Durand-Charre M. (1997), ***The Microstructure of Superalloys***, Gordon and Breach Science Publishers, Amsterdam, The Netherlands.

Dye D, Hunziker O, Reed R C. (2001), ***Numerical Analysis of the Weldability of Superalloys***, Acta Materialia, **Volume 49,** Pages 683-697.

Elsen van M, Al-Bender F, Kruth JP. (2008), ***Application of dimensional analysis to selective laser melting***, Rapid Prototyping Journal, **Volume 14**, Issue 1, Pages 15-22.

Fischer P, Romano V, Weber H P, Karapatis N P, Boillat E, Glardon R. (2003), ***Sintering of commercially pure titanium powder with a Nd:YAG laser source***, Acta Materialia, **Volume 51, Pages** 1651–1662.

Gäumann M. (1999a), ***Epitaxial Laser Metal Forming of Single Crystal Superalloy***, PhD Theses Number 1907, Ecole Polytechnique Federale du Lausanne, Switzerland.

Gäumann M, Henry S, Cléton F, Wagnière J -D, Kurz W. (1999b), ***Epitaxial laser metal forming: analysis of microstructure formation***, Materials Science and Engineering A, 1999b, **Volume 271**, Pages 232–241.

Grundy P J, Jones G A. (1976), ***Electron Microscopy in the Study of Materials***, in ***The Structure and Properties of Solids 7***, Edited by Coles B R, Edward Arnold Limited, Bristol, UK .

Gunaraj V, Murugan N. (1999), ***Application of Response Surface Methodology for Predicting Weld Bead Quality in Submerged Arc Welding of Pipes***, Journal of Materials Process Technology, **Volume 88**, Pages 266-275.

Hofmeister W, Wert M, Smugeresky J, Philliber J A, Griffith M, Ensz M. (1999), ***Investigating Solidification with the Laser-Engineered Net Shaping (LENS^{TM}) Process,*** JOM, Volume 51, Issue 7.

Hollander D A, von Walter M, Wirtz T, Sellei R, Schmidt-Rohlfing B, Paar O, Erli H -J, Structural. (2006), ***mechanical and in vitro characterization of individually structured Ti–6Al–4V produced by direct laser forming***, Biomaterials, **Volume 27**, Pages 955–963.

Hopkins N, Hague R J M, Dickens P M. (2005), ***Rapid Manufacturing: An Industrial Revolution for the Digital Age***, J Wiley & Sons Ltd, Chichester, UK.

Hunziker O, Dye D, Reed R C. (2000), ***On The Formation of a Centreline Grain Boundary During Fusion Welding***, Acta Materialia, **Volume 48**, Pages 4191-4201.

Ion J C. (2005), ***Laser Processing of Engineering Materials: Principals, Procedure and Industrial***, Elsevier Butterworth-Heinemann, Oxford, UK.

Jeong Y, Sahu J K, Payne D N, Nilsson J. (2004), ***Ytterbium-doped large-core fiber laser with 1.36 kW continuous-wave output power***, Optics Express, **Volume 12** Issue 25, Pages 6088-6092.

Kobryn P A, Moore E H, Semiatin S L. (2000), ***The Effect of Laser Power and Traverse Speed on Microstructure, Porosity and Build Height in Laser-deposited Ti-6Al-4V***, Scripta Materialia, **Volume 43**, Pages 299-305.

Kobryn P A, Semiatin S L. (2003), ***Microstructure and texture evolution during solidification processing of Ti–6Al–4V***, Journal of Materials Processing Technology, **Volume 135**, Pages 330–339.

Kruth J P, Wang X, Laoui T, Froyen L. (2003), ***Lasers and materials in selective laser sintering***, Assembly Automation, **Volume 23**, Issue 4, Pages 357–371.

Kruth J P, Froyen L, Vaerenbergh van J, Mercelis P, Romboutsb M, Lauwers B. (2004), ***Selective laser melting of iron-based powder***, Journal of Materials Processing Technology, **Volume 149**, Pages 616–622.

Kurz W, Fisher D J. (1992), ***Fundamentals of Solidification 3rd Ed.***, Trans Tech Publications, Switzerland.

Kurz W, Bezençon C, Gäumann M. (2001), ***Columnar to Equiaxed Transition in Solidification Proceassing***, Science and Technology of Advanced Materials, **Volume 2**, Pages 185-191.

Labudovic M, Hu D, Kovacevic R. (2003), ***A Three Dimensional Model for Direct Laser Metal Powder Deposition and Rapid Prototyping***, Journal of Materials Science, **Volume 38**, Pages 35-49.

Limmaneevichitr C, Kou S. (2000), ***Visualisation of Marangoni Convection in simulated Weld Pools*** Welding Research Supplement to The Welding Journal, **May 2000**, Pages 126-135.

Liu W, DuPont J N. (2004), ***Effects of melt-pool geometry on crystal growth and microstructure development in laser surface-melted superalloy single crystals. Mathematical modelling of single-crystal growth in a melt pool (part I)***, Acta Materialia, **Volume 52**, Pages 4833 – 4837.

Liu Y, Huang X, Li Y, Peng H. (2006), ***Microstructure and Mechanical Properties of Laser Net Shape Manufactured Inconel 718 and Ti-6Al-4V Components***, ICALEO 2006 Congress Proceedings, Laser Materials Processing Conference, **Paper 301**, Pages 110-116.

Liu J, Li L. (2007), ***Effects of Process Variables on Laser Direct Formation of Thin Wall***, Optics & Laser Technology, **Volume 39**, Pages 231-236.

Maeda K, Childs T H C. (2004), ***Laser sintering (SLS) of hard metal powders for abrasion resistant coatings*** , Journal of Materials Processing Technology, **Volume 149**, Issues 1-3, Pages 609-615.

Mahan G D, Bartkowiak M. (1999), ***Wiedemann-Franz Law at Boundaries***, Applied Physics Letters, **Volume 74**, Issue 7, Pages 953-954.

Matsumoto M, Shiomi M, Osakada K, Abe F. (2002), ***Finite element analysis of single layer forming on metallic powder bed in rapid prototyping by selective laser processing***, International Journal of Machine Tools & Manufacture, **Volume 42**, Pages 61–67.

Matz J E, Eagar T W. (2002), ***Carbide Formation in Alloy 718 during Electron-Beam Solid Freeform Fabrication***, Metallurgical and Materials Transactions A, **Volume 33A**, Pages 2559-2567.

Mazumder J, Schifferer A, Choi J. (1999), ***Direct materials deposition: designed macro and microstructure***, Materials Research Innovations, **Volume 3**, Pages 118–131.

McLean M. (1983), ***Directionally Solidified Materials For High Temperature Service***, The Metals Society, Bristol, UK.

Meacock C, Vilar R. (2008), ***Laser powder micro deposition of CP2 Titanium***, Materials & Design, **Volume 9**, Pages 353-361.

Mercelis P, Kruth J P. (2006), ***Residual stresses in selective laser sintering and selective laser melting***, Rapid Prototyping Journal, **Volume 12**, Issue 5, Pages 254–265.

Milewski J O, Dickerson P G, Nemec R B, Lewis G K, Fonseca J C. (1999), ***Application of a manufacturing model for the optimization of additive processing of Inconel alloy 690***, Journal of Materials Processing Technology, **Volume 91**, Issues 1-3, Pages 18-28.

Moat R J. (2009), ***Microstructure and Residual Stress Characterisation of Laser Deposited Nickel-based Superalloy Test Structures***, PhD Thesis, University of Manchester, Manchester, UK.

Montgomery D C. (1997), ***Design and Analysis of Experiments, 4th Ed.***, John Wiley & Sons Inc., New York, US.

Murali K, Chatterjee A N, Saha P, Palai R, Kumar S, Roy S K, Mishra P K, Choudhury A R. (2003), ***Direct selective laser sintering of iron–graphite powder mixture***, Journal of Materials Processing Technology, **Volume 136**, Pages 179–185.

Myers R H, Montgomery D C. (2002), ***Response Surface Methodology: Process and Product Optimisation Using Designed Experiments***, John Wiley & Sons Inc., New York, US.

Nguyen N T, Ohta A, Matsuoka K, Suzuki N, Maeda Y. (1999), ***Analytical Solutions for Transient Temperature if Semi-Infinite Body Subject to 3-D Moving Heat Sources***, Welding Research Supplement to The Welding Journal, **August 1999**, Pages 265-274.

Nickel A H, Barnett D M, Prinz F B. (2001), ***Thermal stresses and deposition patterns in layered manufacturing***, Materials Science and Engineering A, **Volume 317**, 59–64.

NIST/SEMATECH ***e-Handbook of Statistical Methods***, http://www.itl.nist.gov/div898/handbook/, Accessed on 28/06/2009, (created on 01/06/2003).

Nurminen J, Riihimäki J, Näkki J, Vuoristo P. (2006), ***Comparison of Laser Cladding with Powder and Hot and Cold Wire Techniques***, ICALEO 2006 – Congress Proceedings, Laser Materials Processing Conference, Paper Number 1006, Pages 635-637.

Ohta A, Suzuki N, Maeda Y, Hiraoka K, Nakamura T. (1999), ***Superior fatigue crack growth properties in newly developed weld Metal***, International Journal of Fatigue, **Volume 21**, Pages 113–S118.

Olivera de U, Ocelik V, Dehosson J Th M. (2005), ***Analysis of coaxial laser cladding processing conditions***, Surface & coatings technology, **Volume 197**, Pages 127-136.

O'Neill W, Sutcliffe C J, Morgan R, Landsborough A, Hon K K B. (1999), ***Investigation on Multi Layer Direct Metal Laser Sintering of 316L Stainless Steel Powder Beds***, Annals of the CIRP, **Volume 48**, Issue 1, 151-154.

Peng L, Taiping Y, Sheng L, Dongsheng L, Qianwu H, Weihao X, Xiaoyan Z. (2005), ***Direct laser fabrication of nickel alloy samples***, International Journal of Machine Tools and Manufacture, **Volume 45**, Issue 11, Pages 1288-1294.

Peyre P, Aubry P, Braham C, Fabbro R. (2006), ***Results on Laser Direct Manufacturing of Graded Materials***, ICALEO 2006 – Congress Proceedings, Laser Materials Processing Conference, Paper Number 303, Pages 127-132.

Pinkerton A J, Li L. (2004a), ***Modelling the Geometry of a Moving Laser Melt pool and Deposition Track Via Energy and Mass Balances,*** Journal of Physics D: Applied Physics, **Volume 37,** Pages 1885-1895,

Pinkerton A J, Li L. (2004b), ***The significance of deposition point standoff variations in multiple-layer coaxial laser cladding (coaxial cladding standoff effects)***, International Journal of Machine Tools & Manufacture, **Volume 44**, Pages 573–584.

Pinkerton A J, Li L. (2005a), ***Direct additive laser manufacturing using gas- and water atomized H13 tool steel powders***, International Journal of Advanced Manufacturing Technology, **Volume 25**, Issue 5-6, Pages 471-479.

Pinkerton A J, Li L. (2005b), ***Multiple-layer laser deposition of steel components using gas- and water-atomised powders: the differences and the mechanisms leading to them***, Applied Surface Science, **Volume 247**, Pages 175–181.

Pinkerton A J, Karadge M, Ul Haq Syed W, Li L. (2006), ***Thermal and microstructural aspects of the laser direct metal deposition of Waspaloy***, Journal of Laser Applications, **Volume 18**, Issue 3, Pages 216-226.

Polmear I J. (1995), ***Light Alloys: Metallurgy of Light Metals***, J Wiley & Sons, New York, US.

Porter D A, Easterling K E. (1988), ***Phase Transformations in Metal and Alloys***, Van Nostrand Reinhold (International) Co. Ltd, Wokingham, UK.

Randle V, Engler O. (2000), ***Introduction to Texture Analysis: Macrotexture, Microtexture & Orientation Mapping***, Gordon and Breach Science Publishers, Amsterdam, The Netherlands.

Reed R C. (2006), ***The Superalloys: Fundamentals and Applications***, Cambridge University Press, Cambridge, UK.

Rosenthal D. (1946), ***The Theory of Moving Sources of Heat and Its Application to Metal Treatments***, Transactions of the ASME, **Volume 68**, Pages 849-866.

Simchi A, Petzoldt F, Pohl H. (2003), ***On the development of direct metal laser sintering for rapid tooling***, Journal of Materials Processing Technology, **Volume 141**, Issue 3, Pages 319-328.

Snitzer E. (1991), ***Perspective and Overview***, in France P W, ***Optical Fibre Lasers and Amplifiers***, Blackie & Sons, East Kilbride, Scotland.

Special Metals (2006), ***Inconel Alloy 625***, Publication Number SMC-063, Special Metals Corporation, 2006 (Jan 06).

Steen W M. (1991), ***Laser Materials Processing***, Springer-Verlag, Berlin, Germany.

Strondl A, Fischer R, Frommeyer G, Schneider A. (2008), ***Investigations of MX and γ'/γ" precipitates in the nickel-based superalloy 718 produced by electron beam melting***, Materials Science and Engineering A, **Volume 480**, Pages 138–147.

Surtronic 3+ Operators Handbook, Taylor/Hobson Pneumo, Publication Number THP-HB-103, Issued Feb 1993.

Suzuki N. Ohta A. Maeda Y. (2004), ***Repair of fatigue cracks initiated around box welds using low transformation temperature welding material***, Welding International, **Volume 18**, Pages112-117.

Tin S, Lee P D, Kermanpur A, Rist M, McLean M. (2005), ***Integrated Modelling for the Manufacture of Ni-based Superalloy Discs from Solidification to Final Heat Treatment***, Metallurgical and Materials Transactions A, **Volume 36A**, Pages 2493-2504.

Ul Haq Syed W, Pinkerton A J, Li L. (2006), ***Combining wire and coaxial powder feeding in laser direct metal deposition for rapid prototyping***, Applied Surface Science, **Volume 252**, Pages 4803–4808.

University of Cambridge, DoITPoMs Micrograph Library, www.doitpoms.ac.uk/miclib/images/713-1.gif accessed on 24/2/2007.

Vasinonta A, Beuth J L, Griffith M L. (2001), ***A Process Map for Consistent Build Conditions in the Solid Freeform Fabrication of Thin-Walled Structures,*** Journal of manufacturing Science and Engineering, **Volume 123**, Pages 615-622.

Wang X C, Laoui T, Bonse J, Kruth J P, Lauwers B, Froyen L. (2002), ***Direct Selective Laser Sintering of Hard Metal Powders: Experimental Study and Simulation***, International Journal of Advanced Manufacturing Technology, **Volume 19**, Issue 5, Pages 351-357.

Wang W, Lee P D, McLean M. (2003), ***A model of solidification microstructures in nickel-based superalloys: predicting primary dendrite spacing selection***, Acta Materialia, **Volume 51**, Issue 10, Pages 2971-2987.

Wang L, Felicelli S. (2006a), ***Analysis of thermal phenomena in LENS™ deposition***, Materials Science and Engineering A, **Volume 435–436**, Pages 625–631.

Wang F, Mei J, Wu X. (2006b), ***Microstructure study of direct laser fabricated Ti alloys using powder and wire***, Applied Surface Science, **Volume 253**, Issue 3, Pages 1424-1430.

Wang L, Felicelli S. (2007), ***Process Modelling in Laser Depositoin of Multilayer SS410*** Steel, Transactions of the ASME, **Volume 129**, Pages 1028-1034.

Watkins K G, Edwardson S P, Magee J, Dearden G, French P. (2001), ***Laser Forming of Aerospace Alloys***, AMTC, Seattle, September 2001, (Society of Automotive Engineers, **Paper Number 2001-01-2610**).

Williams J C, Starke Jr. E A. (2003), ***Progress in structural materials for aerospace systems,*** Acta Materialia, **Volume 51**, Issue 19, Pages 5775-5799.

Withers P J, Bhadeshia H K D H. (2001), ***Residual stress Part 1 – Measurement techniques***, Materials Science and Technology, **Volume 17**, Pages 355-365.

Withers P J, Bhadeshia H K D H. (2001), ***Residual stress Part 2 – Nature and origins***, Materials Science and Technology, **Volume 17**, Pages 366-375.

Wu X, Sharman R, Mei J, Voice W. (2004), ***Microstructure and Properties of a Laser Fabricated Burn-resistant Ti Alloy***, Materials and Design, **Volume 25**, Pages 103-109.

Wu X, Liang J, Mei J, Mitchell C, Goodwin P S, Voice W. (2004), ***Microstructures of laser deposited Ti–6Al–4V***, Materials and Design, **Volume 25**, Pages 137–144.

Xie J W, Fox P, O'Neill W, Sutcliffe C J. (2005), ***Effect of direct laser re-melting processing parameters and scanning strategies on the densification of tool steels***, Journal of Materials Processing Technology, **Volume 170**, Pages 516–523.

Yoshimoto T, Ishihara S, Goshima T, McEvily A J, Ishizaki T. (1999), ***An Improved Method for the Determination of the Maximum Thermal Stress Induced During a Quench Test***, Scripta Materialia, **Volume 41**, Issue 5, Pages 553–559.

Zhang K, Liu W, Shang X. (2007), ***Research on the processing experiments of laser metal deposition shaping***, Optics & Laser Technology, **Volume 39**, Issue 3, Pages 549-557.

Zhao H, White D R, DebRoy T. (1999), ***Current issues and problems in laser welding of automotive aluminium alloys***, International Materials Reviews, **Volume 44**, Number 6, pp. 238-266.